Differential cross-section measurements of the associated production of top quarks with a photon at 13 TeV with the ATLAS detector

DISSERTATION
zur Erlangung des Grades eines
Doktors der Naturwissenschaften
(Dr. rer. nat.)

vorgelegt von
John Meshreki, M.Sc.
aus
Alexandria, Ägypten

eingereicht bei der Naturwissenschaftlich-Technischen Fakultät
der Universität Siegen
Siegen 2021

Betreuer und erster Gutachter:	Prof. Dr. Ivor Fleck Universität Siegen
Zweiter Gutachter:	Prof. Dr. Markus Cristinziani Universität Siegen
Tag der Disputation:	15.06.2021

Acknowledgements

I would like to sincerely thank my supervisor Prof. Dr. Ivor Fleck for giving me the opportunity to pursue my doctoral research at one of the top-tier experiments at CERN, which was a dream to me since I was a bachelor student and first heard about CERN and all the exciting research done there. I am most grateful for my supervisor's continuous support and for all the skills and professional experiences I built as a member of his group, and for supporting me to attend workshops and conferences in Germany and abroad. I would also like to thank Prof. Dr. Markus Cristinziani for reviewing and grading my thesis as the second reviewer as well as the other members of my Ph.D. committee, Prof. Dr. Markus Risse and Prof. Dr. Wolfgang Kilian.

I am thankful to all my colleagues in Siegen, Göttingen, Bonn and CERN with whom I collaborated over the years, learnt from and made this work possible. I would like to thank Dr. Carmen Diez Pardos for the day-to-day supervision, numerous discussions and helpful feedback, for pushing forward the analysis leading to a publication, and for her careful revision and comments on the thesis' draft which helped me to improve its quality. I would like to take this opportunity to express my gratitude to Dr. Yichen Li who helped me a lot in gaining technical skills as well as simplifying many of the new topics I faced at the beginning of my Ph.D. I can not thank you enough for all the support you gave me. I was also lucky to have wonderful, cheerful, and supportive colleagues in my $t\bar{t}\gamma$ Siegen group. I would like to thank Amartya Rej and Binish Batool for all the countless discussions and all the fun moments we shared in the office and in the schools and conferences we attended together. I am also thankful to Dr. Knut Zoch for his contribution to the $t\bar{t}\gamma$ $e\mu$ analysis as the lead analyser for the inclusive measurement.

I would like to express my gratitude to all my friends and especially Andreas Albu who has been there for me all along and supported me as a true, honest and reliable friend.

Last but not least, I would like to thank my family for making the impossible possible and for their constant encouragement and support. I would like to express my fullest and deepest gratitude to my mother for helping me achieve my dreams and for all the sacrifices she made so that my dreams come true. I am also very fortunate and ever grateful for having my beloved wife Reham who supported me in all the difficult times and has always believed in me and I am thankful to her for consistently giving me hope and strength to keep on going forward claiming my dreams.

Abstract

Absolute and normalised differential cross-sections for the associated production of top quarks with a photon are measured in proton-proton collisions data at a centre-of-mass energy of 13 TeV. The data were collected by the ATLAS detector during the full Run 2 of the LHC with an integrated luminosity of $139\,\text{fb}^{-1}$. The measurements are performed in the electron-muon decay channel in a fiducial phase space at parton level. The signal region is characterised by events with exactly one hard photon, one electron and one muon of opposite charge, at least two jets, among which at least one is b-tagged, and missing transverse energy. The differential cross-sections are measured as functions of photon kinematic observables, the minimum angular distance between the photon and the leptons, and angular separations between the two leptons. The results are compared to the most recent theory prediction at next-to-leading-order accuracy in QCD and state-of-the-art Monte Carlo simulations. The measurements are found to be in agreement with the Standard Model predictions within uncertainties.

Zusammenfassung

Absolute und normalisierte differentielle Wirkungsquerschnitte für die assoziierte Produktion von Top-Quarks mit einem Photon bei Proton-Proton-Kollisionen mit einer Schwerpunktsenergie von 13 TeV werden gemessen. Die Daten wurden vom ATLAS-Detektor während des gesamten Laufs 2 des LHC mit einer integrierten Luminosität von 139 fb^{-1} aufgezeichnet. Die Messungen werden im Elektron-Muon-Zerfallskanal in einem wohldefinierten Phasenraum auf Partonenebene durchgeführt. Der Signalbereich ist charakterisiert durch ein hochenergetisches Photon, ein Elektron und ein Myon mit entgegengesetzter Ladung, mindestens zwei Jets, von denen mindestens einer b-tagged ist, und fehlenden transversalen Impuls. Die differentiellen Wirkungsquerschnitte werden als Funktionen kinematischer Observablen des Photons, des minimalen Winkelabstands zwischen dem Photon und den Leptonen, und Winkelabstände zwischen den beiden Leptonen gemessen. Die Ergebnisse werden mit der neuesten Theorievorhersage mit NLO-Genauigkeit in QCD und dem Stand der Technik entsprechenden Monte-Carlo-Simulationen verglichen. Die Messungen sind in Übereinstimmung mit den Vorhersagen des Standardmodells im Rahmen der Unsicherheiten.

Contents

CHAPTER 1

Introduction

The Standard Model (SM) of elementary particles is the most successful theory to date in describing the building blocks of the universe and their interactions. Its current structure was completed in the 1970s, and since then, its predictions have been extensively tested. Through these experimental tests, all predictions of the SM have been confirmed. Despite its impressive success, however, the SM is not a final theory. For example, it does not explain the matter-antimatter asymmetry and does not yet include the gravitational force. These unreconciled topics, among others, are the main drive to continuously test predictions of the SM to the best achievable accuracy and simultaneously search for hints of new physics.

One of the pillars of the SM is the top quark. It is the heaviest elementary particle and the last quark to be discovered, found at the Tevatron Collider in 1995 [1, 2]. Its heavy mass implies a large Yukawa coupling to the Higgs boson, which points to its unique role in the electroweak symmetry breaking of the SM. The top quark has a very short lifetime and decays before hadronisation, allowing for studying its properties through its decay products. One of these properties is the electroweak coupling between the top quark and the photon. Such coupling can be probed at the Large Hadron Collider (LHC) by studying the associated production of a top-quark pair with a photon ($t\bar{t}\gamma$).

The evidence of the $t\bar{t}\gamma$ process was found with a 3.0 σ significance at the Tevatron Collider in proton-antiproton ($p\bar{p}$) collisions at centre-of-mass energy ($\sqrt{s}$) of 1.96 TeV, with an integrated luminosity of 6 fb^{-1} in 2011 [3]. The $t\bar{t}\gamma$ process was later observed by the ATLAS experiment in proton-proton (pp) collisions at $\sqrt{s}$ = 7 TeV at the LHC in 2015 [4]. The observation was perfomred in the lepton+jets channel with an integrated luminosity of 4.59 fb^{-1} and achieved a 5.0 σ significance. In 2017, the ATLAS experiment performed the first differential $t\bar{t}\gamma$ measurement at $\sqrt{s}$ = 8 TeV with an integrated luminosty of 20.2 fb^{-1} [5]. In the same year and at the same $\sqrt{s}$ of 8 TeV, the CMS experiment measured the ratio of cross-sections of $t\bar{t}\gamma$ to $t\bar{t}$ with an integrated luminosity of 19.7 fb^{-1} [6]. In 2019, the inclusive and differential $t\bar{t}\gamma$ cross-sections were measured in both the single lepton and dilepton channels. The measurements were performed by the ATLAS experiment at $\sqrt{s}$ = 13 TeV using collisions data with an integrated luminosity of 36.1 fb^{-1} [7]. This thesis presents the

most recent differential measurement of the production of top quarks in association with a photon, performed in the $e\mu$ channel at $\sqrt{s} = 13$ TeV using data from the ATLAS experiment, with an integrated luminosity of 139 fb^{-1} [8]. The measurements are compared for the first time to a full calculation at next-to-leading order in Quantum Chromodynamics, which includes resonant and non-resonant diagrams, interferences, and off-shell effects of the top quark [9]. Hence, the signal process of the measurements is the combined $t\bar{t}\gamma$ production and single top-quark production in association with a W boson and a photon ($tW\gamma$), which is referred to as $t\bar{t}\gamma + tW\gamma$.

This thesis is organised as follows. Chapter 2 presents a brief overview of the SM and discusses the physics of the top quark and the production of the $t\bar{t}\gamma$ process. An overview of the LHC and the experimental setup of the ATLAS detector is introduced in Chapter 3. A description of the algorithms used to reconstruct and select physics objects relevant to this work is detailed in Chapter 4. In Chapter 5, a method to improve the agreement of distributions related to the energy deposits of photons (referred to as shower shapes) between data and Monte Carlo simulations is presented. The data and Monte Carlo samples of signal and backgrounds and the selection applied at an object- and event-levels are described in Chapters 6 and 7, respectively. The fiducial phase-space definition, the strategy to perform the differential measurements, and the unfolding procedure and related studies are detailed in Chapter 8. Chapter 9 describes the systematic uncertainties considered in this work. The results of the absolute and normalised cross-sections are reported in Chapter 10, which is followed by conclusions and an outlook in Chapter 11.

Natural units are used throughout this thesis, $\hbar = c = 1$, where $\hbar$ and c are the reduced Planck constant and speed of light in vacuum, respectively. The electric charge of particles is measured in units of the elementary charge (e). Masses, momenta and energies of particles are measured in units of electronvolt (eV) and its (metric prefixes) multiples such as MeV, GeV and TeV.

CHAPTER 2

Top quark at the Standard Model

2.1 The Standard Model

The SM is a theory that describes elementary particles and their interactions at the most miniature scale. It uses a quantum field formalism which describes particles as excitation states of the corresponding quantum field; hence, it is a Quantum Field Theory (QFT). It includes three fundamental forces of nature: the strong force mediated by the exchange of the massless and electrically neutral gluons, the weak force mediated by the exchange of the massive neutral Z bosons and charged W bosons, and the electromagnetic force mediated by the massless and electrically neutral photons. The theory of Quantum Chromodynamics (QCD) [10–12] describes the strong force, whereas the weak and electromagnetic forces are unified together and described by the electroweak theory [13–15]. The gauge symmetry group of the SM have the structure:

$$SU(3)_C \otimes SU(2)_L \otimes U(1)_Y \,, \tag{2.1}$$

where $SU(3)_C$ is the gauge group of QCD and $SU(2)_L \otimes U(1)_Y$ is the gauge group of the electroweak interaction. The subscript C refers to colour charge, whereas the subscripts L and Y refer to left-handed isospin and hypercharge, respectively. The fourth force of nature, which is the gravitational one, is not included in the SM.

Elementary particles are considered the building blocks, hence, the name *elementary*, of the visible matter of our universe, which comprises only around 5% of the total density of the universe. There are twelve fermions in the SM, where fermions are particles with half-integer spin. Such particles interact by exchanging one of five particles called gauge bosons, particles with integer spin. Fig. 2.1 display all these elementary particles of the SM.

There are two types of fermions: leptons and quarks. They are classified into three families or generations, which increase in mass when going from the first to the third generation. Leptons that are electrically charged have a charge of 1 e. Such charged leptons are electrons, muons, and taus which are denoted as e, μ, and τ, respectively. Both muons and taus are

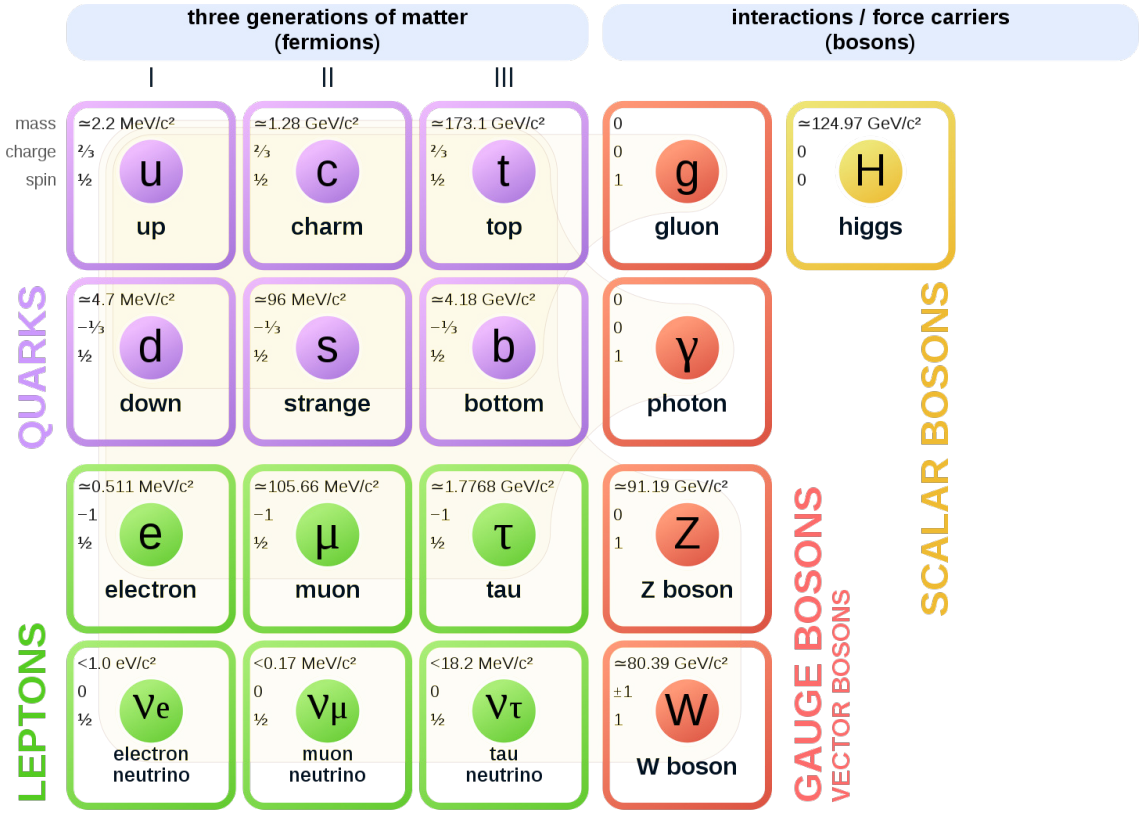

Figure 2.1: Overview of elementary particles in the SM. Three families of fermions, along with the gauge and Higgs bosons, are shown. The figure is sourced from Ref. [16] and modified.

unstable particles, and they decay spontaneously, whereas the electron is stable. Furthermore, leptons in each generation form a weak isospin doublet where each charged lepton has a corresponding electrically neutral particle called a neutrino, e.g. the e forms with the electron neutrino (ν_e) an isospin doublet. The muon neutrino and tau neutrino are denoted as ν_μ and ν_τ, respectively. Moreover, charged leptons have their corresponding antiparticles, which have the same mass and spin but an opposite sign of the relevant quantum numbers, e.g. the electron has an electric charge of -1 e, whereas its antiparticle, the positron, has a charge of +1 e. Neutrinos are distinguished from their corresponding antiparticles, denoted as antineutrinos, by differing in the sign of the lepton number and the chirality of the particle (right- or left-handed). For simplicity, charged leptons hereafter are called leptons, and they refer to particles and their corresponding antiparticles as well, unless explicitly stated otherwise.

Quarks have a non-integer electric charge of either +2/3 e such as the up, charm, and

top quarks, denoted as u, c, and t, respectively, or -1/3 e such as the down, strange, and bottom quarks, denoted as d, s, and b, respectively. Like leptons, quarks are also grouped into weak isospin doublets that differ by one unit of electric charge, e.g. the up and down quarks. In addition to an electric charge, quarks have a colour charge. Quarks also have their corresponding antiparticles, called antiquarks, e.g. the antitop and antibottom quarks denoted as $\bar{t}$ and $\bar{b}$, respectively.

The strong interaction

The strong force is, as the name suggests, the most potent force of nature. It acts at the shortest distances and is responsible for holding the protons together in the nucleus, despite their electric repulsion. Furthermore, it is also responsible for holding together the quarks inside the proton or the neutron.

The quantum number of the strong interaction is called colour, and it has three states: red, green, and blue. Quarks carry one unit of colour charge, while antiquarks carry one unit of anticolour. Gluons carry one unit of colour and one unit of anticolour, and they exist in an octet of linear combinations of the three colours. Since gluons are colour charged, they can interact with one another in addition to their interactions with the quarks.

The strength of the strong interaction is determined by the strong coupling constant (α_S). The coupling constant is also called *running* coupling constant, since it is not a constant quantity but rather runs with respect to the four-momentum transfer (Q):

$$\alpha_S(Q^2) = \frac{12\pi}{(33 - 2\mathrm{n}_f)\log(\mathrm{Q}^2/\Lambda^2_{\mathrm{QCD}})}\,, \tag{2.2}$$

where n_f is the number of quark flavors and Λ_{QCD} is the fundamental scale of QCD which allows the evaluation of the coupling constant at a scale of $Q > \Lambda_{\mathrm{QCD}}$.

The dependence of α_S on Q, which can be seen in Fig. 2.2, probes two characteristic properties of QCD:

- *Colour confinement* which states that at small Q^2, colour-charged particles —quarks and gluons—cannot exist as isolated particles. When quarks are pulled apart, the potential energy increases so that it is enough to produce quark and antiquark pairs, forming colourless bound-states called hadrons. There are two types of hadrons, mesons consisting of a quark and an antiquark, and baryons composed of either three quarks or three antiquarks. The process of forming hadrons is called hadronisation which is described in Chapter 6.

- *Asymptotic freedom* which states that at large Q^2, quarks and gluons interact weakly or behave like free particles [18].

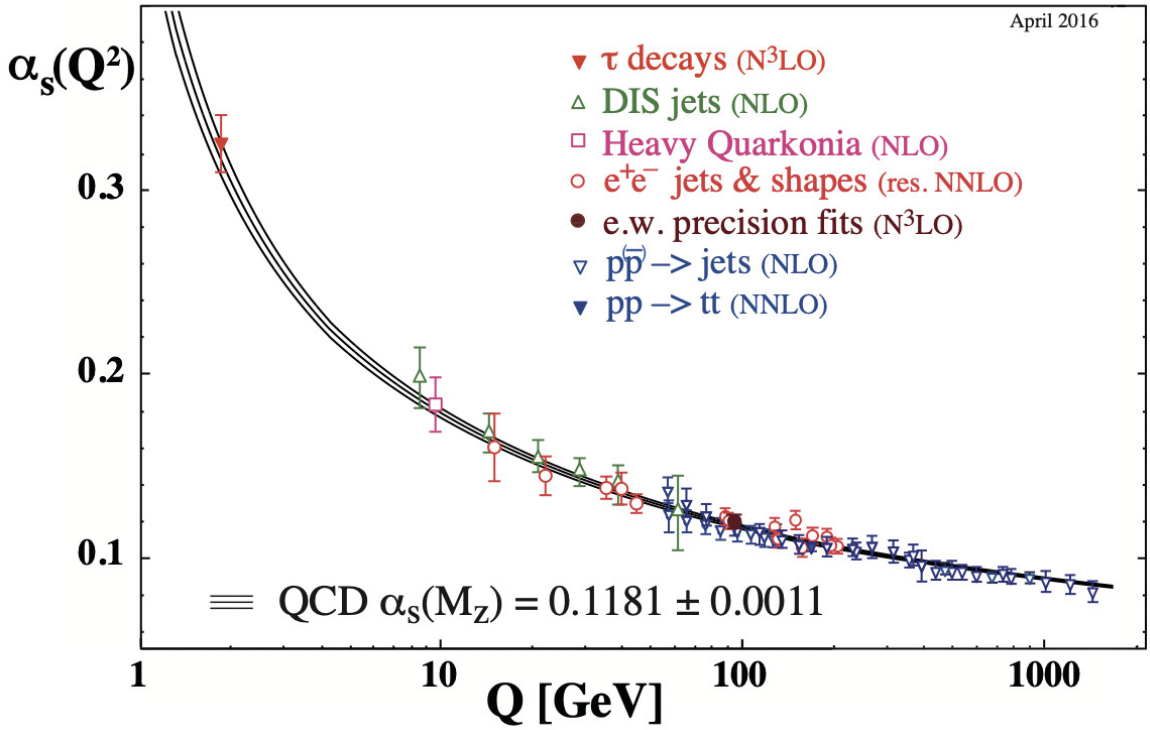

Figure 2.2: Summary of measurements of α_S as a function of Q. The respective degree of QCD perturbation theory is indicated in parenthesis. The figure is sourced from Ref. [17].

The electroweak interaction

The theories of Quantum Electrodynamics (QED) and weak interactions were initially developed separately. The electromagnetic interaction describes the interactions between electrically charged particles through mediating photons. The strength of the electromagnetic force is represented by the coupling constant (g_e), which is expressed as α_e:

$$\alpha_e = \frac{g_e^2}{4\pi} \approx \frac{1}{137} \tag{2.3}$$

The weak interaction describes the interactions of particles via mediating charged $W^{\pm}$ bosons (also denoted simply as W bosons) or neutral Z bosons. Leptons do not participate in the strong interaction since they do not carry colour, and neutrinos do not interact electromagnetically, as they have no electric charge. However, all leptons and quarks interact weakly, i.e. participate in the weak interaction.

In the 1960s, a gauge-invariant theory was constructed, which combined the electromagnetic and weak forces. This unification of forces was the work of Glashow [13], Salam [14], and Weinberg [15], which is referred to as the electroweak unification. The resulting electroweak

interaction is described by the $SU(2)_L \otimes U(1)_Y$ symmetry group. The gauge symmetry requires the W and Z bosons to be massless, although experimentally, they are observed to be massive [19]. The origin of their masses was understood by introducing another quantum field, the so-called Higgs field [20–23], which leads to the spontaneous breaking of the electroweak symmetry. The Higgs field was introduced as a complex scalar SU(2) doublet. Through the electroweak symmetry breaking, fermions acquire their masses through interactions with the Higgs field, where their masses are proportional to the vacuum expectation value of the Higgs field and the corresponding Yukawa coupling. Quantum excitation of the Higgs field produces the Higgs boson, which was was discovered experimentally in 2012 by ATLAS [24] and CMS [25].

2.2 Top-quark physics

The top quark is the heaviest elementary particle in the SM with a mass of 173.34 ± 0.76 GeV [26]. Its heavy mass provides access to the largest Yukawa coupling, which is predicted to be close to unity. This points to its unique role in validating predictions of the SM. Furthermore, it has a very short lifetime of 10^{-24} s. This remarkably brief record permits it to decay before forming a bound state, which allows measuring its properties by examining its decay products. One of these properties which is accessible experimentally and not washed out by hadronisation is the spin information of the top quark. The top-quark pair ($t\bar{t}$) spin correlation can be probed through the angular distributions of the decay products of the t and $\bar{t}$ (see Section 8.2 for observables that are sensitive to the $t\bar{t}$ spin correlation). Deviations from the angular distributions predicted by the SM would indicate new physics.

Production of top-quark pairs

At hadron colliders, top quarks are produced in pairs or as a single top, where the former is the dominant process. The $t\bar{t}$ are produced predominantly through the strong interaction via gluon-gluon (gg) fusion and $q\bar{q}$ annihilation, for which representative diagrams at leading order (LO) in QCD are shown in Fig. 2.3. At the LHC, 90% of the production is through the gg fusion at $\sqrt{s} = 14$ TeV. The reason for such a high rate is that the $q\bar{q}$ annihilation is suppressed since antiquarks in protons exist only as sea quarks.

The $t\bar{t}$ production cross-section can be calculated with the help of the factorisation theorem [27]. This theorem separates the calculation of the long-distance interactions of partons from the short-distance ones (hard interaction) by introducing a factorisation scale (μ_F). The value of μ_F is arbitrarily chosen, but it is typically set to the momentum transfer of the hard process. The hard interaction terms can be calculated with the perturbation theory, while the terms corresponding to the long-distance interactions are calculated using structure functions, known as Parton Distribution Functions (PDF) [28–30].

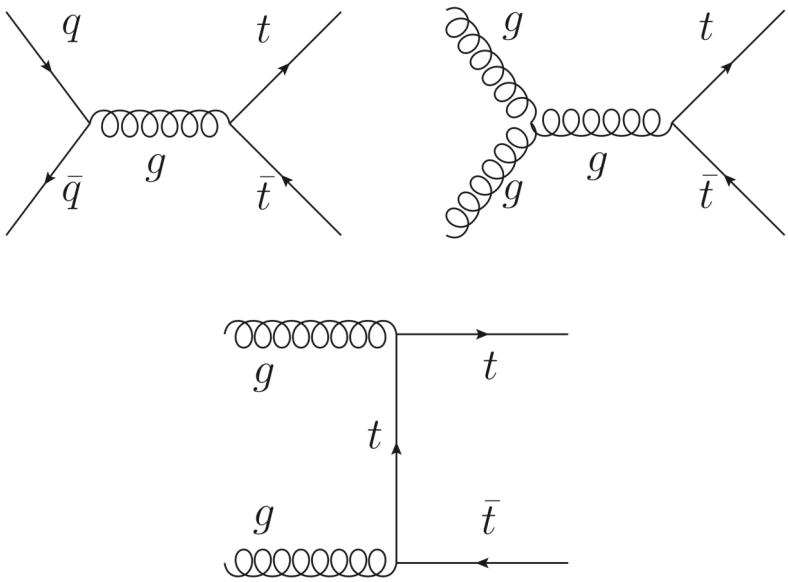

Figure 2.3: Representative Feynman diagrams of the top-quark pair production at leading order in QCD via $q\bar{q}$ annihilation (top left) and gg fusion (top right and bottom).

Let two hadrons, A and B, collide creating a final state X. The inclusive cross-section for such a process is given as:

$$\sigma_{AB\to X} = \sum_{ab} \int_{x_a} \int_{x_b} dx_a dx_b \; f_{a,A}(x_a, \mu_F) \; f_{b,B}(x_b, \mu_F) \times \hat{\sigma}_{ab\to X} \,, \tag{2.4}$$

where $\hat{\sigma}_{ab\to X}$ is the partonic cross-section of the hard interaction. The indices a and b represent partons in hadrons A and B, respectively, where partons are valence quarks, sea quarks and gluons. The terms $f_{a,A}(x_a, \mu_F)$ and $f_{b,B}(x_b, \mu_F)$ are the PDFs of the hadrons A and B, respectively, where x_a and x_b are the fractions of the momentum carried by the corresponding parton. Therefore, the inclusive cross-section ($\sigma_{pp\to t\bar{t}}$) of pp collisions to create a final state of $t\bar{t}$ can be calculated with Eq. (2.4). At $\sqrt{s} = 13\,\text{TeV}$, assuming a top-quark mass of 172.5 GeV, $\sigma_{pp\to t\bar{t}}$ is predicted to be $831.8\,^{+19.8}_{-29.2}(\text{scale})^{+35.1}_{-35.1}(\text{PDF})$ pb at the LHC [17]. The cross-section is obtained at next-to-next-to-leading order (NNLO) in QCD and next-to-next-to-leading-logarithmic (NNLL) soft-gluon resummation with the TOP++2.0 program [31].

Production of single top quarks

The single top quark is produced via the electroweak interaction in three channels: s-channel, t-channel, and tW-channel, at LO in QCD. In the s-channel and t-channel, the

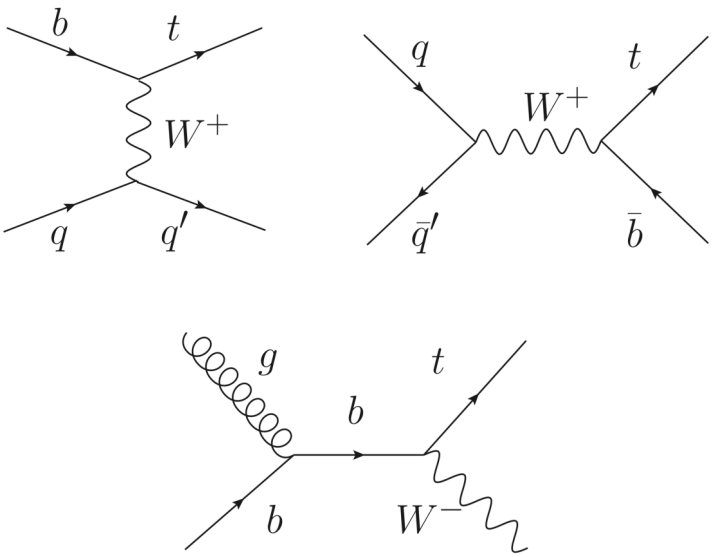

Figure 2.4: Representative Feynman diagrams of the single-top production at LO in QCD in the t-channel (top left), s-channel (top right), and tW-channel (bottom).

top quark is produced by the exchange of a virtual W boson, whereas in the tW-channel, it is produced in association with a real W boson. Examples of Feynman diagrams for the three channels at LO in QCD are shown in Fig. 2.4. At $\sqrt{s} = 13\,\text{TeV}$, assuming a top-quark mass of 172.5 GeV, the cross-sections of the s-channel, t-channel, and tW-channel for the top quark and antitop quark components at the LHC are $10.32\,^{+0.29}_{-0.24}(\text{scale})^{+0.27}_{-0.27}(\text{PDF})$ pb, $216.99\,^{+6.62}_{-4.64}(\text{scale})^{+6.16}_{-6.16}(\text{PDF})$ pb, and $71.7\,^{+1.8}_{-1.8}(\text{scale})^{+3.40}_{-3.40}(\text{PDF})$ pb, respectively [32]. The cross-sections are obtained at NLO in QCD with the HATHOR (v2.1) program [33, 34].

Top-quark decay

The top quark decays via the weak interaction to a W boson and a down-type quark (d, s, or b). The decay to a W boson and a b-quark is the predominant process with a Branching Ratio (BR) close to 1 [35]. The decay to s- or d-quark is heavily suppressed owing to their substantially weak mixing in the Cabibbo–Kobayashi–Maskawa matrix. The W boson then decays to leptons (a charged lepton and its corresponding neutrino) or quarks (a quark and an antiquark of the first two generations). Therefore, the $t\bar{t}$ decay can be categorised in three decay channels, for which the branching ratios are shown in Fig. 2.5, according to the decay products of the W boson:

- *Dileptonic:* both W bosons decay to two leptons: $t\bar{t} \rightarrow l^+\nu_l b l^-\bar{\nu}_l\bar{b}$, where $l = e$, μ, or τ. This channel has the advantage of being very clean with the lowest background contamination. However, it has the smallest BR of 9%.

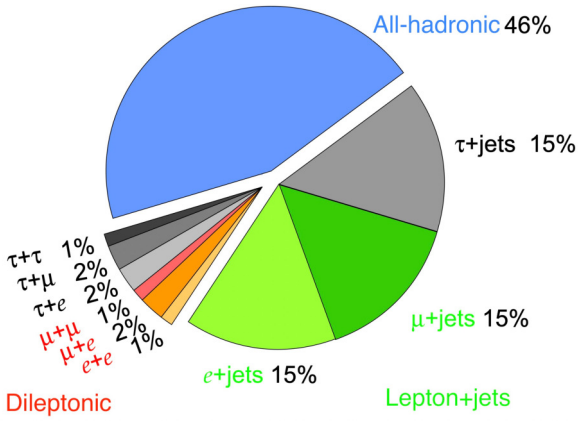

Figure 2.5: Branching ratios of the $t\bar{t}$ decay channels. The figure is sourced from Ref. [36] and modified.

- *All-hadronic:* both W bosons decay to two quarks: $t\bar{t} \rightarrow q_1\bar{q}_2q_3\bar{q}_4b\bar{b}$, where $q = u$, d, s, or c. This channel has the largest BR of 46%, but it suffers from a large contribution of background processes.

- *Single lepton* or *lepton+jets*: one W boson decays hadronically, whereas the other one decays leptonically: $t\bar{t} \rightarrow l^+\nu_l b q_1\bar{q}_2\bar{b}$ or $t\bar{t} \rightarrow q_1\bar{q}_2 b l^-\bar{\nu}_l\bar{b}$ where $l = e$, μ, or τ and $q = u$, d, s, or c. This channel is called the *golden channel* since it has a rather high BR of 45% while the background contamination is moderate.

2.3 Top-quark production in association with photons

The study of the $t\bar{t}\gamma$ process plays a vital role in testing predictions of the SM and possible new physics. For example, it has access to the $t\gamma$ electroweak coupling. The SM predicts such coupling, and deviation from such prediction would indicate new physics [37, 38]. Furthermore, at the LHC, the $t\bar{t}\gamma$ couplings can be probed with a high precision (a few per cent level), which allows to scrutinise the SM predictions and put constraints on the anomalous dipole moments of the top quark [37, 38]. Moreover, precise measurements of the $t\bar{t}\gamma$ permit interpretations in the context of effective field theories [39].

Photons being massless can be radiated from any electrically charged particle and not only the top quark. The $t\bar{t}\gamma$ process can be classified in two categories:

- In *radiative top-quark production*, the photon is radiated during the production of the $t\bar{t}$. At LO in QCD, such production can occur in a $q\bar{q}$ annihilation or a gg fusion, as shown in the example diagrams of Fig. 2.6. The photon is radiated either from an incoming charged parton or an off-shell top quark in these diagrams.

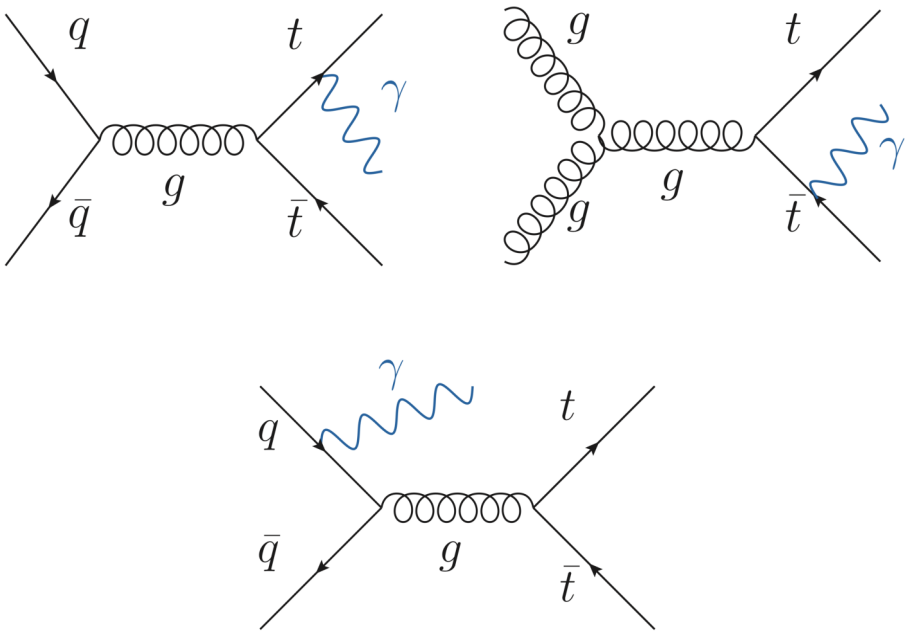

Figure 2.6: Representative Feynman diagrams at LO in QCD of the radiative top-quark production. The photon can be radiated from an off-shell top quark in $q\bar{q}$ annihilation (top left) or gg fusion (top right). The incoming partons can also emit the photon (bottom).

- In *radiative top-quark decay*, the photon is radiated from an on-shell top quark or any of the electrically charged particles in the decay chain. Examples of Feynman diagrams are shown in Fig. 2.7. In the diagrams, the photon is emitted from the top quark, the b-quark, the W boson, or the electrically charged decay product of the W boson.

  Both radiative production and decay of the top quark yield the same final state in the detector.

A non-exhaustive summary of the theoretical calculations of the $t\bar{t}\gamma$ process is discussed in the following section, including the theory calculation used for comparison to the measurements reported in this thesis.

Theory calculations

The earliest calculation of the $t\bar{t}\gamma$ process at next-to-leading order (NLO) in QCD was performed in 2009 [40]. This calculation used the Born approximation for top quarks, i.e. considering them as stable particles. Later in 2011, the $t\bar{t}\gamma$ calculation was further extended by considering a decaying top quark [41], i.e. including the two processes: radiative production and decay of the top quark. When considering top quarks to be truly unstable, non-factorisable QCD corrections emerge [42–44]. The 2011 calculation [41] overcame such an issue by treating the top quarks in the narrow width approximation. However, using the

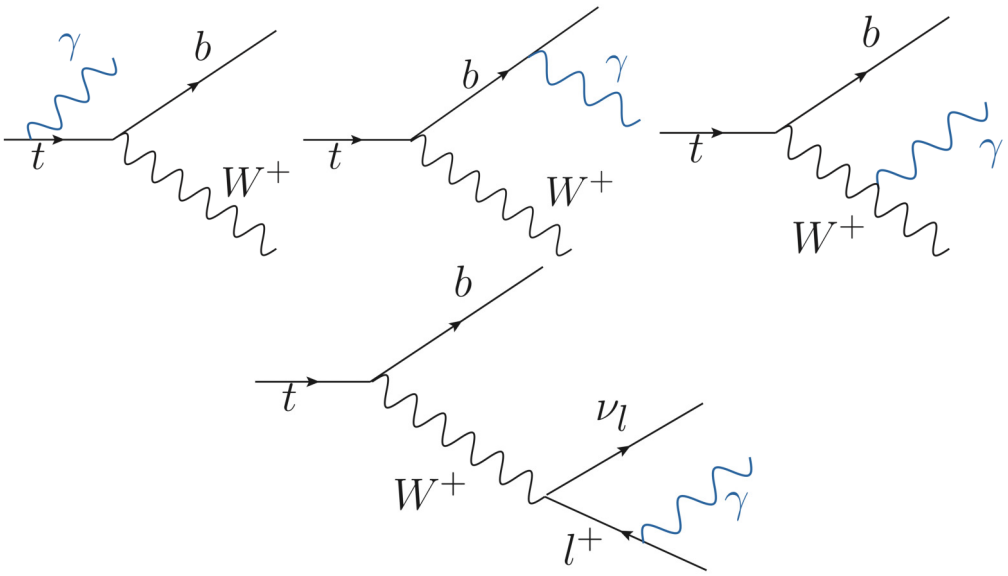

Figure 2.7: Representative Feynman diagrams at LO in QCD of the radiative top-quark decay. The photon can be radiated from the on-shell top quark (top left), the b-quark (top-middle), or the W^+ boson (top right). It can also be emitted from the electrically charged lepton, the l^+ (bottom).

narrow width approximation means that off-shell contributions are neglected, and hence the interference between the top-quark production and decay is ignored.

In 2018, the first full computation of the $t\bar{t}\gamma$ process at NLO in QCD was performed [9]. It included resonant and non-resonant contributions, interferences, and off-shell effects of the top quark and the W boson. This calculation considered the $e\mu$ final state: $pp \to be^+\nu_e\bar{b}\mu^-\bar{\nu}_\mu\gamma$ at $\sqrt{s} = 13\,\text{TeV}$. Example Feynman diagrams of the double resonant, single resonant and non-resonant top-quark diagrams are shown in Fig. 2.8. There are two top-quark resonances in the double-resonant case, whereas there is only one top quark in the single resonant one. In the non-resonant case, no top-quark resonances are present. The three cases contribute to the same final state of $be^+\nu_e\bar{b}\mu^-\bar{\nu}_\mu\gamma$. The top-quark mass was set to 173.2 GeV. The electroweak coupling was derived from the Fermi constant G_μ, where it was set to $\alpha_{G_\mu} \approx 1/132$. A value of $\alpha = 1/137$ was used to describe the real photon emission. The calculation considered two scenarios for the chosen factorisation (μ_F) and normalisation (μ_R) scales. The first scenario used a fixed scale for both scales, which were set to $\mu_F = \mu_R = m_t/2$ where m_t is the mass of the top quark. The second scenario used a dynamic scale, which was set to $\mu_F = \mu_R = S_\text{T}/4$. The S_T is defined as the total transverse momentum of the system, i.e. the sum of transverse momenta of the leptons, photon, b-jets, and the missing transverse momentum from the escaping neutrinos. The second scenario was found to stabilise the shapes in the high region of the transverse momentum of the photon and provided smaller theoretical uncertainties as well. Therefore, it is chosen for the comparison with the measurements reported in this thesis.

The authors of Ref. [9] have done a dedicated recalculation in the fiducial phase space of the measurement (see Section 8.1). The NLO fiducial inclusive cross-section of the

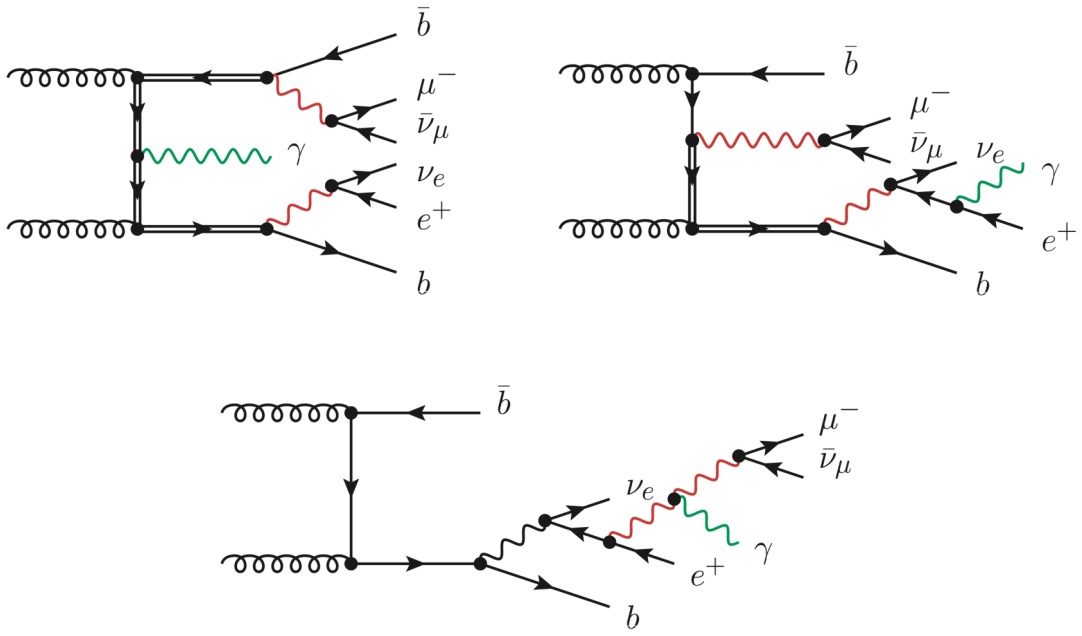

Figure 2.8: Representative Feynman diagrams at LO in QCD of the double resonant (top left), single resonant (top right), and non-resonant (bottom) top quark. The figure is sourced from Ref. [9].

process $pp \to be^+\nu_e\bar{b}\mu^-\bar{\nu_\mu}\gamma$ using the CT14 PDF set [45] and dynamical scale of $S_T/4$ was calculated to be:

$$\sigma_{\text{fid}} = 38.50\,^{+0.56}_{-2.18}\,(\text{scale})\,^{+1.04}_{-1.18}\,(\text{PDF})\,\text{fb} \tag{2.5}$$

Besides the inclusive cross-section, the calculation also computed results of various differential distributions at LO and NLO in QCD. Distributions as functions of observables that are relevant for searches beyond the SM were included. An example is the transverse momentum of the photon, which can be seen in Fig. 2.9. For such an observable, corrections up to 13% is observed. The uncertainty bands in the figure also show that the NLO uncertainty is smaller than the LO one.

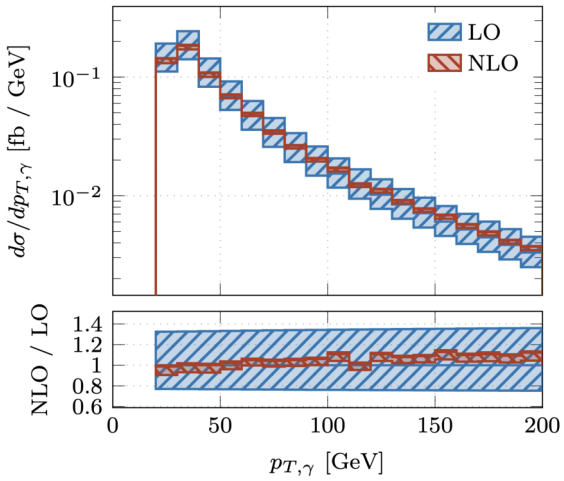

Figure 2.9: Transverse momentum of the photon, using the dynamic scale of $\mu_F = \mu_R = S_T/4$. The LO and NLO predictions and their uncertainty bands are shown in the upper panel, and their ratio is shown in the lower panel. The figure is sourced from Ref. [9].

CHAPTER 3

Experimental Setup

LHC is the most powerful particle accelarator across the globe, which is built by the biggest laboratory of high energy physics, CERN, the *European Organization for Nuclear Research*. The LHC has a 27 km circular tunnel, which lies approximately 120 m underground on the border between France and Switzerland. It is a pp collider which is designed to accelerate and collide protons at $\sqrt{s} = 14$ TeV. It has four collision points at which four main experiments are placed. The four experiments are A Toroidal LHC ApparatuS (ATLAS) [46, 47], Compact Muon Solenoid (CMS) [48], Large Hadron Collider beauty (LHCb) [49], and A Large Ion Collider Experiment (ALICE) [50], which can be seen in Fig. 3.1. The ATLAS and CMS are called multipurpose detectors since they cover a broad spectrum of physics analyses. The LHCb experiment focuses on the physics of B hadrons, while ALICE investigates the quark-gluon plasma in heavy-ion collisions.

Physics analyses often use three quantities when describing physics processes at the LHC:

- *The integrated luminosity (L)* : it is the number of collisions which are collected over a certain period of time interval and unit area. Its unit is expressed in the inverse of area units, e.g. inverse picobarn ($\text{pb}^{-1} = 10^{40}\text{m}^{-2}$) or inverse femtobarn ($\text{fb}^{-1} = 10^{43}\text{m}^{-2}$), where barn is a metric unit of area (1 barn = 10^{-28}m^2). It is obtained by integrating the instantaneous luminosity (L_{inst}) over the corresponding period of time ($\text{d}t$):

$$L = \int L_{\text{inst}} \text{d}t \, . \tag{3.1}$$

  The instantaneous luminosity is defined as:

$$L_{\text{inst}} = \frac{N_b^2 n_b^2 f_{\text{rev}} \gamma}{4\pi\sigma_x\sigma_y} \, F \, , \tag{3.2}$$

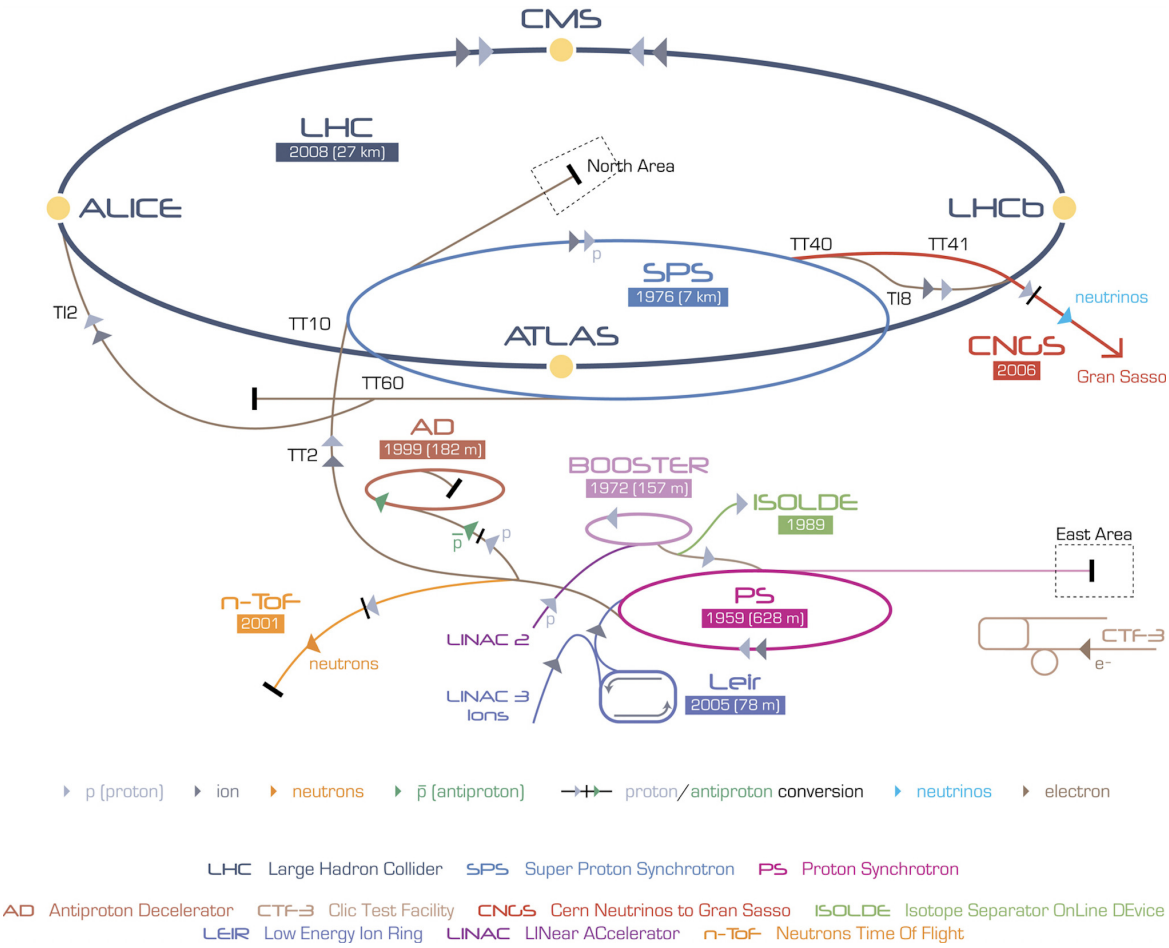

Figure 3.1: A schematic view of the accelerator complex at CERN. The LHC is the uppermost ring (dark grey ellipse) with the four main experiments (orange-colored circles) at the designed collision points (©2008-2021 CERN). The figure is sourced from Ref. [51].

where N_b is the number of particles per bunch, n_b is the number of bunches per beam, f_{rev} is the revolution frequency, and γ is the relativistic gamma factor. The quantity F represents the geometric luminosity reduction factor, and σ_x and σ_y are the beam cross-sections in x and y directions, respectively.

- *The cross-section (σ)*: it represents the probability that an event or several events occur as a result of particles' collisions with a given luminosity.
- *The number of events (N)*: it is the expected number of events of a particular physics process for a given cross-section and luminosity.

The relation between the three quantities can be expressed as:

$$N = \sigma \cdot L \,. \tag{3.3}$$

3.1 The ATLAS detector

The ATLAS detector is constructed to perform precise measurements of the SM and beyond. One of its primary goals was to search for the Higgs boson, which was discovered in 2012 by both experiments, ATLAS [24] and CMS [25].

The detector has an overall length of 44 m and a diameter of 25 m, weighing nearly 7×10^6 kg. It is constructed so that different subdetector systems are built in concentric layers around the designed interaction point. The subdetector systems are classified into three systems, as shown in Fig. 3.2:

- *The Inner Detector (ID)*: it is the innermost part of the ATLAS detector, which is contained within a cylindrical envelope surrounded by a solenoidal magnetic field. The ID is responsible for tracking the paths of charged particles, i.e. it acts as a tracking system. Besides, it measures their electric charge and momenta, as well as identifying primary and secondary interaction vertices. The vertex is called primary [52] when two protons collide with each other and secodary if it is associated with a decay of a particle coming from the primary vertex.
- *The calorimeters*: they are placed outside the solenoidal magnetic field. They are responsible for measuring the deposited energy of charged and neutral particles. They are designed to stop most of the particles that pass through except muons and neutrinos.
- *The Muon Spectrometer (MS)*: it is the outermost part of the detector. It is immersed in a toroidal magnetic field and is responsible for measuring the properties of muons since they travel relatively longer distances than other particles and are less likely to interact with other systems of the detector.

The coordinates of the detector and more details on the three subdetector systems are described in the following sections.

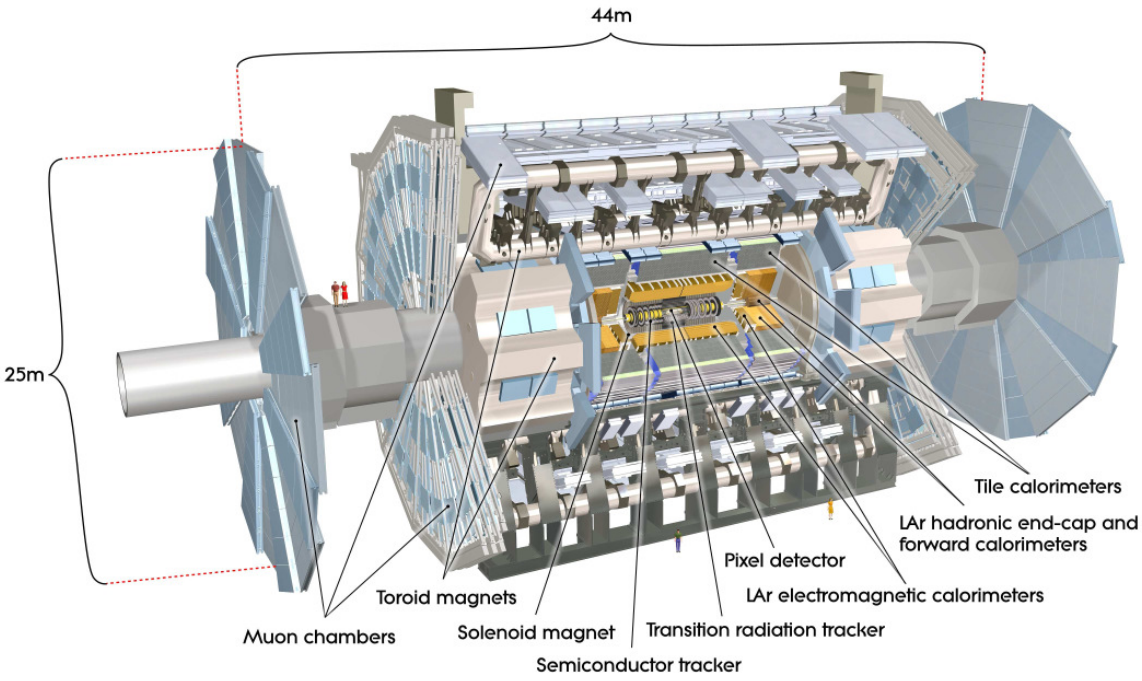

Figure 3.2: A schematic overview of the ATLAS detector. The figure is sourced from Ref. [53]

3.1.1 Coordinates of the detector

The ATLAS detector uses a right-handed coordinate system, denoted as (ϕ, η, z). The z-coordinate is an axis defined by the beam direction, whereas the ϕ- and η-coordinates are the azimuthal angle and pseudorapidity defined in terms of the Cartesian coordinates (x, y, z). The (x, y, z) coordinates are defined such that the origin $(0, 0, 0)$ is located at the designed interaction point at the centre of the detector. The x-axis points towards the centre of the LHC ring, the y-axis points towards the surface of the earth, and the z-axis points along the direction of the counterclockwise beam. The angle ϕ is defined in the x-y plane (denoted as the transverse plane) with respect to the positive direction of the x-axis and around the z-axis. The quantity η is defined as the angle relative to the z-axis and can be given as:

$$\eta = -\ln \tan\left(\frac{\theta}{2}\right), \tag{3.4}$$

where θ is the polar angle with respect to the positive z-axis.

To define the third component of the system, η is used for massless particles, whereas for massive particles, the rapidity (y) is employed. The y-quantity can be defined in terms of the energy E and the z-component of the momentum of the particle:

$$y = \frac{1}{2} \ln \left(\frac{E + p_z}{E - p_z} \right) . \tag{3.5}$$

At the LHC, particles have large transverse momenta compared to their rest masses so that their rapidity is equivalent to their pseudorapidity. The latter is the common coordinate used within the ATLAS Collaboration, which is preferred over θ since differences in η are Lorentz invariant under boosts along the z-axis. Using ϕ and η, the distance between two objects can be expressed as:

$$\Delta R = \sqrt{(\Delta\eta)^2 + (\Delta\phi)^2} , \tag{3.6}$$

where $\Delta\phi$ and $\Delta\eta$ are the differences in azimuthal angles and pseudorapidities between the two objects, respectively.

The transverse momentum p_{T} and transverse energy E_{T} are defined in the x-y plane as follows:

$$p_{\mathrm{T}} = p \sin\theta , E_{\mathrm{T}} = E \sin\theta , \tag{3.7}$$

where p and E are the momentum and energy of the particle, respectively.

3.1.2 Magnet systems

The magnet systems in the ATLAS detector are the magnetic field sources needed to bend the trajectories of charged particles. They allow measurements of the momentum and charge of particles to be performed. The ATLAS magnet systems comprise four magnets :

- *Solenoid magnet*: it is aligned around the beam axis and placed between the ID and the calorimeters. It provides a 2 T axial magnetic field.
- *Toroid magnets*: there are three of them, with one central and two end-cap toroids. They provide a 4 T magnetic field to the MS.

The ID, calorimeters and MS are described in the following sections.

3.1.3 Inner Detector

The ID is a tracking system that enables the reconstruction of the paths of charged particles (called tracks) and measures their momenta. It can perform measurements of transverse momenta within a pseudorapidity coverage of $|\eta| < 2.5$. The ID consists of three systems, which can be seen in Fig. 3.3:

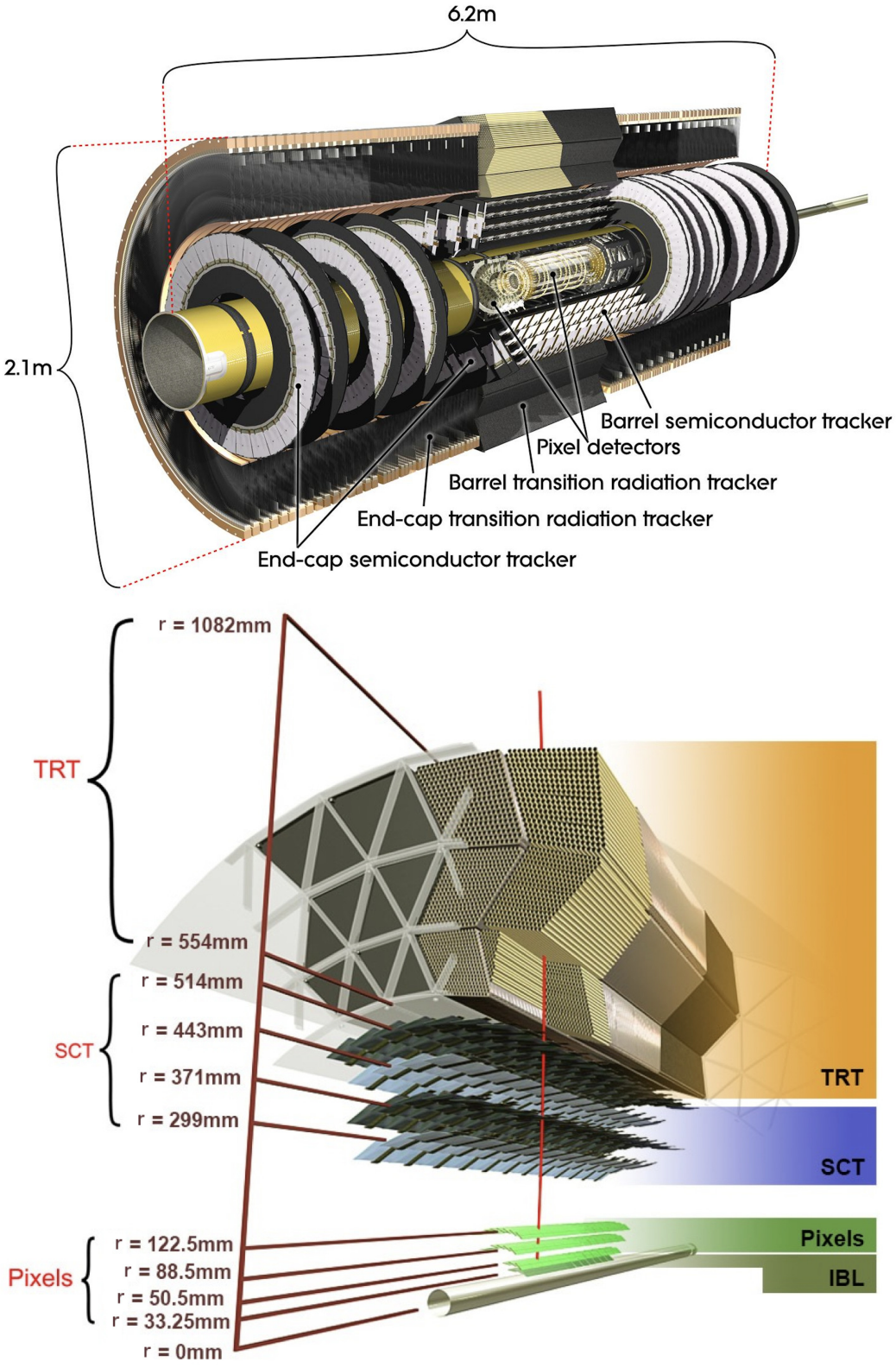

Figure 3.3: Cut-away (top) and cross-sectional (bottom) views of the ATLAS ID. The figures are sourced from Ref. [53, 54].

- *Pixel detector*: it is the innermost system of the ID. It has a very fine granularity of silicon sensors, which supports detecting short-lived particles like b-quarks and τ leptons. For Run 2 of the LHC, a new system was installed in the pixel detector as its innermost barrel layer (called Insertable B-layer or IBL) to improve tracking performance.

- *Semiconductor Tracker (SCT)*: it is placed outside the pixel detector with four-barrel layers in the central region and nine disk layers in the end-caps region. Similar to the pixel detector, the SCT layers consist of silicon sensors. It has strips parallel to the beam pipe, whereas, in the end-cap region, the strips are perpendicular to the beam. Complementary to the pixel detector, SCT provides tracking information with a high resolution along the z-coordinate and transverse plane.

- *Transition Radiation Tracker (TRT)*: it is the outermost system of the ID. In addition to performing tracking measurements, it plays a special role in distinguishing between electrons and pions based on their transition radiation. It uses a different technology from the pixel detector and SCT, where it operates drift tubes instead of silicon sensors.

3.1.4 Calorimeters

The calorimeters are placed outside the ID and solenoid magnets. They are designed to measure the deposited energy of photons, electrons, and hadrons. There are three types of calorimeters, as shown in Fig. 3.4:

- *Electromagnetic Calorimeter (ECAL)*: it is the inner part of the calorimeters and consists of one liquid argon (LAr) electromagnetic barrel and two LAr Electromagnetic End-Caps (EMEC) covering the range of $|\eta| < 3.2$. It is designed to perform high-resolution measurements of the energies of photons and electrons.

- *Hadronic Calorimeter (HCAL)*: it is the outer part of the calorimeters and consists of one *central tile barrel*, two *extended tile barrels*, and two end-caps. It is designed to enable precise measurement of energies of hadrons, e.g. protons, neutrons, and pions.

- *Forward Calorimeter (FCAL)*: it extends the coverage of the calorimeters in the forward region of pseudorapidity ($3.1 < |\eta| < 4.9$). It provides measurements of both electromagnetic and hadronic particles.

3.1.5 Muon Spectrometer

The MS is the outermost part of the ATLAS detector, designed to perform precise measurements of tracks and momenta of muons coming out of the barrel and end-cap calorimeters. Being immersed in a toroidal magnetic field enables the MS to perform such measurements.

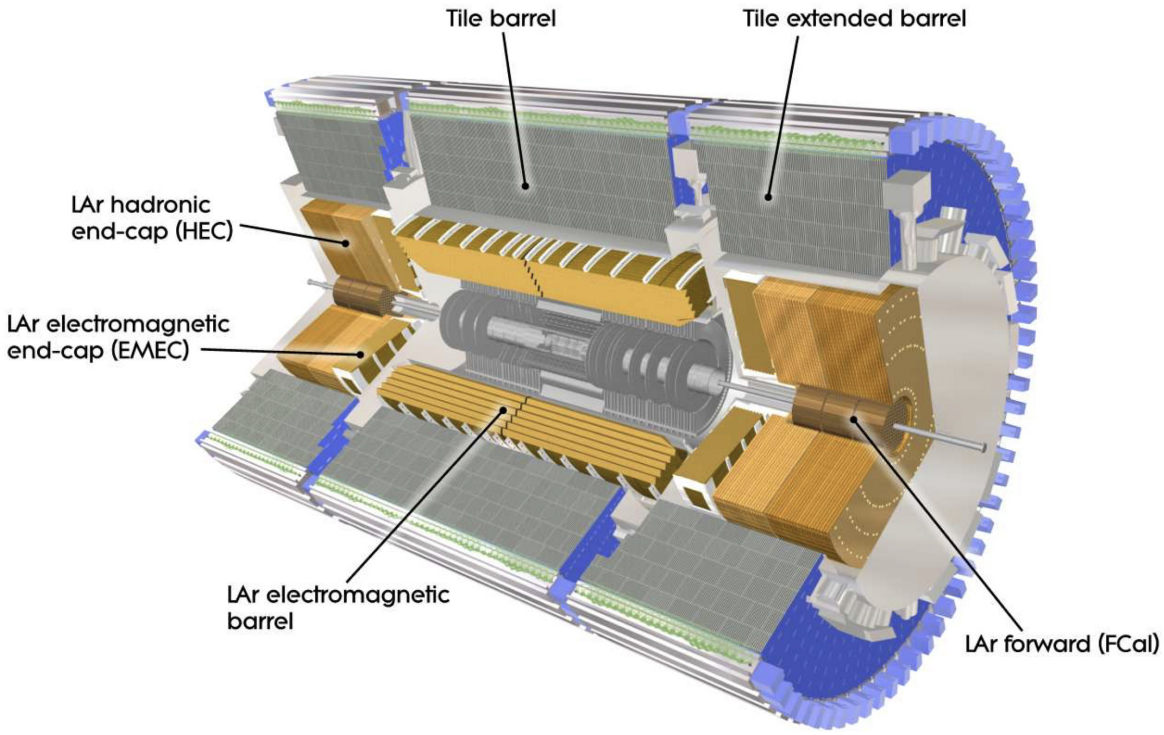

Figure 3.4: An overview of the ATLAS ECAL and HCAL calorimeters. The figure is sourced from Ref. [53].

While the solenoidal magnetic field is parallel to the beam pipe, the toroidal one is aligned in the transverse plane bending trajectories of muons in the η-direction. The MS consists of four systems, which are shown in Fig. 3.5:

- *Monitored Drift Tubes (MDTs)*: they are pressurised drift tubes made of aluminium and filled with argon and carbon dioxide gases. Having coverage of $|\eta| < 2.0$ and $|\eta| < 2.7$ in the inner and outer barrels, respectively, allows the MDTs to measure the positions of muons with a resolution of 35 µm per chamber.
- *Cathode Strip Chambers (CSCs)*: they are multiwire proportional chambers with strips of cathode planes, which are used in the forward region of $|\eta| > 2$. CSCs provide a spatial resolution of 40 µm in the transverse plane for four CSCs layers.
- *Resistive Plate Chambers (RPCs)*: they are chambers filled with gas mixtures and placed between two resistive bakelite plates. Complementary to MDTs, which have η-coverage, the RPCs have coverage in both η- and ϕ-directions.
- *Thin Gap Chambers (TGCs)*: they are multiwire proportional chambers with two cathode plates connected through an anode wire. TGCs provide optimal position and ϕ-resolutions.

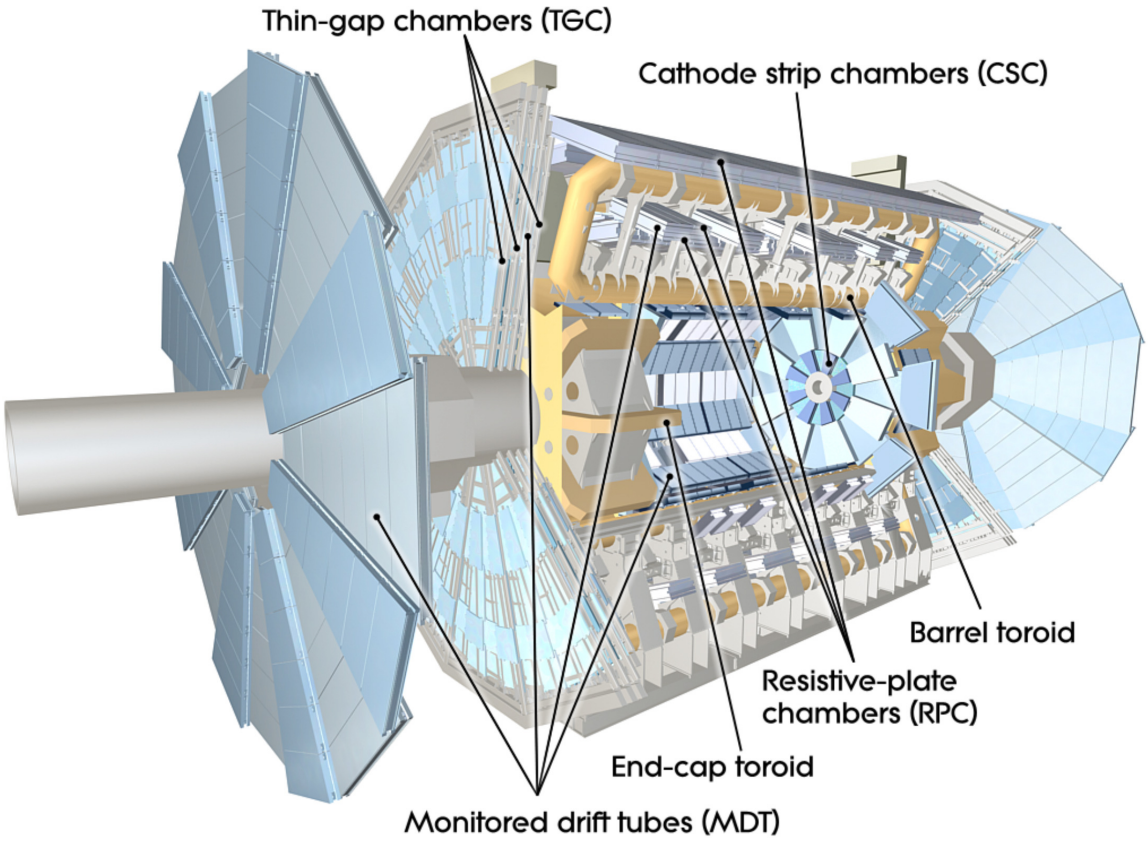

Figure 3.5: An overview of the ATLAS MS. The figure is sourced from Ref. [55].

3.1.6 Trigger system

The LHC produces a huge number of collisions per second (around 1 billion collisions per second in Run 2). It is quite impossible to store and analyse this huge amount of data. Therefore, a decision has to be made whether to keep or discard a given event. Such a decision is determined by the Trigger AND Data Acquisition (TDAQ) system [56]. The ATLAS TDAQ system consists of two trigger levels:

- *Low-level (L1)* trigger: it is a hardware-based trigger consisting of a central unit that receives information from the calorimeters and the RPCs and TGCs of the MS. The L1 trigger defines Regions-of-Interest (ROIs) for each event, based on the information of η, ϕ, and transverse momenta. The ROIs highlight interesting candidate objects such as muons, electromagnetic clusters, or large transverse momenta.
- *High-level Trigger (HLT)*: it is a software-based trigger, which receives information from all ATLAS components. The HLT determines whether to keep or discard events, and if an event is accepted, it is then written to the disks and stored.

CHAPTER 4

Object definition

In order to analyse data, physics objects have to be reconstructed by processing the signals which are recorded in the detector. Reconstruction algorithms are based on combining information from the hits in the tracking systems and energy deposits in the calorimeters. The reconstructed physics objects considered in this work are electrons, muons, photons, jets and missing transverse energy. After the reconstruction of physics objects, certain criteria are required to improve the purity of the selected objects. These criteria are referred to as identification and isolation working points (WPs). The identification algorithms are adopted to select prompt signal-like objects and reject background-like objects. The isolation algorithms are used to further suppress background-like objects by selecting those objects which are more isolated. Correction factors are used to improve the agreement between data and MC, i.e. to calibrate the objects in the MC simulation to match those in data.

In the following sections of this chapter, a description of the different algorithms of reconstruction, identification, and isolation in ATLAS is given. The ones used in this work are also highlighted.

4.1 Electrons

4.1.1 Reconstruction

Electrons are reconstructed by matching deposited energy in the central region of the ECAL to possible tracks in the ID. When charged particles move in a magnetic field, they radiate photons, known as Bremsstrahlung. Photons can be converted or unconverted, where the former undergoes a pair production creating an electron-positron pair before reaching the ECAL system. Therefore, there is a reconstruction ambiguity between electrons and converted photons since both would leave tracks in the ID and deposit energies in the ECAL. This ambiguity is resolved by performing the reconstruction of electrons and photons in parallel while checking the ID tracks and whether a conversion vertex exists or not (see Section 4.3.1).

The electron reconstruction is based on three consecutive steps, which are described in

more detail in Ref. [57].

- First, a seed cluster is created as follows. The η-ϕ space is transformed into a grid of 200×256 elements (towers) of size $\Delta\eta \times \Delta\phi = 0.025 \times 0.025$. Energy deposits per tower from the presampler, first, second, and third layers of the ECAL are summed together. Then a sliding-window algorithm [58] is used to seed these energy deposits, forming clusters of electromagnetic energy. The algorithm uses a window size of 3×5 towers in $\eta \times \phi$ to span the whole grid.

- After creating a seed cluster, a track reconstruction is performed. Track reconstruction is based on forming track seeds from hits in the ID layers by clustering them. This is followed by two steps: pattern recognition and a track fit. The pattern recognition step uses a pion model to account for the energy loss due to the interaction with the material of the detector, whereas the track fit is performed using the ATLAS Global χ^2 Track Fitter [59] under either the pion or the electron hypothesis of energy loss.

- As a final step, the reconstruction of the electron candidate is performed where the calorimeter seed cluster in the ECAL is matched to the reconstructed track in the ID. In the case of more than one track match, the decision is to be taken after considering hits in the silicon layers and pixel, conversion vertex, energy, and momentum of the candidate electron. Electron candidates are required to originate from the primary vertex requiring that longitudinal impact parameter $|z_0 \sin(\theta)| < 0.5\,\text{mm}$[1] and transverse impact parameter d_0[2] with significance $|d_0/\sigma_{d_0}| < 5$ where σ_{d_0} is the uncertainty on d_0 and to be calibrated with the procedure described in Ref. [60].

4.1.2 Identification and isolation

The identification of electrons is based on a multivariate-analysis likelihood-based (LH) approach, which takes variables based on measurements from the tracker and calorimeter systems as inputs. Such variables, collectively called *shower shapes*, are shown in Table 4.1. The ATLAS Collaboration defines four different LH discriminant values, so-called identification WPs: *VeryLoose*, *Loose*, *MediumLH*, and *TightLH*. The efficiencies of identifying a prompt electron with $E_\text{T} = 40\,\text{GeV}$ with *Loose*, *MediumLH*, and *TightLH* are 93%, 88%, and 80%, respectively. In this work, electron candidates are selected with the identification WP *TightLH* [57]. Furthermore, to distinguish between prompt electrons, semileptonic decays of hadrons and hadrons misidentified as electrons, specific criteria called isolation are imposed on the activity in the vicinity around the electron candidate. The isolation criteria for the electron candidates are based on the sum of E_T of clusters in the calorimeter or p_T of tracks in a cone of $\Delta R = \sqrt{\Delta\eta^2 + \Delta\phi^2}$ around the electron candidate. In other words, the isolation

[1] z_0 is the distance of closest approach to the primary vertex along the the z-axis.
[2] d_0 is the transverse impact parameter relative to the beam-line.

WPs are defined based on the sum of energies of topological clusters [57] within a cone of size $\Delta R = 0.2$ around the electron candidate and excluding cells corresponding to the electron's energy cluster (calorimeter-based isolation) and/or the p_{T} of all tracks within a cone of size $\Delta R = 0.3$ around the electron candidate and excluding the electron's track itself (tracking-based isolation). In this work, electron candidates are isolated with the isolation WP *Gradient*. This WP has an isolation efficiency (ϵ_{iso}) dependent on the p_{T} of the electron candidate but uniform in η ($\epsilon_{\mathrm{iso}} = 90\ (99)\%$ at 25 (60) GeV).

4.2 Muons

4.2.1 Reconstruction

Muons are reconstructed from track segments which are built independently in the ID and the MS systems [61]. The ID gives information regarding the tracks of the muon candidates and distances from the interaction point (IP), while the MS provides information on the momentum of the candidates with high precision. Furthermore, the calorimeters provide useful information for reconstruction, especially in case of an energy loss. The reconstruction of muon tracks in the ID is the same procedure as for electrons (described in Section 4.1), whereas in the MS the track reconstruction is performed by fitting hits from the segments in the MDT, RPC, TGC and CSC systems. Based on the information from the different components of the ATLAS detector, four types of muon candidates are reconstructed:

- *Combined (CB) muons* are reconstructed using a global refit to the hits in the ID and MS. First, the tracks are reconstructed independently in the ID and MS. Then, two matching procedures are performed: firstly an inward extrapolation starting from the MS tracks and matching them to the ID ones, and second an outward extrapolation starting from the ID tracks and matching them to the MS ones. The second procedure recovers the missing tracks of low p_{T}, which did not form a track segment in the first procedure. The CB muon candidates have the highest purity among all types of muons.

- *Segment-tagged muons* have only one track segment in the MDT or CSC chambers, which is matched to a track extrapolated from the ID. Such muon candidates either have low p_{T} or pass through the low-acceptance region of the MS.

- *Calorimeter-tagged muons* are reconstructed from tracks in the ID, which are matched to energy deposits consistent with minimum-ionising particles. Even though these muon candidates have the lowest purity among all types of muons, they still recover regions of low acceptance of the MS, which are not fully instrumented due to the busy environment of cables and equipment.

- *Extrapolated muons* are reconstructed from hits in the MS, forming a track which is assumed to originate close to the IP. The track parameters take into account the

Table 4.1: Shower shape variables of electrons and photons.

Name	Description	Variable
Hadronic leakage	Ratio of E_{T} in the first layer of the HCAL to E_{T} of the ECAL cluster (range: $\lvert\eta\rvert < 0.8$ or $\lvert\eta\rvert > 1.52$).	R_{had1}
	Ratio of E_{T} in the HCAL to E_{T} of the ECAL cluster (range: $0.8 < \lvert\eta\rvert < 1.37$).	R_{had}
Second layer of ECAL	Lateral shower width in the second layer of ECAL, $\sqrt{(\Sigma E_i \eta_i^2)/(\Sigma E_i) - ((\Sigma E_i \eta_i)/(\Sigma E_i))^2}$, where E_i is the energy and η_i is the pseudorapidity of cell i and the sum is calculated within a window of 3×5 cells.	$w_{\eta 2}$
	Ratio of the energy in 3×3 cells over the energy in 3×7 cells centred at the electron cluster position.	R_{ϕ}
	Ratio of the energy in 3×7 cells over the energy in 7×7 cells centred at the electron cluster position.	R_{η}
First (strip) layer of ECAL	Shower width in the first layer of ECAL, $\sqrt{(\Sigma E_i (i - i_{\mathrm{max}})^2)/(\Sigma E_i)}$, where i runs over all strips in a window of $\Delta\eta \times \Delta\phi \approx 0.0625 \times 0.2$, corresponding typically to 20 strips in η, and i_{max} is the index of the highest energy strip.	w_{stot}
	Ratio of the energy difference between the maximum energy deposit and the energy deposit in a secondary maximum in the cluster to the sum of these energies.	E_{Ratio}
	Difference between the energy of the second maximum and the energy with the minimum value between the first and second maxima.	ΔE
	Ratio of the energy in the first layer to the total energy in the ECAL.	f_1
	Ratio of the energy outside the core of the three central strips while still within seven strips to the energy within three central strips.	f_{side}

energy loss in the calorimeter. These muon candidates expand the muons' acceptance to regions that are not covered by the ID ($2.5 < |\eta| < 2.7$).

Since there is more than one type of muons, an overlap removal procedure is used to remove the duplication of muon candidates sharing the same ID track, which is done as follows. CB muon candidates have the highest priority, followed by the segment-tagged, while the lowest priority is given to the calorimeter-tagged type. Furthermore, based on the goodness of the fit and the number of hits, the overlap with the extrapolated muon candidates is removed. In this work, only *CB muons* are considered since they have the highest purity and provide coverage of $|\eta| < 2.5$.

Similar to electron candidates they are required to originate from the primary vertex, where the longitudinal impact parameter $|z_0 \sin(\theta)| < 0.5\,\text{mm}$ and transverse impact parameter d_0 with significance $|d_0/\sigma_{d_0}| < 3$. The candidates are also calibrated with the procedure described in Ref. [61].

4.2.2 Identification and isolation

Muon identification criteria are needed to distinguish prompt muons from muons coming from hadron decays, mainly from pions and kaons decays. The various identification WPs are defined using different requirements on quantities, like the number of hits in the ID and/or the MS, the charge/momentum ratio between the ID and the MS tracks, and the goodness of the combined-track fit. In this work, the *Medium* identification WP [61] is used, which has the advantage of having minimum systematic uncertainties during calibration and reconstruction. Similar to the isolation of electrons, the isolation of muons is also done by placing requirements on track-based and calorimeter-based isolation variables. Here, the *FCTight_FixedRad* isolation WP is used, which requires that muons satisfy:

- $E_{\text{T}}^{\text{topocone20}}/p_{\text{T}}(\mu) < 0.15$ and
- for $p_{\text{T}} < 50\,\text{GeV}$: $p_{\text{T}}^{\text{varcone30}}/p_{\text{T}}(\mu) < 0.04$,
  for $p_{\text{T}} > 50\,\text{GeV}$: $p_{\text{T}}^{\text{cone20}}/p_{\text{T}}(\mu) < 0.04$,

where $E_{\text{T}}^{\text{topocone20}}$ is a calorimeter-based isolation variable defined as the sum of energies of topological clusters around the muon candidate excluding the energy of the muon itself and $p_{\text{T}}(\mu)$ is the transverse momentum of the muon. Both of $p_{\text{T}}^{\text{varcone30}}$ and $p_{\text{T}}^{\text{cone20}}$ are track-based isolation variables defined as the scalar sum of all tracks' transverse momenta with a cone of ΔR around the muon candidate, excluding the muon track itself where the former uses a variable-radius cone of $\Delta R = \min(10\,\text{GeV}/p_{\text{T}}(\mu), 0.3)$ while the latter uses a fixed-radius cone of $\Delta R = 0.2$.

4.3 Photons

4.3.1 Reconstruction

Photons and electrons produce similar signatures, in the form of electromagnetic showers, when interacting with the ECAL. Therefore, their reconstruction is performed in parallel. Photons are reconstructed using the same procedure as for electrons. Energy deposits in the ECAL are clustered using a sliding-window algorithm. Then tracks are reconstructed in the ID and matched to the clusters in the ECAL to check if the candidate is a converted/unconverted photon or simply an electron. If the ECAL clusters do not correspond to either a conversion vertex or any track in the ID, then the candidate is reconstructed as an unconverted photon. However, if the ECAL clusters are matched to a conversion vertex, the candidate is reconstructed as a converted photon. Both types, converted and unconverted photons, are considered in this work. Energies of the photon candidates are calibrated with the procedure described in Ref. [62].

4.3.2 Identification and isolation

Photons in this work are identified using rectangular cuts on the shower shape variables described in Table 4.1. The identification of photons distinguishes between prompt photons and background photons originating from decays of neutral hadrons (e.g. $\pi^0 \to \gamma\gamma$) or QCD jets mimicking photons (jets deploying large energy fractions in the ECAL and are mis-reconstructed as photons). The distinction is performed based on the prompt photons depositing narrower energies in the ECAL and have smaller leakage to the HCAL compared to background photons. Furthermore, non-prompt photons from $\pi^0 \to \gamma\gamma$ decays are characterised by two separate local energy maxima in the first layer of the ECAL. There are two WPs for the identification of photons: *Loose* and *Tight*. The *Loose* identification is based on the shower shapes in the second layer of the ECAL and on the energy deposits in the HCAL. The *Tight* identification makes use of the same info as in the *Loose*, but it adds to it additional info from the finely segmented strip layer of the calorimeter. Since unconverted and converted photons have slightly different shower shapes, the *Tight* identification criteria are optimised separately for each of them. Moreover, due to the calorimeter geometry and the effect on the shower shapes from different detector material, the identification WPs are optimised as a function of the reconstructed photon candidate $|\eta|$. In order to enhance the number of prompt photons, photons are required to be isolated. Isolation of photons is based on the transverse energy in a cone of angular size ΔR around the photon candidate. Such transverse energy depends on two quantities, calorimeter isolation and track isolation.

- $E_{\mathrm{T}}^{\mathrm{iso}}$ is the calorimeter isolation and is defined as the sum of transverse energies of topological clusters [57] after subtracting the energy of the photon candidate and the contribution from the underlying event and pile-up.

Table 4.2: Isolation WPs of photons.

WP	Calorimeter isolation	Track isolation
FixedCutLoose	$E_{\mathrm{T}}^{\mathrm{iso}}\big\vert_{\Delta R<0.2} < 0.065 \cdot E_{\mathrm{T}}(\gamma)$	$p_{\mathrm{T}}^{\mathrm{iso}}\big\vert_{\Delta R<0.2} < 0.05 \cdot E_{\mathrm{T}}(\gamma)$
FixedCutTight	$E_{\mathrm{T}}^{\mathrm{iso}}\big\vert_{\Delta R<0.4} < 0.022 \cdot E_{\mathrm{T}}(\gamma) + 2.45\,\mathrm{GeV}$	$p_{\mathrm{T}}^{\mathrm{iso}}\big\vert_{\Delta R<0.2} < 0.05 \cdot E_{\mathrm{T}}(\gamma)$
FixedCutTightCaloOnly	$E_{\mathrm{T}}^{\mathrm{iso}}\big\vert_{\Delta R<0.4} < 0.022 \cdot E_{\mathrm{T}}(\gamma) + 2.45\,\mathrm{GeV}$	–

- $p_{\mathrm{T}}^{\mathrm{iso}}$ is the track isolation and is defined as the sum of transverse momenta of all the tracks with transverse momentum above 1 GeV. Further requirements of having a distance to the primary vertex [52] along the beam axis $|z_0 \sin\theta| < 3$ mm and exclusion of tracks associated with photon conversions must also be satisfied. In the ATLAS Collaboration, there are three isolation WPs shown in Table 4.2. This work uses the WPs *Tight* for the identification and *FixedCutTight* for the isolation of photons.

4.3.3 Shower shapes reweighting

As already discussed earlier, shower shapes play a major role in the identification and isolation of photons. The simulation of the shower shapes in MC differs from the distributions in data. This could happen owing to a mis-modelling of the simulation or/and a leakage from the hadronic calorimeter, among other reasons. Therefore, a correction of the shower shapes is needed so that the MC shapes match the data ones. A method to perform this correction is described in Chapter 5.

4.4 Jets

4.4.1 Reconstruction

Quarks and gluons are colour-charged particles and, hence, they can not be observed experimentally due to the colour confinement property of QCD. These partons hadronise very quickly, forming a hadron which in turn decays to a collimated cascade of particles collectively called a *jet*. Jets have associated tracks in the ID system and energy deposits in both the ECAL and HCAL systems. In order to reconstruct a jet, a clustering algorithm is needed to combine tracks in the ID system and energy deposits in the ECAL and HCAL calorimeters. Such an algorithm must be collinear and infrared safe. This means it must ensure that the jets are robust to collinear splittings and soft infrared radiations. In the ATLAS Collaboration, the most commonly used algorithm is the anti-k_t algorithm [63]. It is a sequential clustering algorithm that uses topological cell clusters [64] as inputs. These clusters are treated as massless pseudo-particles with four-momentum defined from the energy

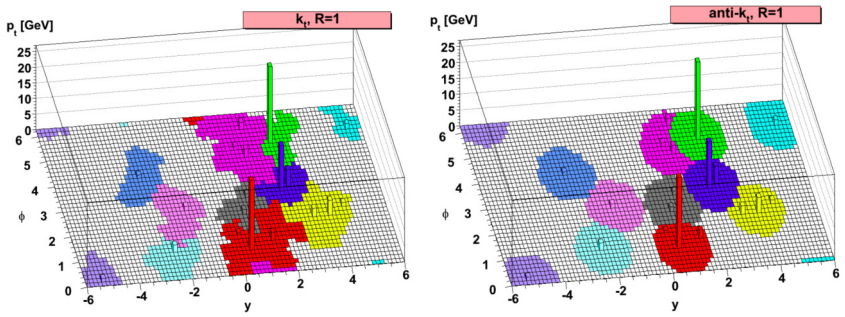

Figure 4.1: Jet clustering example using the k_t (left) and anti-k_t (right) algorithms. The figures are sourced from Ref. [63].

and direction weighted by the barycentre of the cell cluster. The algorithm calculates two parameters, the distance d_{ij} between each pair of inputs, i and j, and the distance d_{iB} between each input i and the beam axis as follows:

$$d_{ij} = \min(k_{t,i}^{2p}, k_{t,j}^{2p}) \frac{\Delta R_{ij}^2}{R^2}, \tag{4.1a}$$

$$d_{iB} = k_{t,i}^{2p}, \tag{4.1b}$$

where $\Delta R_{ij}^2 = (y_i - y_j)^2 - (\phi_i - \phi_j)^2$ and k_t , y, and ϕ are the transverse momentum, rapidity, and azimuthal angle of the input particle, respectively. R is the radius parameter which controls the approximate cone size of the final jet. The parameter p determines the order of the clustering where in the case of the anti-k_t algorithm, $p = -1$, while in the case of k_t algorithm [65], $p = 1$. If p is positive, then the algorithm will cluster particles from softest to hardest, while if it is negative, it behaves the other way around. The anti-k_t algorithm then identifies the smallest distance, which is the minimum of d_{ij} and d_{iB}. If the smallest distance is d_{ij}, then clusters i and j are combined. If d_{iB} is the smallest, then i is called a jet and removed from the list of clusters. This process is repeated for all the topological clusters until no clusters are left in the list. The anti-k_t algorithm results in more cone-like jets compared to clusters combined with the k_t algorithm which can be seen in Fig. 4.1.

In this work, jets are reconstructed using the anti-k_t algorithm in the FastJet implementation [66] with a radius parameter $R = 0.4$.

4.4.2 Calibration

Once jets are reconstructed, calibration techniques are used to calibrate their four-momenta in the MC simulation and data. In general, there are two methods used in combination: MC-based and in-situ techniques. The former is to correct the four-momenta of the reconstructed jet to the particle-level truth jet, while the latter is to correct for the differences in jet response

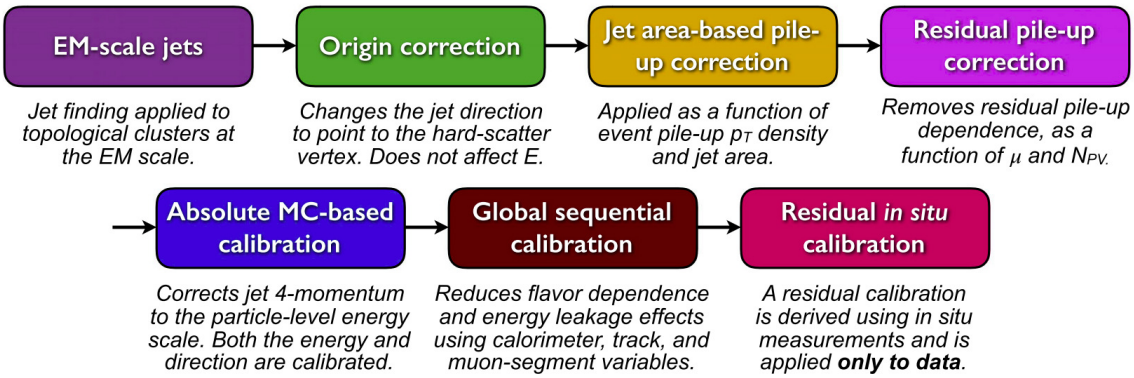

Figure 4.2: A schematic overview of the jet calibration steps in the ATLAS detector. The figure is sourced from Ref. [67].

between data and MC. The calibration of jets is divided into several steps, as shown in Fig. 4.2. First, the origin of the jet is corrected so that it points to the primary vertex rather than the centre of the detector, which improves the resolution in η. Next, the excess in energy originating from the *in-time* and *out-of-time* pile-up is removed. In-time (out-of-time) pile-up is defined as additional pp interactions from the same (neighbouring) bunch crossings. This correction is done by subtracting the per-event pile-up contribution to the p_{T} of each jet according to its area, hence an area-based correction. After this pile-up correction, a dependency of the anti-k_t jet p_{T} on the amount of pile-up remains. Therefore, a further correction is applied, which is called residual pile-up correction. After pile-up corrections, an MC-based calibration is used. It uses the absolute jet energy scale (JES) and η-calibration to correct the four-momentum of the reconstructed jet to the particle-level true energy scale and account for biases in the jet-η reconstruction. The next step is called the global sequential calibration. It removes the residual dependencies due to differences in the composition of quark- and gluon-initiated jets and accounts for energy leakage effects. The last step in the jet calibration is called residual in-situ. It accounts for differences in the jet response between data and MC due to the mis-modelling of the detector response and detector material in the MC simulation.

4.4.3 *b*-tagging

The distinction between jets originating from hadrons with b-quarks, so-called *b-jets*, and jets from hadrons with other quark flavours is essential for analyses studying properties of the top quark, such as the one presented here. A property of hadrons with b-quarks, called b-hadrons, is that they have a much longer lifetime than light-flavour hadrons and hence travel for a measurable distance before they decay. Light-flavour hadrons are hadrons with u-, d- or s- quarks. Therefore, b-hadrons can be identified by the presence of a secondary vertex displaced from the primary vertex of the hard interaction. Furthermore, they are heavier and

produce more energetic decay products compared to the light-flavour hadrons. In the ATLAS Collaboration, a very common b-tagging algorithm is the MV2c10 [68]. It is a multivariate discriminant algorithm that distinguishes between different jet flavours and uses as input the following b-tagging algorithms:

- *IP2D and IP3D impact parameter algorithms* [69] are techniques that use the transverse and longitudinal track impact parameters of the tracks associated with b-hadron decays to identify the b-hadrons. The outcome of such algorithms is a log-likelihood ratio for the possible combinations of different jet flavours.[3]
- *Secondary vertex SV1* [70] is an algorithm that reconstructs a single displaced secondary vertex inside a jet. The reconstruction is performed by checking all possible two-track vertices and rejecting tracks in agreement with the decay of long-lived particles.
- *JetFitter* [71] performs a topological reconstruction of the b-hadron decays inside the jet. The algorithm is of high importance when a higher level of c- and light jet rejection is needed while maintaining an intermediate b-jet efficiency.

In this work, the MV2c10 [68] algorithm is used with a WP of 85% b-tagging efficiency, which corresponds to c- and light-jet rejection factors of 3.1 and 35, respectively.

4.5 Missing transverse energy

Some particles escape the ATLAS detector without any detection, i.e. they do not leave tracks in the ID and do not deposit energies in the calorimeters. These invisible particles are neutrinos in the case of the SM. They can also hint to other hypothetical weakly-interacting particles in the case of theories beyond the SM. Their presence is detected indirectly owing to the energy and momentum conservation in the transverse plane, and it is quantified as the missing energy $\overrightarrow{E}_T^{\text{miss}}$. It is defined as the magnitude of $p_{\text{T}}^{\text{miss}}$ with an azimuthal coordinate of ϕ^{miss}. The $\overrightarrow{E}_T^{\text{miss}}$ comprises two terms where the first one depends on the different objects (electrons, muons, photons, jets and the hadronically-decaying τ-leptons that come from the primary interaction, i.e. *hard objects*) in an event, and therefore they need to be well-calibrated and reconstructed [72]. The second term is called the soft term, which depends on tracks in the ID system or calorimeter energy deposits that are not associated with physics objects (*soft signals*). The first term has a slight dependence on pile-up since it depends on well-calibrated objects where the pile-up contribution is already accounted for and corrected. However, the second term is not robust against pile-up and therefore further techniques are used to correct it. The $\overrightarrow{E}_T^{\text{miss}}$ has two components E_x^{miss} and E_y^{miss}, which are expressed in the x- and y-components of the $p_{\text{T}}^{\text{miss}}$, $p_{x(y)}^{\text{miss}}$:

[3] The combinations are b- and light jet, b- and c-jet, and c- and light jet, where light jet is a jet with u-, d- or s-quarks.

$$E_{x(y)}^{\text{miss}} = -\sum_{\text{all hard objects}} p_{x(y)}^{\text{miss}} - \sum_{\text{all soft signals}} p_{x(y)}^{\text{miss}}\,, \tag{4.2}$$

from which the E_T^{miss} is calculated as:

$$E_T^{\text{miss}} = \sqrt{(E_x^{\text{miss}})^2 + (E_y^{\text{miss}})^2}\,. \tag{4.3}$$

CHAPTER 5

Shower shapes reweighting for photons

The photon shower shapes differ between MC and data due to mis-modelling of the simulation and/or leakage from the hadronic calorimeter. The motivation for the study in this chapter is to improve the agreement between data and MC shower shapes (for definitions of shower shapes, see Table 4.1) by applying a correction to the MC shapes using a cell-based energy reweighting of the photons. After applying the correction, the MC shower shapes of the photons would better mimic those in the data.

In this chapter, the data and MC samples used in the shower shapes reweighting are presented in Section 5.1. The method of cell-based reweighting of photons is introduced in Section 5.2. The applied event selection and the approaches to obtain a pure sample are described in Sections 5.3 and 5.4, respectively. Results of the study are presented at the end of the chapter in Section 5.5.

5.1 Data and MC samples

This study is performed with pp collision data collected during the years 2 015, 2 016, and 2 017 at $\sqrt{s} = 13$ TeV, with the corresponding integrated luminosities of 3.2 fb^{-1}, 33.0 fb^{-1}, and 44.3 fb^{-1}, respectively. The total collision data correspond to an integrated luminosity of 80.5 fb^{-1} and are required to have been collected while the ATLAS detector was fully operational and satisfied quality criteria. The $Z \to ee\gamma$ MC samples used for this study are generated with SHERPA 2.2.2 using the NNPDF3.0NNLO [73] and CT10 [74] PDF sets.

5.2 Cell-based energy reweighting of photons

The correction of the shower shape variables of photons is performed through a reweighting to the cell-based energies of photons along the η-direction. In order to derive such correction, photons are matched to clusters in the second layer of the ECAL with different sizes of clusters in the η-ϕ space. More specifically, photons are matched to clusters with $\eta \times \phi$ cells

of sizes 3×7 in the barrel and 5×5 in the end-cap regions. In addition, a matching of photons to a bigger-size cluster of 7×11 is also constructed which surrounds the 3×7 and 5×5 clusters. The reason behind the construction of the bigger cluster is to study the lateral energy leakage. To construct the 7×11 cluster, two steps are needed:

- Firstly, the central cell of the cluster has to be located. The closest cell with the minimal ΔR around the photon cluster which passes the selection is stored. Next, within a $\Delta R < 0.5$ around the located cell, a search for the cell with the largest energy deposit is performed; as a result, such cell with the maximum energy is considered to be the central cell of the cluster.
- Secondly, the construction of 7×11 cluster around the central cell is performed. Important information like energies, η and ϕ are stored for the 77 cells; only a complete number of 77 cells are kept.

Once the 7×11 cluster is built, the weights (to correct the MC simulation) are calculated as ratios of the data energy per cell to the MC one along η-direction, $E_i^{\text{data}}/E_i^{\text{MC}}$, where i is the index of the cell.

5.3 Event selection

The cell-based energy reweighting is studied by investigating photons originating from the radiative decay process of the Z boson, i.e. $Z \to ee\gamma$. Such a process has the advantage of having a relatively small fraction of backgrounds. The primary source of background is due to photons originating from jets mimicking photons (from Z+jets). The selection is applied such that events are required to include at least one primary vertex with at least three associated tracks, an electron-positron pair, and one photon. Photons and electrons must fulfil the criteria described in Table 5.1. Furthermore, a requirement on the mass of the electron-positron pair is placed: $40 < m_{ee} < 83$ GeV. Despite the object and event selection requirements, there still exists a large portion of background, as shown in the $m_{ee\gamma}$ distribution in Fig. 5.1. Therefore, additional approaches are needed to select a pure $Z \to ee\gamma$ sample, as discussed in the following section.

5.4 Pure $Z \to ee\gamma$ sample

In order to study the effect of the cell reweighting on the shower shapes of prompt photons, it is necessary to have a pure $Z \to ee\gamma$ sample. The aim is to remove the background contamination in data, mainly in the peak region of the $m_{ee\gamma}$ distribution (see Fig. 5.1). After applying the selection in Section 5.3, the remaining background contribution is accounted for by a reweighting based on the signal fraction or by tightening the selection requirements. Therefore, two approaches are tested where the first one is used as the benchmark, whereas the second is used as a verification:

Table 5.1: Object definition of electrons and photons for the cell-based energy reweighting of photons. The *MediumLH* identification WP has an efficiency of 88% for selecting a prompt electron with $E_T = 40\,\text{GeV}$. The *GradientLoose* isolation WP has an isolation efficiency of 95 (99)% at 25 (60) GeV [57].

	Electrons	Photons
Acceptance	$p_T > 10\,\text{GeV}$ $\lvert\eta\rvert < 1.37$, $1.52 < \lvert\eta\rvert < 2.47$ $\lvert d_0 / \sigma_{d_0} \rvert < 10$ $\lvert z_0 \sin(\theta)\rvert < 10\,\text{mm}$	$E_T > 10\,\text{GeV}$ $\lvert\eta\rvert < 1.37$, $1.52 < \lvert\eta\rvert < 2.37$ — —
Identification	*MediumLH*	—
Isolation	*GradientLoose*	—

- The **first approach** is based on a signal fraction reweighting. This is performed by fitting the $m_{ee\gamma}$ distribution in data, followed by a window cut of $80 < m_{ee\gamma} < 100\,\text{GeV}$. The fit function is a combination of a Crystal-ball function (for signal) and fourth-order Bernstein polynomial (for background). The fit is performed for each of the measured $Z \rightarrow ee\gamma$ datasets (2015–2017) independently. An example of the fit for the dataset of the year 2017 can be seen in Fig. 5.2. The fits for the datasets corresponding to 2015 and 2016 can be seen in Appendix A. Afterwards, from the post-fit results a signal fraction weight W_{sf} is estimated in each bin of the $m_{ee\gamma}$:

$$W_{\text{sf}} = \frac{\text{signal}}{\text{signal} + \text{background}} \,. \tag{5.1}$$

  These weights are then applied to the shower shapes of data to correct for the background contamination. An example of the weights calculated from the fit to the 2017 dataset can be seen in Fig. 5.3. The weights corresponding to the datasets of the years 2015 and 2016 can be found in Appendix A.

- Additionally, a **second approach** is used to verify the first one, by applying a photon isolation WP *FixedCutLoose*[1] , followed by a window cut of $80 < m_{ee\gamma} < 100\,\text{GeV}$.

The two approaches are compared to the nominal case where the latter represents applying only the event selection (see Section 5.3) without any further requirements to reduce the background. The results of the two approaches in the inclusive η region for converted and unconverted photons are discussed in Section 5.5.1. The results of the cell reweighting correction are shown in Section 5.5.2.

[1] This WP is chosen as loose as possible to avoid causing a bias in the shower shapes, which are intended to be corrected in the first place.

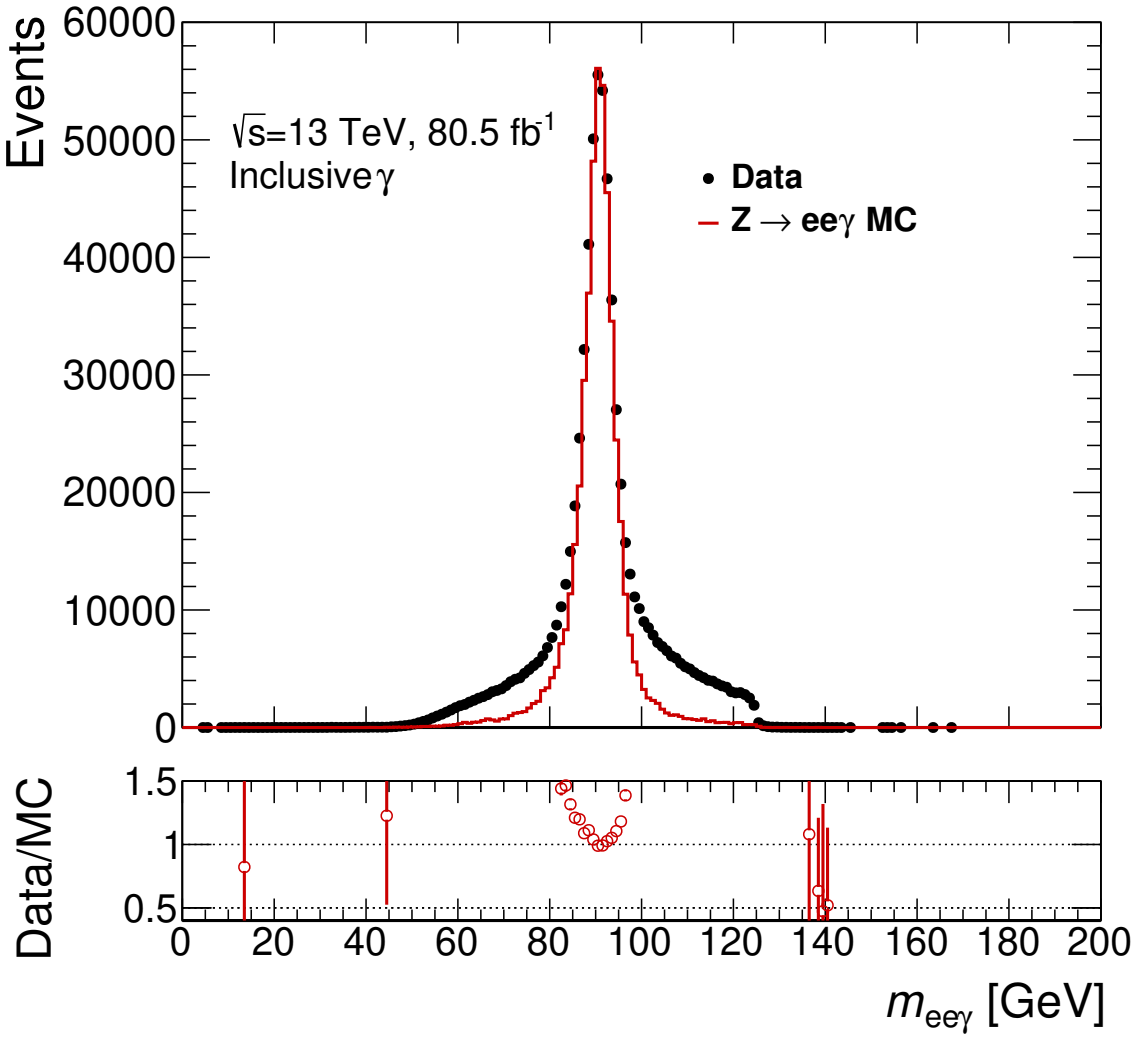

Figure 5.1: Invariant mass distribution of $m_{ee\gamma}$ in data (black) and MC (red) in the inclusive η region: $0 < |\eta(\gamma)| < 1.37$ or $1.52 < |\eta(\gamma)| < 2.37$ for inclusive (converted and unconverted) photons.

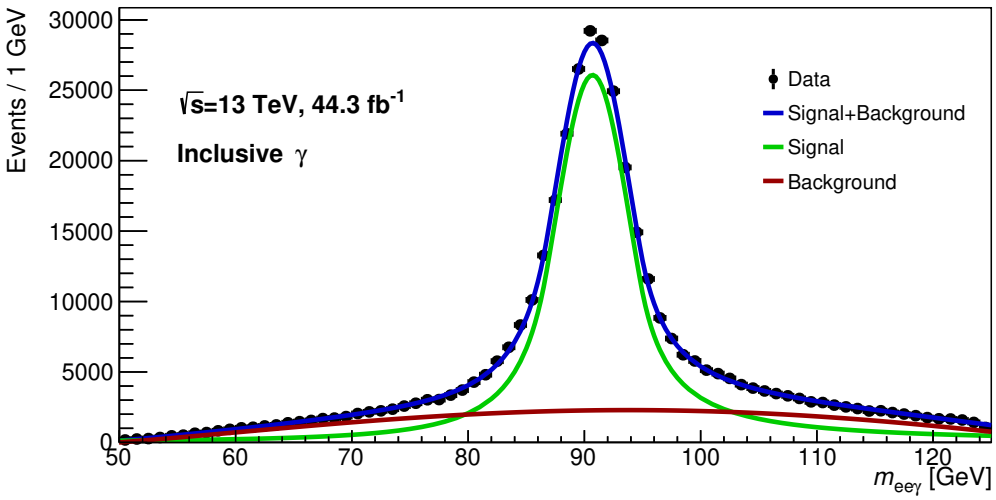

Figure 5.2: Example of the fit to the $m_{ee\gamma}$ distribution of $Z \to ee\gamma$ data for the year 2017, where a Crystal-ball function and 4th order Bernstein polynomial are used to model signal and background, respectively.

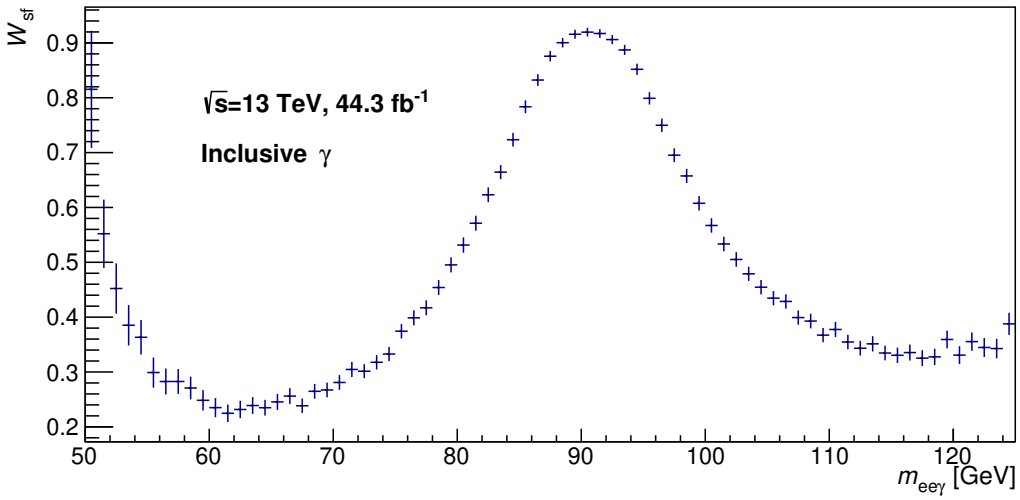

Figure 5.3: Example of signal fraction weights W_{sf}, calculated from the post-fit results of the $Z \to ee\gamma$ data for the year 2017 using Eq. (5.1).

5.5 Results of cell-based reweighting

5.5.1 Background reduction

Fig. 5.4 shows the $m_{ee\gamma}$ distribution in the data and the MC simulation for converted (left column) and unconverted (right column) photons. The first row displays the data distributions without applying any additional requirements beyond the selection in Section 5.3. The second and third rows show the data distributions after applying the first and second approaches, respectively. The behaviour of the two approaches is similar, where most of the background contribution is removed. The first approach is chosen as the benchmark for all the results in the main body of the thesis, while the results of the second approach and more studies, such as showing the distributions in different slices of η, can be found in Appendix A.

5.5.2 Cell-based energy reweighting

As an example, in the case of R_η distribution, the top and bottom plots of Fig. 5.5 show the modelling of the shower shape for converted and unconverted photons, respectively. The data distributions to the right have the first approach applied to them, whereas the data distributions to the left do not have any requirements beyond the event selection. The shapes of the data in the left column look similar to those of the right, indicating no bias due to the first approach background reduction. This can be seen for the rest of the shower shapes as well.

In order to examine the impact of the cell-based reweighting correction, the MC shower shapes before and after correction are compared to those of the data , which can be seen, for example, for R_η in the right plots of Fig. 5.5. The correction for R_η gives a better agreement with data for both converted and unconverted photons. For R_ϕ, the correction, in general, does not improve the agreement significantly, as can be seen in Fig. 5.6. For R_{had}, f_1, E_{Ratio} and ΔE, they are similar to R_ϕ, and are shown in Appendix A. The correction for $w_{\eta 2}$ provides a better agreement with data, as shown in Fig. 5.7. The improvement for converted photons is more enhanced than the unconverted photons. For w_{stot}, the correction gives a moderate improvement at the lower and higher tails of both converted and unconverted photons distributions, as shown in Fig. 5.8. For f_{side}, the correction gives a noticeable improvement in the case of converted photons as can been seen in Fig. 5.9, while for unconverted photons, the correction slightly improves the agreement with data.

In summary, the results of the cell-based energy reweighting of photons show a good improvement in the agreement between data and MC shower shapes, especially for the R_η, $w_{\eta 2}$, w_{stot} and f_{side} shower shapes. However, for the rest of the shower shapes, i.e., R_ϕ, R_{had1}, f_1, E_{Ratio} and ΔE, the correction does not improve the data/MC agreement significantly.

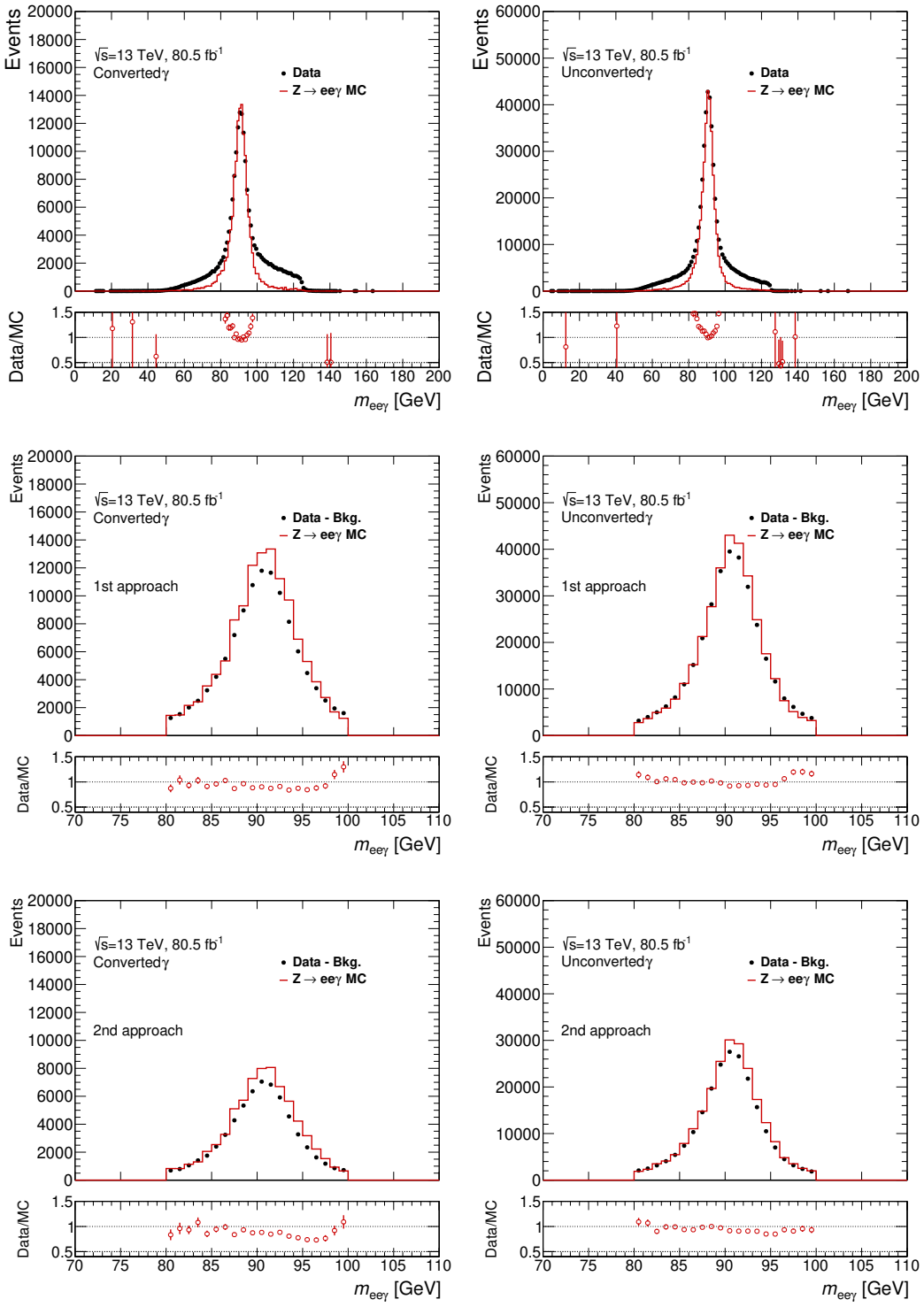

Figure 5.4: Invariant mass distributions of $m_{ee\gamma}$ in data (black) and MC (red) in the inclusive η region: $0 < |\eta(\gamma)| < 1.37$ or $1.52 < |\eta(\gamma)| < 2.37$. The left (right) column shows for converted (unconverted) photons, three distributions: nominal event selection case (top), first approach (middle), and second approach (bottom). In the middle and bottom rows, the background contribution in $Z \rightarrow ee\gamma$ data has been further reduced using either the first or second approach, respectively, while in the top row, no requirements are added beyond the event selection described in Section 5.3.

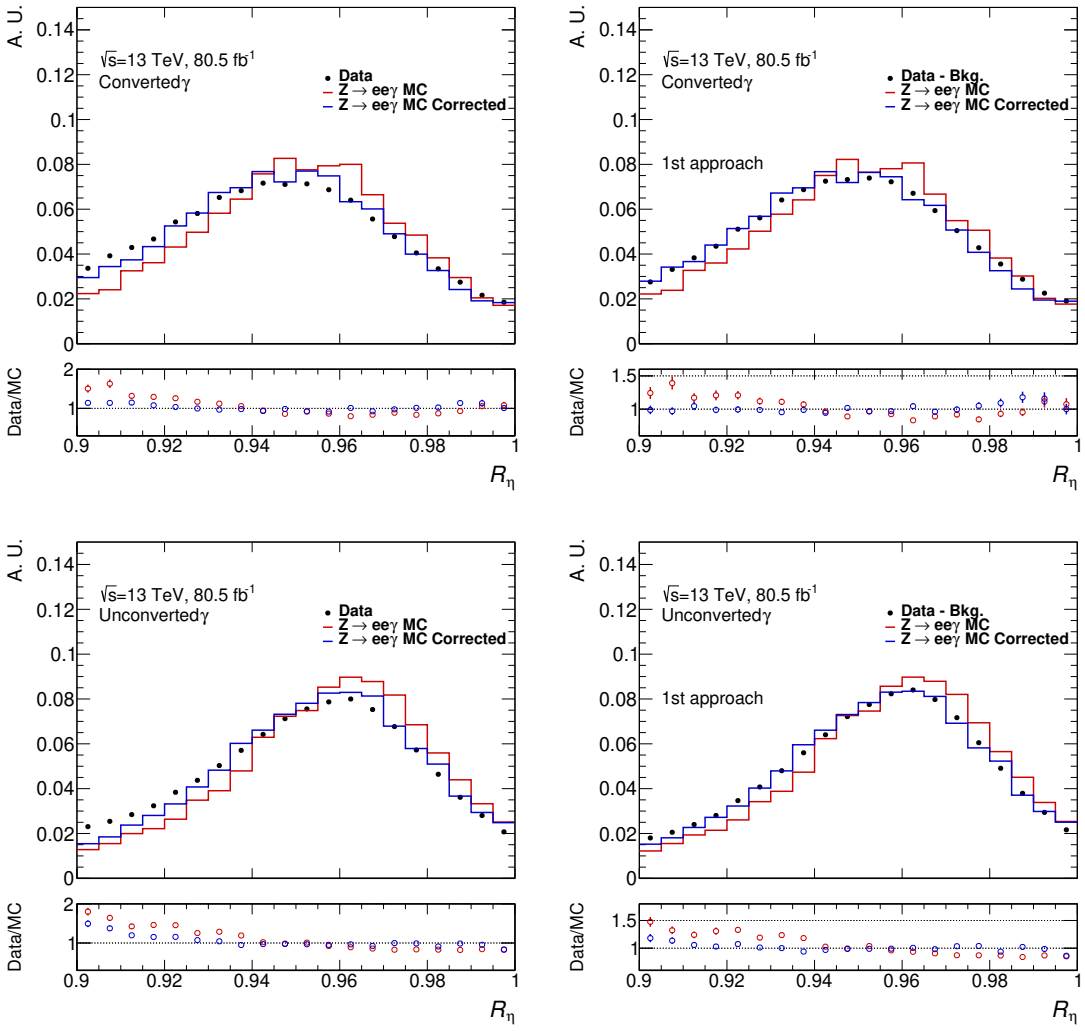

Figure 5.5: R_η distributions in data (black) and MC before (red) and after (blue) cell-based correction in the inclusive η region: $0 < |\eta(\gamma)| < 1.37$ or $1.52 < |\eta(\gamma)| < 2.37$. In the top (bottom) row for converted (unconverted) photons, two distributions are shown: nominal event selection case (left) and first approach (right).

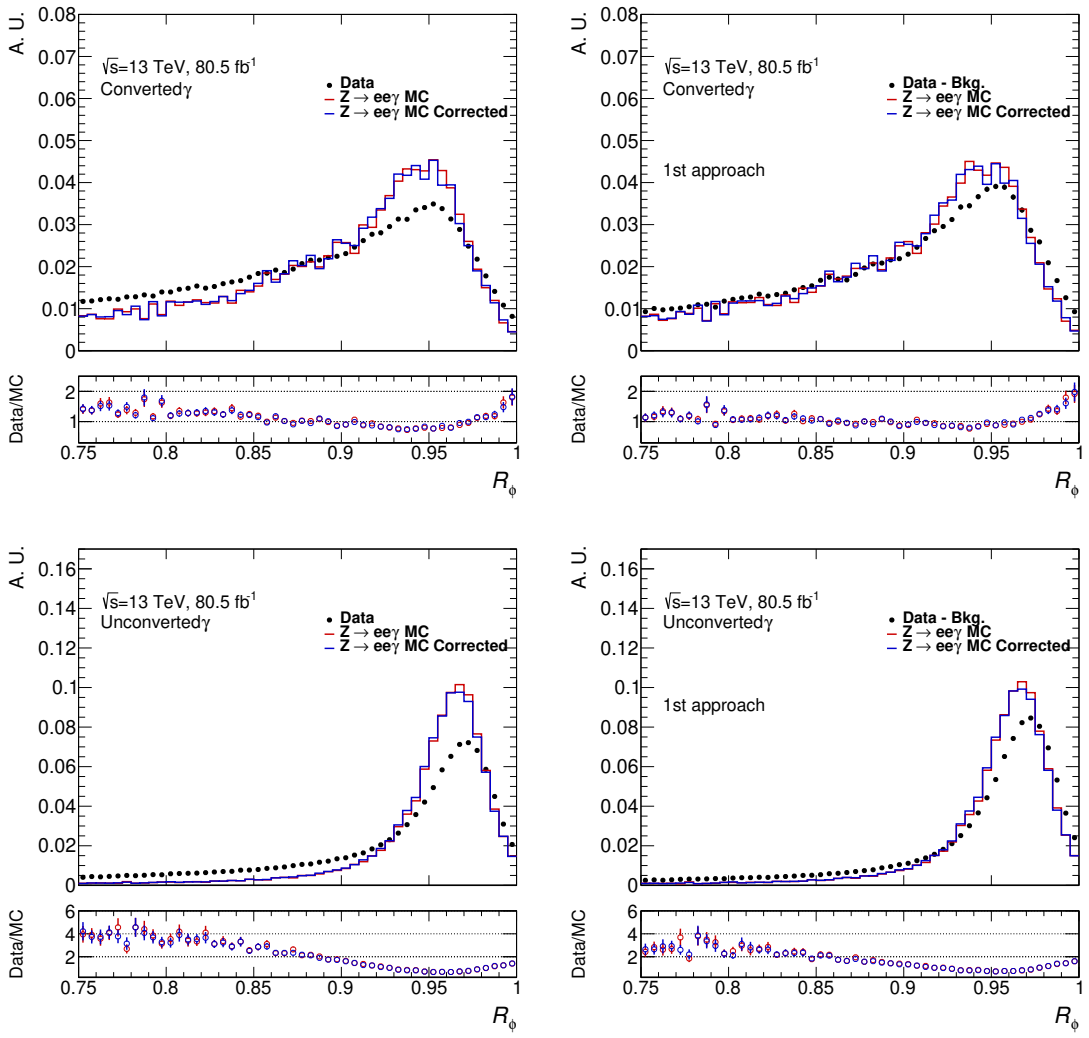

Figure 5.6: R_ϕ distributions in data (black) and MC before (red) and after (blue) cell-based correction in the inclusive η region: $0 < |\eta(\gamma)| < 1.37$ or $1.52 < |\eta(\gamma)| < 2.37$. In the top (bottom) row for converted (unconverted) photons, two distributions are shown: nominal event selection case (left) and first approach (right).

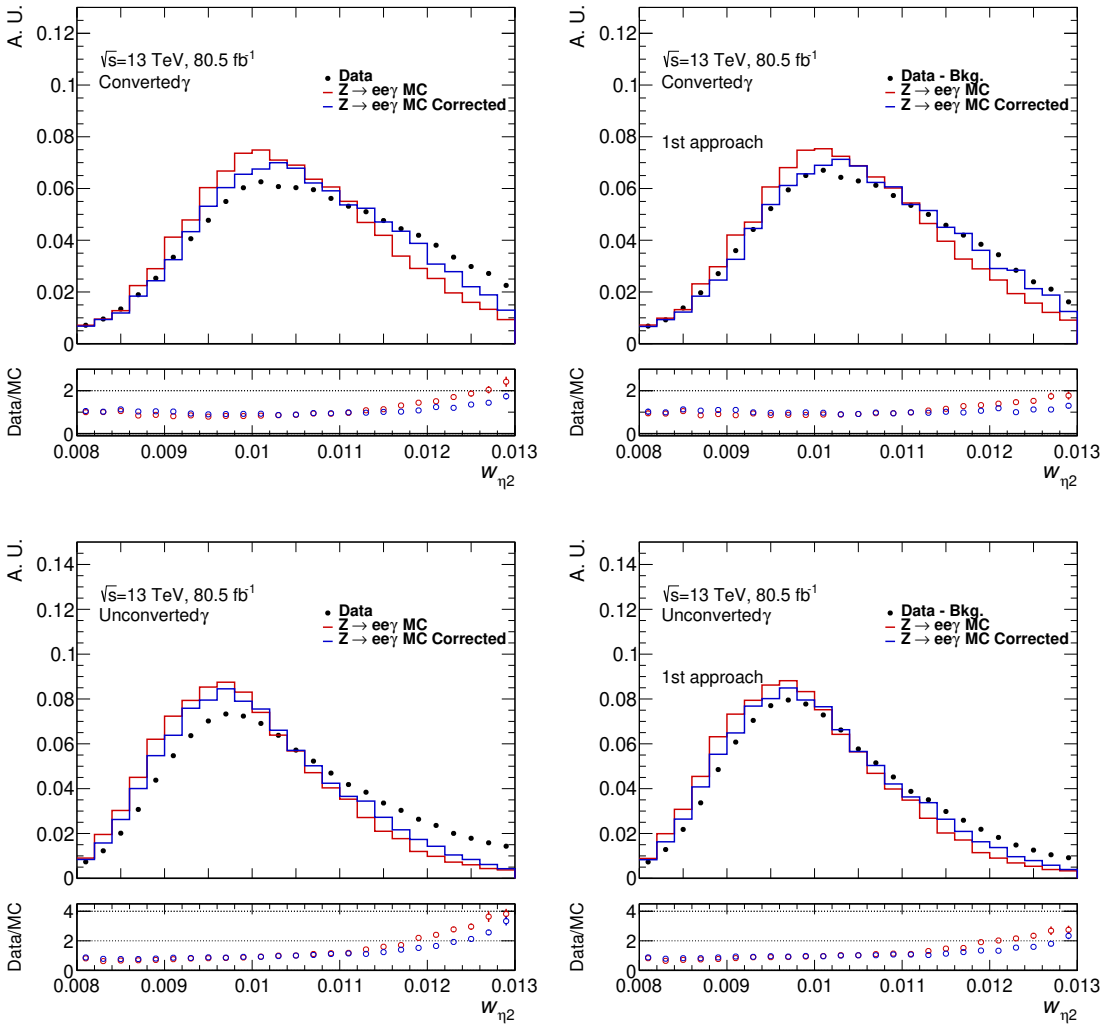

Figure 5.7: $w_{\eta 2}$ distributions in data (black) and MC before (red) and after (blue) cell-based correction in the inclusive η region: $0 < |\eta(\gamma)| < 1.37$ or $1.52 < |\eta(\gamma)| < 2.37$. In the top (bottom) row for converted (unconverted) photons, two distributions are shown: nominal event selection case (left) and first approach (right).

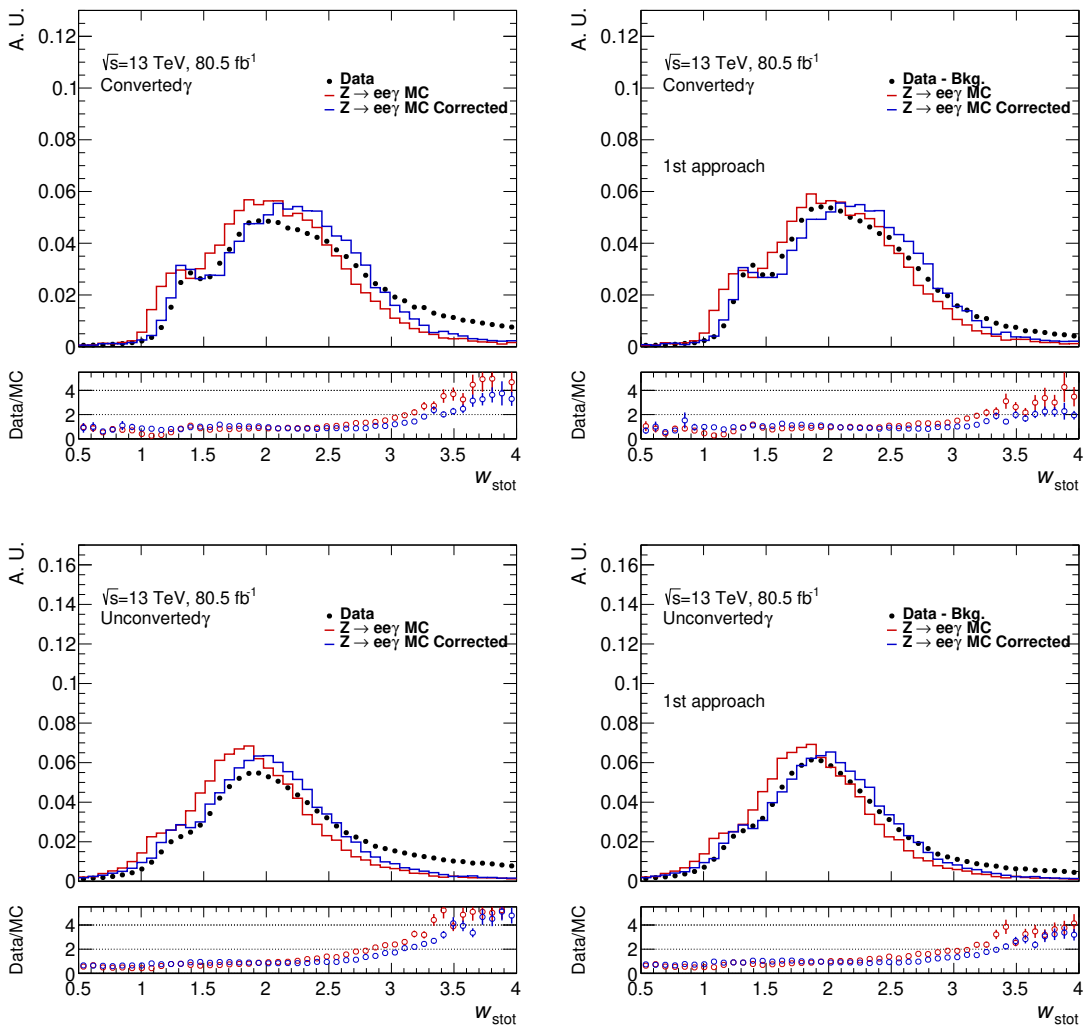

Figure 5.8: w_{stot} distributions in data (black) and MC before (red) and after (blue) cell-based correction in the inclusive η region: $0 < |\eta(\gamma)| < 1.37$ or $1.52 < |\eta(\gamma)| < 2.37$. In the top (bottom) row for converted (unconverted) photons, two distributions are shown: nominal event selection case (left) and first approach (right).

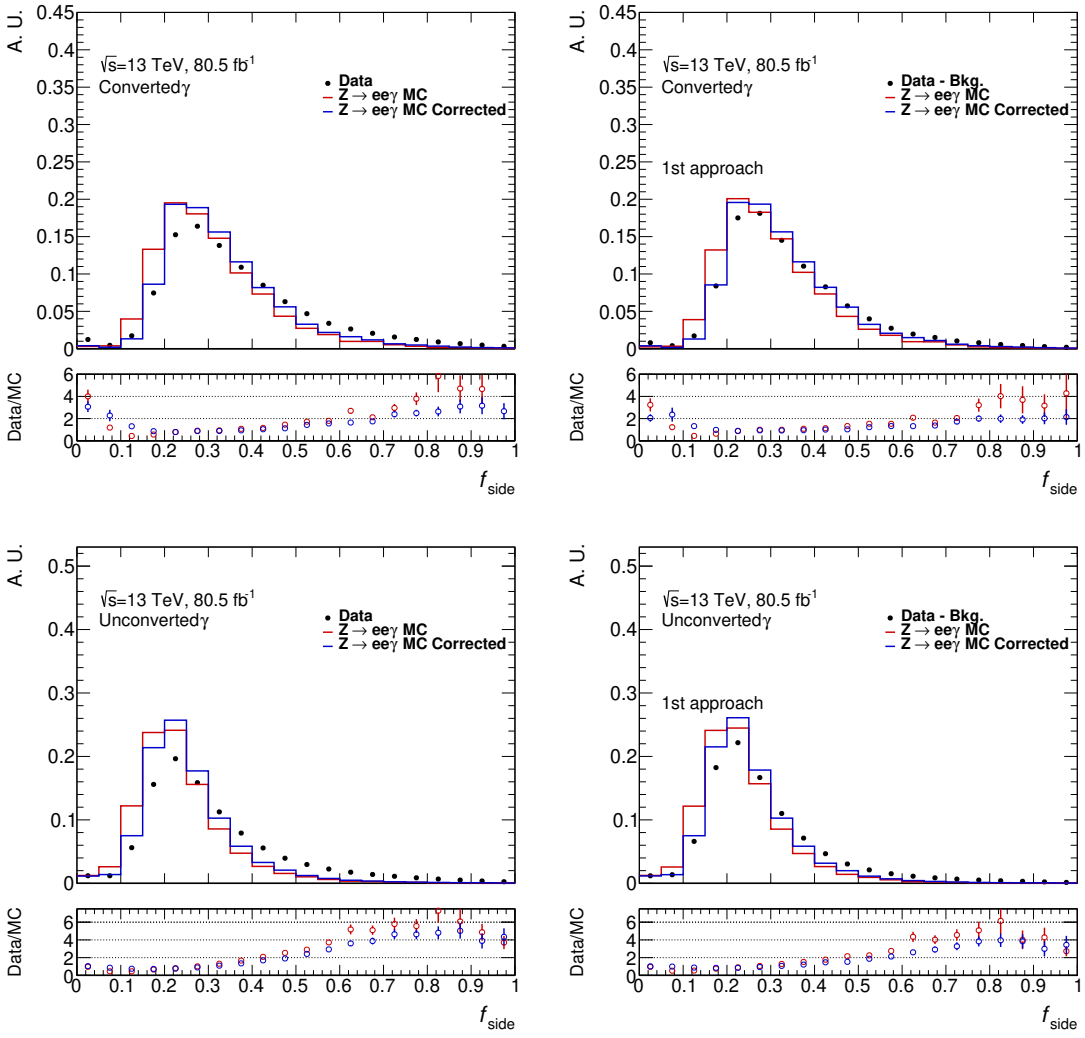

Figure 5.9: f_{side} distributions in data (black) and MC before (red) and after (blue) cell-based correction in the inclusive η region: $0 < |\eta(\gamma)| < 1.37$ or $1.52 < |\eta(\gamma)| < 2.37$. In the top (bottom) row for converted (unconverted) photons, two distributions are shown: nominal event selection case (left) and first approach (right).

CHAPTER 6

Data and MC simulation for $t\bar{t}\gamma$ + $tW\gamma$ measurement

In this thesis, the fiducial differential cross-section of the combined $t\bar{t}\gamma$ and $tW\gamma$ process in the $e\mu$ decay channel is measured. The signature of signal events can be mimicked by other physics processes, which are called background processes. Therefore, MC simulations are compared to data to determine the composition of signal and background processes.

In this chapter, the data used to perform the measurement is discussed in Section 6.1. A summary of steps to generate an MC simulation is discussed in Section 6.2. The simulation of signal and background processes is discussed in Section 6.3 and Section 6.4, respectively. The method of overlap removal between the samples is illustrated in Section 6.5.

6.1 Data

The measurements presented here are performed with data collected by the ATLAS detector during Run 2 of the LHC in the period of 2 015–2 018 at $\sqrt{s}$ = 13 TeV. A subset of the total collected data is considered good if the detector was fully operational and the recorded data satisfied certain quality criteria. These data correspond to integrated luminosities of 3.2, 33.0, 44.3, and 58.5 fb^{-1} for the the years 2 015 to 2 018, respectively, i.e. a total integrated luminosity of 139 fb^{-1}. The mean number of interactions per bunch crossing (pile-up) for the data recorded in the years 2 015–2 018 with the ATLAS detector is shown in Fig. 6.1.

6.2 MC simulation

MC simulations are needed to estimate the contribution of different physics processes in the measured data. They are also used to evaluate efficiencies, migration, and acceptance, which are discussed in Chapter 8. Furthermore, they are used to account for the in-time and out-of-time pile-up by superimposing hard-scattering (discussed below) events with

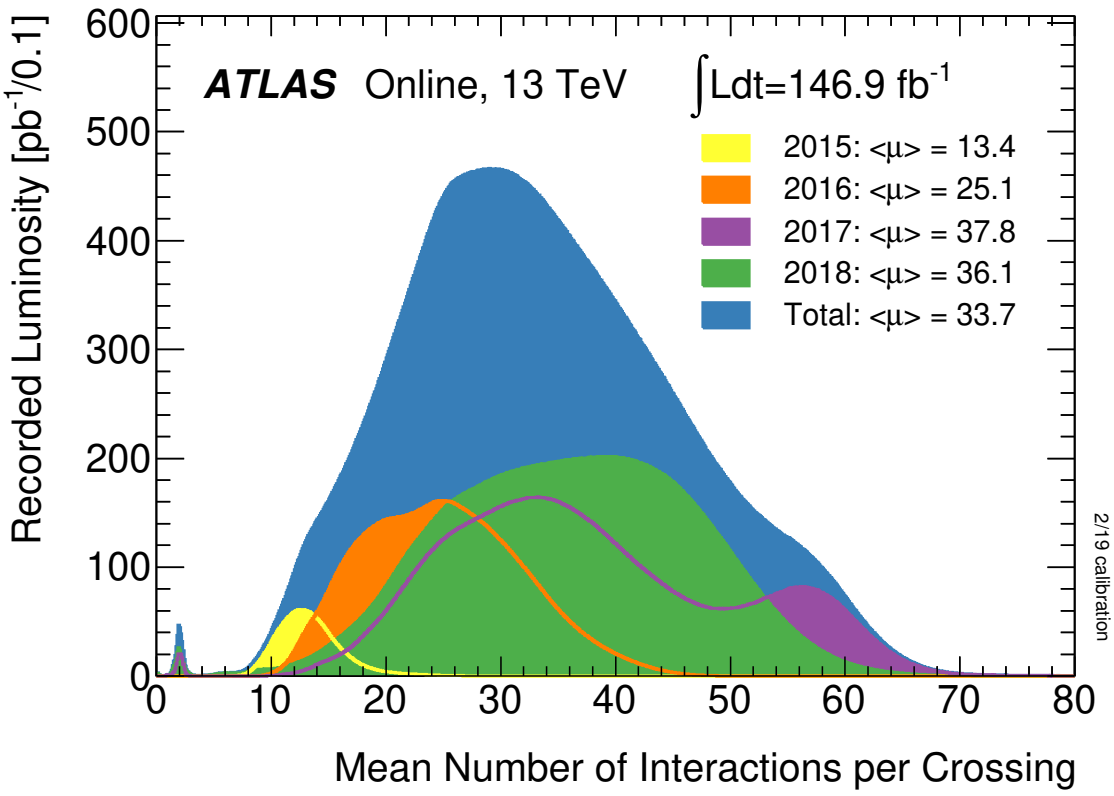

Figure 6.1: Pile-up distributions for the data recorded by the ATLAS experiment in the years 2 015–2 018. The figure is sourced from Ref. [75].

minimum-bias interactions generated with PYTHIA 8 [76]. The MC simulations are produced through different steps: event generation, detector simulation and digitisation of the deposited energy. The final output of these simulations can then be run through the ATLAS trigger and reconstruction algorithms to compare the corresponding objects in the measurement and the simulation.

Event generation

The first step is to generate events mimicking the production rate and kinematic properties of the processes under study. This step is called event generation, and it comprises different consequent processes; the first one is called hard scattering. The Matrix Element (ME) calculation of the hard scattering process is performed in the perturbation theory at fixed order. In the hard scattering, collisions of protons are simulated where the PDF determines the probability that the partons in the protons collide.

Next is the showering process, which simulates the radiation of gluons and photons, called QCD and QED radiations, respectively. These radiations are called Initial State Radiation

(ISR) if they come from the incoming partons and Final State Radiation (FSR) if coming from the outgoing particles. The simulation of such radiations is a complex process because partons radiate gluons, which can, in turn, emit further gluons—since gluons carry color—or produce $q\bar{q}$ pairs. This leads to the formation of a cascade of particles called the *parton shower*.

The last step in the event generation is the hadronisation process, where partons form hadrons and decay to stable particles. Hadronisation occurs due to the confinement property of QCD (see Section 2.1).

Detector simulation and digitisation

Once events are generated, they are fed to the second step which is the detector simulation. The full simulation of the ATLAS detector is done using the GEANT4 [77–79] by modelling the physics of the traversing particles and their interactions (hits) through their trajectories in the different systems of ATLAS. Such simulation is continuously updated so that it becomes faster and more accurate. Furthermore, to estimate some of the modelling uncertainties, a fast simulation known as ATLFAST-II [79, 80] is employed to avoid the intensive computation needed for the full simulation.

6.3 Simulation of signal

This thesis aims to compare the measurement with the NLO theory prediction of the process $pp \to b\ell\nu b\ell\nu\gamma$ in the $e\mu$ channel [9]. It was not feasible to simulate this $2 \to 7$ process, so the signal process is instead simulated as the combination of the double-resonant $t\bar{t}\gamma$ and single-resonant $tW\gamma$.

Double-resonant $t\bar{t}\gamma$

The $t\bar{t}\gamma$ process is simulated as a $2 \to 7$ process with the MADGRAPH5_aMC@NLO generator [81] and the NNPDF2.3LO PDF set where the ME is at LO accuracy in QCD including the decay of the top quarks and using a filter to produce final states with at least one charged lepton. The events are generated for the process $pp \to blvblv\gamma$ where the photon is radiated off the incoming charged partons (ISR radiations from the $q\bar{q}$ annihilation), intermediate top quarks, b-quarks, intermediate W bosons, or the charged decay products of the intermediate W bosons. To ensure infrared and collinear safety, photons are required to have $p_{\mathrm{T}} > 15\,\mathrm{GeV}$ and $|\eta| < 5.0$ and leptons to have $|\eta| < 5.0$. Furthermore, the photons are ensured to be isolated where a $\Delta R > 0.2$ between the photon and any charged lepton of the seven final-state particles is kept. The top-quark mass is set to 172.5 GeV in this and all other samples, including top quarks. The renormalisation μ_{R} and factorisation μ_{F} scales are chosen to be dynamic and are calculated as

$$\mu_{\mathrm{R}} = \mu_{\mathrm{F}} = \frac{1}{2} \times \Sigma_i \sqrt{m_i^2 + p_{\mathrm{T},i}^2}\,, \tag{6.1}$$

where m_i and $p_{\mathrm{T},i}$ are the mass and transverse momentum of particle i, respectively, where i runs over all particles generated from the ME calculation. In order to model the parton showers, the hadronisation, the fragmentation, and the underlying event, the event generation is interfaced to Pythia 8 (v8.212) with the A14 [76] parameter tune. The EvtGen [82] is employed to model the heavy-flavour hadron decays.

Single-resonant $tW\gamma$

The $tW\gamma$ process is simulated with two complementary samples generated with the MadGraph5_aMC@NLO generator at LO in QCD and the NNPDF2.3LO PDF set. The first sample simulates the $pp \to tW\gamma$ process in the five-flavour scheme while assuming the top quark to be stable. In the five-flavour scheme, the b-quarks are treated as massless where they are assumed to be in the initial state, meaning that they are considered partons in the protons. This simplifies and gives a more accurate calculation compared to the four-flavour scheme. The first sample includes photons radiated during the production of the top quark and the W boson or radiated from the initial state particles. The second sample simulates the $pp \to bWbW\gamma$ process in the five-flavour scheme where the photon is radiated from any other charged final-state particle. The two samples are complementary since the first one simulates the radiation of photons during production while the second simulates the photons during decay, which are combined to give the full simulation of the $tW\gamma$ process. Similar to the $t\bar{t}\gamma$ sample, both $tW\gamma$ samples are interfaced with Pythia 8 (v8.212) for parton showering using the A14 tune and use EvtGen to model the heavy-flavour hadron decays. Also similarly to the $t\bar{t}\gamma$ sample, photons are required to have $p_{\mathrm{T}} > 15\,\mathrm{GeV}$ and photons and leptons are required to have $|\eta| < 5.0$. Furthermore, a $\Delta R > 0.2$ between the photon and any charged lepton of the seven final-state particles is maintained.

6.4 Simulation of background processes

The background events come from different processes, which are simulated using the samples enlisted below.

$(W\gamma/Z\gamma)$ + jets

The $W\gamma$+jets and $Z\gamma$+jets processes are generated using different versions of the Sherpa generator [83, 84]. The $W\gamma$+jets events are generated with the Sherpa 2.2.4 at NLO accuracy in QCD using the NNPDF3.0NNLO PDF set, and the $Z\gamma$+jets events are generated with Sherpa 2.2.4 using the same PDF set. All $W\gamma$+jets/$Z\gamma$+jets events are normalised to the

cross-sections of the corresponding MC simulation. The SHERPA generator simulates all the event generation steps, from the hard scattering to the final observable particles—including the parton showering step. All the samples are matched and merged by the SHERPA-internal parton showering based on Catani–Seymour dipoles [85, 86] with the MEPS@NLO prescription [87–89]. Virtual corrections for the NLO accuracy in QCD in the matrix element are provided by the OpenLoops library [90, 91].

$t\bar{t}$

Inclusive $t\bar{t}$ production is generated with POWHEG-BOX v2 [92–94] at NLO accuracy in QCD. The PDF set used is the NNPDF3.0NNLO [73]. The generated $t\bar{t}$ sample is interfaced with PYTHIA 8 (v8.230) with the A14 tune [95]. The $t\bar{t}$ events are normalised to NNLO in perturbative QCD using the TOP++2.0 program which includes a soft-gluon resummation to NNLL precision (see Ref. [31] and references therein).

(W/Z) + jets

Production of a W or a Z boson in association with additional jets is simulated using SHERPA 2.2.1 [83, 84] at NLO accuracy in QCD. The simulation is performed using NNPDF3.0NNLO in combination with a dedicated tune provided by the SHERPA authors. The samples are normalised to the NNLO cross-sections in perturbative QCD [96].

Diboson

Events with two vector bosons, i.e. $W\,W$, $W\,Z$ and $Z\,Z$, are generated with SHERPA 2.2.2 for the purely leptonic decays and with SHERPA 2.2.1 for all other decays, at LO accuracy in QCD. The simulation is done using the NNPDF3.0NNLO PDF set combined with a dedicated tune provided by the Sherpa authors. The samples are normalised to NLO cross-sections in QCD [97].

$t\bar{t}V$

Events with a $t\bar{t}$ pair produced in association with a W or a Z boson ($t\bar{t}V$) are generated at NLO at the ME level with MADGRAPH5_aMC@NLO using the NNPDF3.0NNLO PDF set. The parton shower is simulated with PYTHIA 8 (v8.210) for which the A14 tune is used in conjunction with the NNPDF2.3LO PDF set. The samples are normalised to NLO cross-sections in QCD and electroweak theory [98].

6.5 Overlap removal between samples

This analysis uses two types of samples, *dedicated* and *inclusive*. Inclusive samples simulate processes generated at ME level without explicitly including a photon in the final state. Dedicated samples are those that simulate processes generated where photons are included in the ME. The dedicated samples have the advantage of having higher accuracy in simulating photon radiations compared to the inclusive ones. However, the dedicated samples have kinematic requirements placed on the photons to avoid infrared and collinear limits, where the emission angles and momentum fractions of photons are small. As a result, events with photons below the kinematic thresholds can only be estimated from the inclusive samples. The samples for $t\bar{t}\gamma$, $tW\gamma$, and $V\gamma$ are all dedicated samples where V is either a W or a Z boson. Inclusive samples do not include photons from the ME; however, they include photons radiated during the parton shower, i.e. they include both ISR and FSR. This means that there is a probability of double-counting the events when both dedicated and inclusive samples are used together, e.g. when using the $t\bar{t}\gamma$, $tW\gamma$, and $V\gamma$ dedicated samples together with the corresponding $t\bar{t}$, associated tW, and V+jets inclusive samples. Therefore, an overlap removal procedure is required.

Since the dedicated samples have photons simulated with higher accuracy compared to the inclusive ones, the events in the dedicated samples are kept whenever an overlap occurs—while removing the events in the inclusive samples. The dedicated samples have kinematic requirements applied to the photons at the ME level of $\mathrm{p_T}(\gamma) > 15\,\mathrm{GeV}$ and $\Delta R(\gamma, l)_{\mathrm{min}} > 0.2$. Therefore, all events in the inclusive samples with a parton-level photon in the phase space defined by the above requirements are removed.

In order to perform such a procedure, first, the overlap removal algorithm makes a list of photon and charged-lepton candidates that are generated at the ME level. These candidates are ensured to be true photons and true charged leptons using their PDG ID[1] values. Furthermore, they must originate from the primary interaction and not from hadronic activity or interactions with the detector. Once the list is created, photon candidates are removed if they do not have $p_{\mathrm{T}} > 15\,\mathrm{GeV}$. The remaining photon candidates are checked if they have a nearby charged lepton candidate within a cone of $\Delta R = 0.2$. If they do, then such photon candidates are removed. After the last removal step, if photon candidates are still present, the event is tagged to fall in the overlap region, and the event is removed for the inclusive samples.

[1] It is a particle numbering scheme following the Particle Data Group (PDG) conventions to identify (ID) particles.

CHAPTER 7

Object and event selection

The $t\bar{t}\gamma + tW\gamma$ events in the $e\mu$ decay channel are characterised by the presence of exactly one high-p_{T} γ, $1e$, 1μ, missing transverse energy, and b-jets from the decay of the top quarks. In order to select those events and reject background processes, object and event selections are chosen. The object-level and event-level selections are described in Section 7.1 and Section 7.2, respectively.

7.1 Object-level selection

The selection applied to the objects used in this thesis: electrons, muons, photons, jets, and b-jets is described below. The definition of such objects, i.e. their reconstruction and their identification and isolation, are described in more details in Chapter 4.

Electrons

Electron candidates are required to have $p_{\mathrm{T}} > 25\,\mathrm{GeV}$ and calorimeter cluster pseudorapidity $|\eta_{\mathrm{clus}}| < 2.47$, excluding the crack region between the barrel and the end-caps of the ECAL ($1.37 < |\eta_{\mathrm{clus}}| < 1.52$). They are also required to pass the *TightLH* and *Gradient*, identification and isolation WPs (described in Section 4.1), respectively.

Muons

Muon candidates are required to have $p_{\mathrm{T}} > 25\,\mathrm{GeV}$ and $|\eta| < 2.47$. They are also required to pass the *Medium* and *FCTight_FixedRad*, identification and isolation WPs (described in Section 4.2), respectively.

Photons

Photon candidates are required to have $E_{\mathrm{T}} > 20\,\mathrm{GeV}$ and $|\eta| < 2.37$, excluding the crack region between the barrel and the end-caps of the ECAL ($1.37 < |\eta_{\mathrm{clus}}| < 1.52$). They are also required to pass the *Tight* and *FixedCutTight*, identification and isolation WPs (described in Section 4.3), respectively.

Jets

Jet candidates are required to have $E_{\mathrm{T}} > 25\,\mathrm{GeV}$ and $|\eta| < 2.5$. Candidates that have large contributions from the pile-up are removed once identified by the *Jet Vertex Tagger* [99]. Furthermore, jet candidates are tagged as b-jet candidates using the b-tagging algorithm MV2c10 with a WP of 85% efficiency (described in Section 4.4.3).

Overlap removal

The same energy clusters or tracks could be used more than once to reconstruct objects, which causes overlap between reconstructed objects. This overlap is removed as follows:

- Firstly, electron candidates sharing the tracks with muon candidates are removed. Also, if any jet candidates are found within a cone of $\Delta R = 0.2$ around any remaining electron candidate, the jet candidates are removed.
- Secondly, if any electron candidates are found within a cone of $\Delta R = 0.4$ around any remaining jet candidates, the electron candidates are removed.
- Thirdly, if the distance between any muon candidate and any jet candidate is $\Delta R < 0.4$, then the muon candidate is removed if the jet candidate has more than two associated tracks, otherwise the jet candidate is removed.
- Finally, if any photon candidates are found within a cone of $\Delta R = 0.4$ around any remaining electron or muon candidates, the photon candidates are removed. Furthermore, if any jet candidates are found within a cone of $\Delta R = 0.4$ around any remaining photon candidates, the jet candidates are removed.

7.2 Event-level selection

Events are required to have at least one reconstructed primary vertex, which has at least two reconstructed tracks that are associated with it. Events that fired at least one of the single-lepton triggers in Table 7.1 are selected. Furthermore, events are required to have the following requirements:

Table 7.1: The single-electron [100] and single-muon [101] triggers. Each trigger is represented as HLT_ < type >< p_{T} > _ < ID > _ < ISO >, where type is the object's type whether an electron or a muon, p_{T} is the transverse momentum threshold, and ID and ISO are the identification and isolation WPs, respectively.

Data-taking year	Lepton p_{T}	Single electron	Single muon
2015	> 25 GeV	HLT_e24_lhmedium_L1EM20VH HLT_e60_lhmedium HLT_e120_lhloose	HLT_mu20_iloose_L1MU15 HLT_mu50
2016	> 27 GeV	HLT_e26_lhtight_nod0_ivarloose HLT_e60_lhmedium_nod0 HLT_e140_lhloose_nod0	HLT_mu26_ivarmedium HLT_mu50
2017	> 28 GeV	HLT_e26_lhtight_nod0_ivarloose HLT_e60_lhmedium_nod0 HLT_e140_lhloose_nod0	HLT_mu26_ivarmedium HLT_mu50
2018	> 28 GeV	HLT_e26_lhtight_nod0_ivarloose HLT_e60_lhmedium_nod0 HLT_e140_lhloose_nod0	HLT_mu26_ivarmedium HLT_mu50

- Events are required to have exactly one electron and exactly one muon with $p_{\mathrm{T}} > 25$ GeV for each of them. In each event, the offline p_{T} requirements for the electron and the muon which are matched to a fired single-lepton trigger are 25, 27, and 28 GeV for the years 2015, 2016, and 2017–2018, respectively. This increase in the offline p_{T} thresholds follows the increase in the corresponding thresholds of the single-lepton triggers (see Table 7.1).

- In each event, the electron and the muon must have opposite-sign charges and their total invariant mass $m_{e\mu} > 15$ GeV.

- Events are required to have exactly one photon with $p_{\mathrm{T}} > 20$ GeV, for which the angular distance to any lepton is required to be $\Delta R > 0.4$.

- Events must have at least two jets with $p_{\mathrm{T}} > 25$ GeV, out of which at least one jet is $b-$tagged.

The above event selection is applied to both data and MC samples. Selected events of the signal are $t\bar{t}\gamma$ $e\mu$ and $tW\gamma$ $e\mu$, which represent the events of the $t\bar{t}\gamma$ and $tW\gamma$ processes in the $e\mu$ decay channel, respectively. The $e\mu$ decay channel has the advantage of providing a clean final state with a small background contribution. Selected events of the $t\bar{t}\gamma$ and $tW\gamma$ processes where the W boson decays to an intermediate tau which in turn decays to an electron or a muon, are not included in the signal (following the theory calculation [9]) and are considered to be a background called *Other* $t\bar{t}\gamma/tW\gamma$. This category also includes $t\bar{t}\gamma$ events in the single-lepton decay channel with one prompt lepton and another lepton that

is either non-prompt or a jet that is mis-reconstructed as a lepton. Selected events of the non-$t\bar{t}\gamma$/non-$tW\gamma$ backgrounds can be grouped into three categories:

- h-fake: it corresponds to events where hadronic activity fakes the signature of a photon in the detector, for example, a jet that is mis-reconstructed in the detector as a photon. It also contains events with non-prompt photons coming from hadron decays, e.g. $\pi^0 \to \gamma\gamma$. Furthermore, it includes events with a prompt photon, where the prompt photon is not reconstructed in the detector or does not pass the selection requirements, but instead, an h-fake photon does.

- e-fake: it corresponds to events where an electron mimics a photon signature at the reconstruction level. It also includes events with a prompt photon, where the prompt photon is not reconstructed or does not pass the selection requirements, but instead, an e-fake photon does.

- Prompt γ background: it corresponds to any background events with a prompt photon, e.g. $W\gamma$+jets, $Z\gamma$+jets, $WW + \gamma$, $ZZ + \gamma$, QCD + γ.

The number of selected events in data and signal and background samples after applying the event selection is summarised in Table 7.2. In the table, the combined event yields of the $t\bar{t}\gamma$ $e\mu$, $tW\gamma$ $e\mu$, and *Other* $t\bar{t}\gamma/tW\gamma$ processes are scaled so that the total MC event yields (for all processes: signal and background) match those of the data. The processes $t\bar{t}\gamma$ $e\mu$, $tW\gamma$ $e\mu$, and *Other* $t\bar{t}\gamma/tW\gamma$ are simulated at LO in QCD, whereas the non-$t\bar{t}\gamma$/non-$tW\gamma$ background processes are simulated at NLO in QCD, or their cross-sections are scaled with k-factors to be at NLO. This means that the former underestimate their expected number of events, and hence they are scaled. Moreover, to correct for detector effects, coming from the efficiency of the reconstruction and identification of objects, a correction is applied to the MC simulation to match the data. The uncertainties in the table represent the statistical and systematic uncertainties added in quadrature. A description of the sources of systematic uncertainties is illustrated in Chapter 9.

The $e\mu$ channel has a high signal purity, where the combined $t\bar{t}\gamma$ + $tW\gamma$ signal events comprise 84% of the total MC event yields. This is a huge advantage of the $e\mu$ channel compared to other decay channels, e.g. the single lepton channel suffers from a much larger background contribution of around 40% [7]. Fig. 7.1 shows the percentage of each of the different MC simulations for signal and backgrounds. The largest background is the *Other* $t\bar{t}\gamma/tW\gamma$ category with a contribution of 9%, followed by the h-fake and the prompt γ background categories with 3% each. The e-fake category has the smallest contribution of only 1%.

In order to examine the description of data by the simulation, distributions of various observables are shown in Fig. 7.2. The top row of the figure shows examples of the distributions of the transverse momentum of the electron and the muon, while the lower row shows the distributions of the S_{T} observable and the invariant mass of the two leptons. The S_{T} is defined as the scalar sum of the transverse momenta of the electron, the muon, the photon,

Table 7.2: Event yields after event selection in data and MC simulation. The MC simulation is corrected with factors that compensate for detector effects. The $t\bar{t}\gamma$ and $tW\gamma$ samples are scaled to match the event yields in data. The quoted uncertainties represent the quadrature sum of the statistical and systematic uncertainties (see Chapter 9).

	Events
$t\bar{t}\gamma$ $e\mu$	2 391 ± 130
$tW\gamma$ $e\mu$	156 ± 15
Other $t\bar{t}\gamma/tW\gamma$	279 ± 15
h-fake	78 ± 40
e-fake	23 ± 12
Prompt γ bkg.	87 ± 40
Total	3 014 ± 160
Data	3014

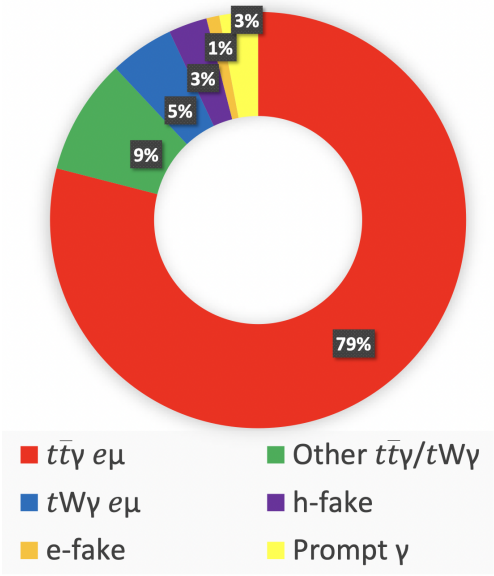

Figure 7.1: Percentages of reconstructed events of signal and background processes after applying event selection.

jets, and the missing transverse momentum. Similar to Table 7.2, the combined yields of the $t\bar{t}\gamma$ $e\mu$, $tW\gamma$ $e\mu$, and *Other* $t\bar{t}\gamma/tW\gamma$ categories are scaled to match the event yields of data. A good agreement between the shape of the distributions in data and MC within uncertainties is observed, where the shaded bands include both the statistical and systematic uncertainties added in quadrature.

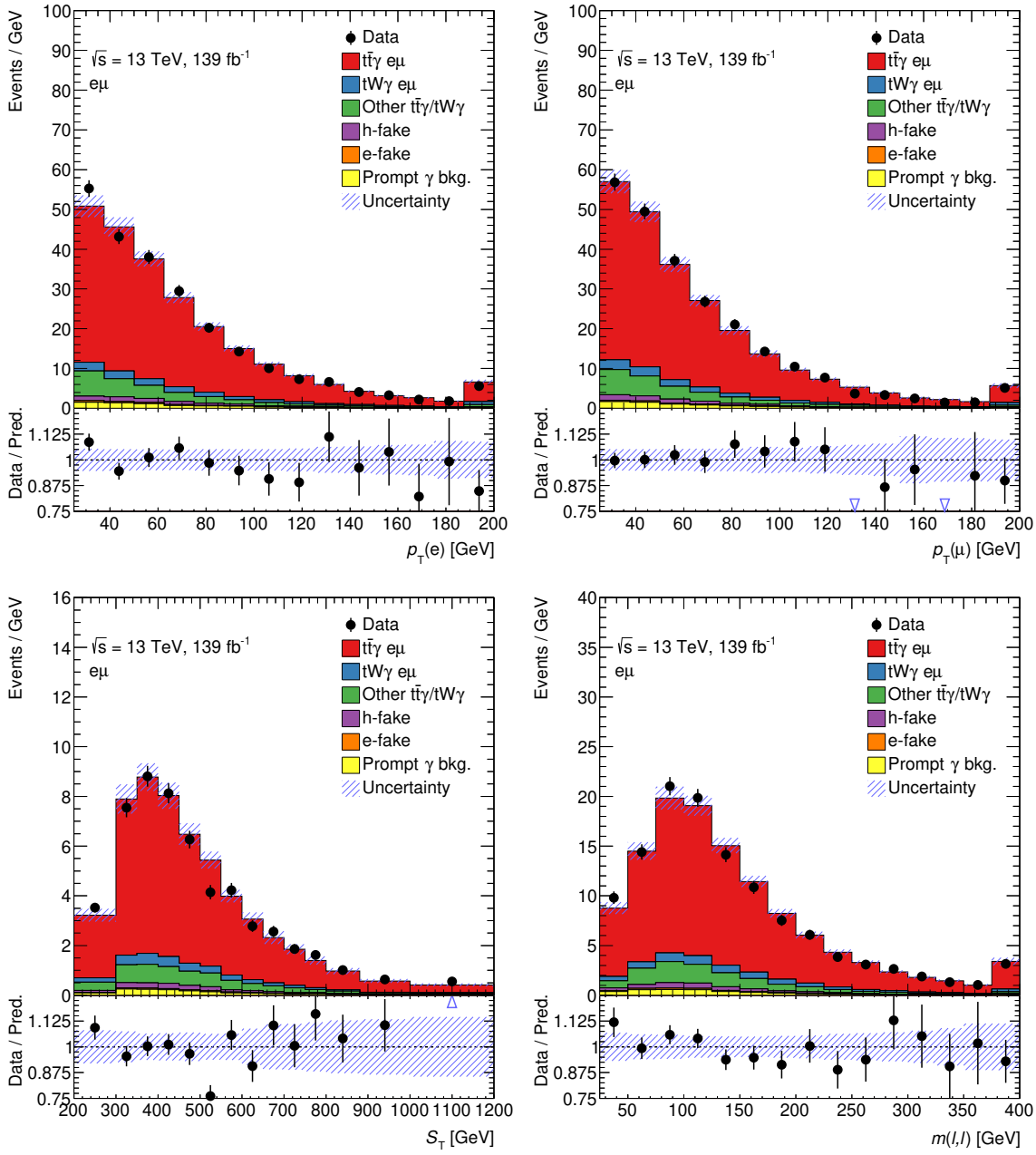

Figure 7.2: From left to right and top to bottom: Distributions of electron p_{T}, muon p_{T}, S_{T}, and invariant mass of the two leptons $m(l,l)$. The combined yields of the $t\bar{t}\gamma$ $e\mu$, $tW\gamma$ $e\mu$, and *Other* $t\bar{t}\gamma/tW\gamma$ categories are scaled to match the event yields of data. The distributions include the overflow in the last bin, and in the case of the S_{T}, the underflow is included in the first bin. The distributions show the number of events divided by the bin width. The shaded bands represent the total statistical and systematic uncertainties (see Chapter 9), and the vertical error bars represent the Poissonian statistical fluctuations on the data points. The ratio of data to the MC prediction is shown at the bottom of each distribution.

CHAPTER 8

Analysis strategy

This analysis presents measurements of the combined $t\bar{t}\gamma + tW\gamma$ differential cross-section in the $e\mu$ channel. The measurements are performed in a fiducial phase space defined at parton level. They are measured as functions of photon kinematic observables, the angular distance between the photon and the leptons, and angular separations between the two leptons. Furthermore, this analysis studies both the absolute and normalised differential cross-sections. The absolute differential cross-sections probe the $t\bar{t}\gamma + tW\gamma$ production rate and the associated shape of the distributions as a function of the measured observable, whereas the normalised ones investigate only the shapes of the distributions but with higher precision. Moreover, the measured signal is corrected to remove distortions introduced by the detector due to its limited efficiency, acceptance, and resolution. This correction is done with the unfolding procedure. The performance of such a procedure is validated with various statistical tests.

The fiducial phase-space definition is described in Section 8.1. The description of the absolute and normalised differential cross-sections is discussed in Section 8.2. Section 8.3 introduces the description of the unfolding method and its validation tests as well as the binning optimisation study.

8.1 Fiducial phase-space definition

The fiducial phase space is chosen as close as possible to the kinematic requirements applied at detector level, such that final-state physics objects are produced within the detector acceptance. It has the advantage of allowing the comparison between theory and experiment without any extrapolation beyond the experimental acceptance. Another advantage is that different experiments can compare their results of the same process if they use a common definition of the fiducial phase space. In practice, this phase space is chosen according to the kinematic requirements of the signal process. In order to compare with the theory predictions, the definition of the fiducial region was discussed with the authors of Ref. [9] who provided a dedicated calculation that matches that of the fiducial one of the experiment. The kinematic requirements in the dedicated predictions are looser than those of Ref. [9], which reduces

the statistical uncertainties of the measurements—looser kinematic requirements translate to more events passing the selection and hence smaller statistical uncertainties.

The fiducial phase space is defined at parton level, meaning that objects are coming from the matrix element calculation and before the showering and hadronisation processes. Objects are defined as follows.

Leptons (e, μ)

Leptons are defined as stable particles after FSR and they are *dressed*[1] with nearby photon radiations within a cone of $\Delta R = 0.1$ around the lepton. They must originate from the W boson decays and are required to have $p_{\mathrm{T}} > 25\,\mathrm{GeV}$ and $|\eta| < 2.5$.

Photons

Photons are required not to come from hadron decays. They are required to be well isolated from any nearby jets using a modified-cone approach which is described in detail in Ref. [102]. The approach ensures a $\Delta R > 0.4$ between the photon and the $b/\bar{b}$-jet. This approach is also used in defining photons in the theory calculation [9], so that soft and collinear safety is ensured. Photons must have $E_{\mathrm{T}} > 20\,\mathrm{GeV}$ and $|\eta| < 2.37$.

b-jets

b-jets are obtained by running the anti-k_t algorithm over all radiated partons from the two b-quarks —including the b-quarks themselves—and from the two initial partons using a distance parameter $R = 0.4$. b-jets are required to include a b-quark coming from the decay of the top quark. Additionally, they are required to have $p_{\mathrm{T}} > 25\,\mathrm{GeV}$ and $|\eta| < 2.5$.

Events are required to fulfil the following criteria.

- Exactly one electron and exactly one muon coming from the W boson decays. Events with leptons coming from intermediate τ-leptons are rejected.
- Exactly one photon.
- Exactly one b-jet and exactly one $\bar{b}$-jet.
- A $\Delta R > 0.4$ between objects is required; between the lepton and the photon, the lepton and the $b/\bar{b}$-jet, the electron and the muon, and between the b-jet and the $\bar{b}$-jet .

[1] Dressed leptons mean that the four-momenta of the photons that do not come from hadron decays (soft emission radiation) and are nearby the lepton are added to the four-momentum of the lepton.

8.2 Differential cross-sections

The measurements are carried out as functions of various observables which allow probing interesting keystones of the SM, such as the tγ coupling. The chosen observables are listed below.

- Transverse momentum of the photon: $\mathrm{p_T}(\gamma)$.
- Absolute pseudorapidity of the photon: $|\eta(\gamma)|$.
- Minimum angular distance between the photon and the leptons: $\Delta R(\gamma, l)_{\mathrm{min}}$.
- Absolute angular separation along the η-direction between the two leptons: $|\Delta\eta(l, l)|$.
- Angular separation along the ϕ-direction between the two leptons: $\Delta\phi(l, l)$.

The photon-related observables allow probing the tγ coupling. One example of a sensitive observable is the $\Delta R(\gamma, l)_{\mathrm{min}}$, which is related to the angle between the top quark and the photon. The $|\Delta\eta(l, l)|$ and $\Delta\phi(l, l)$ observables are sensitive to the $t\bar{t}$ spin correlation.

The agreement between data and MC simulation for $\mathrm{p_T}(\gamma)$, $|\eta(\gamma)|$, $\Delta R(\gamma, l)_{\mathrm{min}}$, $\Delta\phi(l, l)$ and $|\Delta\eta(l, l)|$, using the same binning as the differential cross-sections (see Section 8.3.2) can be seen in Figs. 8.1 and 8.2. Similar to the distributions in Fig. 7.2, the total yields of the $t\bar{t}\gamma$ $e\mu$, $tW\gamma$ $e\mu$, and *Other* $t\bar{t}\gamma$/$tW\gamma$ categories are scaled to match the event yields of data. The shaded bands in the figure represent statistical and systematic uncertainties added in quadrature, while the vertical error bars represent Poissonian statistical fluctuations on the data points. From the figure, the MC simulation agrees well with the data as a function of $\mathrm{p_T}(\gamma)$, $|\eta(\gamma)|$ and $|\Delta\eta(l, l)|$ within the total uncertainty, while for $\Delta R(\gamma, l)_{\mathrm{min}}$ and $\Delta\phi(l, l)$ the simulation tends to smaller and higher values than data, respectively.

The differential measurements are performed in bins i of an observable X. The absolute differential cross-sections are obtained by dividing the number of unfolded events in bin i, N_i^{unfold}, by the integrated luminosity L and the bin width ΔX_i of bin i.

$$\frac{d\sigma}{dX_i} = \frac{N_i^{\mathrm{unfold}}}{L \times \Delta X_i} \,. \tag{8.1}$$

The value of N^{unfold} is derived by following two steps:

- Firstly, the number of observed signal events, N_{reco}, is obtained by subtracting the background contribution from the measured data events:

$$N_{\mathrm{reco}} = (N_{\mathrm{data}} - N_{\mathrm{bkgs}}) \times f_{e\mu} \,, \tag{8.2}$$

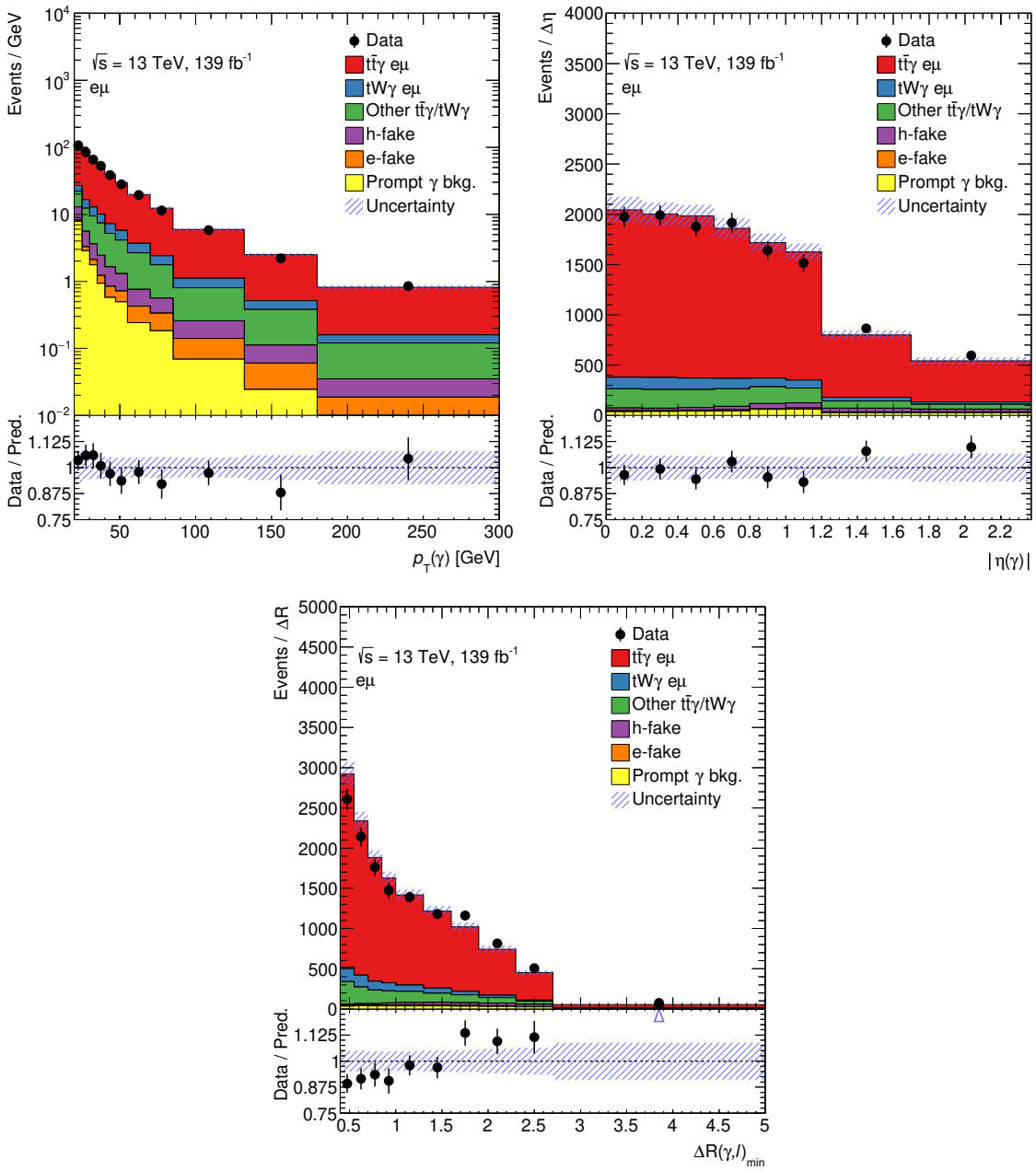

Figure 8.1: Distributions of $p_T(\gamma)$ (top left), $|\eta(\gamma)|$ (top right), and $\Delta R(\gamma, l)_{\text{min}}$ (bottom). The distributions display the data and MC events after event selection, where the total yields of the $t\bar{t}\gamma$ $e\mu$, $tW\gamma$ $e\mu$, and *Other* $t\bar{t}\gamma/tW\gamma$ categories are scaled to match the event yields of data. The distributions do not include the overflow. The shaded bands represent the quadrature sum of the statistical uncertainty of the MC and systematic uncertainties, and the vertical error bars represent the statistical uncertainty of the data.

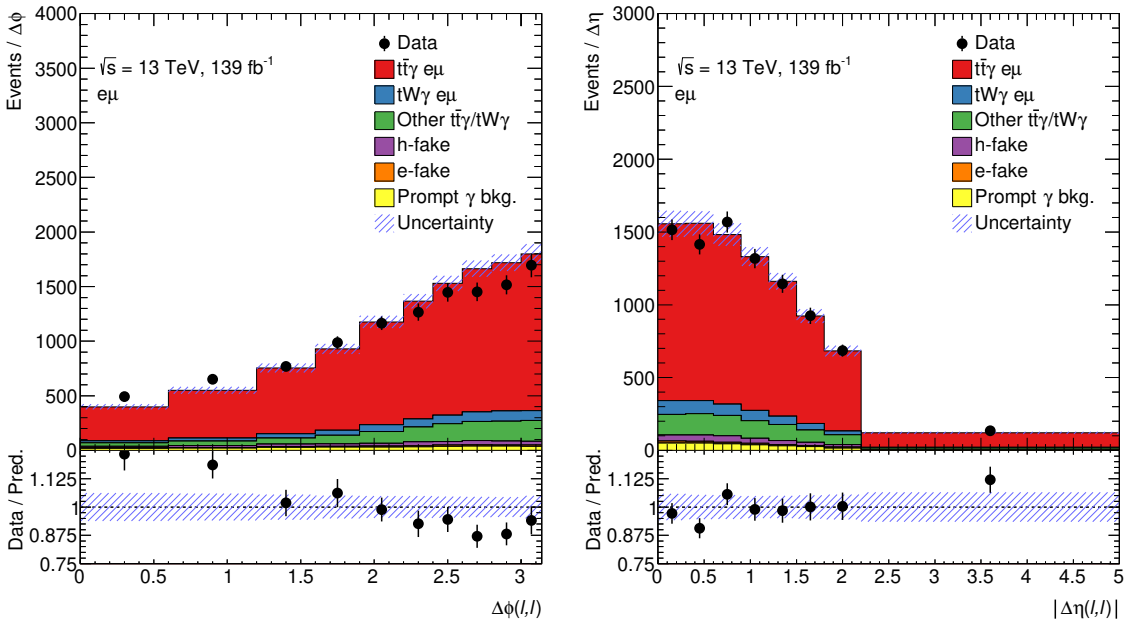

Figure 8.2: Distributions of $\Delta\phi(l,l)$ (left) and $|\Delta\eta(l,l)|$ (right). The distributions display the data and MC events after event selection, where the total yields of the $t\bar{t}\gamma\ e\mu$, $tW\gamma\ e\mu$, and *Other* $t\bar{t}\gamma/tW\gamma$ categories are scaled to match the event yields of data. The distributions do not include the overflow. The shaded bands represent the quadrature sum of the statistical uncertainty of the MC and systematic uncertainties, and the vertical error bars represent the statistical uncertainty of the data.

where N_{data} is the number of measured data events and N_{bkgs} is the number of estimated non-$t\bar{t}\gamma$/non-$tW\gamma$ background events in bin i at detector level. The $f_{e\mu}$ is defined as the ratio of the total number of selected signal $t\bar{t}\gamma\ e\mu$ and $tW\gamma\ e\mu$ events to the total number of all selected $t\bar{t}\gamma$ and $tW\gamma$ events in bin i at detector level. All selected $t\bar{t}\gamma$ and $tW\gamma$ events are calculated as the sum of the $t\bar{t}\gamma\ e\mu$, $tW\gamma\ e\mu$, and *Other* $t\bar{t}\gamma/tW\gamma$ events. $f_{e\mu}$ is in the order of 90%. Applying the $f_{e\mu}$ ratio ensures that the dependency on the signal cross-section, which is already used in the normalisation of the measurement, is eliminated.

- Secondly the Iterative Bayesian unfolding method is used to correct N_{reco} using the ingredients of migration matrix and correction factors for acceptance $1 - f_{\text{out}}$ and efficiency ϵ (see Section 8.3.1).
  - The migration matrix represents the probability of signal events to pass the parton-level and detector-level selections. The migration matrices (normalised per bin at detector level and shown as percentages) as functions of the observables $p_T(\gamma)$, $|\eta(\gamma)|$, $\Delta R(\gamma,l)_{\text{min}}$, $\Delta\phi(l,l)$, and $|\Delta\eta(l,l)|$ are shown in Fig. 8.3. The matrices have the majority of events (all events in the case of $\Delta\phi(l,l)$ and $|\Delta\eta(l,l)|$) to lie on its diagonal, indicating that the chosen binning results in a small migration effect

(no migration for $\Delta\phi(l,l)$ and $|\Delta\eta(l,l)|$). More specifically, for $p_T(\gamma)$, $|\eta(\gamma)|$, and $\Delta R(\gamma,l)_{\text{min}}$, at least 82% of the events are non-migration, i.e. events correctly reconstructed in a bin in which they were originally generated. For $\Delta\phi(l,l)$ and $|\Delta\eta(l,l)|$, an excellent non-migration percentage of 100% is observed.

– The acceptance factor $1 - f_{\text{out}}$ accounts for events that do not pass the parton-level selection, i.e. generated outside the fiducial phase space, but pass the detector-level selection. It is calculated as:

$$1 - f_{\text{out}} = \frac{N_{\text{reco}}^{\text{fid}}}{N_{\text{reco}}}, \tag{8.3}$$

where N_{reco} is the number of all reconstructed events which pass the detector-level selection, and $N_{\text{reco}}^{\text{fid}}$ is the number of events which are generated and reconstructed in the fiducial phase space, i.e. passing both the detector- and parton-level selections.

– The efficiency factor ϵ corrects for events that pass the parton-level selection, i.e. generated inside the fiducial phase space, but do not pass the detector-level selection. It is calculated as:

$$\epsilon = \frac{N_{\text{reco}}^{\text{fid}}}{N_{\text{part}}^{\text{fid}}}, \tag{8.4}$$

where $N_{\text{part}}^{\text{fid}}$ is the number of events which pass only the parton-level selection.

– The efficiency ϵ and acceptance $1 - f_{\text{out}}$ factors can be combined into one factor, called the correction factor C. It is calculated as:

$$C = \frac{\epsilon}{1 - f_{\text{out}}}. \tag{8.5}$$

The distributions of ϵ, $1 - f_{\text{out}}$ and the resulting C for the observables $p_T(\gamma)$, $|\eta(\gamma)|$, $\Delta R(\gamma,l)_{\text{min}}$, $\Delta\phi(l,l)$, and $|\Delta\eta(l,l)|$ are shown in Fig. 8.4. $1 - f_{\text{out}}$ shows a plateau for all the observables, with values slightly higher than 60%. ϵ increases from 20% to 40% with the $p_T(\gamma)$ causing the correction factor C to also increase across the $p_T(\gamma)$ range. However, C remains flat with values around 30% for $\Delta R(\gamma,l)_{\text{min}}$, $\Delta\phi(l,l)$, $|\Delta\eta(l,l)|$, and most of the bins of $|\eta(\gamma)|$ due to the stable behaviour of ϵ. In the last two bins of $|\eta(\gamma)|$, ϵ drops due to a reconstruction-level requirement to exclude photons in the crack region of the detector ($1.37 < |\eta_{\text{clus}}| < 1.52$, see Chapter 7).

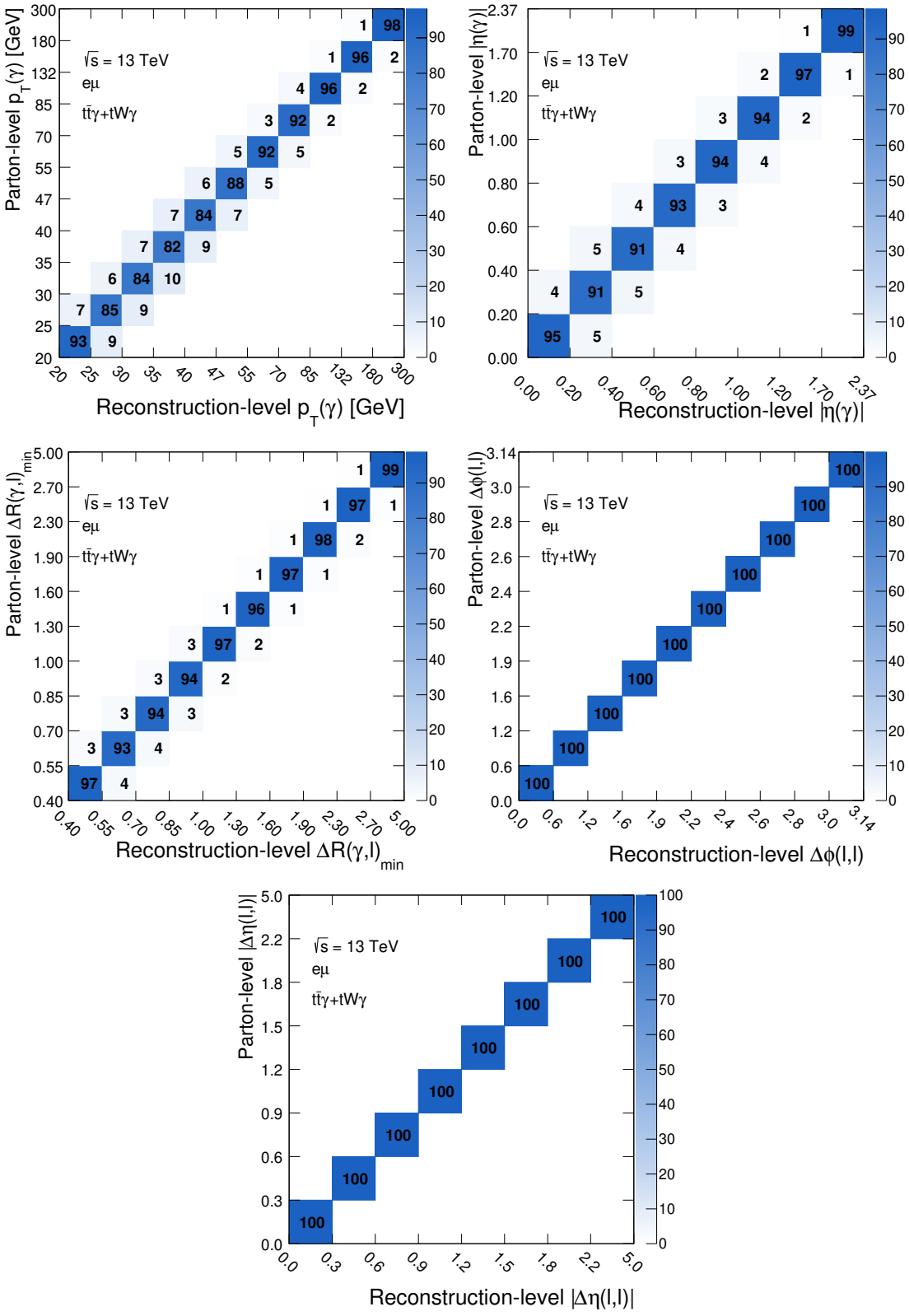

Figure 8.3: Migration matrices (normalised per bin at detector level and shown as percentages) as functions of $p_T(\gamma)$, $|\eta(\gamma)|$, $\Delta R(\gamma, l)_{\text{min}}$, $\Delta\phi(l, l)$ and $|\Delta\eta(l, l)|$ (from left to right and top to bottom).

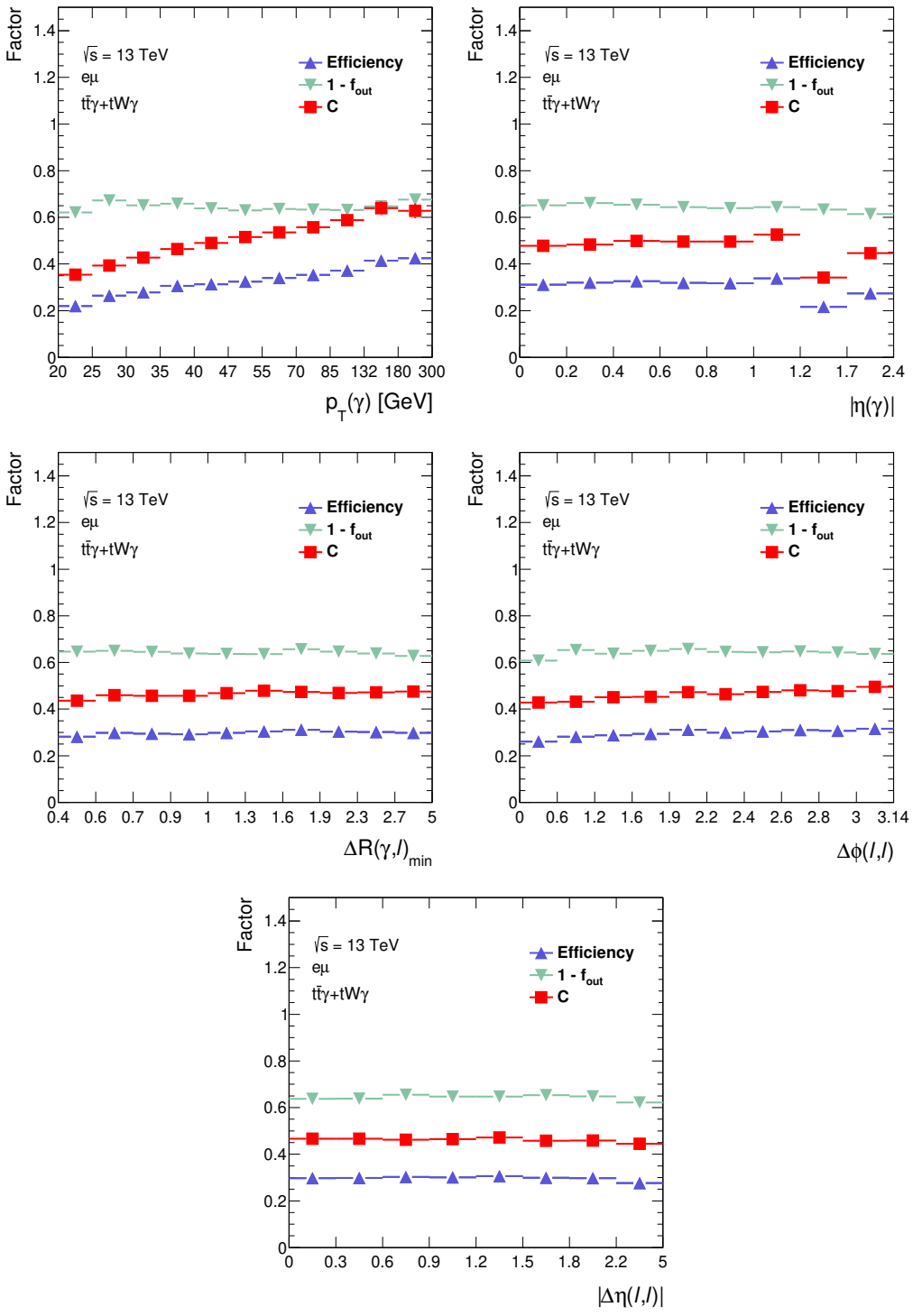

Figure 8.4: Selection efficiency ϵ, acceptance $1 - f_{\text{out}}$, and the resulting C correction factor as a function of $p_T(\gamma)$, $|\eta(\gamma)|$, $\Delta R(\gamma, l)_{\text{min}}$, $\Delta\phi(l, l)$ and $|\Delta\eta(l, l)|$ (from left to right and top to bottom).

8.3 Unfolding methodology

Spectra of physics objects measured in the detector are distorted due to detector effects—finite efficiency, acceptance and resolution. In the context of differential cross-sections, the correction for such effects is performed by applying an unfolding procedure.

The unfolding procedure can be described as follows: t is a true value of a one-dimensional observable O, which is distributed according to a function $f_{\text{true}}(t)$. Due to the detector effects mentioned above, the true spectrum of the observable O would be smeared, and the reconstructed measured value r would follow the function $f_{\text{meas}}(r)$. The relation between the t and r events could be represented by a conditional probability $P(r|t)$. This is represented with a matrix R_{ij} called the *migration* or *response* matrix. The matrix has events in bin i at reconstruction level and bin j at parton level, r_i and t_j, respectively. This means it takes into account effects due to migration of events between bins, i.e. events generated within some bin boundaries and got reconstructed outside these boundaries (in a different bin).

The number of expected true events μ_j in bin j is given as:

$$\mu_j = \mu_{\text{tot}} \int_j f_{\text{true}}(t)\, dt\,, \tag{8.6}$$

where μ_{tot} is the total number of expected true events.

Similarly the number of expected reconstructed events ν_i in bin i is given as:

$$\nu_i = \nu_{\text{tot}} \int_i f_{\text{meas}}(r)\, dr\,, \tag{8.7}$$

where ν_{tot} is the total number of expected reconstructed events.

The expected reconstructed events ν_i could be obtained from the expected true events μ_i using the response matrix R_{ij}, and in the presence of background processes, an extra term β_i has to be included:

$$\nu_i = \sum_j R_{ij}\, \mu_j + \beta_i\,. \tag{8.8}$$

The unfolding procedure is simply to find a solution for μ_j from the information of ν_i, β_i, and the response matrix R_{ij}. This can be solved in different ways, for example, by using a correction factor, as the case in the bin-by-bin unfolding method or using regularisation as in the SVD method or using Bayes theorem as in the Iterative Bayesian unfolding.

8.3.1 Iterative Bayesian unfolding

Unfolding can be performed using different techniques, which have different mathematical approaches to solve Eq. (8.8), to find the true signal. One of these techniques is the Iterative Bayesian unfolding (IBS) used in this work. The IBS is based on Ref. [103] and implemented in RooUnfold package [104]. It follows —as the name suggests—a Bayesian approach in the description of the relation between ν_i and μ_j in terms of conditional probabilities, using the notion of cause and effect.

In IBS, the true events are the causes C_j ($j = 1, 2, 3, ..., n_C$), while the measured events are the effects E_i ($i = 1, 2, 3, ..., n_E$), where n_C and n_E are the maximum number of causes and effects, respectively. Each cause can produce many effects, but for a given effect, the exact cause is unknown. The relationship between causes and effects can be expressed using Bayes theorem as follows.

$$P(C_j|E_i) = \frac{P(E_i|C_j)\ P_0(C_j)}{\sum_{k=1}^{n_C} P(E_i|C_k)\ P_0(C_k)}\,, \tag{8.9}$$

where C_j is a given cause in bin j, while E_i is the probable effect in bin i. $P_0(C_j)$ is the initial a-priori probability of the j$^{\text{th}}$ cause. $P(E_i|C_j)$ is the conditional probability of the cause in bin j, C_j, to produce the effect in bin i, E_i. The conditional probability $P(E_i|C_j)$ is the migration matrix. The a-priori $P_0(C_j)$ can be a flat distribution or can be taken from the MC simulation.

The estimator of the number of true causes in bin j can be given as:

$$\hat{n}(C_j) = \frac{1}{\epsilon_j} \sum_{i=1}^{n_E} P(C_j|E_i)(1 - f_{\text{out},i})n(E_i)\,, \tag{8.10}$$

where $n(E_i)$ is the number of effects in bin i, ϵ_j is the efficiency that the cause C_j has an effect E_i, and $f_{\text{out},i}$ is the factor that corrects for the acceptance loss (outside-migration). The terms ϵ_j, and $f_{\text{out},i}$ are explained in the previous section.

It is then possible to evaluate a posterior probability of each cause C_j as:

$$\hat{P}(C_j) = \frac{\hat{n}(C_j)}{\sum_{j=1}^{n_C} \hat{n}(C_j)}\,. \tag{8.11}$$

For the first iteration, $P_0(C)$ which is the initial probability of causes and $n_0(C)$, which is the initial expected number of causes, are taken from the signal MC samples. Then, the estimators $\hat{n}(C_j)$ and $\hat{P}(C_j)$ are computed. For the second iteration, $n_0(C)$ and $P_0(C)$ are replaced by the estimators from the first iteration, i.e. $\hat{n}(C)$ and $\hat{P}(C)$, respectively. A χ^2 test

is performed between the estimators from the first and second iterations. If the χ^2 value is small enough (e.g. close to 1), then the procedure is completed, otherwise the same procedure is repeated until a sufficiently small value is reached. The optimised number of iterations will then be used as the regularisation parameter of the method.

The IBS is chosen for this analysis to perform the unfolding of data since it is theoretically well-grounded, does not involve matrix inversion, and can obtain the correlation matrix of the results. It also can take into account all kinds of detector effects.

8.3.2 Binning optimisation

In order to examine the shapes of the distributions closely, a fine granular binning is needed. However, infinitely fine binning is not possible due to the finite number of events and the limited resolution of the detector. Furthermore, having too many bins would enhance the migration effect. The unfolding procedure can account for the migration effect; however, it can be tricky if the effect is large, requiring careful selection of the unfolding procedure. Therefore, certain factors have to be accounted for in choosing the binning.

For this thesis, the main factors are the statistical uncertainty per bin and the resolution of the kinematic observable. The first factor is the statistical uncertainty, which is required to be below 10% across all bins. The second factor is the resolution of the kinematic observable, which has to be smaller than the bin width. The resolution is checked by looking at the width of the difference between parton- and reconstruction-level values. Also, the precision on the mean of such a difference is checked. Therefore, the criterion for the binning choice is as follows: the bin width has to be larger than twice the observable's resolution, and the statistical uncertainty has to be less than 10% across all bins.

The resolution of $\mathrm{p_T}(\gamma)$, the precision on the mean of the difference between reconstructed and truth $\mathrm{p_T}(\gamma)$, the comparison of the bin width to the resolution, and the expected statistical uncertainty of the resulting bin width can be seen in Fig. 8.5. The corresponding distributions for $|\eta(\gamma)|$, $\Delta R(\gamma, l)_{\mathrm{min}}$, $\Delta\phi(l, l)$, and $|\Delta\eta(l, l)|$ can be seen in Figs. 8.6–8.9. The resolution of $\mathrm{p_T}(\gamma)$ is around 1 GeV for the p_{T}-range up to 100 GeV, while for the higher range the resolution goes up to around 4 GeV. At low $|\eta(\gamma)|$-region, the resolution is around 0.02, while for the higher region, it improves to be better than 0.01. The resolution of $\Delta R(\gamma, l)_{\mathrm{min}}$ is better than 0.01, while for $\Delta\phi(l, l)$ and $|\Delta\eta(l, l)|$ it is better than 0.001. The precision on the mean for all observables is checked where it is close to zero within uncertainties. The bottom row in the figures shows that the limiting factor in choosing a finer binning is the statistical uncertainty. The final chosen binning is listed in Table 8.1.

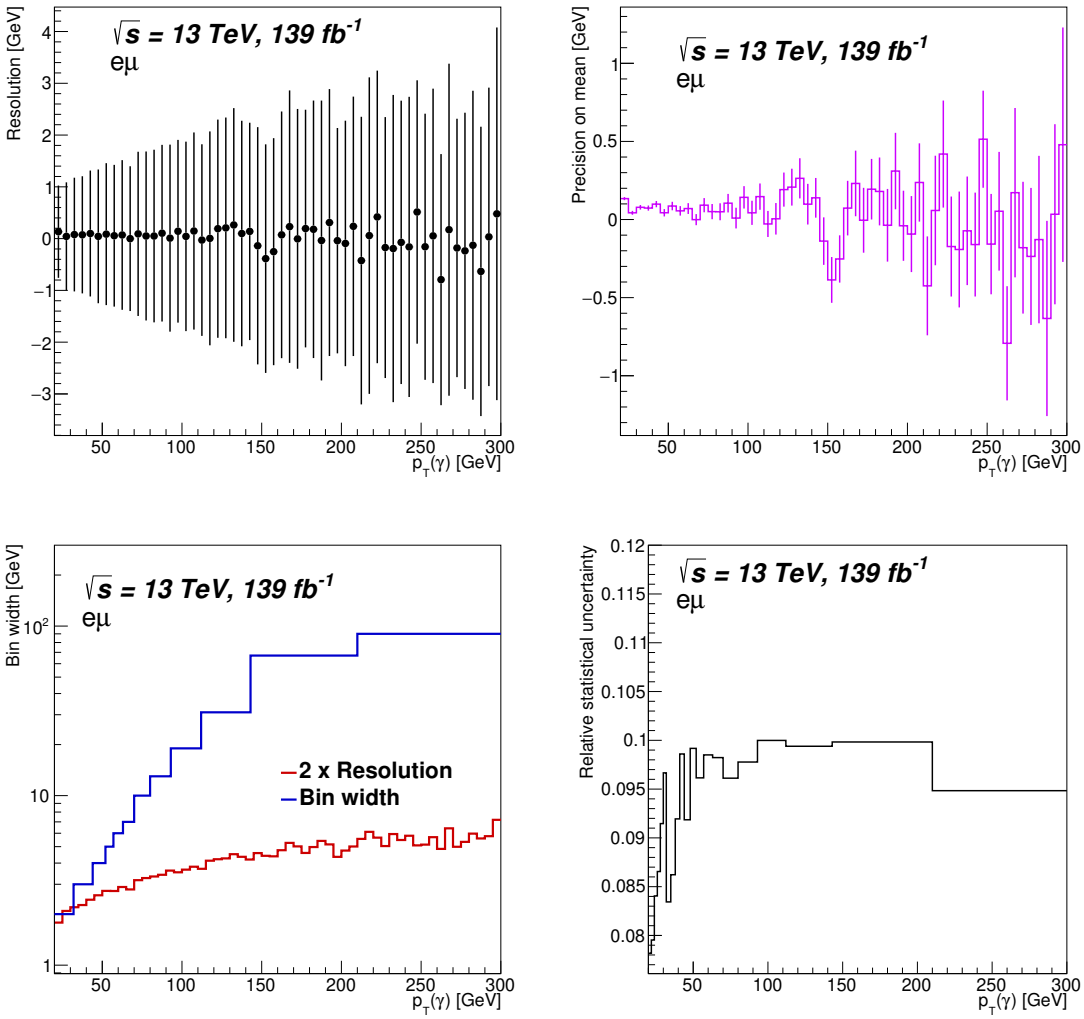

Figure 8.5: Top-left: resolution of the $p_T(\gamma)$ where the y-axis is the mean of the difference between reconstructed and truth $p_T(\gamma)$ in GeV, and the error bars represent one standard deviation around that mean. Top-right: precision on the mean where the y-axis is the mean of the difference between reconstructed and truth $p_T(\gamma)$ in GeV, and the error bars represent the error on the mean. Bottom-left: the bin width in blue is compared to the resolution multiplied by 2 in red. Bottom-right: the relative statistical uncertainty of the resulting bin.

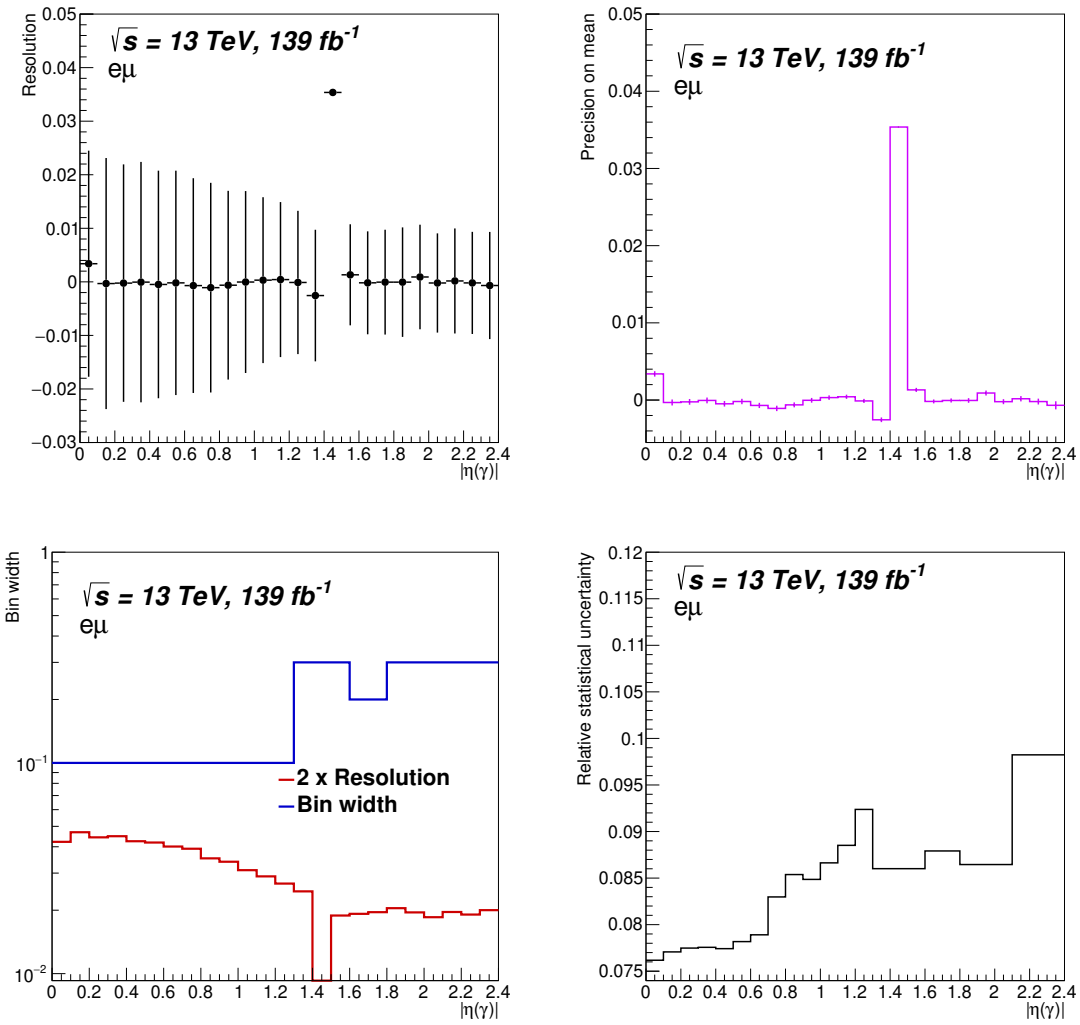

Figure 8.6: Top-left: resolution of the $|\eta(\gamma)|$ where the y-axis is the mean of the difference between reconstructed and truth $|\eta(\gamma)|$, and the error bars represent one standard deviation around that mean. Top-right: precision on the mean where the y-axis is the mean of the difference between reconstructed and truth $|\eta(\gamma)|$, and the error bars represent the error on the mean. Bottom-left: the bin width in blue is compared to the resolution multiplied by 2 in red. Bottom-right: the relative statistical uncertainty of the resulting bin.

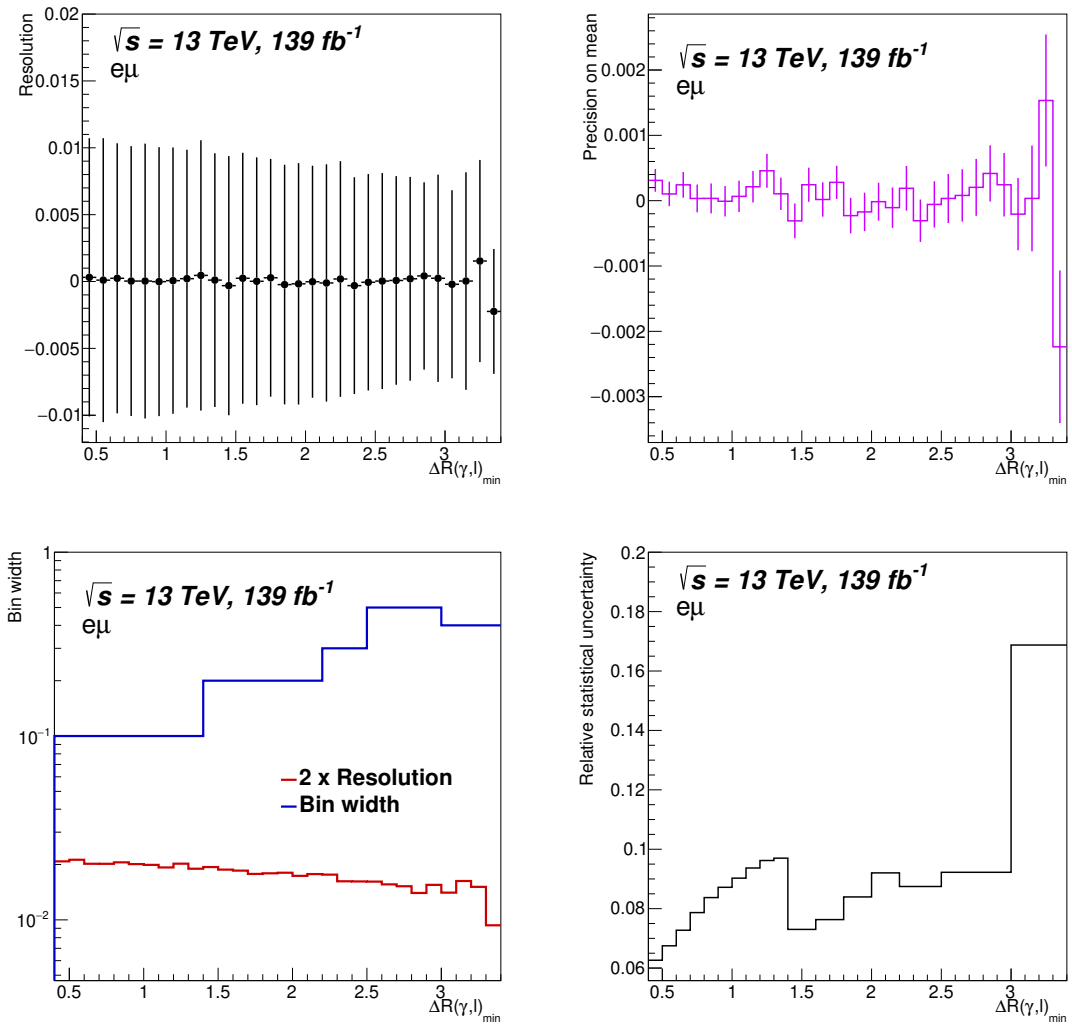

Figure 8.7: Top-left: resolution of the $\Delta R(\gamma, l)_{\text{min}}$ where the y-axis is the mean of the difference between reconstructed and truth $\Delta R(\gamma, l)_{\text{min}}$, and the error bars represent one standard deviation around that mean. Top-right: precision on the mean where the y-axis is the mean of the difference between reconstructed and truth $\Delta R(\gamma, l)_{\text{min}}$, and the error bars represent the error on the mean. Bottom-left: the bin width in blue is compared to the resolution multiplied by 2 in red. Bottom-right: the relative statistical uncertainty of the resulting bin.

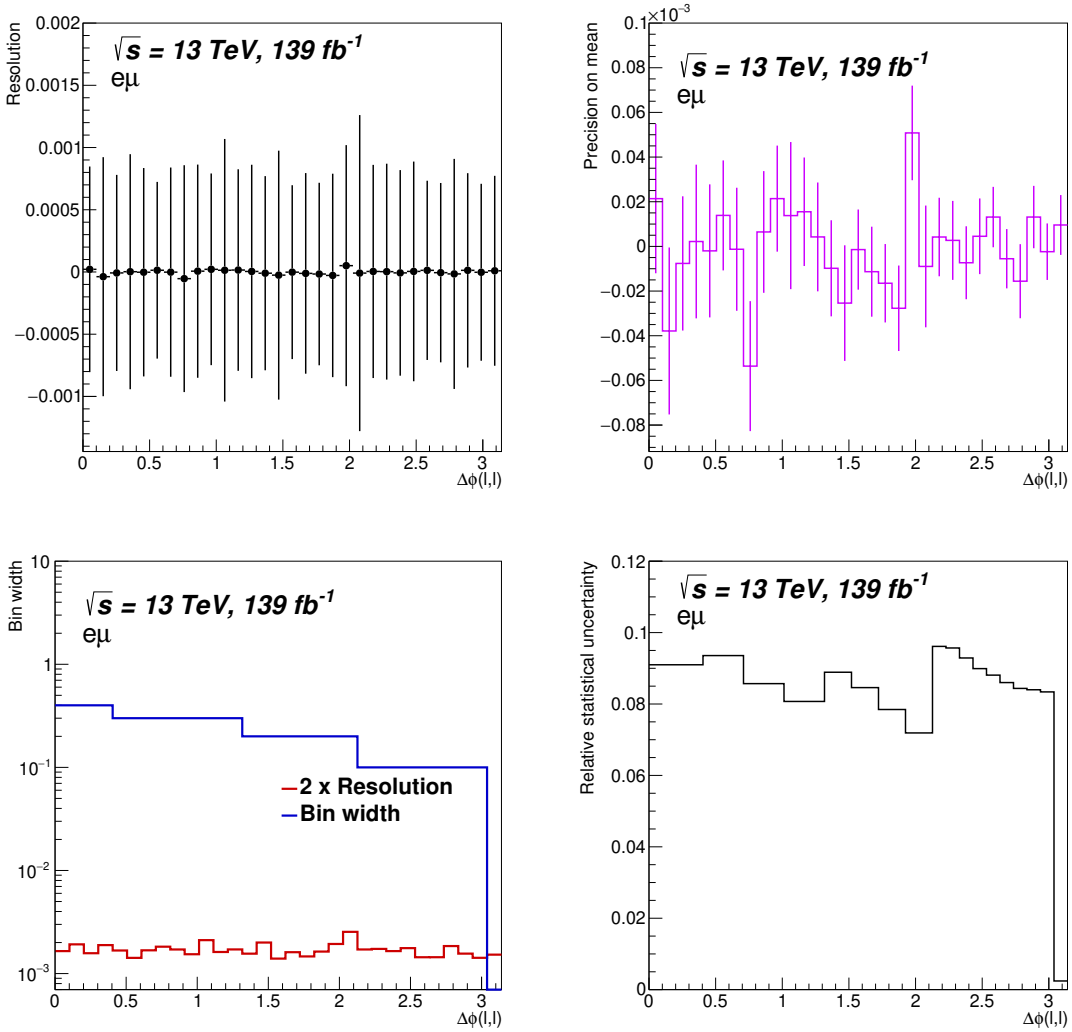

Figure 8.8: Top-left: resolution of the $\Delta\phi(l,l)$ where the y-axis is the mean of the difference between reconstructed and truth $\Delta\phi(l,l)$, and the error bars represent one standard deviation around that mean. Top-right: precision on the mean where the y-axis is the mean of the difference between reconstructed and truth $\Delta\phi(l,l)$, and the error bars represent the error on the mean. Bottom-left: the bin width in blue is compared to the resolution multiplied by 2 in red. Bottom-right: the relative statistical uncertainty of the resulting bin.

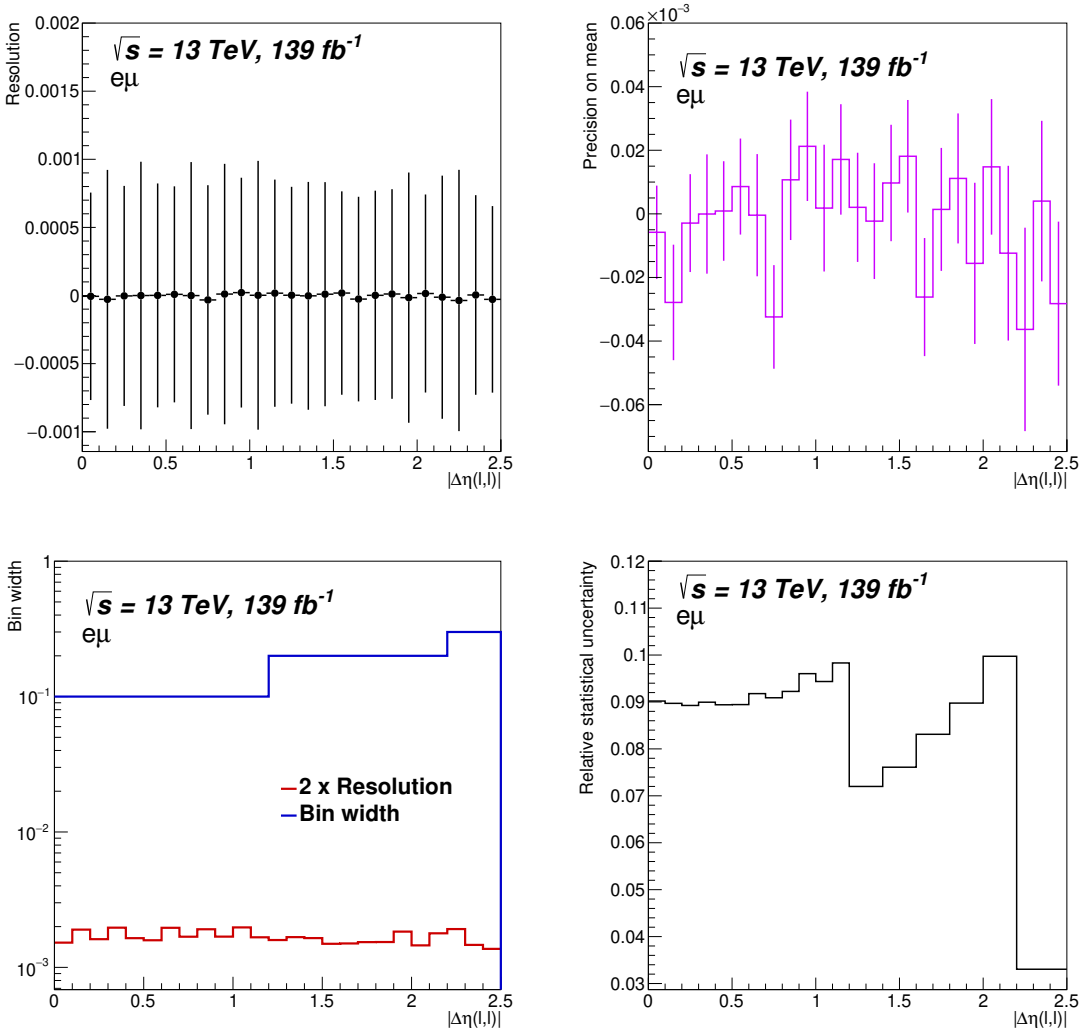

Figure 8.9: Top-left: resolution of the $|\Delta\eta(l,l)|$ where the y-axis is the mean of the difference between reconstructed and truth $|\Delta\eta(l,l)|$, and the error bars represent one standard deviation around that mean. Top-right: precision on the mean where the y-axis is the mean of the difference between reconstructed and truth $|\Delta\eta(l,l)|$, and the error bars represent the error on the mean. Bottom-left: the bin width in blue is compared to the resolution multiplied by 2 in red. Bottom-right: the relative statistical uncertainty of the resulting bin.

Table 8.1: List of number of bins and bin boundaries for the observables: $p_T(\gamma)$, $|\eta(\gamma)|$, $\Delta R(\gamma, l)_{min}$, $\Delta\phi(l, l)$ and $|\Delta\eta(l, l)|$. The last bin boundary for all the observables except the $p_T(\gamma)$ is the physical limit of such observables.

Observable	No. of bins	Bin boundaries
$p_T(\gamma)$ [GeV]	11	20, 25, 30, 35, 40, 47, 55, 70, 85, 132, 180, 300
$\|\eta(\gamma)\|$	8	0.00, 0.20, 0.40, 0.60, 0.80, 1.00, 1.20, 1.70, 2.37
$\Delta R(\gamma, l)_{min}$	10	0.40, 0.55, 0.70, 0.85, 1.00, 1.30, 1.60, 1.90, 2.30, 2.70, 5.00
$\Delta\phi(l, l)$	10	0.00, 0.60, 1.20, 1.60, 1.90, 2.20, 2.40, 2.60, 2.80, 3.00, 3.14
$\|\Delta\eta(l, l)\|$	8	0.0, 0.3, 0.6, 0.9, 1.2, 1.5, 1.8, 2.2, 5.0

8.3.3 Performance and optimisation studies using pseudo-data

In order to validate the unfolding procedure and perform the necessary checks, pseudo-data are used. Signal MC events are randomly divided into two samples, *testing* and *training*, such that the testing sample has the equivalent statistical power as the data. Then, pseudo-data are constructed from the testing sample. In all of the unfolding checks, pseudo-data are unfolded using the a-priori and migration matrix information from the training sample.

Regularisation parameter

The IBS method is an iterative process which means that the optimised number of iterations, at which a stable result is obtained has to be found. The number of iterations, which is the regularisation parameter of the IBS method, is determined by making a χ^2 test for each iteration between unfolded pseudo-data and the corresponding truth distributions. A total of 1000 pseudo-experiments are generated using a Poisson distribution, and generated pseudo-data are unfolded. Afterwards, χ^2 tests are performed between the unfolded distributions and the corresponding parton-level ones, taking into account the covariance matrices of the unfolded distributions. The mean of the χ^2/NDF for all the chosen observables can be seen in Fig. 8.10. For two iterations, the χ^2/NDF is small, and for iterations higher than two, it shows a plateau, where the mean is approximately constant within its Root Mean Square (RMS) value. Therefore, the optimised number of iterations is fixed to two. This number is used in unfolding when performing all the checks as well as the differential cross-section results.

Closure test

A closure test is performed to check if the unfolding procedure can recover the truth spectrum. In order to do that, pseudo-data from the testing sample are unfolded using the training

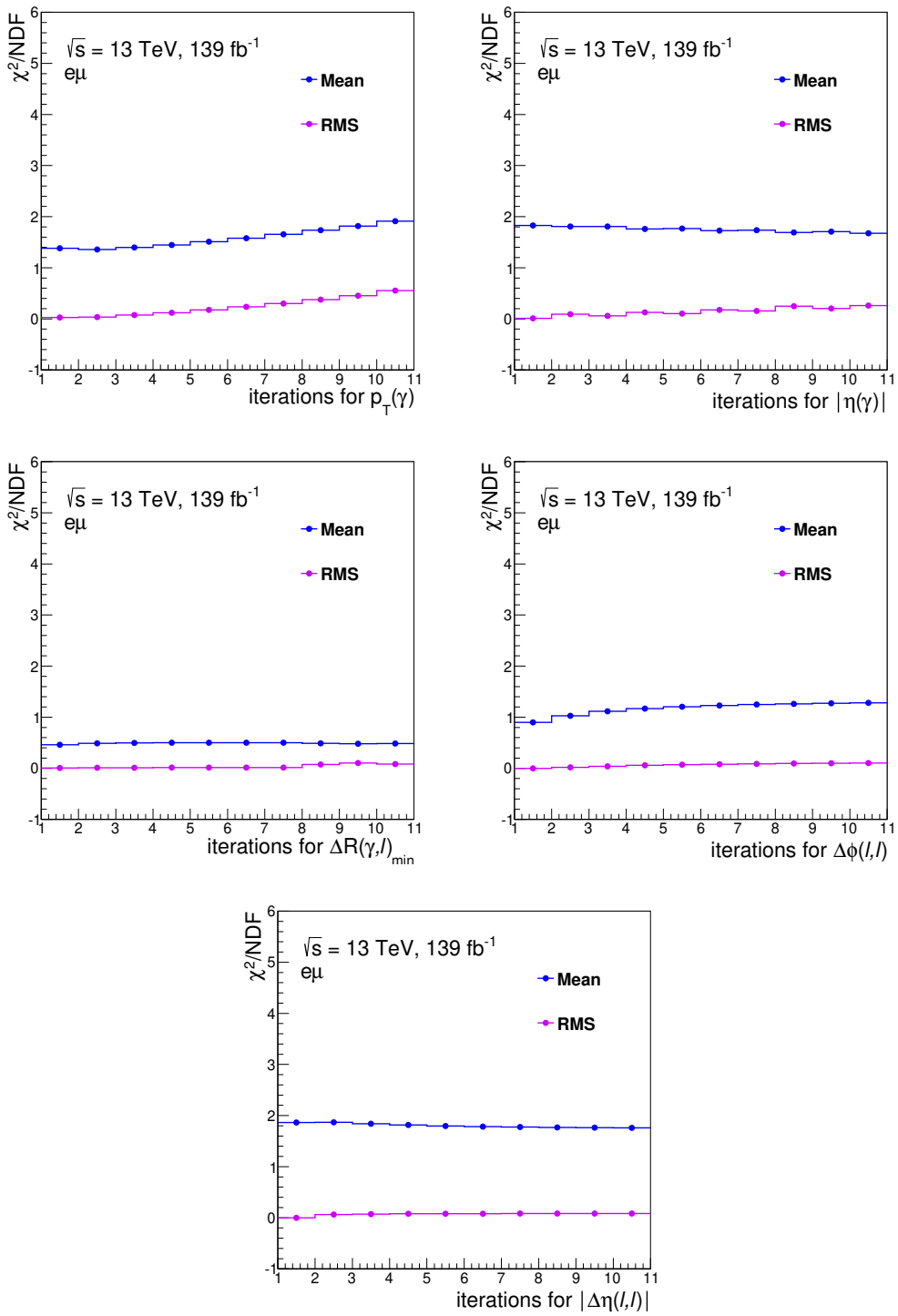

Figure 8.10: χ^2 test with mean in blue and RMS in violet for $p_T(\gamma)$, $|\eta(\gamma)|$, $\Delta R(\gamma, l)_{\text{min}}$, $\Delta\phi(l, l)$ and $|\Delta\eta(l, l)|$ (from left to right and top to bottom).

Table 8.2: χ^2/NDF values between unfolded pseudo-data and truth distributions for the $p_T(\gamma)$, $|\eta(\gamma)|$, $\Delta R(\gamma, l)_{min}$, $\Delta\phi(l, l)$ and $|\Delta\eta(l, l)|$.

Variable	$p_T(\gamma)$	$\lvert\eta(\gamma)\rvert$	$\Delta R(\gamma, l)_{min}$	$\lvert\Delta\eta(l, l)\rvert$	$\Delta\phi(l, l)$
χ^2/NDF	1.3	1.2	0.5	2.0	1.0

sample. The result of the closure test of pseudo-data can be seen in Fig. 8.11. The unfolded distributions of pseudo-data are compared to the corresponding parton-level truth distributions, which show a good closure within uncertainties. The χ^2 values between the unfolded and parton-level distributions are shown in Table 8.2. The values illustrate a good performance of the unfolding procedure in recovering the truth spectrum using information from a statistically independent sample.

Pull test

Pull tests are performed to check the stability of the results with the chosen binning. A total of 1000 pseudo-experiments are generated from the testing sample at reconstruction level using a Poisson distribution, and generated pseudo-data are unfolded. Afterwards, the pulls are calculated as:

$$\text{Pull}_j = \frac{(t_j^n - u_j^n)}{\sigma_j}, \tag{8.12}$$

where t_j^n and u_j^n are the truth and unfolded values in bin j of the pseudo-experiment n, respectively, while σ_j is the statistical uncertainty estimated in bin j. The resulting pull distributions are fitted by a Gaussian function to extract the mean and width. Fig. 8.12 shows the mean and width values of the pulls, where the mean values are close to zero with widths close to one, indicating that there is no bias in the chosen binning and that the statistical uncertainty is estimated correctly.

Stress test

The stress test is performed to verify that the unfolding procedure is not biased towards the simulation used to perform the measurement. The test is performed by modifying the shape of the parton-level and reconstruction-level distributions from the testing sample with a reweighting procedure. The reweighted distribution at reconstruction-level is unfolded using the training sample, and the unfolded distributions are compared to the corresponding parton-level ones. There are two weights considered to smear distributions. The first is to have a linear skewness of the shape. Such weight is defined for each observable as the following:

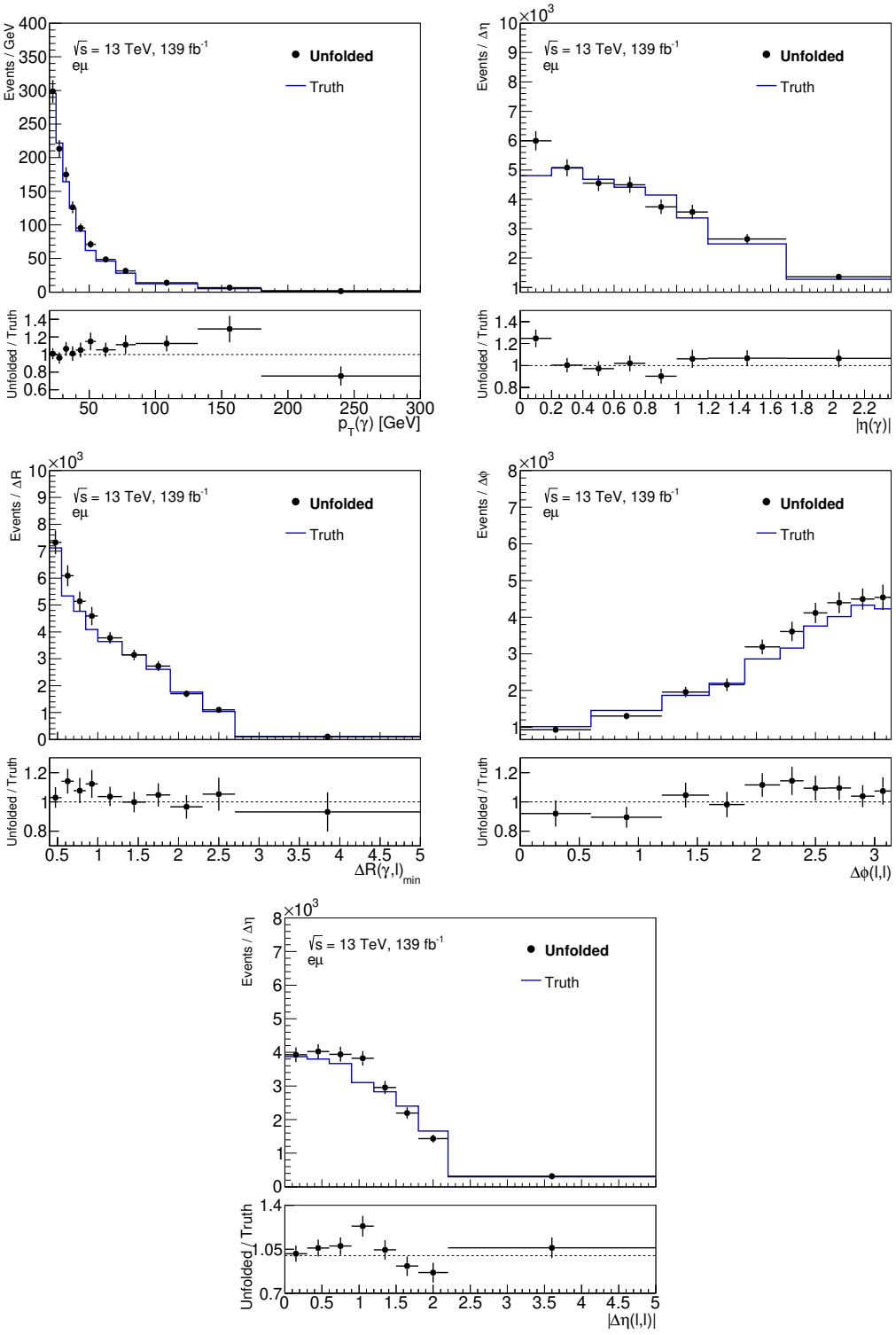

Figure 8.11: Overlay of unfolded pseudo-data and truth distributions as a function of $p_T(\gamma)$, $|\eta(\gamma)|$, $\Delta R(\gamma, l)_{\text{min}}$, $\Delta\phi(l, l)$ and $|\Delta\eta(l, l)|$ (from left to right and top to bottom). The error bars represent the statistical uncertainties on the unfolded values.

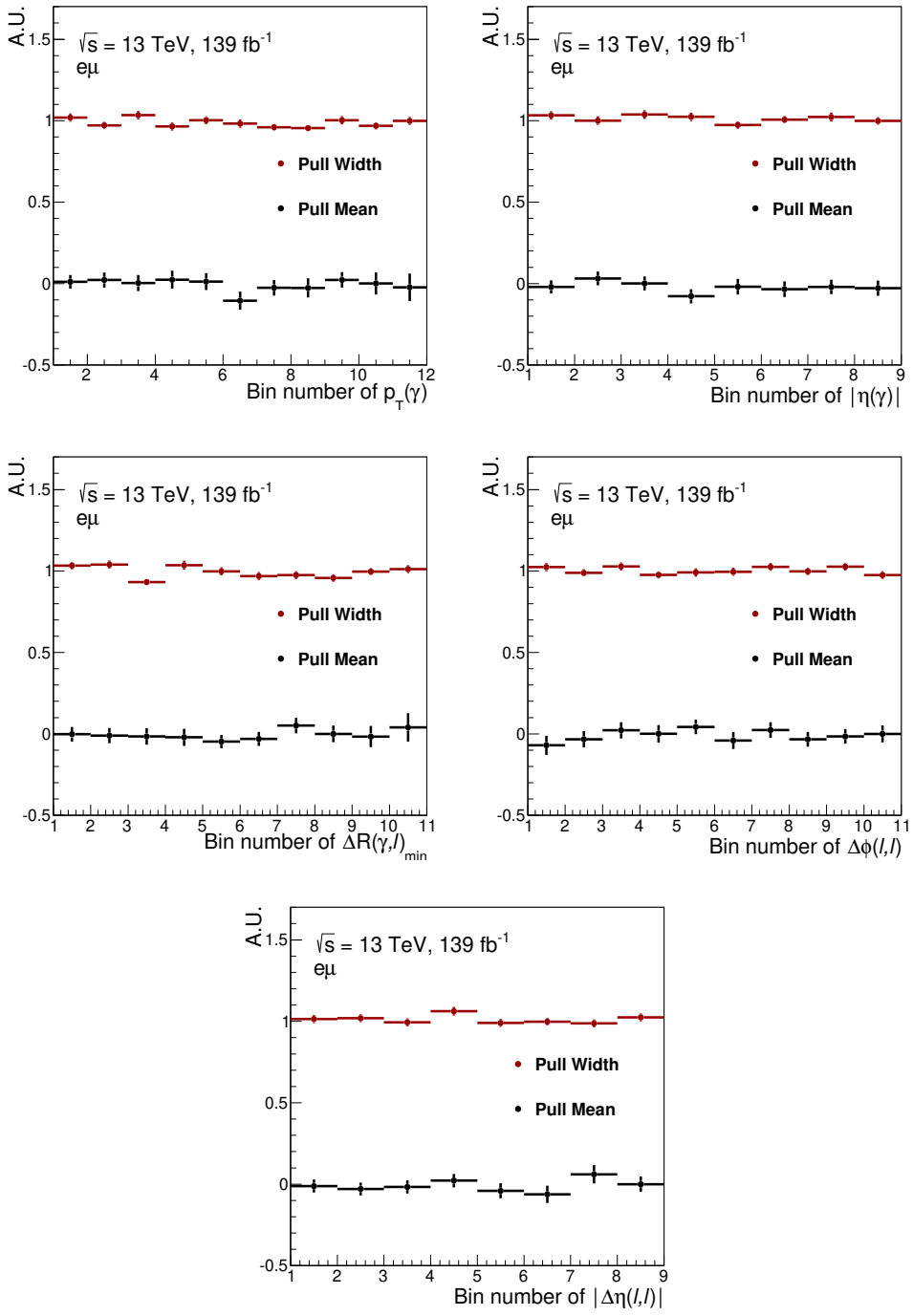

Figure 8.12: Pull test for the $p_T(\gamma)$, $|\eta(\gamma)|$, $\Delta R(\gamma, l)_{\text{min}}$, $\Delta\phi(l, l)$ and $|\Delta\eta(l, l)|$ (from left to right and top to bottom), where the pull mean is shown in black and the pull width in red.

- $p_T(\gamma)$:

$$\text{weight} = 1 + \frac{100 - i}{300} = 1 + X\,. \tag{8.13}$$

- $|\eta(\gamma)|$:

$$\text{weight} = 1 + \frac{1.2 - i}{2.37} = 1 + X\,. \tag{8.14}$$

- $\Delta R(\gamma, l)_{\text{min}}$:

$$\text{weight} = 1 + \frac{1.8 - i}{6} = 1 + X\,. \tag{8.15}$$

- $\Delta\phi(l, l)$:

$$\text{weight} = 1 + \frac{1.75 - i}{3.14} = 1 + X\,. \tag{8.16}$$

- $|\Delta\eta(l, l)|$:

$$\text{weight} = 1 + \frac{1.2 - i}{2.5} = 1 + X\,. \tag{8.17}$$

The index i is the bin centre. The second weight is chosen by taking the difference at reconstruction level between number of data N_i^{data} and MC N_i^{MC} events in bin i, which is calculated as:

$$\text{weight} = 1 + \frac{N_i^{\text{data}} - N_i^{\text{MC}}}{N_i^{\text{data}}} = 1 + Y\,. \tag{8.18}$$

The results of the test can be seen in Fig. 8.13, where unfolded distributions of the reweighted spectra are compared to the corresponding truth-level ones. The unfolding procedure is able to recover the shape of the reweighted distributions, and there is not a bias towards the shape of the truth parton-level distributions used in training.

Alternative unfolding methods

The unfolding of pseudo-data with the IBS method is compared to two alternative approaches: bin-by-bin and Singular Value Decomposition (SVD). The two approaches are summarised below.

Bin-by-bin

Bin-by-bin is a simple technique to perform unfolding, in which a factor is used to correct detector effects. As mentioned in Section 8.3, the aim of the unfolding procedure is to find a solution for μ in Eq. (8.8) with the help of information of ν, β, and the response matrix R. Assuming the same binning for μ and ν, and that R is a diagonal matrix with negligible bin-to-bin migrations, μ_i can be estimated from:

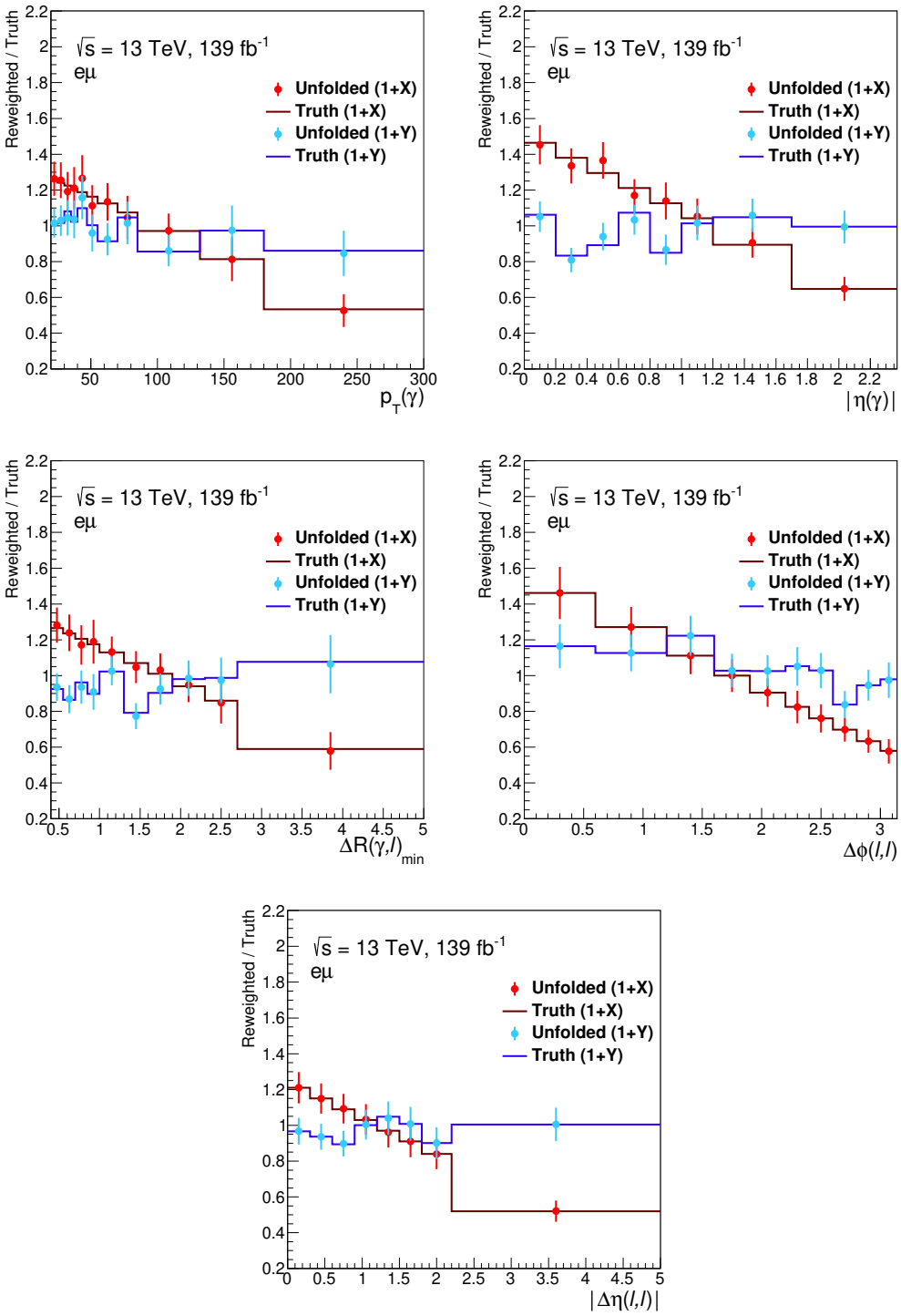

Figure 8.13: Ratios of the reweighted unfolded (dots) and reweighted truth (lines) distributions to the truth ones from the training sample. The reweighted distributions are from the testing sample. The ratios are shown as functions of $p_T(\gamma)$, $|\eta(\gamma)|$, $\Delta R(\gamma, l)_{\text{min}}$, $\Delta\phi(l, l)$ and $|\Delta\eta(l, l)|$ (from left to right and top to bottom). X is defined in Equations (8.13)–(8.17), while Y in Eq. (8.18).

$$\hat{\mu_i} = C_i \, (n_i - \beta_i) \, , \tag{8.19}$$

where n_i is the number of measured data events in bin i, β_i is the number of background events, and C_i is the bin-by-bin correction which is derived from the simulation.

For this thesis, C_i is estimated from the signal MC samples and it is given as:

$$C_i = \frac{\mu_i}{\nu_i} \, , \tag{8.20}$$

where μ_i and ν_i are the expected number of events at parton and reconstruction level, respectively. This method might introduce a bias towards the model prediction.

SVD

SVD or Tikhonov SVD is a regularised unfolding method, described in Ref. [105], which simplifies the inversion of the migration matrix R by decomposing it into three matrices:

$$R = USV^T \, , \tag{8.21}$$

where U and V are orthogonal quadratic matrices, and S is a diagonal matrix.

This decomposition simplifies the computation of the inverse of the migration matrix, R^{-1}, since only the diagonal matrix S must be inverted:

$$R^{-1} = (USV^T)^{-1} = (V^T)^{-1}(S)^{-1}(U)^{-1} = VS^{-1}U^T \, . \tag{8.22}$$

In this method, to reduce the sensitivity of the estimators to small statistical fluctuations in the input values, a regularisation term is added.

Comparison of alternative methods

As a cross-check to the IBS method, used as a benchmark, the bin-by-bin and SVD methods are compared to the IBS by performing a closure test. For each of the three unfolding methods, the pseudo-data distributions from the testing sample are unfolded using the signal MC events from the training sample. For SVD, the regularisation parameters are set to their default values as implemented in the RooUnfold package [104]. The three unfolded distributions are compared per observable to the same truth distribution, which can be seen in Fig. 8.14. The three methods agree with each other and the corresponding truth distributions within uncertainties for all observables. The bin-by-bin unfolded distributions have the highest statistical uncertainties, while the SVD ones have slightly lower uncertainties than the IBS.

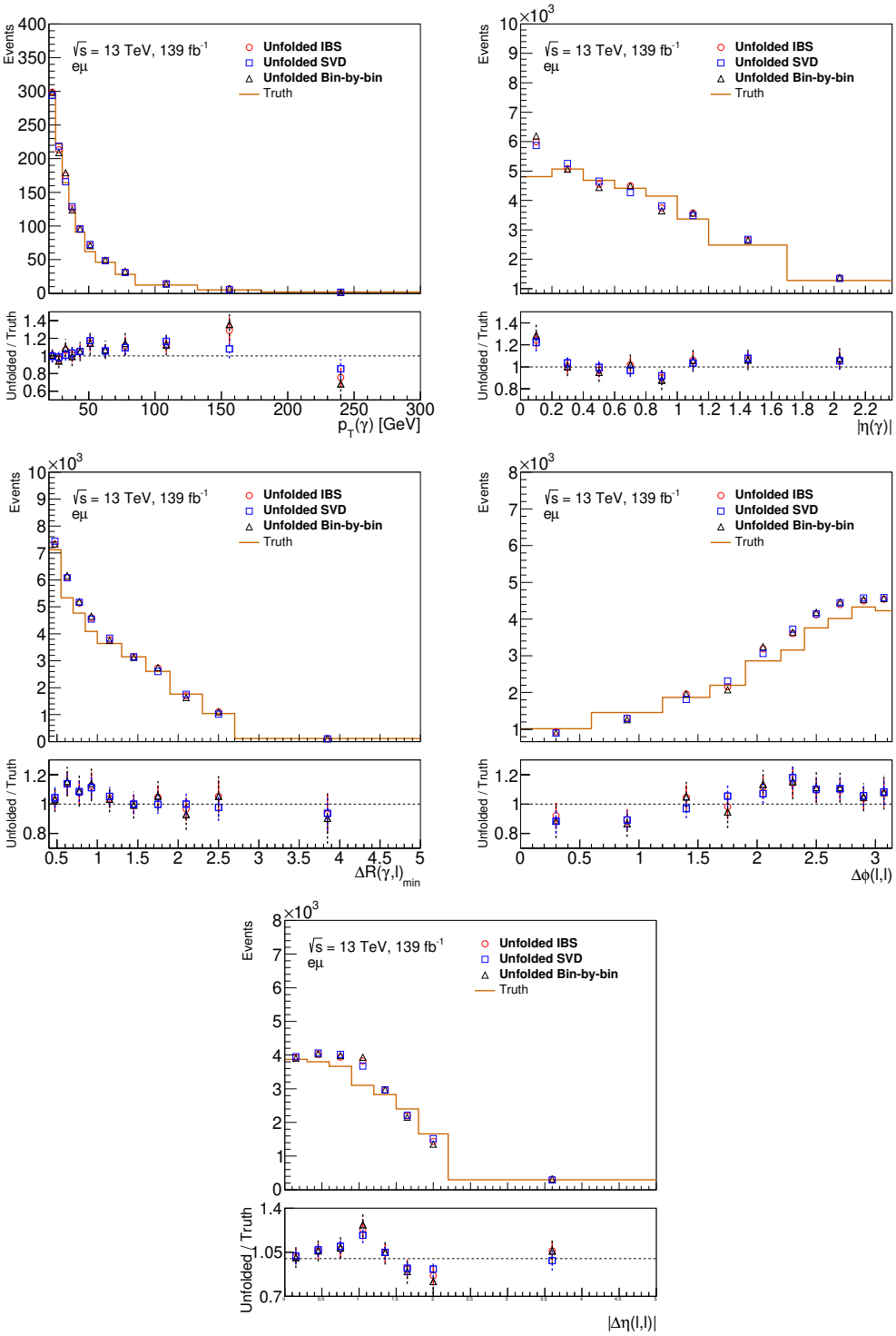

Figure 8.14: Comparison between unfolded distributions obtained using the bin-by-bin, SVD and IBS methods for the $p_T(\gamma)$, $|\eta(\gamma)|$, $\Delta R(\gamma, l)_{\text{min}}$, $\Delta\phi(l, l)$ and $|\Delta\eta(l, l)|$ (from left to right and top to bottom). Error bars represent statistical uncertainties on the unfolded distributions.

CHAPTER 9

Systematic uncertainties

Statistical and systematic uncertainties limit the precision of measurements. The statistical uncertainty results from the stochastic fluctuations due to the finite number of observations in a measurement. It quantifies the variation in the repeated observations of the same phenomena. Systematic uncertainties come from effects related to the measuring apparatus or the assumptions or models used in the measurement.

The systematic uncertainties of the measurements presented here can be classified into two categories: experimental and modelling uncertainties. The first category represents uncertainties associated with the reconstruction and identification efficiency of the detector. It includes uncertainties on reconstructed physics objects related to their momenta and energy scale and resolution, jet flavour tagging, jet vertex tagger (JVT), and detector trigger efficiency, in addition to uncertainties on pile-up and integrated luminosity. The second category represents uncertainties that are related to simulations of the signal and background processes. It includes uncertainties on the chosen renormalisation and factorisation scales, parton shower, ISR/FSR, and PDFs of gluons and quarks.

The systematic uncertainties on the differential cross-sections are estimated using alternative samples, e.g. parton shower uncertainties, or through reweighting the nominal (original) sample, e.g. experimental uncertainties. They are estimated individually in each bin of the measurement. Depending on the type of the uncertainty —experimental, signal modelling, or background modelling—uncertainties are estimated as follows.

- For experimental uncertainties, training pseudo-data are built using the nominal signal distributions at parton and reconstruction levels. The input (to be unfolded) is varied with the corresponding experimental source, resulting in a shift in the normalisation and shape of both signal and background distributions. Then, the varied input is unfolded using the training pseudo-data. The resulting unfolded distribution is compared to the unfolded distribution of the nominal. The difference between these two unfolded distributions is taken as the uncertainty.

- For background modelling uncertainties on non-$t\bar{t}\gamma$/non-$tW\gamma$ backgrounds, i.e. on h-fake, e-fake and prompt γ Bkg (the Other $t\bar{t}\gamma$/$tW\gamma$ modelling uncertainty is included

in the signal modelling), they are calculated similarly to the experimental ones. Training pseudo-data are constructed from the nominal signal distributions, and the input is varied using the corresponding background source. The varied input is then unfolded using the training pseudo-data. The difference between the resulting unfolded distribution and the unfolded distribution of the nominal is taken as the uncertainty.

- For signal modelling uncertainties, the procedure is different, where training pseudo-data are built using an alternative sample or the nominal reweighted one, i.e. using varied pseudo-data. The nominal distribution of the signal is unfolded twice; once with the varied pseudo-data and another with the nominal pseudo-data. The difference between the two resulting unfolded distributions is taken as the uncertainty.

By default, many of the systematics uncertainties used in the ATLAS Collaboration are represented by up- and down-variations obtained by a 1 σ shift from the nominal (central) value. For a number of systematic uncertainties, the two variations are asymmetric, and in some other cases, they have the same sign in a few bins. For both scenarios, a *maximum* symmetrisation is used. It is a conservative approach to symmetrise uncertainties where the larger variation is taken as the up- as well as the down-variations. There are other few cases where only one variation (either up or down) is provided. For these uncertainties, a *one-sided* symmetrisation is used where the available variation is mirrored around the nominal value, i.e. taken as the up- and down-variations.

Once all individual systematic uncertainties are estimated, as explained above, they are added in quadrature. This is based on the assumption that the sources of systematic uncertainties are not correlated. The resulting quadrature sum is reported as the systematic uncertainty on the calculated differential cross-section in each bin of the measurement.

The experimental uncertainties on the differential cross-sections are discussed in Section 9.1, while the modelling uncertainties are discussed in Section 9.2.

9.1 Experimental uncertainties

As mentioned earlier, the sources of experimental uncertainties originate from the measuring apparatus, i.e. the ATLAS detector. These sources are discussed below while grouping them in terms of the reconstructed physics objects that they affect.

Leptons

There are two types of uncertainties related to charged leptons (electrons and muons), where the first type is on the scale factors (SFs) that correct trigger, reconstruction, identification and isolation efficiencies. These lepton SFs are used to correct for the mis-modelling of the detector so that charged leptons in the simulation match those in data.

The SFs are estimated by studying a tag-and-probe method on the $Z \to ee$, $Z \to \mu\mu$, and $J/\psi \to ee$ processes. Therefore, the uncertainties are estimated by varying the estimated SFs up and down. The second type of uncertainties is on the SFs that correct the energy scale and resolution of electrons and mouns. They are estimated for electrons in Ref. [60], while for muons in Ref. [61]. Similarly, uncertainties on these SFs are estimated by an up- and down-variation from their nominal values.

Photons

Similar to electrons and muons, photon SFs are applied to the MC simulation of photons to match the data ones. Photon SFs include corrections for the identification and isolation efficiency of photons. These SFs are estimated by studying radiative and non-radiative Z boson decays, $Z \to ee\gamma$ and $Z \to ee$, respectively. The uncertainties associated with these SFs are estimated by shifting them up and down from their nominal values.

The size and shape of the uncertainties on the photon identification and isolation efficiencies are shown in Fig. 9.1. The left subfigure shows systematic uncertainties on the photon identification SF as a function of the $\mathrm{p_T}(\gamma)$. They go up to around 2% below/above the nominal $t\bar{t}\gamma$ $e\mu$ prediction. The MC statistical uncertainties have a similar (bigger) size to that of the down (up) systematic one for most of the p_{T}-range, except at low p_{T} where the size of the systematic uncertainty is slightly bigger. Similarly, the right subfigure shows systematic uncertainties on the photon efficiency isolation SF, which go up to approximately 2% around the nominal MC prediction. However, the MC statistical uncertainties have a bigger size than both the up- and down-variations (except at low p_{T}). The uncertainties on the photon energy scale and resolution are estimated similarly to the electrons.

Jets

Jets are calibrated using the techniques discussed in Section 4.4.2, which are based on a combination of MC-based and in-situ methods to correct the energy scale, η-intercalibration, and energy resolution of the jets, among other effects. All these corrections are considered sources of uncertainties, and they are grouped into two categories.

The first category is called the Jet Energy Scale (JES) uncertainties, and it includes sources such as jet-flavour composition, η-intercalibration, in-situ calibration, punch-through jets, and pile-up corrections. The JES uncertainties are estimated using 30 uncorrelated JES uncertainty components, of which 29 are non-zero based on an event-by-event approach.

The second category of uncertainties is called the Jet Energy Resolution (JER), and it contains eight uncorrelated components. An additional source of uncertainty is the JVT discriminant, estimated by varying the efficiency correction factors.

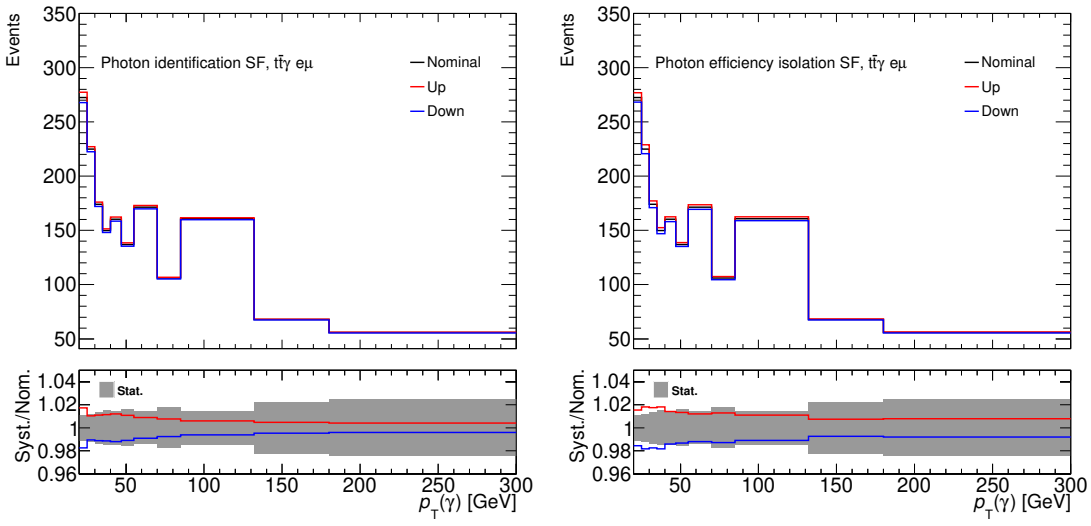

Figure 9.1: Impact of systematic uncertainty on the photon identification SF (left), and photon efficiency isolation SF (right), as a function of $p_T(\gamma)$. The nominal (central) $t\bar{t}\gamma$ $e\mu$ MC prediction is compared to the up- and down-variations. The lower panel shows ratios of both the up- and down-variations to the nominal prediction. The shaded bands represent the MC statistical uncertainties.

b-tagging

The b-tagging of jets so that b-jets are distinguished from c-jets or light-flavour jets is performed with the MV2c10 [68] discriminant algorithm (see Section 4.4.3). The SFs to calibrate the efficiencies of the discriminant performance in the MC simulation to those in the data introduce a number of sources of uncertainties, where the uncertainties are estimated individually for b-jets, c-jets and light-flavour jets [68, 106, 107]. The uncertainties are estimated with 45, 20, and 20 variations in the SFs for b-jets, c-jets and light-flavour jets, respectively, where the uncertainties in each category of jets are considered to be uncorrelated.

Missing transverse momentum

$\overrightarrow{E}_T^{\text{miss}}$ has two terms, where the first one depends on hard objects, e.g. photons, leptons, and jets, and the second term depends on soft signals (see Section 4.5). Therefore, the uncertainties on the $\overrightarrow{E}_T^{\text{miss}}$ are estimated by evaluating uncertainties on the energy scales and resolutions of the hard objects as well as uncertainties on the modelling of the soft signal.

Pile-up

Pile-up SFs are used to correct the pile-up contribution in the MC simulation to the data one. Therefore, the uncertainty on the pile-up is estimated by varying the SFs within their

uncertainties.

Luminosity

The uncertainty on the total integrated luminosity for the years 2015–2018 is 1.7% [108], which is estimated using the LUCID-2 detector [109] for the primary luminosity measurements.

9.2 Modelling uncertainties

The assumptions made to simulate the signal and background processes introduce different sources of uncertainties, which can be split into two categories: signal modelling and background modelling uncertainties. These modelling assumptions include, for example, the factorisation and renormalisation scales and PDFs of gluons and quarks.

Signal modelling

The uncertainties related to the $t\bar{t}\gamma$ simulation originate from different sources such as the chosen QCD scales, the parton shower model, the parameters chosen to model the ISR and FSR radiations as well as the used PDF set. The uncertainties related to QCD scales are estimated by varying the renormalisation μ_R and factorisation μ_F scales separately up and down by a factor of two from their nominal chosen values. In order to reduce the impact of statistical fluctuations, the variation in the scales' values is achieved by reweighting the events in the nominal MadGraph5_aMC@NLO + Pythia 8 sample of $t\bar{t}\gamma$.

The uncertainties on the parton shower (PS) model of the $t\bar{t}\gamma$ samples are estimated by performing a comparison between the MadGraph5_aMC@NLO [81] interfaced with the nominal Pythia 8 [76] and MadGraph5_aMC@NLO interfaced with the alternative Herwig 7 [110, 111]. The Pythia 8 generator uses the string fragmentation model [112], while the Herwig 7 makes use of the cluster fragmentation model [113], which allows estimating possible differences in the showering process.

The uncertainties on ISR and FSR are estimated by comparing two samples of the MadGraph5_aMC@NLO + Pythia 8, where the Pythia 8 A14 tune [76] (called A14 *var3c*) is varied between them.

The uncertainties on the PDF for the $t\bar{t}\gamma$ process are estimated using the standard deviation in each bin of the unfolded distributions, where a set of 100 replicas of the NNPDF set [114] is used.

The sources of uncertainties related to the $tW\gamma$ simulation are estimated similarly to those of the $t\bar{t}\gamma$. The uncertainties on the renormalisation μ_R and factorisation μ_F scales are estimated by varying the nominal chosen values by a factor of two, up and down. The uncertainties on the parton shower are estimated by comparing Pythia 8 and Herwig 7 where both are interfaced with MadGraph5_aMC@NLO.

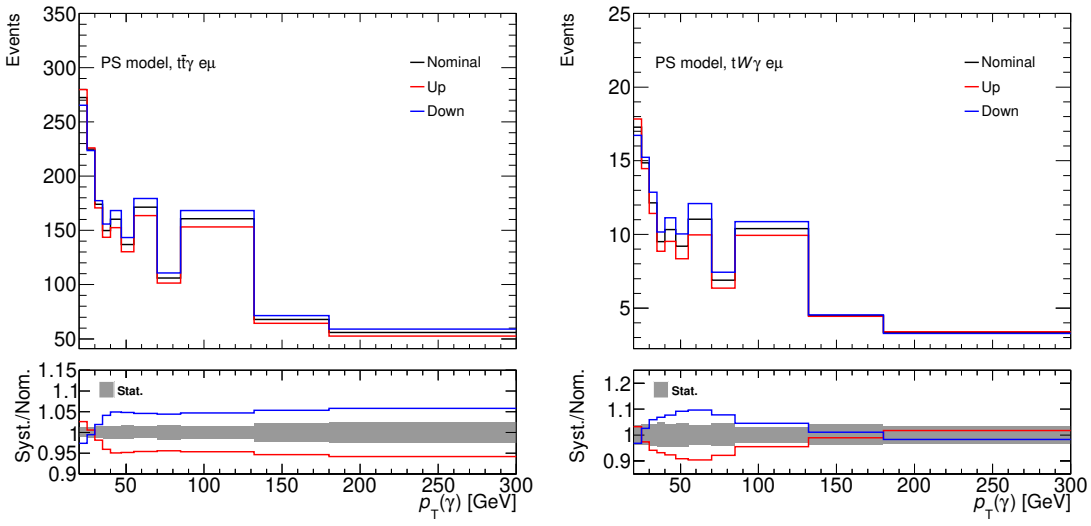

Figure 9.2: Impact of systematic uncertainty on the parton shower modelling for the $t\bar{t}\gamma$ $e\mu$ process (left) and the $tW\gamma$ $e\mu$ process (right), as a function of $\mathrm{p_T}(\gamma)$. The nominal distribution representing the PYTHIA 8 is compared to the up- and down-variations representing the HERWIG 7. The lower panel shows ratios of both the up- and down-variations to the nominal prediction. The shaded bands represent the MC statistical uncertainties.

The impact of the parton shower uncertainties for the $t\bar{t}\gamma$ and $tW\gamma$ samples is shown in Fig. 9.2. The systematic uncertainties of the PS model as a function of the $\mathrm{p_T}(\gamma)$ go up to around 5% below/above the nominal $t\bar{t}\gamma$ $e\mu$ prediction and the direction of the variations is reversed at low p_{T}. The MC statistical uncertainties have a smaller size than the systematic ones of the $t\bar{t}\gamma$ $e\mu$. Similarly, the systematic uncertainties of the PS model go up to approximately 10% around the nominal $tW\gamma$ $e\mu$ prediction, and the direction of the variations is reversed at low/high p_{T}. The MC statistical uncertainties of the $tW\gamma$ $e\mu$ have a smaller size than the systematics ones except at high p_{T}.

An additional uncertainty related to the ME simulation of the $tW\gamma$ process is considered. The $tW\gamma$ process is simulated using the five-flavour scheme at LO in QCD (see Section 6.3), where one of the two b-quarks is not simulated at ME level but is supposed to be added by the PDF in the initial state. This b-quark is missing from a faction of events when applying the fiducial requirements —such as requiring exactly two b-quarks (see Section 8.1)—which has the consequence of having fewer $tW\gamma$ events entering the fiducial region. The fraction of events without a second b-quark is found to be 30% and 50% in the $tW\gamma$ MC samples interfaced with HERWIG 7 and PYTHIA 8, respectively. In order to account for this missing fraction of events, an uncertainty is added by doubling the number of parton-level events while keeping the number of reconstructed-level events constant.

Background modelling

The process of $t\bar{t}$ production has the dominant contribution to the non-$t\bar{t}\gamma$/non-$tW\gamma$ backgrounds: h-fake, e-fake, and prompt γ background. Hence, the uncertainties related to the background simulation are estimated as follows. The shape component of the $t\bar{t}$ modelling uncertainties is varied for the h-fake and prompt γ background since these two categories are the largest ones. These modelling uncertainties account for uncertainties on the chosen QCD scales, the parton showering and hadronisation processes, and the ISR/FSR simulation. Furthermore, a global normalisation uncertainty is added by applying a 50% variation on the simulation of the non-$t\bar{t}\gamma$/non-$tW\gamma$ backgrounds.

The uncertainties associated with the chosen QCD scales are estimated by varying the renormalisation μ_R and factorisation μ_F scales individually up and down by a factor of two from their nominal chosen values. The variation in the scales is done by reweighting the nominal $t\bar{t}$ events to reduce statistical fluctuations.

The uncertainties associated with ISR/FSR are estimated by varying the A14 *var3c* tune of the PYTHIA 8 generator. An additional uncertainty associated with the ISR simulation is estimated by varying the h_{damp} parameter of the POWHEG-BOX by a factor of two, following the measurements done in Ref. [115]. The h_{damp} parameter controls the p_{T} threshold of the first additional emission.

The uncertainty associated with the simulation of the showering and hadronisation processes is estimated by comparing PYTHIA 8 to HERWIG 7 interfaced with the nominal $t\bar{t}$ samples. The impact of the parton shower and hadronisation uncertainty on the h-fake and prompt γ background can be seen in Fig. 9.3. The systematic uncertainties of the PS model as a function of the $\text{p}_{\text{T}}(\gamma)$ go up to approximately 50% below/above the nominal h-fake prediction and the direction of the variations is reversed at low/high p_{T}. The MC statistical uncertainties have a much smaller size than the systematic ones of h-fake. Similarly, the systematic uncertainties of the PS model go up to approximately 20% around the nominal prompt γ Bkg prediction. The MC statistical uncertainties of the prompt γ Bkg have a bigger size than the systematics ones.

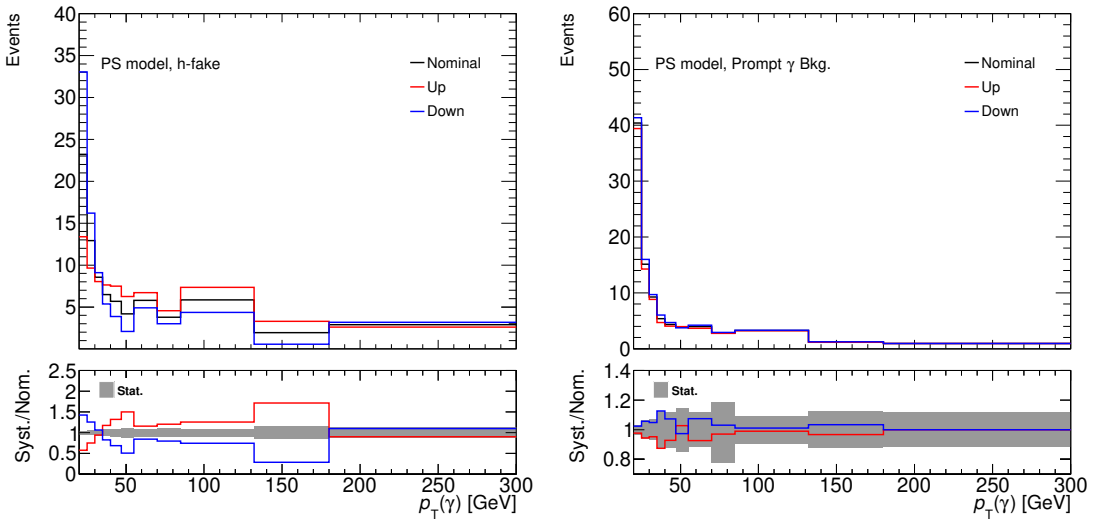

Figure 9.3: Impact of systematic uncertainty on the parton shower modelling for the h-fake background (left) and the prompt γ background (right), as a function of $p_T(\gamma)$. The nominal distribution representing the PYTHIA 8 is compared to the up- and down-variations representing the HERWIG 7. The lower panel shows ratios of both the up- and down-variations to the nominal prediction. The shaded bands represent the MC statistical uncertainties.

CHAPTER 10

Results

In this chapter, the results of the absolute and normalised fiducial differential cross-sections are reported. The unfolded spectra of data are compared to those of the MC predictions (see Section 6.3). Moreover, they are compared to the latest NLO theory calculation (see Section 2.3). The measurements are performed as functions of $p_T(\gamma)$, $|\eta(\gamma)|$, $\Delta R(\gamma, l)_{\text{min}}$, $\Delta\phi(l, l)$, and $|\Delta\eta(l, l)|$. The absolute and normalised cross-section measurements are reported in Section 10.1 and Section 10.2, respectively.

10.1 Absolute cross-section measurements

The absolute fiducial differential cross-sections and the contribution of each category of the systematic uncertainties as functions of $p_T(\gamma)$, $|\eta(\gamma)|$, $\Delta R(\gamma, l)_{\text{min}}$, $\Delta\phi(l, l)$ and $|\Delta\eta(l, l)|$ are shown in Figs. 10.1–10.3. The top-row subfigures show the absolute cross-sections of unfolded data compared to the latest NLO theory prediction [9], where the shaded bands represent the statistical and the total uncertainties. The bottom-row subfigures display the decomposition of the systematic uncertainties and the statistical ones. The cross-section distributions show the number of events divided by the bin width, and they do not include the overflow for $p_T(\gamma)$, whereas for the rest of the distributions, the higher boundary of the last bin is limited by the physical value. A good agreement between the unfolded data and the NLO theory predictions within uncertainties is observed.

The values of the absolute cross-sections and their associated uncertainties are listed in Tables 10.1–10.5. The dominant source of uncertainty is the statistical one. The last row in each table represents the inclusive cross-section obtained by adding the individual cross-sections (multiplied by the corresponding bin width) per observable. From the tables, it can be seen that such fiducial inclusive cross-sections agree with each other within uncertainties, and they also agree with the fiducial inclusive cross-section of $39.6\,^{+2.7}_{-2.3}$ fb, obtained by performing a profile likelihood fit to the S_T distribution [8].

The sources of systematic uncertainties are classified into signal and background modelling and experimental uncertainties (see Chapter 9). The size of these three categories, as well

as of the statistical uncertainty, is shown as a percentage of the measured cross-sections in Tables 10.6–10.10. The signal and background uncertainties dominate the systematic uncertainties. Furthermore, the total uncertainty is roughly in the range of 8%-12% for most of the absolute cross-sections of all variables. At high values of $p_T(\gamma)$ and $\Delta R(\gamma, l)_{\text{min}}$, it goes higher up to 16% and 23%, respectively.

The agreement between the data and NLO theory prediction is quantified using a Pearson χ^2 test:

$$\chi^2 = \sum_{j,k} (\sigma_{j,\text{data}} - \sigma_{j,\text{pred.}}) \cdot C_{jk}^{-1} \cdot (\sigma_{k,\text{data}} - \sigma_{k,\text{pred.}}) \,, \tag{10.1}$$

where C_{jk} is the covariance matrix, calculated as the sum of the covariance matrix of the statistical uncertainty and the covariance matrices of the corresponding systematic uncertainties. The terms σ_{data} and $\sigma_{\text{pred.}}$ are the unfolded and predicted differential cross-sections, and j and k are the binning indices of the distribution. The covariance matrix for each systematic uncertainty is estimated as $\sigma_j \times \sigma_k$, where σ_j and σ_k are the symmetrised uncertainties for bin j and bin k of the unfolded distribution.

The estimation of the statistical correlation between the differential cross-sections as functions of all observables is performed using the bootstrap method. It is based on deriving ten thousand pseudo-experiments by reweighting the measured data sample on an event-by-event basis using a Poisson distribution. The pseudo-experiments are obtained such that the average over all of them for a given event yields exactly one event. Pseudo-data are then unfolded, and the statistical uncertainties and their correlations are calculated from the unfolded distributions. The statistical correlation matrix of the absolute cross-sections of all observables is shown in Fig. 10.4, where no significant correlation between different bins is observed. The full correlation matrices of the absolute fiducial cross-sections as functions of all observables are shown in Appendix B.

The p-values between the data and NLO theory prediction are calculated using the χ^2 and the number of degrees of freedom (ndf) for each observable individually. The χ^2/ndf and the corresponding p-values for the absolute fiducial cross-sections are shown in Table 10.11. The high p-values assert the good agreement between the measured absolute cross-sections and the NLO prediction for all observables.

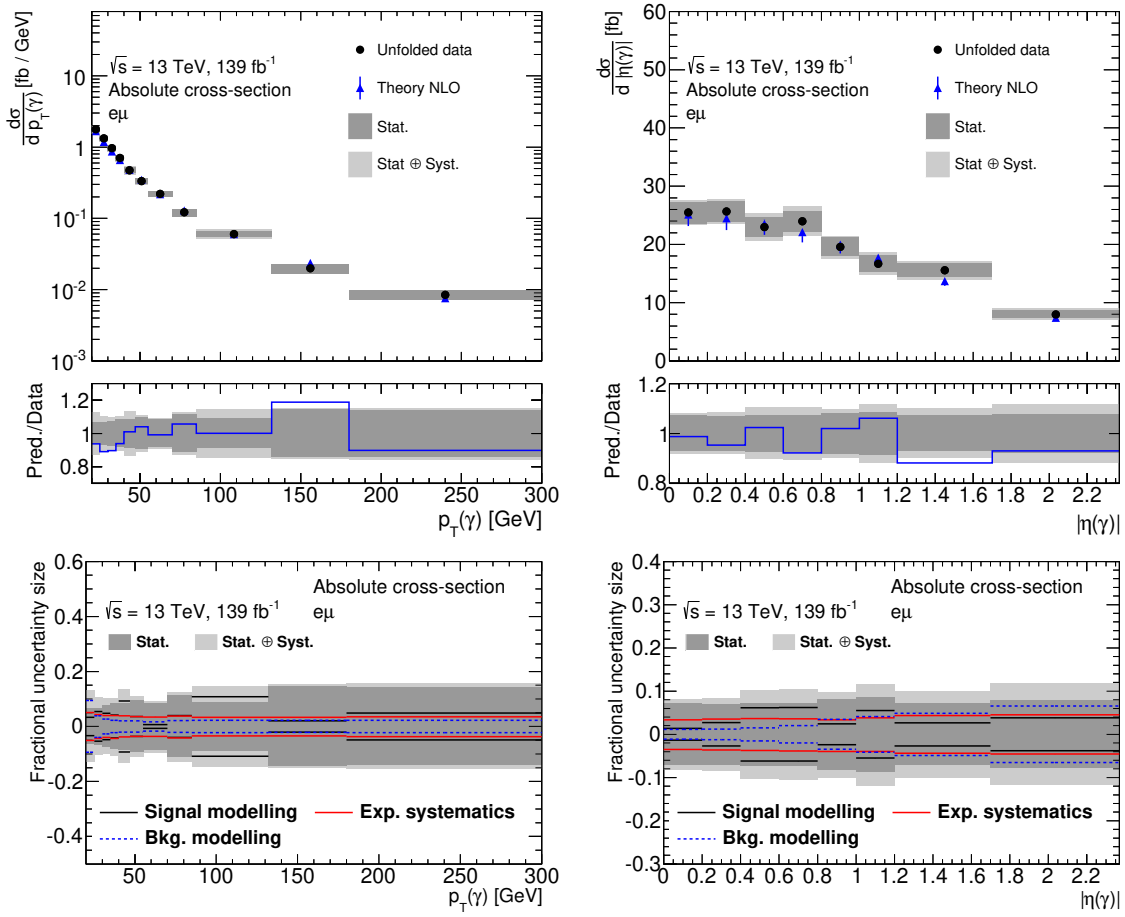

Figure 10.1: Distributions of the absolute fiducial differential cross-sections as functions of $p_T(\gamma)$ and $|\eta(\gamma)|$ in the top row where data are compared to the NLO theory prediction [9]. In the bottom row, the relative statistical and systematic uncertainties are shown in each bin. The systematic uncertainties are decomposed into three categories: signal, background, and experimental.

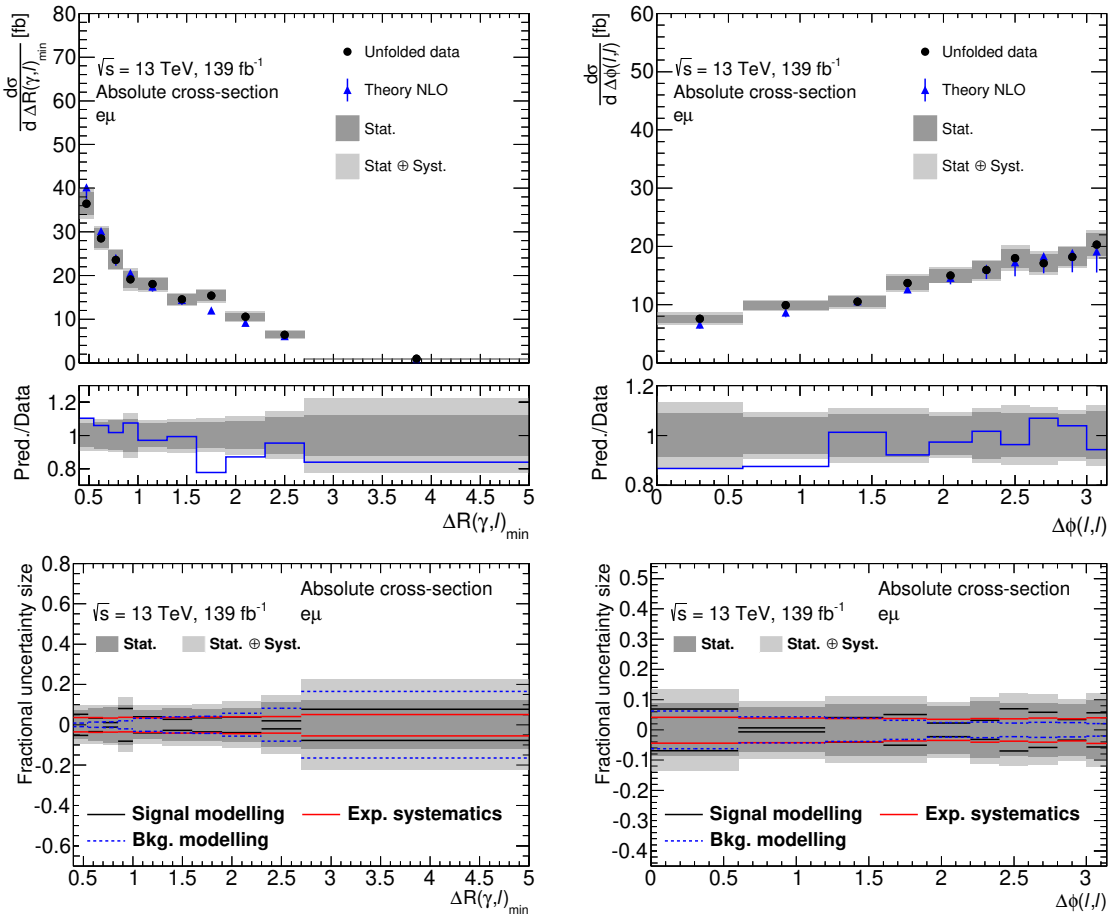

Figure 10.2: Distributions of the absolute fiducial differential cross-sections as functions of $\Delta R(\gamma, l)_{\text{min}}$ and $\Delta\phi(l, l)$ in the top row where data are compared to the NLO theory prediction [9]. In the bottom row, the relative statistical and systematic uncertainties are shown in each bin. The systematic uncertainties are decomposed into three categories: signal, background, and experimental.

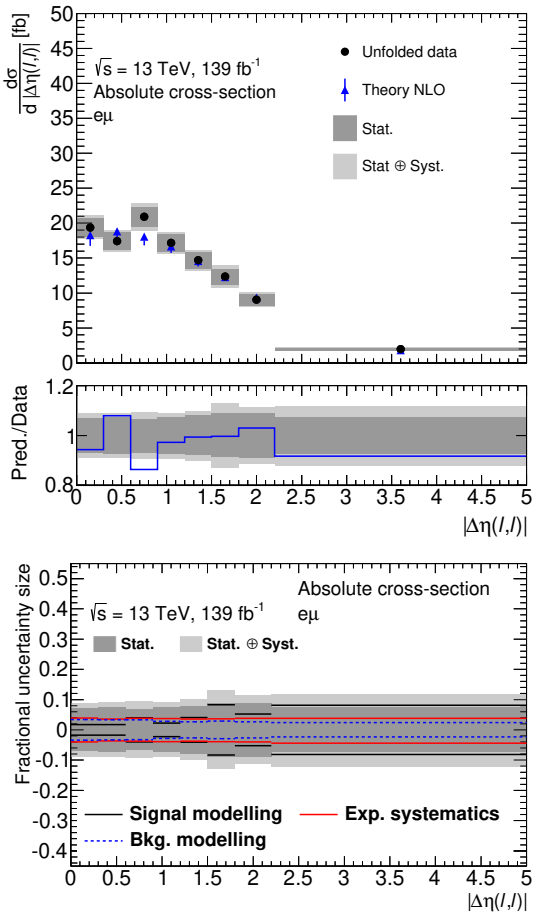

Figure 10.3: Distribution of the absolute fiducial differential cross-section as a function of $|\Delta\eta(l,l)|$ in the top row where data are compared to the NLO theory prediction [9]. In the bottom row, the relative statistical and systematic uncertainties are shown in each bin. The systematic uncertainties are decomposed into three categories: signal, background, and experimental.

Table 10.1: Values of the absolute differential cross-section as a function of $p_T(\gamma)$, divided by the bin width. The first and second associated uncertainties are the statistical and systematic uncertainties, respectively. The sum is calculated by adding the individual cross-sections multiplied by their corresponding bin width, and the uncertainty on the sum is estimated by adding the total statistical and systematic uncertainties in quadrature.

$p_T(\gamma)$ [Gev]	$d\sigma/dx \pm$ (stat.) $\pm$ (syst.) [fb/GeV]
20 – 25	1.78 ± 0.12 ± 0.20
25 – 30	1.33 ± 0.09 ± 0.11
30 – 35	0.966 ± 0.072 ± 0.066
35 – 40	0.705 ± 0.058 ± 0.044
40 – 47	0.474 ± 0.040 ± 0.049
47 – 55	0.333 ± 0.031 ± 0.018
55 – 70	0.221 ± 0.019 ± 0.009
70 – 85	0.122 ± 0.014 ± 0.007
85 – 132	0.0603 ± 0.0053 ± 0.0069
132 – 180	0.0199 ± 0.0029 ± 0.0009
180 – 300	0.0085 ± 0.0012 ± 0.0005
Sum	[39.8 ± 4.7] fb

Table 10.2: Values of the absolute differential cross-section as a function of $|\eta(\gamma)|$, divided by the bin width. The first and second associated uncertainties are the statistical and systematic uncertainties, respectively. The sum is calculated by adding the individual cross-sections multiplied by their corresponding bin width, and the uncertainty on the sum is estimated by adding the total statistical and systematic uncertainties in quadrature.

$\lvert\eta(\gamma)\rvert$	$d\sigma/dx \pm$ (stat.) $\pm$ (syst.) [fb]
0.00 – 0.20	25.5 ± 1.8 ± 1.0
0.20 – 0.40	25.7 ± 1.8 ± 1.2
0.40 – 0.60	23.0 ± 1.7 ± 1.7
0.60 – 0.80	24.0 ± 1.7 ± 1.8
0.80 – 1.00	19.6 ± 1.6 ± 1.1
1.00 – 1.20	16.7 ± 1.4 ± 1.3
1.20 – 1.70	15.6 ± 1.1 ± 1.1
1.70 – 2.37	7.97 ± 0.62 ± 0.71
Sum	[40.0 ± 4.0] fb

Table 10.3: Values of the absolute differential cross-section as a function of $\Delta R(\gamma, l)_{\text{min}}$, divided by the bin width. The first and second associated uncertainties are the statistical and systematic uncertainties, respectively. The sum is calculated by adding the individual cross-sections multiplied by their corresponding bin width, and the uncertainty on the sum is estimated by adding the total statistical and systematic uncertainties in quadrature.

$\Delta R(\gamma, l)_{\text{min}}$	$\mathrm{d}\sigma/\mathrm{d}x$ ± (stat.) ± (syst.) [fb]
0.40 — 0.55	36.4 ± 2.6 ± 2.3
0.55 – 0.70	28.5 ± 2.3 ± 1.5
0.70 – 0.85	23.6 ± 2.1 ± 0.9
0.85 – 1.00	19.2 ± 1.9 ± 1.8
1.00 – 1.30	18.0 ± 1.3 ± 1.1
1.30 – 1.60	14.5 ± 1.2 ± 0.9
1.60 – 1.90	15.4 ± 1.2 ± 1.0
1.90 – 2.30	10.55 ± 0.88 ± 0.84
2.30 – 2.70	6.42 ± 0.70 ± 0.60
2.70 – 5.00	0.98 ± 0.12 ± 0.19
Sum	[39.6 ± 4.4] fb

Table 10.4: Values of the absolute differential cross-section as a function of $\Delta\phi(l, l)$, divided by the bin width. The first and second associated uncertainties are the statistical and systematic uncertainties, respectively. The sum is calculated by adding the individual cross-sections multiplied by their corresponding bin width, and the uncertainty on the sum is estimated by adding the total statistical and systematic uncertainties in quadrature.

$\Delta\phi(l, l)$	$\mathrm{d}\sigma/\mathrm{d}x$ ± (stat.) ± (syst.) [fb]
0.00 – 0.60	7.58 ± 0.66 ± 0.77
0.60 – 1.20	9.89 ± 0.72 ± 0.59
1.20 – 1.60	10.49 ± 0.89 ± 0.71
1.60 – 1.90	13.7 ± 1.2 ± 1.0
1.90 – 2.20	15.0 ± 1.2 ± 0.7
2.20 – 2.40	16.0 ± 1.5 ± 0.9
2.40 – 2.60	18.0 ± 1.6 ± 1.5
2.60 – 2.80	17.1 ± 1.5 ± 1.3
2.80 – 3.00	18.2 ± 1.6 ± 1.0
3.00 – 3.14	20.3 ± 2.0 ± 1.5
Sum	[40.0 ± 4.4] fb

Table 10.5: Values of the absolute differential cross-section as a function of $|\Delta\eta(l,l)|$, divided by the bin width. The first and second associated uncertainties are the statistical and systematic uncertainties, respectively. The sum is calculated by adding the individual cross-sections multiplied by their corresponding bin width, and the uncertainty on the sum is estimated by adding the total statistical and systematic uncertainties in quadrature.

$\|\Delta\eta(l,l)\|$	$d\sigma/dx$ ± (stat.) ± (syst.) [fb]
0.00 – 0.30	19.4 ± 1.3 ± 1.1
0.30 – 0.60	17.4 ± 1.3 ± 0.9
0.60 – 0.90	20.9 ± 1.4 ± 1.4
0.90 – 1.20	17.2 ± 1.3 ± 0.9
1.20 – 1.50	14.7 ± 1.2 ± 0.9
1.50 – 1.80	12.3 ± 1.1 ± 1.2
1.80 – 2.20	9.05 ± 0.80 ± 0.64
2.20 – 5.00	1.97 ± 0.15 ± 0.18
Sum	[39.7 ± 4.0] fb

Table 10.6: Summary of the sources of uncertainty on the absolute differential cross-section as a function of $p_T(\gamma)$, presented as a percentage of the measured cross-section in each bin.

$p_T(\gamma)$ [Gev]	20.0 - 25.0	25.0 - 30.0	30.0 - 35.0	35.0 - 40.0	40.0 - 47.0	47.0 - 55.0
Source	systematic uncertainty (%)					
Signal modelling	±3.4	±5.5	±4.9	±4.2	±9.3	±3.7
Exp. systematics	±5.1	±4.3	±4.0	±4.3	±3.8	±3.6
Bkg. modelling	±9.4	±3.9	±2.7	±2.2	±2.0	±2.0
Total systematics	±11	±8	±7	±6	±10	±6
Data statistics	±7	±7	±8	±8	±8	±9
Total uncertainty	±13	±10	±10	±10	±13	±11

$p_T(\gamma)$ [Gev]	55.0 - 70.0	70.0 - 85.0	85.0 - 132.0	132.0 - 180.0	180.0 - 300.0
Source	systematic uncertainty (%)				
Signal modelling	±1.1	±4.0	±11.0	±2.3	±5.0
Exp. systematics	±3.6	±4.2	±3.4	±3.4	±3.7
Bkg. modelling	±1.7	±2.1	±2.2	±2.2	±2.2
Total systematics	±4	±6	±12	±5	±6
Data statistics	±8	±11	±9	±14	±14
Total uncertainty	±9	±13	±15	±15	±16

Table 10.7: Summary of the sources of uncertainty on the absolute differential cross-section as a function of $|\eta(\gamma)|$, presented as a percentage of the measured cross-section in each bin.

$\lvert\eta(\gamma)\rvert$	0.0 - 0.2	0.2 - 0.4	0.4 - 0.6	0.6 - 0.8	0.8 - 1.0	1.0 - 1.2	1.2 - 1.7
Source	systematic uncertainty (%)						
Signal modelling	±1.6	±2.8	±6.2	±6.3	±2.5	±5.6	±2.8
Exp. systematics	±3.5	±3.6	±3.7	±3.8	±3.9	±4.0	±4.4
Bkg. modelling	±1.1	±1.2	±1.5	±2.0	±3.5	±4.1	±4.9
Total systematics	±4	±5	±7	±7	±5	±8	±7
Data statistics	±7	±7	±7	±7	±8	±9	±7
Total uncertainty	±8	±8	±10	±10	±10	±12	±10

$\lvert\eta(\gamma)\rvert$	1.7 - 2.37
Source	systematic uncertainty (%)
Signal modelling	±3.9
Exp. systematics	±4.6
Bkg. modelling	±6.5
Total systematics	±9
Data statistics	±8
Total uncertainty	±12

Table 10.8: Summary of the sources of uncertainty on the absolute differential cross-section as a function of $\Delta R(\gamma, l)_{\text{min}}$, presented as a percentage of the measured cross-section in each bin.

$\Delta R(\gamma, l)_{\text{min}}$	0.4 - 0.55	0.55 - 0.7	0.7 - 0.85	0.85 - 1.0	1.0 - 1.3	1.3 - 1.6	1.6 - 1.9
Source	systematic uncertainty (%)						
Signal modelling	±5.3	±3.5	±1.5	±8.2	±4.1	±2.9	±3.5
Exp. systematics	±3.6	±3.8	±3.6	±3.5	±3.7	±4.1	±3.9
Bkg. modelling	±0.88	±1.3	±1.4	±1.9	±3.2	±4.0	±4.2
Total systematics	±6	±5	±4	±9	±6	±6	±7
Data statistics	±7	±8	±9	±10	±7	±8	±8
Total uncertainty	±10	±9	±10	±14	±9	±10	±10

$\Delta R(\gamma, l)_{\text{min}}$	1.9 - 2.3	2.3 - 2.7	2.7 - 5.0
Source	systematic uncertainty (%)		
Signal modelling	±3.9	±2.1	±7.7
Exp. systematics	±4.3	±4.2	±5.5
Bkg. modelling	±5.7	±8.2	±16.0
Total systematics	±8	±9	±19
Data statistics	±8	±11	±12
Total uncertainty	±11	±14	±23

Table 10.9: Summary of the sources of uncertainty on the absolute differential cross-section as a function of $\Delta\phi(l,l)$, presented as a percentage of the measured cross-section in each bin.

$\Delta\phi(l,l)$	0.0 - 0.6	0.6 - 1.2	1.2 - 1.6	1.6 - 1.9	1.9 - 2.2	2.2 - 2.4	2.4 - 2.6
Source	systematic uncertainty (%)						
Signal modelling	±6.9	±1.1	±4.2	±5.1	±2.4	±3.3	±7.0
Exp. systematics	±4.4	±4.2	±4.0	±3.6	±3.5	±4.1	±3.7
Bkg. modelling	±6.2	±4.3	±3.9	±3.1	±2.4	±2.6	±2.3
Total systematics	±10	±6	±7	±7	±5	±6	±8
Data statistics	±9	±7	±9	±8	±8	±9	±9
Total uncertainty	±13	±9	±11	±11	±9	±11	±12

$\Delta\phi(l,l)$	2.6 - 2.8	2.8 - 3.0	3.0 - 3.14
Source	systematic uncertainty (%)		
Signal modelling	±5.9	±3.5	±5.8
Exp. systematics	±4.0	±3.7	±4.5
Bkg. modelling	±2.5	±2.4	±2.1
Total systematics	±7	±6	±7
Data statistics	±9	±9	±10
Total uncertainty	±12	±10	±12

Table 10.10: Summary of the sources of uncertainty on the absolute differential cross-section as a function of $|\Delta\eta(l,l)|$, presented as a percentage of the measured cross-section in each bin.

$\lvert\Delta\eta(l,l)\rvert$	0.0 - 0.3	0.3 - 0.6	0.6 - 0.9	0.9 - 1.2	1.2 - 1.5	1.5 - 1.8	1.8 - 2.2
Source	systematic uncertainty (%)						
Signal modelling	±1.9	±2.0	±4.1	±2.4	±4.2	±8.4	±5.3
Exp. systematics	±4.0	±3.7	±3.8	±3.9	±3.8	±3.9	±4.0
Bkg. modelling	±3.4	±3.3	±3.3	±2.8	±2.7	±2.9	±2.6
Total systematics	±6	±5	±7	±5	±6	±10	±7
Data statistics	±7	±7	±7	±7	±8	±9	±9
Total uncertainty	±9	±9	±9	±9	±10	±13	±11

$\lvert\Delta\eta(l,l)\rvert$	2.2 - 5.0
Source	systematic uncertainty (%)
Signal modelling	±8.1
Exp. systematics	±4.4
Bkg. modelling	±2.4
Total systematics	±9
Data statistics	±7
Total uncertainty	±12

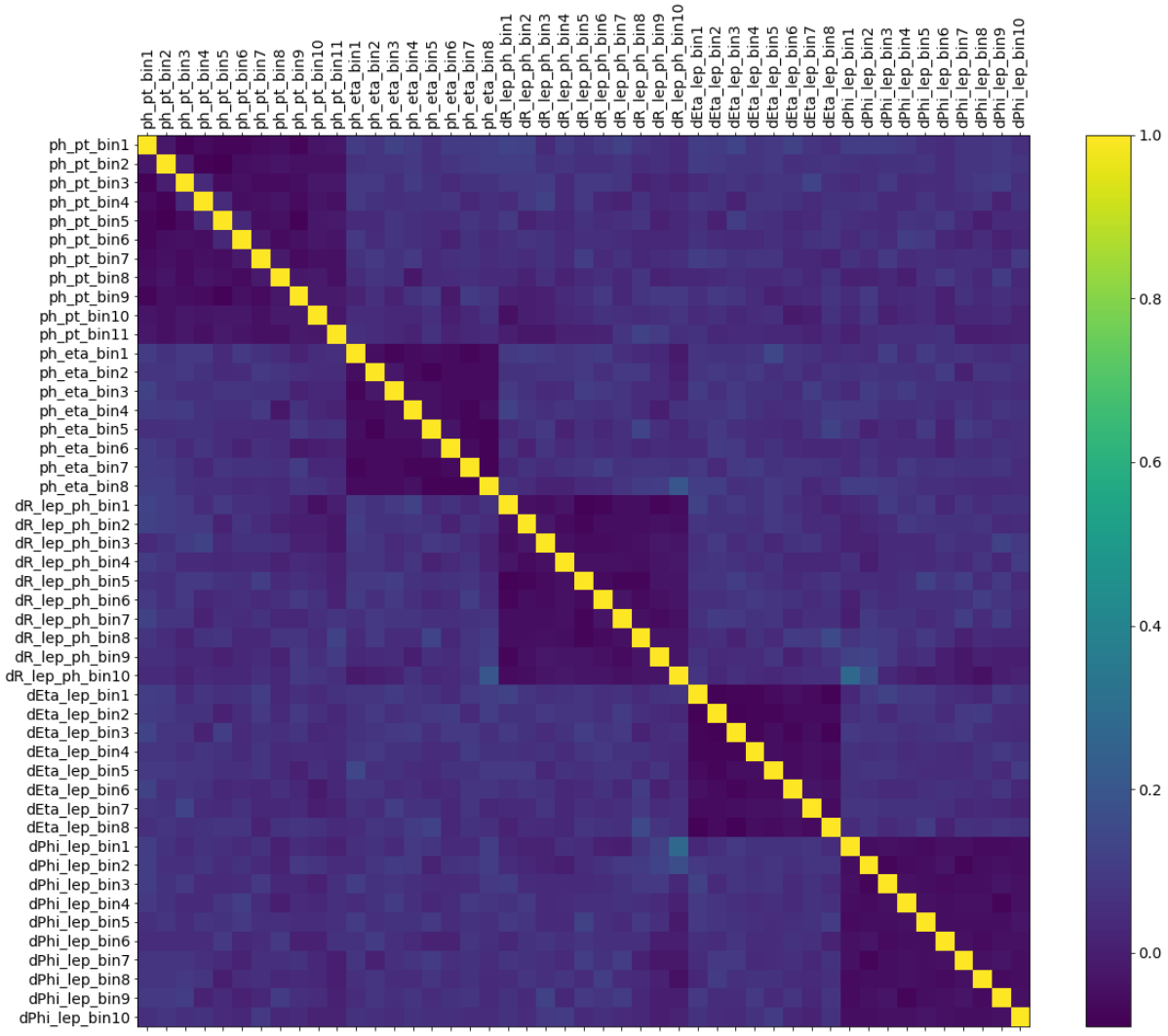

Figure 10.4: Statistical correlation matrix of the absolute fiducial cross-sections, estimated with the bootstrap method. Each bin is represented as < name >_bin< number >, where the *name* tag denotes the observable's name with ph_pt, ph_eta, dR_lep_ph, dEta_lep, and dPhi_lep referring to $p_T(\gamma)$, $|\eta(\gamma)|$, $\Delta R(\gamma, l)_{\text{min}}$, $|\Delta\eta(l, l)|$ and $\Delta\phi(l, l)$, respectively. The *number* tag indicates the bin's number of the respective observable.

Table 10.11: χ^2/ndf and the corresponding p-values between the measured absolute cross-sections and the NLO prediction.

Observable	Theory NLO	
	χ^2/ndf	p-value
$p_T(\gamma)$	6.1/11	0.87
$\lvert\eta(\gamma)\rvert$	4.5/8	0.81
$\Delta R(\gamma, l)_{\text{min}}$	11.7/10	0.31
$\Delta\phi(l, l)$	5.8/10	0.83
$\lvert\Delta\eta(l, l)\rvert$	6.2/8	0.62

10.2 Normalised cross-section measurements

The unfolded distributions are normalised to their total integrals to benefit from the cancellation of the normalisation components in the corresponding systematics while keeping the components that change only the shapes of the distributions. The normalised fiducial differential cross-sections and the contribution of each category of systematic uncertainties as functions of $p_T(\gamma)$, $|\eta(\gamma)|$, $\Delta R(\gamma, l)_{\text{min}}$, $\Delta\phi(l, l)$ and $|\Delta\eta(l, l)|$ are shown in Figs. 10.5–10.7. The top-row subfigures show the normalised cross-sections of unfolded data compared to the latest NLO theory prediction [9] as well as state-of-the-art MC predictions of the combined $t\bar{t}\gamma + tW\gamma$ process, where the latter are generated at LO with MadGraph5_aMC@NLO and interfaced with Pythia 8 and Herwig 7. The corresponding shaded bands represent the statistical and the total uncertainties. The bottom-row subfigures display the decomposition of the systematic uncertainties and the statistical ones. The size of the uncertainties is reduced compared to those of the absolute cross-sections in Figs. 10.1–10.3. As mentioned earlier, this is due to the cancellation of the normalisation components of the respective sources of uncertainties while the shape components are kept. Similar to the absolute cross-sections, the normalised distributions in the figures show the number of events divided by the bin width, and they do not include the overflow for $p_T(\gamma)$, whereas for the rest of the distributions, the higher boundary of the last bin is limited by the physical value. The shape of the measured distributions as functions of $p_T(\gamma)$, $|\eta(\gamma)|$, and $|\Delta\eta(l, l)|$ shows a good agreement between the unfolded data and the predictions within uncertainties. The NLO theory prediction well describes the shape of the measured distributions as functions of $\Delta R(\gamma, l)_{\text{min}}$ and $\Delta\phi(l, l)$, while the LO MC simulations do not model such shape perfectly. Both simulations of MadGraph5_aMC@NLO interfaced with Pythia 8 and Herwig 7, exhibit similar behaviour in modelling the data, which weakens the possibility that the mis-modelling is caused due to the showering algorithm.

The values of the normalised cross-sections and their associated uncertainties are listed in Tables 10.12–10.16. Similar to the absolute cross-sections, the statistical uncertainty is the principal source, while the signal and background modelling dominate the systematic uncertainty.

The size of the systematic and statistical uncertainties are displayed in Tables 10.17–10.21. The total uncertainty is roughly in the range of 8%-10% for most of the normalised cross-sections of all variables (compared to 8%-12% for the absolute cross-sections). At high values of $p_T(\gamma)$ and $\Delta R(\gamma, l)_{\text{min}}$, it goes higher up to 15% and 21%, respectively (compared to 16% and 23% for the $p_T(\gamma)$ and $\Delta R(\gamma, l)_{\text{min}}$ absolute cross-sections, respectively).

The statistical correlation matrix of the normalised cross-sections of all observables, which is estimated using the bootstrap method, is shown in Fig. 10.8, where no significant correlation between different bins is observed. The full correlation matrices of the normalised cross-sections as functions of all observables are shown in Appendix B.

The agreement between the unfolded data and the predictions for the normalised cross-sections is quantified using Eq. (10.1) with one ndf less by removing the last bin in the χ^2 calculation.

The χ^2/ndf and the corresponding p-values for the normalised cross-sections are shown in Table 10.22. The p-values between the data and the NLO prediction confirm the good agreement between them for all the observables. Similarly, the p-values for the $p_T(\gamma)$, $|\eta(\gamma)|$, and $|\Delta\eta(l,l)|$ show a good agreement between the data and the MC predictions. However, for the $\Delta R(\gamma,l)_{\text{min}}$ and $\Delta\phi(l,l)$, the p-values between the data and the MC predictions are very low (close to zero). These values verify that the modelling by the MC predictions is not perfectly compatible with the unfolded data for these observables.

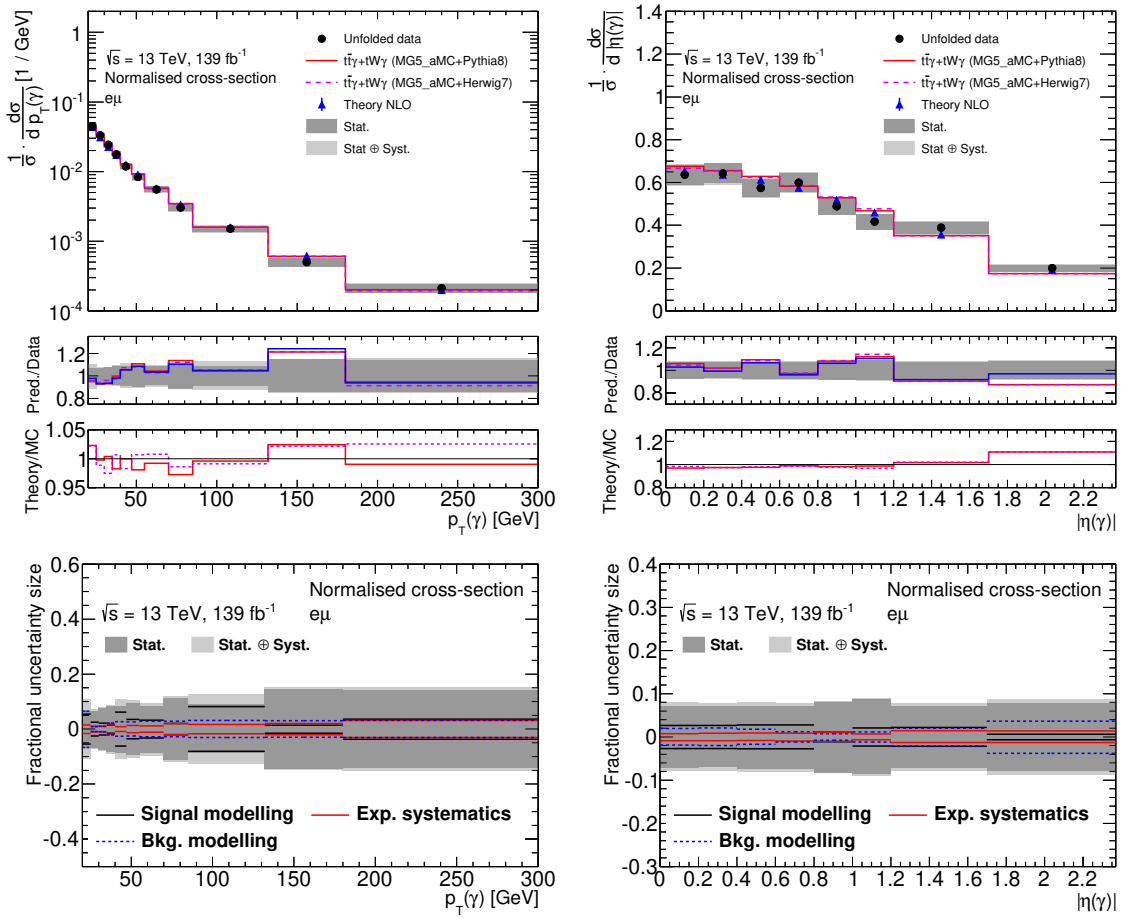

Figure 10.5: Distributions of the normalised fiducial differential cross-sections as functions of $p_T(\gamma)$ and $|\eta(\gamma)|$ in the top row where unfolded data are compared to the NLO theory prediction [9], as well MC predictions at LO which are generated with MadGraph5_aMC@NLO and interfaced with Pythia 8 and Herwig 7. In the bottom row the statistical and systematic uncertainties are shown as fractions of the cross-section in each bin where the systematic uncertainties are decomposed into three categories: signal, background, and experimental.

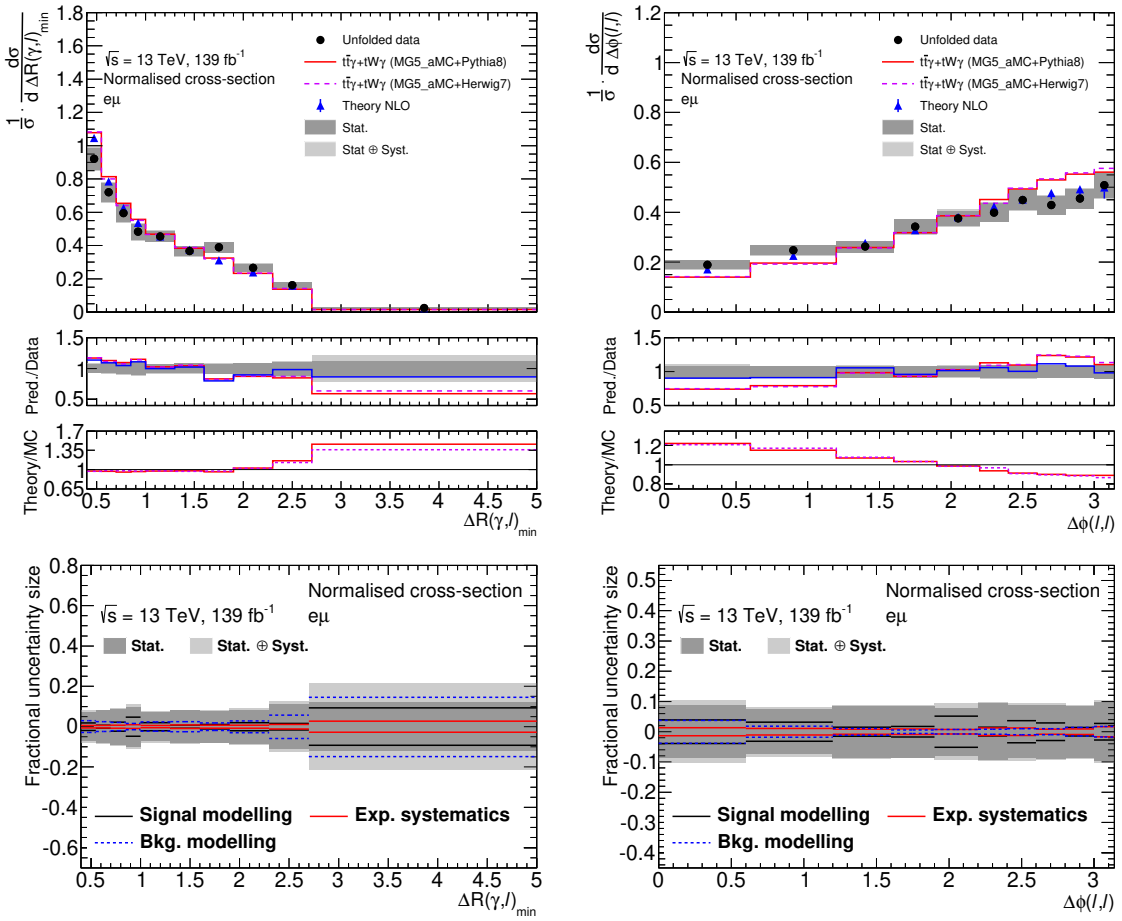

Figure 10.6: Distributions of the normalised fiducial differential cross-sections as functions of $\Delta R(\gamma, l)_{\text{min}}$ and $\Delta\phi(l, l)$ in the top row where unfolded data are compared to the NLO theory prediction [9], as well MC predictions at LO which are generated with MadGraph5_aMC@NLO and interfaced with Pythia 8 and Herwig 7. In the bottom row the statistical and systematic uncertainties are shown as fractions of the cross-section in each bin where the systematic uncertainties are decomposed into three categories: signal, background, and experimental.

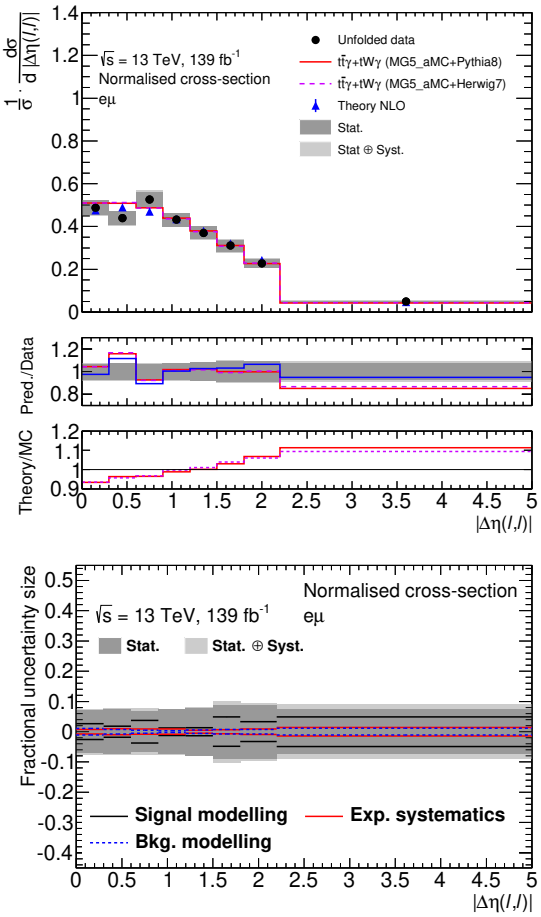

Figure 10.7: Distribution of the normalised fiducial differential cross-section as a function of $|\Delta\eta(l,l)|$ in the top row where unfolded data are compared to the NLO theory prediction [9], as well MC predictions at LO which are generated with MadGraph5_aMC@NLO and interfaced with Pythia 8 and Herwig 7. In the bottom row the statistical and systematic uncertainties are shown as fractions of the cross-section in each bin where the systematic uncertainties are decomposed into three categories: signal, background, and experimental.

Table 10.12: Values of the normalised differential cross-section as a function of $p_T(\gamma)$, divided by the bin width. The first and second associated uncertainties are the statistical and systematic uncertainties, respectively.

$p_T(\gamma)$ [Gev]	$1/\sigma \cdot d\sigma/dx \pm$ (stat.) $\pm$ (syst.) [1/GeV]
20 – 25	0.0447 ± 0.0029 ± 0.0039
25 – 30	0.0333 ± 0.0022 ± 0.0009
30 – 35	0.0243 ± 0.0018 ± 0.0006
35 – 40	0.0177 ± 0.0015 ± 0.0006
40 – 47	0.0119 ± 0.0010 ± 0.0008
47 – 55	0.00836 ± 0.00079 ± 0.00038
55 – 70	0.00554 ± 0.00047 ± 0.00025
70 – 85	0.00305 ± 0.00034 ± 0.00012
85 – 132	0.00151 ± 0.00013 ± 0.00013
132 – 180	0.000501 ± 0.000072 ± 0.000019
180 – 300	0.000212 ± 0.000029 ± 0.000012

Table 10.13: Values of the normalised differential cross-section as a function of $|\eta(\gamma)|$, divided by the bin width. The first and second associated uncertainties are the statistical and systematic uncertainties, respectively.

$\lvert\eta(\gamma)\rvert$	$1/\sigma \cdot d\sigma/dx \pm$ (stat.) $\pm$ (syst.)
0.00 – 0.20	0.637 ± 0.045 ± 0.022
0.20 – 0.40	0.642 ± 0.045 ± 0.022
0.40 – 0.60	0.575 ± 0.042 ± 0.020
0.60 – 0.80	0.600 ± 0.044 ± 0.019
0.80 – 1.00	0.489 ± 0.040 ± 0.008
1.00 – 1.20	0.418 ± 0.036 ± 0.010
1.20 – 1.70	0.389 ± 0.028 ± 0.013
1.70 – 2.37	0.199 ± 0.015 ± 0.008

Table 10.14: Values of the normalised differential cross-section as a function of $\Delta R(\gamma, l)_{\text{min}}$, divided by the bin width. The first and second associated uncertainties are the statistical and systematic uncertainties, respectively.

$\Delta R(\gamma, l)_{\text{min}}$	$1/\sigma \cdot \mathrm{d}\sigma/\mathrm{d}x \pm$ (stat.) $\pm$ (syst.)
0.40 – 0.55	0.921 ± 0.066 ± 0.032
0.55 – 0.70	0.720 ± 0.057 ± 0.019
0.70 – 0.85	0.596 ± 0.053 ± 0.019
0.85 – 1.00	0.484 ± 0.048 ± 0.024
1.00 – 1.30	0.455 ± 0.032 ± 0.014
1.30 – 1.60	0.367 ± 0.029 ± 0.010
1.60 – 1.90	0.390 ± 0.030 ± 0.009
1.90 – 2.30	0.267 ± 0.022 ± 0.009
2.30 – 2.70	0.162 ± 0.018 ± 0.010
2.70 – 5.00	0.0248 ± 0.0029 ± 0.0043

Table 10.15: Values of the normalised differential cross-section as a function of $\Delta\phi(l, l)$, divided by the bin width. The first and second associated uncertainties are the statistical and systematic uncertainties, respectively.

$\Delta\phi(l, l)$	$1/\sigma \cdot \mathrm{d}\sigma/\mathrm{d}x \pm$ (stat.) $\pm$ (syst.)
0.00 – 0.60	0.190 ± 0.016 ± 0.011
0.60 – 1.20	0.247 ± 0.018 ± 0.009
1.20 – 1.60	0.262 ± 0.022 ± 0.005
1.60 – 1.90	0.342 ± 0.029 ± 0.007
1.90 – 2.20	0.376 ± 0.029 ± 0.020
2.20 – 2.40	0.399 ± 0.038 ± 0.008
2.40 – 2.60	0.449 ± 0.039 ± 0.018
2.60 – 2.80	0.428 ± 0.038 ± 0.014
2.80 – 3.00	0.455 ± 0.039 ± 0.010
3.00 – 3.14	0.508 ± 0.049 ± 0.018

Table 10.16: Values of the normalised differential cross-section as a function of $|\Delta\eta(l,l)|$, divided by the bin width. The first and second associated uncertainties are the statistical and systematic uncertainties, respectively.

$\lvert\Delta\eta(l,l)\rvert$	$1/\sigma \cdot \mathrm{d}\sigma/\mathrm{d}x \pm$ (stat.) $\pm$ (syst.)
0.00 – 0.30	0.488 ± 0.034 ± 0.014
0.30 – 0.60	0.439 ± 0.032 ± 0.010
0.60 – 0.90	0.527 ± 0.035 ± 0.020
0.90 – 1.20	0.432 ± 0.032 ± 0.007
1.20 – 1.50	0.370 ± 0.029 ± 0.006
1.50 – 1.80	0.311 ± 0.027 ± 0.015
1.80 – 2.20	0.228 ± 0.020 ± 0.008
2.20 – 5.00	0.0496 ± 0.0037 ± 0.0026

Table 10.17: Summary of the sources of uncertainty on the normalised differential cross-section as a function of $p_T(\gamma)$, presented as a percentage of the measured cross-section in each bin.

$p_T(\gamma)$ [Gev]	20.0 - 25.0	25.0 - 30.0	30.0 - 35.0	35.0 - 40.0	40.0 - 47.0	47.0 - 55.0
Source	systematic uncertainty (%)					
Signal modelling	±5.5	±2.5	±2.1	±1.5	±6.2	±3.6
Exp. systematics	±1.6	±1.0	±0.98	±1.9	±0.9	±1.3
Bkg. modelling	±6.7	±0.9	±1.0	±2.2	±2.6	±2.5
Total systematics	±9	±3	±3	±3	±7	±5
Data statistics	±7	±7	±8	±8	±8	±9
Total uncertainty	±11	±7	±8	±9	±11	±10

$p_T(\gamma)$ [Gev]	55.0 - 70.0	70.0 - 85.0	85.0 - 132.0	132.0 - 180.0	180.0 - 300.0
Source	systematic uncertainty (%)				
Signal modelling	±3.3	±2.1	±8.1	±1.5	±3.7
Exp. systematics	±1.1	±2.0	±1.7	±2.0	±3.1
Bkg. modelling	±2.8	±2.8	±3.1	±3.0	±3.1
Total systematics	±5	±4	±9	±4	±6
Data statistics	±8	±11	±9	±14	±14
Total uncertainty	±10	±12	±13	±15	±15

Table 10.18: Summary of the sources of uncertainty on the normalised differential cross-section as a function of $|\eta(\gamma)|$, presented as a percentage of the measured cross-section in each bin.

$\lvert\eta(\gamma)\rvert$	0.0 - 0.2	0.2 - 0.4	0.4 - 0.6	0.6 - 0.8	0.8 - 1.0	1.0 - 1.2	1.2 - 1.7
Source	systematic uncertainty (%)						
Signal modelling	±2.7	±2.7	±2.8	±2.8	±1.1	±2.1	±2.2
Exp. systematics	±0.86	±0.91	±0.85	±0.95	±0.98	±0.68	±1.3
Bkg. modelling	±1.9	±2.0	±1.7	±1.2	±0.75	±1.2	±2.1
Total systematics	±3	±4	±3	±3	±2	±3	±3
Data statistics	±7	±7	±7	±7	±8	±9	±7
Total uncertainty	±8	±8	±8	±8	±8	±9	±8

$\lvert\eta(\gamma)\rvert$	1.7 - 2.37
Source	systematic uncertainty (%)
Signal modelling	±0.68
Exp. systematics	±1.3
Bkg. modelling	±3.8
Total systematics	±4
Data statistics	±8
Total uncertainty	±9

Table 10.19: Summary of the sources of uncertainty on the normalised differential cross-section as a function of $\Delta R(\gamma, l)_{\text{min}}$, presented as a percentage of the measured cross-section in each bin.

$\Delta R(\gamma, l)_{\text{min}}$	0.4 - 0.55	0.55 - 0.7	0.7 - 0.85	0.85 - 1.0	1.0 - 1.3	1.3 - 1.6	1.6 - 1.9
Source	systematic uncertainty (%)						
Signal modelling	±1.8	±0.75	±2.2	±4.7	±2.0	±0.78	±1.1
Exp. systematics	±0.61	±0.59	±0.8	±0.93	±0.56	±0.87	±0.73
Bkg. modelling	±2.8	±2.4	±2.0	±1.5	±2.3	±2.5	±1.9
Total systematics	±4	±3	±3	±5	±3	±3	±2
Data statistics	±7	±8	±9	±10	±7	±8	±8
Total uncertainty	±8	±8	±9	±11	±8	±8	±8

$\Delta R(\gamma, l)_{\text{min}}$	1.9 - 2.3	2.3 - 2.7	2.7 - 5.0
Source	systematic uncertainty (%)		
Signal modelling	±2.0	±1.6	±9.3
Exp. systematics	±0.75	±1.1	±2.7
Bkg. modelling	±3.0	±5.8	±15.0
Total systematics	±4	±6	±17
Data statistics	±8	±11	±12
Total uncertainty	±9	±12	±21

Table 10.20: Summary of the sources of uncertainty on the normalised differential cross-section as a function of $\Delta\phi(l,l)$, presented as a percentage of the measured cross-section in each bin.

$\Delta\phi(l,l)$	0.0 - 0.6	0.6 - 1.2	1.2 - 1.6	1.6 - 1.9	1.9 - 2.2	2.2 - 2.4	2.4 - 2.6
Source	systematic uncertainty (%)						
Signal modelling	±3.9	±3.1	±1.5	±1.7	±5.2	±1.4	±3.6
Exp. systematics	±1.3	±1.1	±0.84	±0.92	±0.76	±1.2	±1.3
Bkg. modelling	±3.8	±1.9	±1.1	±0.6	±0.72	±0.81	±0.98
Total systematics	±6	±4	±2	±2	±5	±2	±4
Data statistics	±9	±7	±9	±8	±8	±9	±9
Total uncertainty	±10	±8	±9	±9	±9	±10	±10

$\Delta\phi(l,l)$	2.6 - 2.8	2.8 - 3.0	3.0 - 3.14
Source	systematic uncertainty (%)		
Signal modelling	±2.9	±1.4	±2.7
Exp. systematics	±0.82	±0.92	±1.6
Bkg. modelling	±0.98	±1.4	±1.7
Total systematics	±3	±2	±4
Data statistics	±9	±9	±10
Total uncertainty	±9	±9	±10

Table 10.21: Summary of the sources of uncertainty on the normalised differential cross-section as a function of $|\Delta\eta(l,l)|$, presented as a percentage of the measured cross-section in each bin.

$\lvert\Delta\eta(l,l)\rvert$	0.0 - 0.3	0.3 - 0.6	0.6 - 0.9	0.9 - 1.2	1.2 - 1.5	1.5 - 1.8	1.8 - 2.2
Source	systematic uncertainty (%)						
Signal modelling	±2.6	±1.8	±3.7	±1.2	±1.3	±4.9	±3.3
Exp. systematics	±0.75	±0.98	±0.87	±0.87	±0.52	±0.63	±0.88
Bkg. modelling	±1.1	±0.79	±0.53	±0.29	±0.58	±0.77	±0.76
Total systematics	±3	±2	±4	±2	±2	±5	±4
Data statistics	±7	±7	±7	±7	±8	±9	±9
Total uncertainty	±8	±8	±8	±8	±8	±10	±10

$\lvert\Delta\eta(l,l)\rvert$	2.2 - 5.0
Source	systematic uncertainty (%)
Signal modelling	±4.9
Exp. systematics	±1.4
Bkg. modelling	±1.1
Total systematics	±5
Data statistics	±7
Total uncertainty	±9

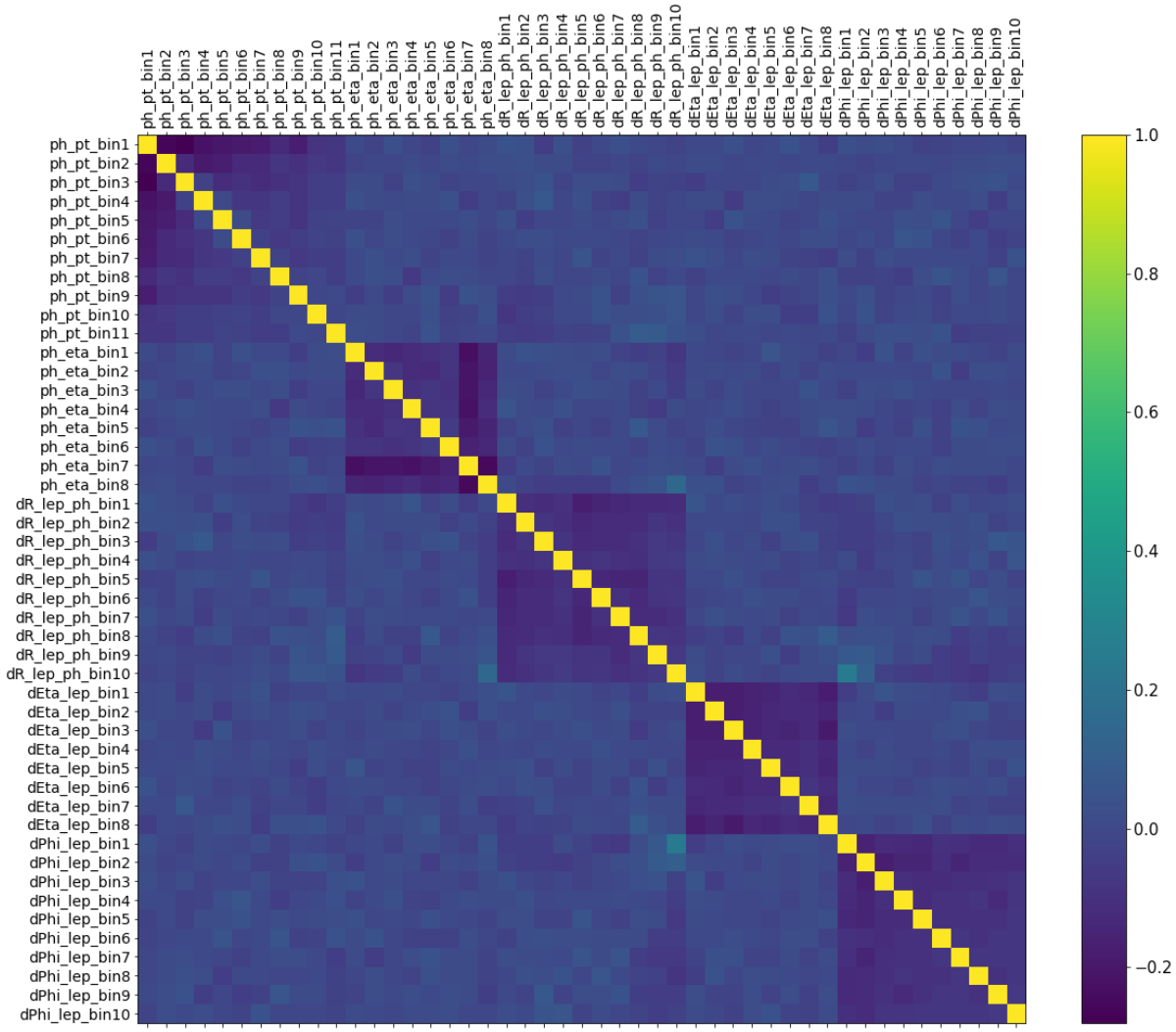

Figure 10.8: Statistical correlation matrix of the normalised fiducial cross-sections, estimated with the bootstrap method. Each bin is represented as < name >_bin< number >, where the *name* tag denotes the observable's name with ph_pt, ph_eta, dR_lep_ph, dEta_lep, and dPhi_lep referring to $p_T(\gamma)$, $|\eta(\gamma)|$, $\Delta R(\gamma, l)_{\text{min}}$, $|\Delta\eta(l, l)|$ and $\Delta\phi(l, l)$, respectively. The *number* tag indicates the bin's number of the respective observable.

Table 10.22: χ^2/ndf and the corresponding p-values between the measured normalised cross-sections and the MC predictions as well as the NLO theory calculation.

Observable	MG5_aMC+Pythia8		MG5_aMC+Herwig7		Theory NLO	
	χ^2/ndf	p-value	χ^2/ndf	p-value	χ^2/ndf	p-value
$p_T(\gamma)$	6.3/10	0.79	5.3/10	0.87	6.0/10	0.82
$\lvert\eta(\gamma)\rvert$	7.3/7	0.40	7.7/7	0.36	4.5/7	0.72
$\Delta R(\gamma, l)_{\text{min}}$	20.1/9	0.02	18.9/9	0.03	13.5/9	0.14
$\Delta\phi(l, l)$	30.8/9	<0.01	31.6/9	<0.01	5.8/9	0.76
$\lvert\Delta\eta(l, l)\rvert$	6.5/7	0.48	6.8/7	0.45	5.6/7	0.59

CHAPTER 11

Conclusions and outlook

This work presents differential cross-section measurements of the combined $t\bar{t}\gamma + tW\gamma$ process in the $e\mu$ decay channel. The measurements are performed in this decay channel due to its high signal purity and to compare with the most recent theory calculation at NLO in QCD [9]. The data used in this work were collected by the ATLAS detector at the LHC in pp collisions at $\sqrt{s} = 13$ TeV, with an integrated luminosity of $139\,\text{fb}^{-1}$.

The signal region of the measurements is characterised by the presence of exactly one hard photon, one electron and one muon of opposite charge, at least two jets among which at least one is b-tagged, and missing transverse energy. The reconstructed distributions of data are corrected for acceptance and efficiencies of the detector using the IBS unfolding method. The performance of the IBS method is tested and optimised, leading to a reliable unfolding procedure.

The differential measurements are performed in a fiducial phase space at parton level, as functions of $\mathrm{p_T}(\gamma)$, $|\eta(\gamma)|$, $\Delta R(\gamma, l)_{\text{min}}$, $\Delta\phi(l, l)$, and $|\Delta\eta(l, l)|$. Fiducial phase-space requirements mimic the selection in the dedicated theoretical calculation, provided by the authors of Ref. [9].

For the first time, the combined $t\bar{t}\gamma + tW\gamma$ cross-section measurements are compared to a full calculation at NLO in QCD, including resonant and non-resonant contributions and off-shell effects. Furthermore, the measurements are compared to state-of-the-art MC simulations at LO in QCD. They are found to be in good agreement with the calculation and the MC simulations within uncertainties. The overall shape of the measured distributions is described better by the calculation than the MC simulations, especially for the $\Delta R(\gamma, l)_{\text{min}}$ and $\Delta\phi(l, l)$ distributions.

The precision of the results presented here surpasses that of the differential measurements performed at an integrated luminosity of $36\,\text{fb}^{-1}$ [7]. However, results can not be directly compared since they are performed in a different fiducial phase space. The results have overall total uncertainties of approximately 8%-12% and 8%-10% for most absolute and normalised differential cross-sections, respectively. Only in regions with a small number of events, such as at high values of $\mathrm{p_T}(\gamma)$ and $\Delta R(\gamma, l)_{\text{min}}$, the total uncertainty increases

to 16% and 23%, respectively, for the absolute cross-sections and 15% and 21%, for the normalised ones. Statistical uncertainties limit the precision of the measurements, whereas signal and background modelling dominate the systematic uncertainties.

The measurements presented here are compared with the NLO theory calculation focusing on the $e\mu$ channel. The statistical uncertainty for future measurements, being the limiting factor, can be reduced by including more decay channels, with minor background contaminations, such as the ee and $\mu\mu$ channels, i.e. performing the measurements in the full dilepton channel. Despite having relatively small BRs, these decay channels combined, i.e. ee and $\mu\mu$, would still double the number of collected data events. Furthermore, having a small background contribution would mean that the uncertainties related to background processes will not outperform the possible decrease in the statistical uncertainty. Moreover, systematic uncertainties of the measurements presented in this work approach in size the statistical ones. Hence, using an unfolding procedure that correlates the sources of uncertainties, e.g. employing a fit where the uncertainties are included as nuisance parameters, can lessen such systematic uncertainties. For example, techniques such as a likelihood profiling based on HistFitter [116] and Fully Bayesian Unfolding [117] offer such advantage.

The modelling of $\Delta R(\gamma, l)_{\text{min}}$ and $\Delta\phi(l, l)$ distributions by the MC simulations at LO in QCD requires further investigation, and higher-order corrections are needed to describe the data better. Additionally, other measurements can be performed using the full Run 2 data in the single lepton and dilepton channels. Such measurements with a large number of data events can unravel the possibility to perform double-differential measurements, for example, as a function of $\text{p}_\text{T}(\gamma)$ in different $|\eta(\gamma)|$ regions. These measurements are sensitive to the gluon parton distribution functions.

The differential measurements can be interpreted in effective field theories by testing higher-dimensional operators sensitive to the $t\bar{t}\gamma$ vertex [39]. Such an interpretation would be a stringent test to SM predictions where any deviation would point to new physics.

Bibliography

[1] CDF Collaboration, *Observation of Top Quark Production in $\bar{p}p$ Collisions with the Collider Detector at Fermilab*, Phys. Rev. Lett. **74** (14 1995) 2626 (cit. on p. 1).

[2] D0 Collaboration, *Observation of the Top Quark*, Phys. Rev. Lett. **74** (14 1995) 2632 (cit. on p. 1).

[3] CDF Collaboration, *Evidence for $t\bar{t}\gamma$ production and measurement of $\sigma_{t\bar{t}\gamma}/\sigma_{t\bar{t}}$*, Phys. Rev. D **84** (2011) (cit. on p. 1).

[4] ATLAS Collaboration, *Observation of top-quark pair production in association with a photon and measurement of the $t\bar{t}\gamma$ production cross section in pp collisions at $\sqrt{s}$ = 7 TeV using the ATLAS detector*, Phys. Rev. D **91** (7 2015) 072007 (cit. on p. 1).

[5] ATLAS Collaboration, *Measurement of the $t\bar{t}\gamma$ production cross section in proton-proton collisions at $\sqrt{s}$ = 8 TeV with the ATLAS detector*, JHEP **11** (2017) 086, arXiv: 1706.03046 [hep-ex] (cit. on p. 1).

[6] CMS Collaboration, *Measurement of the semileptonic $t\bar{t}+\gamma$ production cross section in pp collisions at $\sqrt{s}$ = 8 TeV*, JHEP **10** (2017) 006, arXiv: 1706.08128 [hep-ex] (cit. on p. 1).

[7] ATLAS Collaboration, *Measurements of inclusive and differential fiducial cross-sections of $t\bar{t}\gamma$ production in leptonic final states at $\sqrt{s}$ = 13 TeV in ATLAS*, Eur. Phys. J. C **79** (2019), arXiv: 1812.01697 [hep-ex] (cit. on pp. 1, 58, 119).

[8] ATLAS Collaboration, *Measurements of inclusive and differential cross-sections of combined $t\bar{t}\gamma$ and $tW\gamma$ production in the $e\mu$ channel at 13 TeV with the ATLAS detector*, JHEP **09** (2020) 049, arXiv: 2007.06946 [hep-ex] (cit. on pp. 2, 95).

[9] G. Bevilacqua et al., *Hard photons in hadroproduction of top quarks with realistic final states*, JHEP **10** (2018) 158, arXiv: 1803.09916 [hep-ph] (cit. on pp. 2, 12–14, 51, 57, 61, 62, 95, 97–99, 107–110, 119).

[10] H. D. Politzer, *Reliable Perturbative Results for Strong Interactions?*, Phys. Rev. Lett. **30** (26 1973) 1346 (cit. on p. 3).

[11] D. J. Gross and F. Wilczek, *Asymptotically Free Gauge Theories. I*, Phys. Rev. D **8** (10 1973) 3633 (cit. on p. 3).

[12] H. David Politzer, *Asymptotic freedom: An approach to strong interactions*, Phys. Rep. **14** (1974) 129 (cit. on p. 3).

[13] S. L. Glashow, *Partial-symmetries of weak interactions*, Nucl. Phys. **22** (1961) 579 (cit. on pp. 3, 6).

[14] A. Salam and J. C. Ward, *Electromagnetic and weak interactions*, Phys. Lett. **13** (1964) 168 (cit. on pp. 3, 6).

[15] S. Weinberg, *A Model of Leptons*, Phys. Rev. Lett. **19** (21 1967) 1264 (cit. on pp. 3, 6).

[16] Wikimedia Commons, *Standard Model of Elementary Particles and Gravity*, 2017, URL: https://commons.wikimedia.org/w/index.php?curid=59970304 (cit. on p. 4).

[17] M. Tanabashi et al., *Review of Particle Physics*, Phys. Rev. D **98** (2018) (cit. on pp. 6, 8).

[18] D. J. Gross and F. Wilczek, *Ultraviolet Behavior of Non-Abelian Gauge Theories*, Phys. Rev. Lett. **30** (1973) 1343 (cit. on p. 5).

[19] ALEPH Collaboration, CDF Collaboration, D0 Collaboration, DELPHI Collaboration, L3 Collaboration, OPAL Collaboration, SLD Collaboration, LEP Electroweak Working Group, Tevatron Electroweak Working Group, SLD electroweak and heavy flavour groups, *Precision Electroweak Measurements and Constraints on the Standard Model*, 2011, arXiv: 1012.2367 [hep-ex] (cit. on p. 7).

[20] P. W. Higgs, *Broken Symmetries and the Masses of Gauge Bosons*, Phys. Rev. Lett. **13** (16 1964) 508 (cit. on p. 7).

[21] P. W. Higgs, *Broken symmetries, massless particles and gauge fields*, Phys. Lett. **12** (1964) 132 (cit. on p. 7).

[22] F. Englert and R. Brout, *Broken Symmetry and the Mass of Gauge Vector Mesons*, Phys. Rev. Lett. **13** (9 1964) 321 (cit. on p. 7).

[23] G. S. Guralnik, C. R. Hagen and T. W. B. Kibble, *Global Conservation Laws and Massless Particles*, Phys. Rev. Lett. **13** (20 1964) 585 (cit. on p. 7).

[24] ATLAS Collaboration, *Observation of a new particle in the search for the Standard Model Higgs boson with the ATLAS detector at the LHC*, Phys. Lett. B **716** (2012) 1 (cit. on pp. 7, 17).

[25] CMS Collaboration, *Observation of a new boson at a mass of 125 GeV with the CMS experiment at the LHC*, Phys. Lett. B **716** (2012) 30 (cit. on pp. 7, 17).

[26] ATLAS, CDF, CMS and D0 Collaborations, *First combination of Tevatron and LHC measurements of the top-quark mass*, 2014, arXiv: 1403.4427 [hep-ex] (cit. on p. 7).

[27] J. C. Collins, D. E. Soper and G. F. Sterman,
Factorization of Hard Processes in QCD,
Adv. Ser. Direct. High Energy Phys. **5** (1989) 1, arXiv: hep-ph/0409313
(cit. on p. 7).

[28] J. D. Bjorken, *Asymptotic Sum Rules at Infinite Momentum*,
Phys. Rev. **179** (5 1969) 1547 (cit. on p. 7).

[29] J. D. Bjorken and E. A. Paschos,
Inelastic Electron-Proton and γ-Proton Scattering and the Structure of the Nucleon,
Phys. Rev. **185** (5 1969) 1975 (cit. on p. 7).

[30] R. P. Feynman, *Very High-Energy Collisions of Hadrons*,
Phys. Rev. Lett. **23** (24 1969) 1415 (cit. on p. 7).

[31] M. Czakon and A. Mitov, *Top++: A program for the calculation of the top-pair cross-section at hadron colliders*, Comput. Phys. Commun. **185** (2014) 2930,
arXiv: 1112.5675 [hep-ph] (cit. on pp. 8, 53).

[32] LHCTopWG,
NLO single-top channel cross sections: ATLAS-CMS recommended predictions for single-top cross sections using the Hathor v2.1 program (topic revision: r34), 2017,
URL: https://twiki.cern.ch/twiki/bin/view/LHCPhysics/SingleTopRefXsec
(cit. on p. 9).

[33] M. Aliev et al.,
HATHOR – HAdronic Top and Heavy quarks crOss section calculatoR,
Comput. Phys. Commun. **182** (2011) 1034, arXiv: 1007.1327 [hep-ph]
(cit. on p. 9).

[34] P. Kant et al., *HATHOR for single top-quark production: Updated predictions and uncertainty estimates for single top-quark production in hadronic collisions*,
Comput. Phys. Commun. **191** (2015) 74, arXiv: 1406.4403 [hep-ph] (cit. on p. 9).

[35] K. Olive, *Review of Particle Physics*, Chin. Phys. C **40** (2016) 100001 (cit. on p. 9).

[36] D0 Collaboration, *Useful Diagrams of Top Signals and Backgrounds*, 2011,
URL: https://www-d0.fnal.gov/Run2Physics/top/top_public_web_pages/top_feynman_diagrams.html (cit. on p. 10).

[37] S. M. Etesami, S. Khatibi and M. M. Najafabadi,
Measuring anomalous $WW\gamma$ and $t\bar{t}\gamma$ couplings using top+γ production at the LHC,
Eur. Phys. J. C **76** (2016), arXiv: 1606.02178 [hep-ex] (cit. on p. 10).

[38] U. Baur et al.,
Probing electroweak top quark couplings at hadron and lepton colliders,
Nucl. Phys. B Proc. Suppl. **160** (2006) 17, arXiv: hep-ph/0606264 (cit. on p. 10).

[39] O. Bessidskaia Bylund et al., *Probing top quark neutral couplings in the Standard Model Effective Field Theory at NLO in QCD*, JHEP **05** (2016) 052, arXiv: 1601.08193 [hep-ph] (cit. on pp. 10, 120).

[40] P.-F. Duan et al., *QCD corrections to associated production of $t\bar{t}\gamma$ at hadron colliders*, Phys. Rev. D **80** (1 2009) 014022 (cit. on p. 11).

[41] K. Melnikov, M. Schulze and A. Scharf, *QCD corrections to top quark pair production in association with a photon at hadron colliders*, Phys. Rev. D **83** (7 2011) 074013 (cit. on p. 11).

[42] V. S. Fadin, V. A. Khoze and A. D. Martin, *Interference radiative phenomena in the production of heavy unstable particles*, Phys. Rev. D **49** (5 1994) 2247 (cit. on p. 11).

[43] K. Melnikov and O. Yakovlev, *Top near threshold: all α_S corrections are trivial*, Phys. Lett. B **324** (1994) 217 (cit. on p. 11).

[44] K. Melnikov and O. Yakovlev, *Final state interaction in the production of heavy unstable particles*, Nucl. Phys. B **471** (1996) 90 (cit. on p. 11).

[45] S. Dulat et al., *New parton distribution functions from a global analysis of quantum chromodynamics*, Phys. Rev. D **93** (2016) 033006, arXiv: 1506.07443 [hep-ph] (cit. on p. 13).

[46] ATLAS Collaboration, *ATLAS detector and physics performance: Technical Design Report, 1*, CERN-LHCC-99-014, ATLAS-TDR-14, CERN, 1999, URL: https://cds.cern.ch/record/391176 (cit. on p. 15).

[47] *ATLAS detector and physics performance: Technical Design Report, 2*, CERN-LHCC-99-015, ATLAS-TDR-15, CERN, 1999, URL: https://cds.cern.ch/record/391177 (cit. on p. 15).

[48] CMS Collaboration, *CMS Physics: Technical Design Report Volume 1: Detector Performance and Software*, CERN-LHCC-2006-001, CMS-TDR-8-1, CERN, 2006, URL: https://cds.cern.ch/record/922757 (cit. on p. 15).

[49] LHCb Collaboration, *LHCb : Technical Proposal*, CERN-LHCC-98-004, LHCC-P-4, CERN, 1998, URL: https://cds.cern.ch/record/622031 (cit. on p. 15).

[50] ALICE Collaboration, *ALICE: Technical proposal for a Large Ion collider Experiment at the CERN LHC*, CERN-LHCC-95-71, LHCC-P-3, CERN, 1995, URL: http://cds.cern.ch/record/293391 (cit. on p. 15).

[51] C. Lefévre, *The CERN Accelerator Complex. Complexe des accélérateurs du CERN*, URL: http://cds.cern.ch/record/1260465 (cit. on p. 16).

[52] ATLAS Collaboration, *Reconstruction of primary vertices at the ATLAS experiment in Run 1 proton–proton collisions at the LHC*, Eur. Phys. J. **C77** (2017) 332, arXiv: 1611.10235 [physics.ins-det] (cit. on pp. 17, 31).

[53] ATLAS Collaboration, *The ATLAS Experiment at the CERN Large Hadron Collider*, JINST **3** (2008) S08003 (cit. on pp. 18, 20, 22).

[54] ATLAS Collaboration, *Performance of the ATLAS track reconstruction algorithms in dense environments in LHC Run 2*, Eur. Phys. J. C **77** (2017) (cit. on p. 20).

[55] E. Diehl, *Calibration and Performance of the ATLAS Muon Spectrometer*, 2011, arXiv: 1109.6933 [physics.ins-det] (cit. on p. 23).

[56] ATLAS Collaboration, *Performance of the ATLAS trigger system in 2015*, Eur. Phys. J. C **77** (2017), arXiv: 1611.09661 [hep-ex] (cit. on p. 23).

[57] ATLAS Collaboration,
Electron reconstruction and identification in the ATLAS experiment using the 2015 and 2016 LHC proton–proton collision data at $\sqrt{s}$ = 13 TeV,
Eur. Phys. J. **C79** (2019) 639, arXiv: 1902.04655 [physics.ins-det]
(cit. on pp. 26, 27, 30, 39).

[58] W. Lampl et al., *Calorimeter Clustering Algorithms: Description and Performance*, ATL-LARG-PUB-2008-002, ATL-COM-LARG-2008-003, CERN, 2008, URL: https://cds.cern.ch/record/1099735 (cit. on p. 26).

[59] T. Cornelissen et al., *The global χ^2 track fitter in ATLAS*, J. Phys. Conf. Ser. **119** (2008) 032013 (cit. on p. 26).

[60] ATLAS Collaboration, *Electron and photon performance measurements with the ATLAS detector using the 2015–2017 LHC proton–proton collision data*, JINST **14** (2019) P12006, arXiv: 1908.00005 [hep-ex] (cit. on pp. 26, 89).

[61] ATLAS Collaboration, *Muon reconstruction performance of the ATLAS detector in proton–proton collision data at $\sqrt{s}$ = 13 TeV*, Eur. Phys. J. **C76** (2016) 292, arXiv: 1603.05598 [hep-ex] (cit. on pp. 27, 29, 89).

[62] ATLAS Collaboration, *Electron and photon energy calibration with the ATLAS detector using 2015–2016 LHC proton–proton collision data*, JINST **14** (2019) P03017, arXiv: 1812.03848 [hep-ex] (cit. on p. 30).

[63] M. Cacciari, G. P. Salam and G. Soyez, *The anti-k_t jet clustering algorithm*, JHEP **04** (2008) 063, arXiv: 0802.1189 [hep-ph] (cit. on pp. 31, 32).

[64] ATLAS Collaboration, *Topological cell clustering in the ATLAS calorimeters and its performance in LHC Run 1*, Eur. Phys. J. C **77** (2017) 490, arXiv: 1603.02934 [hep-ex] (cit. on p. 31).

[65] S. D. Ellis and D. E. Soper,
Successive combination jet algorithm for hadron collisions,
Phys. Rev. D **48** (1993) 3160 (cit. on p. 32).

[66] M. Cacciari, G. P. Salam and G. Soyez, *FastJet user manual*,
Eur. Phys. J. C **72** (2012) 1896, arXiv: 1111.6097 [hep-ph] (cit. on p. 32).

[67] ATLAS Collaboration, *Jet energy scale measurements and their systematic uncertainties in proton-proton collisions at $\sqrt{s}$ = 13 TeV with the ATLAS detector*,
Phys. Rev. D **96** (2017) 072002 (cit. on p. 33).

[68] ATLAS Collaboration, *Measurements of b-jet tagging efficiency with the ATLAS detector using $t\bar{t}$ events at $\sqrt{s}$ = 13 TeV*, JHEP **08** (2018) 089,
arXiv: 1805.01845 [hep-ex] (cit. on pp. 34, 90).

[69] ATLAS Collaboration, *Optimisation and performance studies of the ATLAS b-tagging algorithms for the 2017-18 LHC run*, ATL-PHYS-PUB-2017-013,
CERN, 2017, URL: https://cds.cern.ch/record/2273281 (cit. on p. 34).

[70] ATLAS Collaboration,
Secondary vertex finding for jet flavour identification with the ATLAS detector,
ATL-PHYS-PUB-2017-011, CERN, 2017,
URL: https://cds.cern.ch/record/2270366 (cit. on p. 34).

[71] ATLAS Collaboration, *Topological b-hadron decay reconstruction and identification of b-jets with the JetFitter package in the ATLAS experiment at the LHC*,
ATL-PHYS-PUB-2018-025, CERN, 2018,
URL: https://cds.cern.ch/record/2645405 (cit. on p. 34).

[72] ATLAS Collaboration, *Performance of missing transverse momentum reconstruction with the ATLAS detector using proton-proton collisions at $\sqrt{s}$ = 13 TeV*,
Eur. Phys. J. C **78** (2018) 903, arXiv: 1802.08168 [hep-ex] (cit. on p. 34).

[73] A. D. Martin et al., *Parton distributions for the LHC*, Eur. Phys. J. C **63** (2009) 189,
arXiv: 0901.0002 [hep-ph] (cit. on pp. 37, 53).

[74] H.-L. Lai et al., *New parton distributions for collider physics*,
Phys. Rev. D **82** (7 2010) 074024,
URL: https://link.aps.org/doi/10.1103/PhysRevD.82.074024
(cit. on p. 37).

[75] ATLAS Collaboration, *Luminosity Public Results*, 2018, URL: https://twiki.cern.ch/twiki/bin/view/AtlasPublic/LuminosityPublicResultsRun2
(cit. on p. 50).

[76] ATLAS Collaboration, *ATLAS Pythia 8 tunes to 7 TeV data*,
ATL-PHYS-PUB-2014-021, CERN, 2014,
URL: https://cds.cern.ch/record/1966419 (cit. on pp. 50, 52, 91).

[77] S. Agostinelli et al., *GEANT4 – a simulation toolkit*, Nucl. Instrum. Meth. A **506** (2003) 250 (cit. on p. 51).

[78] ATLAS Collaboration, *The ATLAS Simulation Infrastructure*, Eur. Phys. J. C **70** (2010) 823 (cit. on p. 51).

[79] ATLAS Collaboration, *The new Fast Calorimeter Simulation in ATLAS*, ATL-SOFT-PUB-2018-002, CERN, 2018, URL: https://cds.cern.ch/record/2630434 (cit. on p. 51).

[80] ATLAS Collaboration, *The simulation principle and performance of the ATLAS fast calorimeter simulation FastCaloSim*, ATL-PHYS-PUB-2010-013, CERN, 2010, URL: https://cds.cern.ch/record/1300517 (cit. on p. 51).

[81] J. Alwall et al., *The automated computation of tree-level and next-to-leading order differential cross sections, and their matching to parton shower simulations*, JHEP **07** (2014) 079, arXiv: 1405.0301 [hep-ph] (cit. on pp. 51, 91).

[82] D. J. Lange, *The EvtGen particle decay simulation package*, Nucl. Instrum. Meth. A **462** (2001) 152 (cit. on p. 52).

[83] T. Gleisberg et al., *Event generation with SHERPA 1.1*, JHEP **02** (2009) 007, arXiv: 0811.4622 [hep-ph] (cit. on pp. 52, 53).

[84] S. Höche et al., *QCD matrix elements and truncated showers*, JHEP **05** (2009) 053, arXiv: 0903.1219 [hep-ph] (cit. on pp. 52, 53).

[85] T. Gleisberg and S. Höche, *Comix, a new matrix element generator*, JHEP **12** (2008) 039, arXiv: 0808.3674 [hep-ph] (cit. on p. 53).

[86] S. Schumann and F. Krauss, *A parton shower algorithm based on Catani–Seymour dipole factorisation*, JHEP **03** (2008) 038, arXiv: 0709.1027 [hep-ph] (cit. on p. 53).

[87] S. Höche et al., *A critical appraisal of NLO+PS matching methods*, JHEP **09** (2012) 049, arXiv: 1111.1220 [hep-ph] (cit. on p. 53).

[88] S. Catani et al., *QCD Matrix Elements + Parton Showers*, JHEP **11** (2001) 063, arXiv: hep-ph/0109231 [hep-ph] (cit. on p. 53).

[89] S. Höche et al., *QCD matrix elements + parton showers. The NLO case*, JHEP **04** (2013) 027, arXiv: 1207.5030 [hep-ph] (cit. on p. 53).

[90] F. Cascioli, P. Maierhöfer and S. Pozzorini, *Scattering Amplitudes with Open Loops*, Phys. Rev. Lett. **108** (2012) 111601, arXiv: 1111.5206 [hep-ph] (cit. on p. 53).

[91] A. Denner, S. Dittmaier and L. Hofer, *COLLIER: A fortran-based complex one-loop library in extended regularizations*, Comput. Phys. Commun. **212** (2017) 220, arXiv: 1604.06792 [hep-ph] (cit. on p. 53).

[92] P. Nason,
A new method for combining NLO QCD with shower Monte Carlo algorithms,
JHEP **11** (2004) 040, arXiv: hep-ph/0409146 (cit. on p. 53).

[93] S. Frixione, P. Nason and C. Oleari, *Matching NLO QCD computations with parton shower simulations: the POWHEG method*, JHEP **11** (2007) 070,
arXiv: 0709.2092 [hep-ph] (cit. on p. 53).

[94] S. Alioli et al., *A general framework for implementing NLO calculations in shower Monte Carlo programs: the POWHEG BOX*, JHEP **06** (2010) 043,
arXiv: 1002.2581 [hep-ph] (cit. on p. 53).

[95] ATLAS Collaboration, *Summary of ATLAS Pythia 8 tunes*,
ATL-PHYS-PUB-2012-003, CERN, 2012,
URL: https://cds.cern.ch/record/1474107 (cit. on p. 53).

[96] ATLAS Collaboration, *Measurement of $W^{\pm}$ and Z-boson production cross sections in pp collisions at $\sqrt{s}$ = 13 TeV with the ATLAS detector*,
Phys. Lett. B **759** (2016) 601, arXiv: 1603.09222 [hep-ex] (cit. on p. 53).

[97] J. M. Campbell and R. K. Ellis,
Update on vector boson pair production at hadron colliders,
Phys. Rev. D **60** (1999) 113006, arXiv: hep-ph/9905386 (cit. on p. 53).

[98] D. de Florian et al., *Handbook of LHC Higgs cross sections: 4. Deciphering the nature of the Higgs sector*, 2016, arXiv: 1610.07922 [hep-ph] (cit. on p. 53).

[99] ATLAS Collaboration,
Tagging and suppression of pileup jets with the ATLAS detector,
ATLAS-CONF-2014-018, CERN, 2014,
URL: https://cds.cern.ch/record/1700870 (cit. on p. 56).

[100] ATLAS Collaboration,
Performance of electron and photon triggers in ATLAS during LHC Run 2,
Eur. Phys. J. C **80** (2020) 47, arXiv: 1909.00761 [hep-ex] (cit. on p. 57).

[101] ATLAS Collaboration, *Performance of the ATLAS muon triggers in Run 2*,
CERN-EP-2020-031, 2020, arXiv: 2004.13447 [hep-ex] (cit. on p. 57).

[102] S. Frixione, *Isolated photons in perturbative QCD*, Phys. Lett. B **429** (1998) 369,
arXiv: hep-ph/9801442 [hep-ph] (cit. on p. 62).

[103] G. D'Agostini, *A multidimensional unfolding method based on Bayes' theorem*,
Nucl. Instrum. Meth. A **362** (1995) 487 (cit. on p. 70).

[104] T. Adye, *Unfolding algorithms and tests using RooUnfold*, 2011,
arXiv: 1105.1160 [physics.data-an] (cit. on pp. 70, 84).

[105] J. B. Bell, A. N. Tikhonov and V. Y. Arsenin, *Solutions of Ill-Posed Problems.*,
Math. Comput **32** (1978) 1320 (cit. on p. 84).

[106] ATLAS Collaboration, *Measurement of b-tagging efficiency of c-jets in $t\bar{t}$ events using a likelihood approach with the ATLAS detector*, ATLAS-CONF-2018-001, CERN, 2018, URL: https://cds.cern.ch/record/2306649 (cit. on p. 90).

[107] ATLAS Collaboration, *Calibration of light-flavour b-jet mistagging rates using ATLAS proton–proton collision data at $\sqrt{s}$ = 13 TeV*, ATLAS-CONF-2018-006, CERN, 2018, URL: https://cds.cern.ch/record/2314418 (cit. on p. 90).

[108] ATLAS Collaboration, *Luminosity determination in pp collisions at $\sqrt{s}$ = 13 TeV using the ATLAS detector at the LHC*, ATLAS-CONF-2019-021, CERN, 2019, URL: https://cds.cern.ch/record/2677054 (cit. on p. 91).

[109] G. Avoni et al., *The new LUCID-2 detector for luminosity measurement and monitoring in ATLAS*, JINST **13** (2018) P07017 (cit. on p. 91).

[110] M. Bahr et al., *Herwig++ physics and manual*, Eur. Phys. J. C **58** (2008) 639, arXiv: 0803.0883 [hep-ph] (cit. on p. 91).

[111] J. Bellm et al., *Herwig 7.0/Herwig++ 3.0 release note*, Eur. Phys. J. C **76** (2016) 196, arXiv: 1512.01178 [hep-ph] (cit. on p. 91).

[112] B. Andersson et al., *Parton fragmentation and string dynamics*, Phys. Rep. **97** (1983) 31 (cit. on p. 91).

[113] B. Webber, *A QCD model for jet fragmentation including soft gluon interference*, Nucl. Phys. B **238** (1984) 492 (cit. on p. 91).

[114] J. Pumplin et al., *New Generation of Parton Distributions with Uncertainties from Global QCD Analysis*, JHEP **07** (2002) 012, arXiv: hep-ph/0201195 (cit. on p. 91).

[115] ATLAS Collaboration, *Improvements in $t\bar{t}$ modelling using NLO+PS Monte Carlo generators for Run 2*, ATL-PHYS-PUB-2018-009, CERN, 2018, URL: https://cds.cern.ch/record/2630327 (cit. on p. 93).

[116] ATLAS Collaboration, *HistFitter software framework for statistical data analysis*, Eur. Phys. J. C **75** (2015) 153, arXiv: 1410.1280 [hep-ex] (cit. on p. 120).

[117] G. Choudalakis, *Fully Bayesian Unfolding*, 2012, arXiv: 1201.4612 [physics.data-an] (cit. on p. 120).

Appendix

APPENDIX A

Additional shower shapes and fit results

The fits performed to the $m_{ee\gamma}$ distribution for the 2015 and 2016 $Z \rightarrow ee\gamma$ data events are shown in Fig. A.1. The signal fraction weights W_{sf} calculated from the fits are shown in Fig. A.2. The shower shapes are compared between the first and second approaches as well as the nominal event selection case. They are shown in Figs. A.3–A.18 in 4 different $|\eta|$-regions: $0 < |\eta(\gamma)| < 0.6$, $0.6 < |\eta(\gamma)| < 1.37$, $1.52 < |\eta(\gamma)| < 1.81$, and $1.81 < |\eta(\gamma)| < 2.37$.

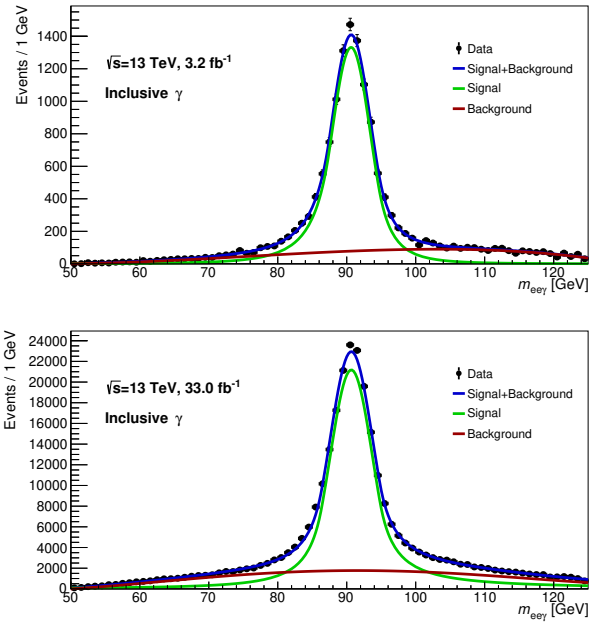

Figure A.1: Fits to the $m_{ee\gamma}$ distribution of $Z \rightarrow ee\gamma$ data for the years 2015 (top) and 2016 (bottom), where a Crystal-ball function and 4th order Bernstein polynomial are used to model singal and background, respectively.

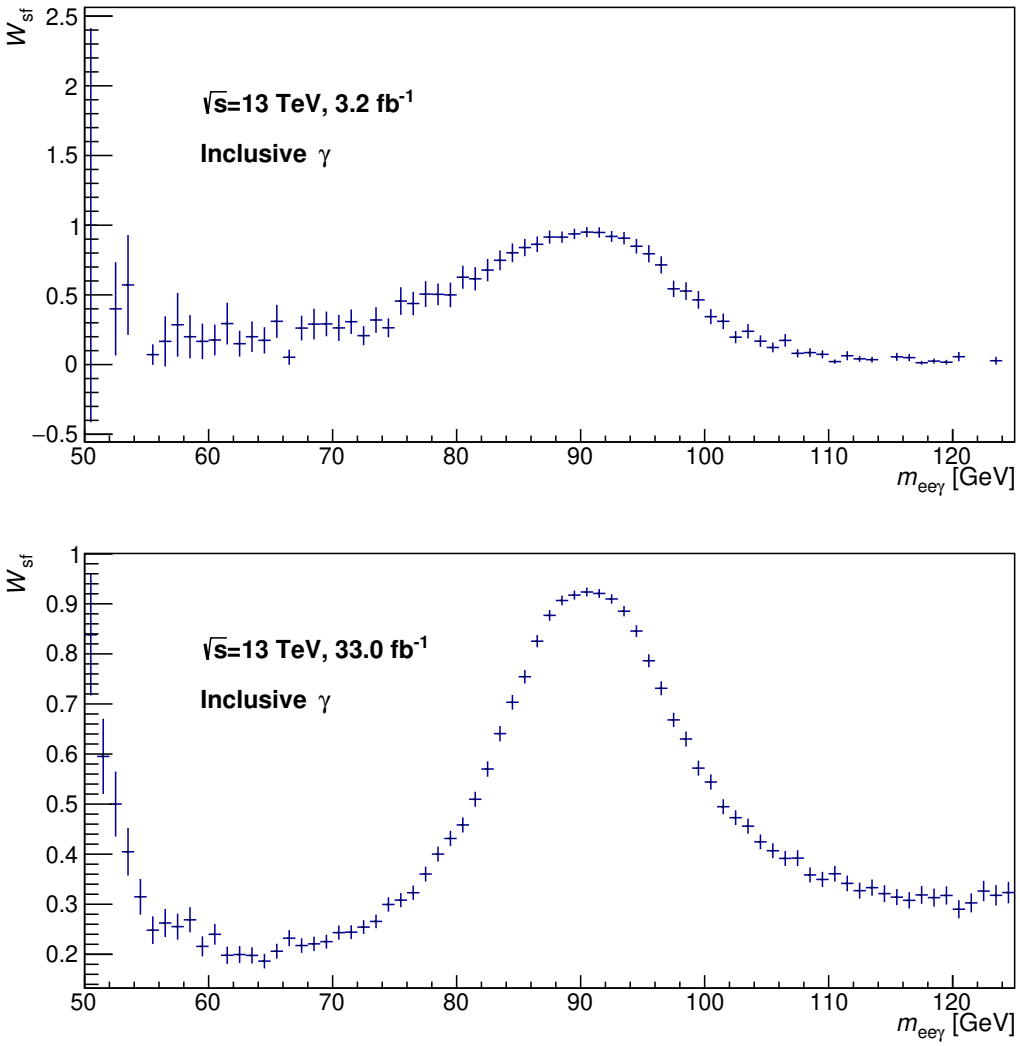

Figure A.2: Signal fraction weights W_{sf} calculated from post-fit results of the $Z \to ee\gamma$ data for the years 2015 (top) and 2016 (bottom) using Eq. (5.1).

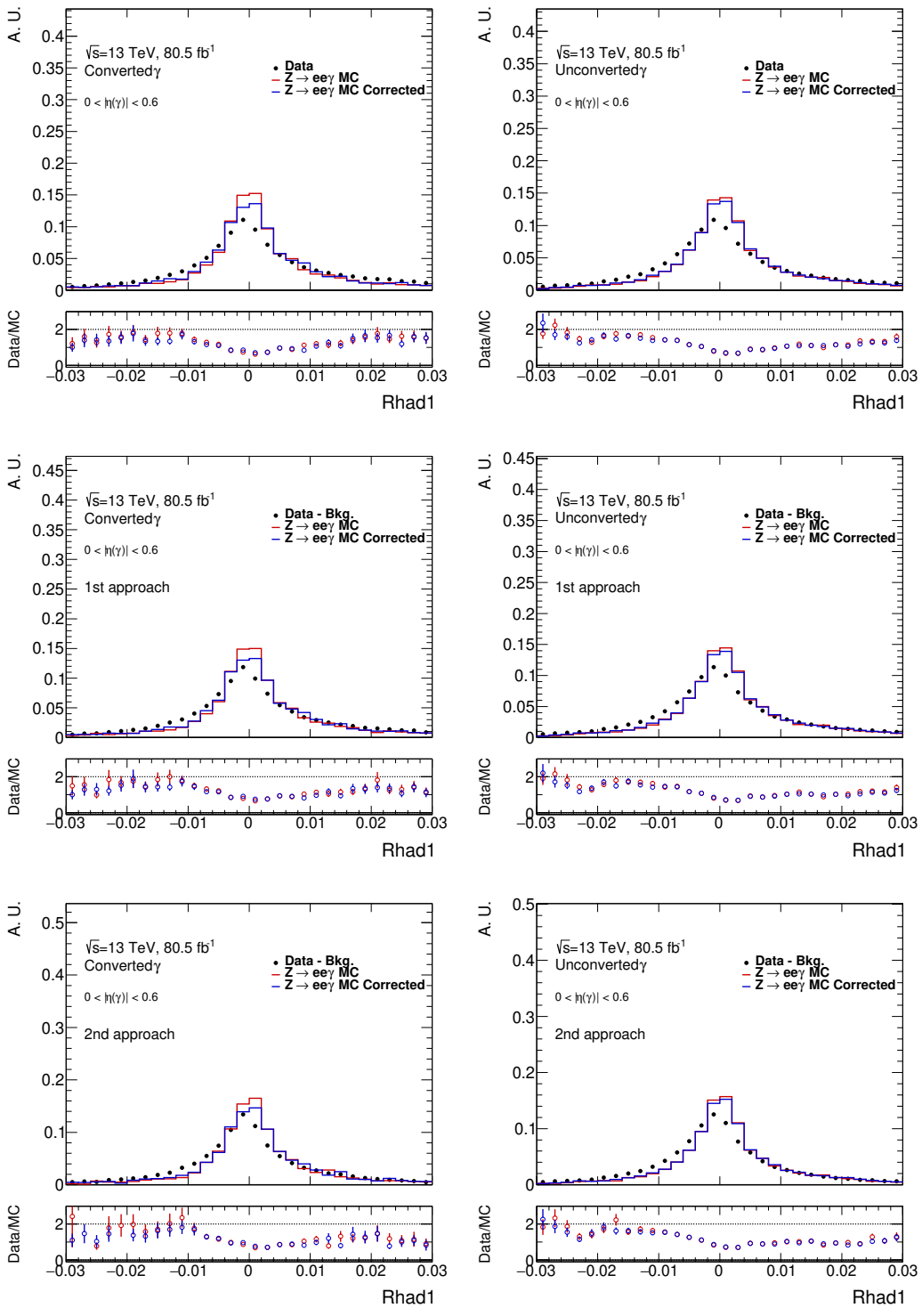

Figure A.3: Rhad1 distributions in data (black) and MC before (red) and after (blue) correction in the 1st eta region $0 < |\eta(\gamma)| < 0.6$. The left (right) column shows for converted (unconverted) photons, three distributions: nominal event selection case (top), 1st approach (middle), and 2nd approach (bottom) applied.

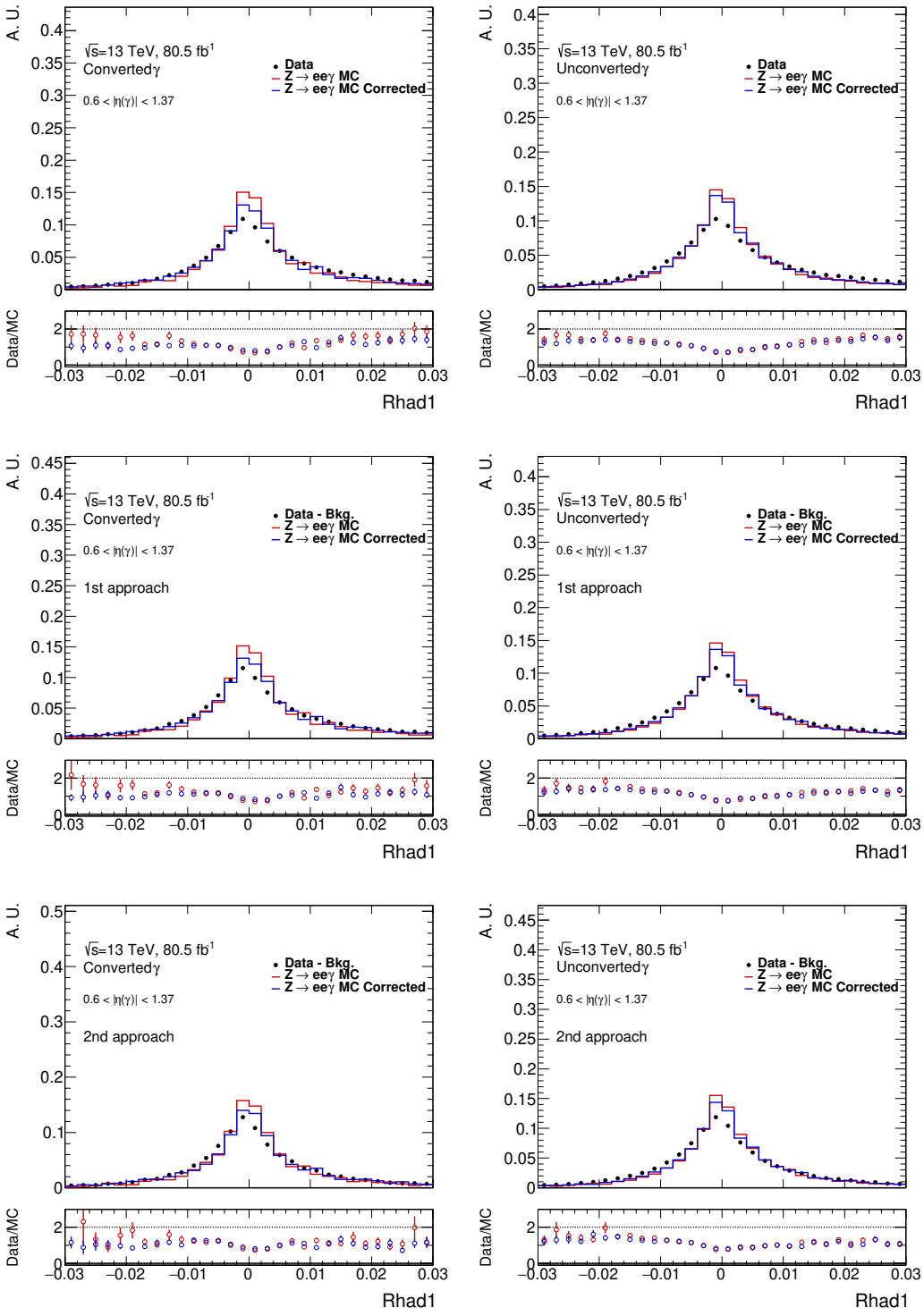

Figure A.4: Rhad1 distributions in data (black) and MC before (red) and after (blue) correction in the 2nd eta region $0.6 < |\eta(\gamma)| < 1.37$. The left (right) column shows for converted (unconverted) photons, three distributions: nominal event selection case (top), 1st approach (middle), and 2nd approach (bottom) applied.

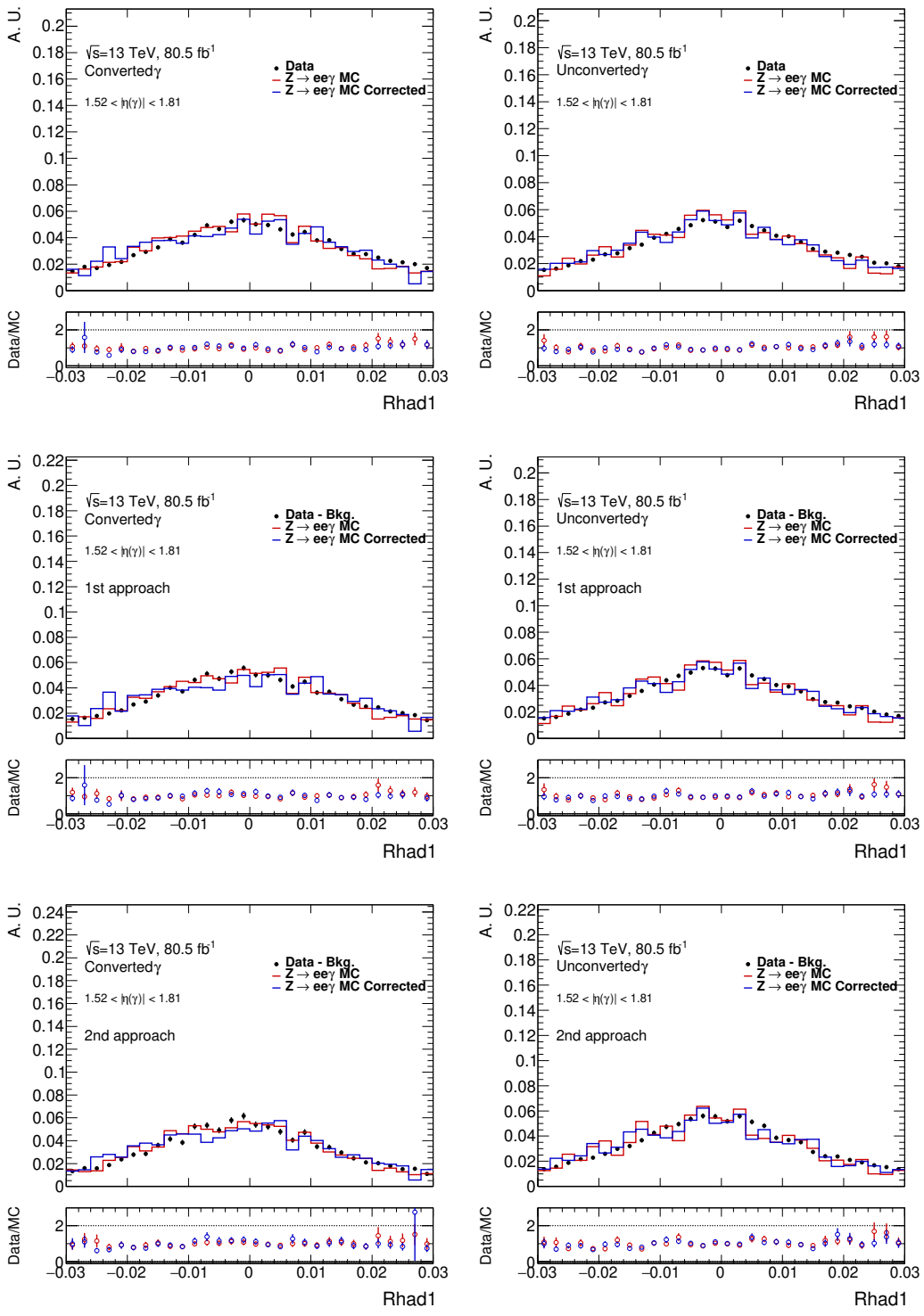

Figure A.5: Rhad1 distributions in data (black) and MC before (red) and after (blue) correction in the 3rd eta region $1.52 < |\eta(\gamma)| < 1.81$. The left (right) column shows for converted (unconverted) photons, three distributions: nominal event selection case (top), 1st approach (middle), and 2nd approach (bottom) applied.

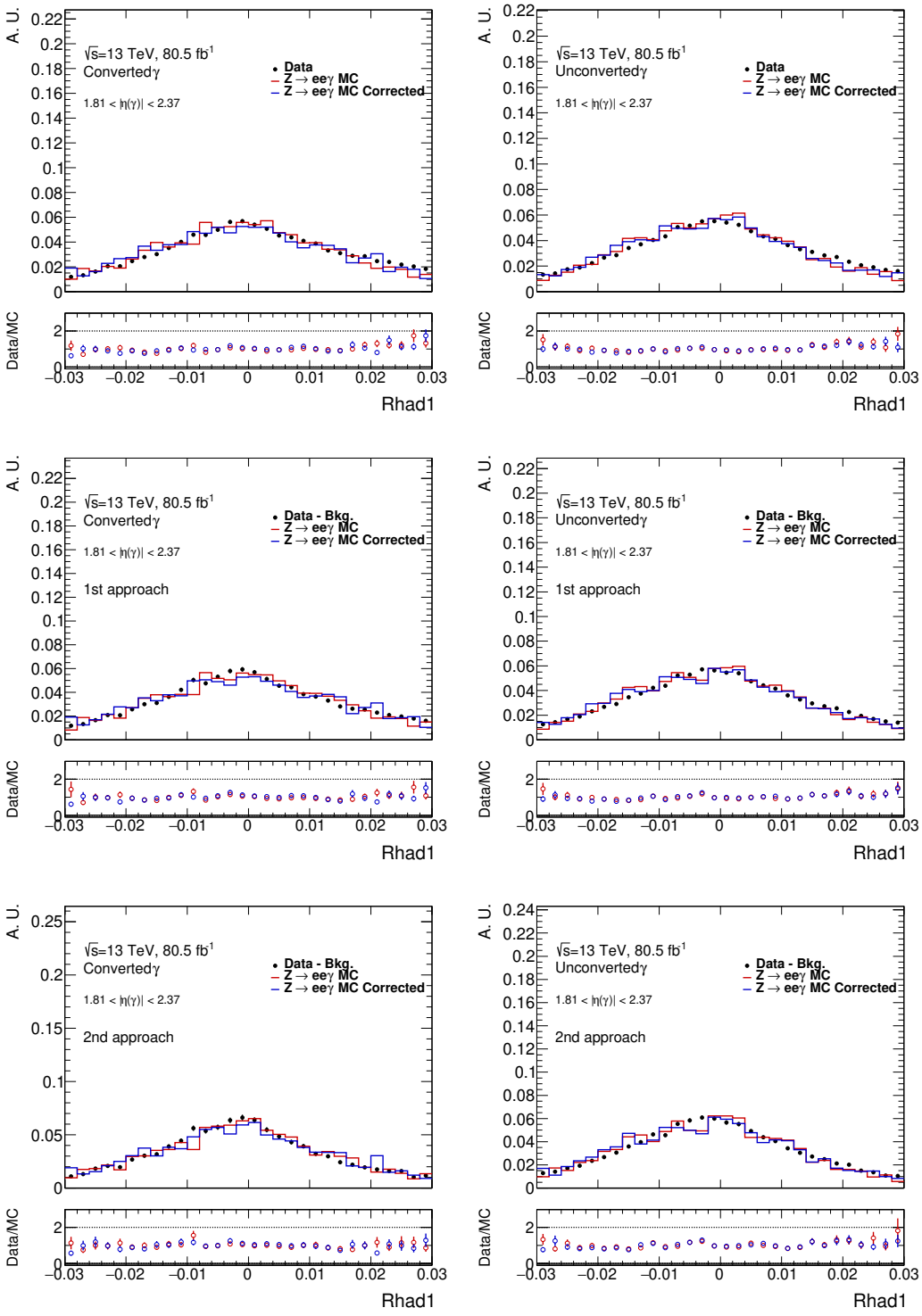

Figure A.6: Rhad1 distributions in data (black) and MC before (red) and after (blue) correction in the 4th eta region $1.81 < |\eta(\gamma)| < 2.37$. The left (right) column shows for converted (unconverted) photons, three distributions: nominal event selection case (top), 1st approach (middle), and 2nd approach (bottom) applied.

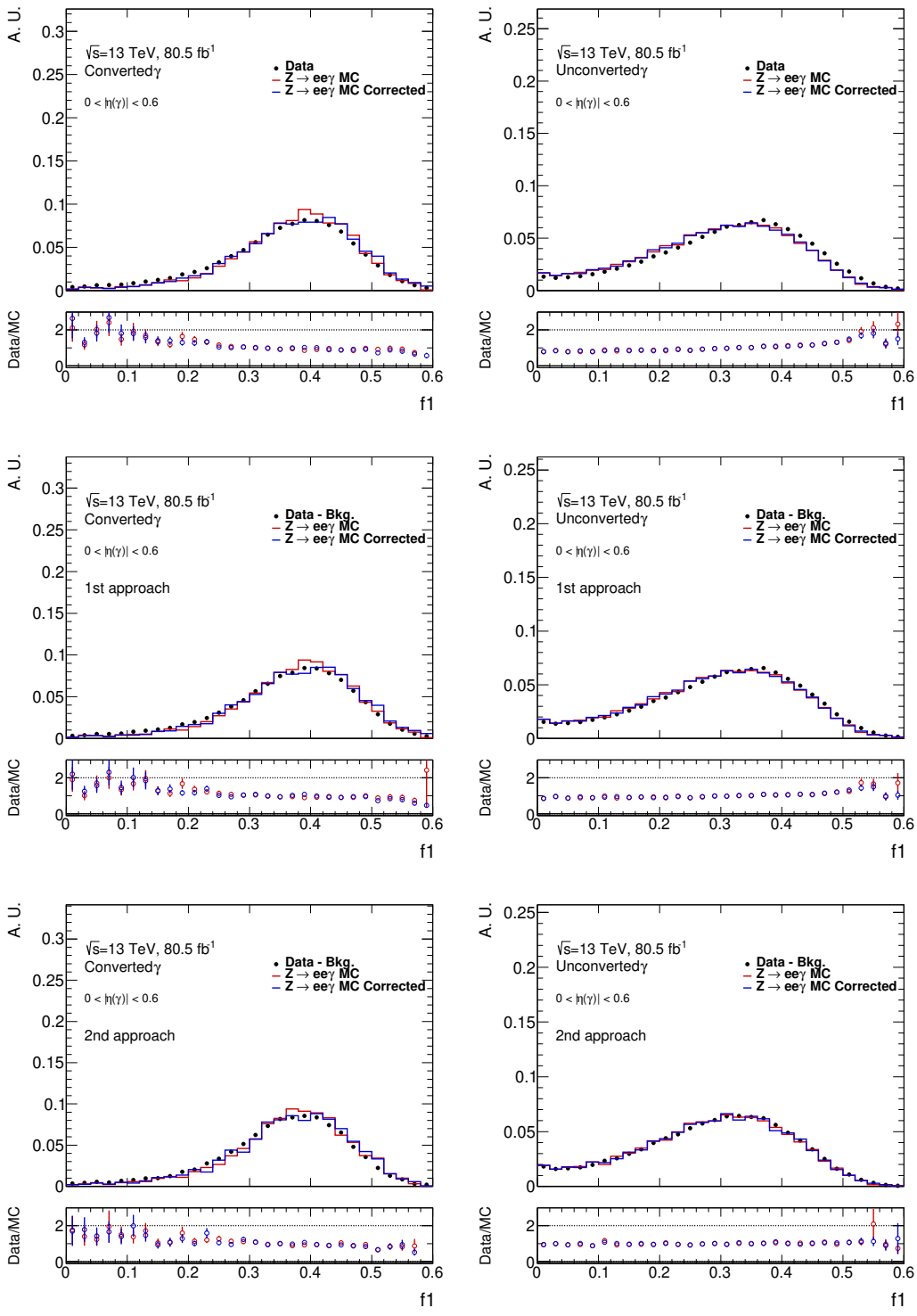

Figure A.7: f1 distributions in data (black) and MC before (red) and after (blue) correction in the 1st eta region $0 < |\eta(\gamma)| < 0.6$. The left (right) column shows for converted (unconverted) photons, three distributions: nominal event selection case (top), 1st approach (middle), and 2nd approach (bottom) applied.

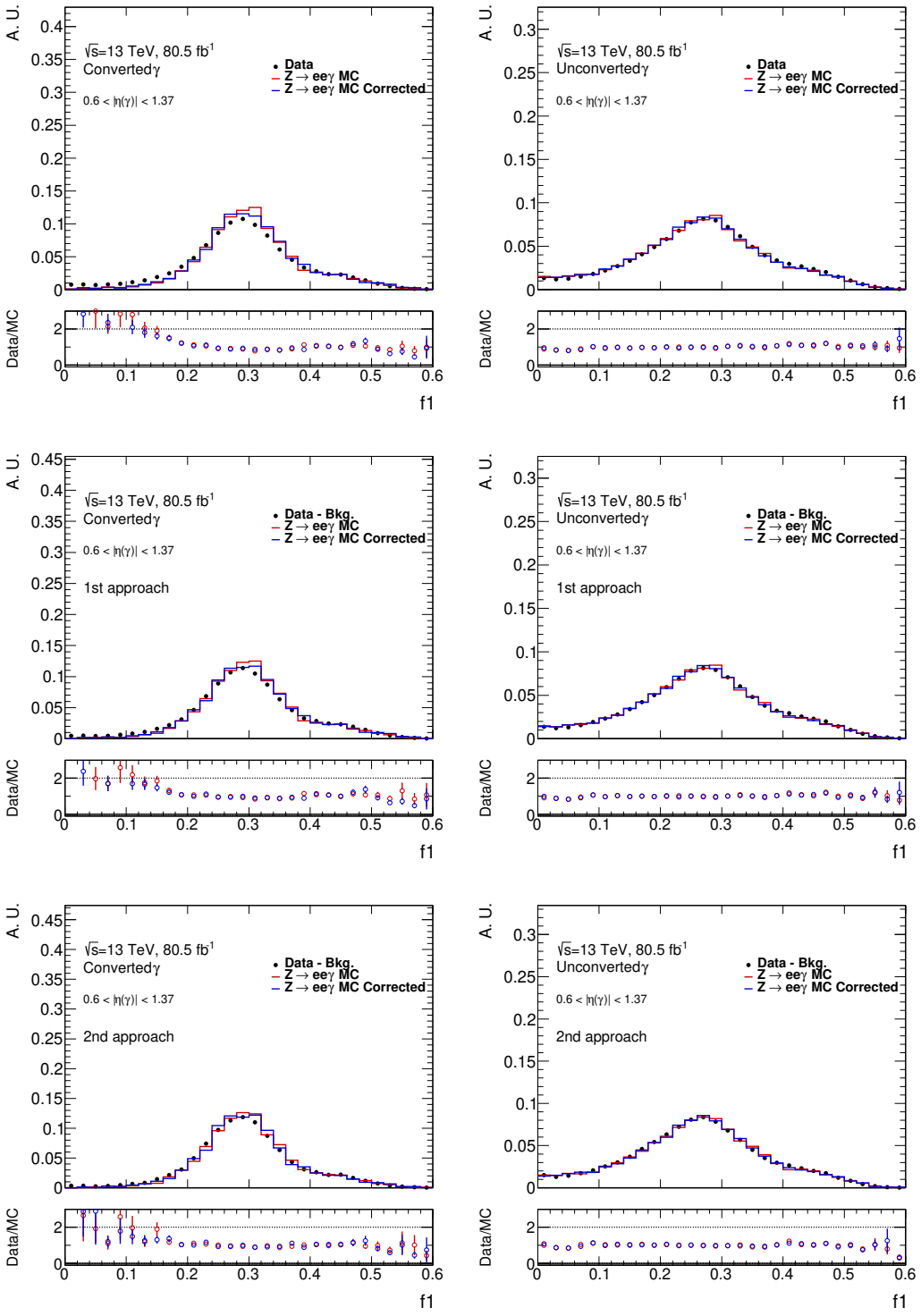

Figure A.8: f1 distributions in data (black) and MC before (red) and after (blue) correction in the 2nd eta region $0.6 < |\eta(\gamma)| < 1.37$. The left (right) column shows for converted (unconverted) photons, three distributions: nominal event selection case (top), 1st approach (middle), and 2nd approach (bottom) applied.

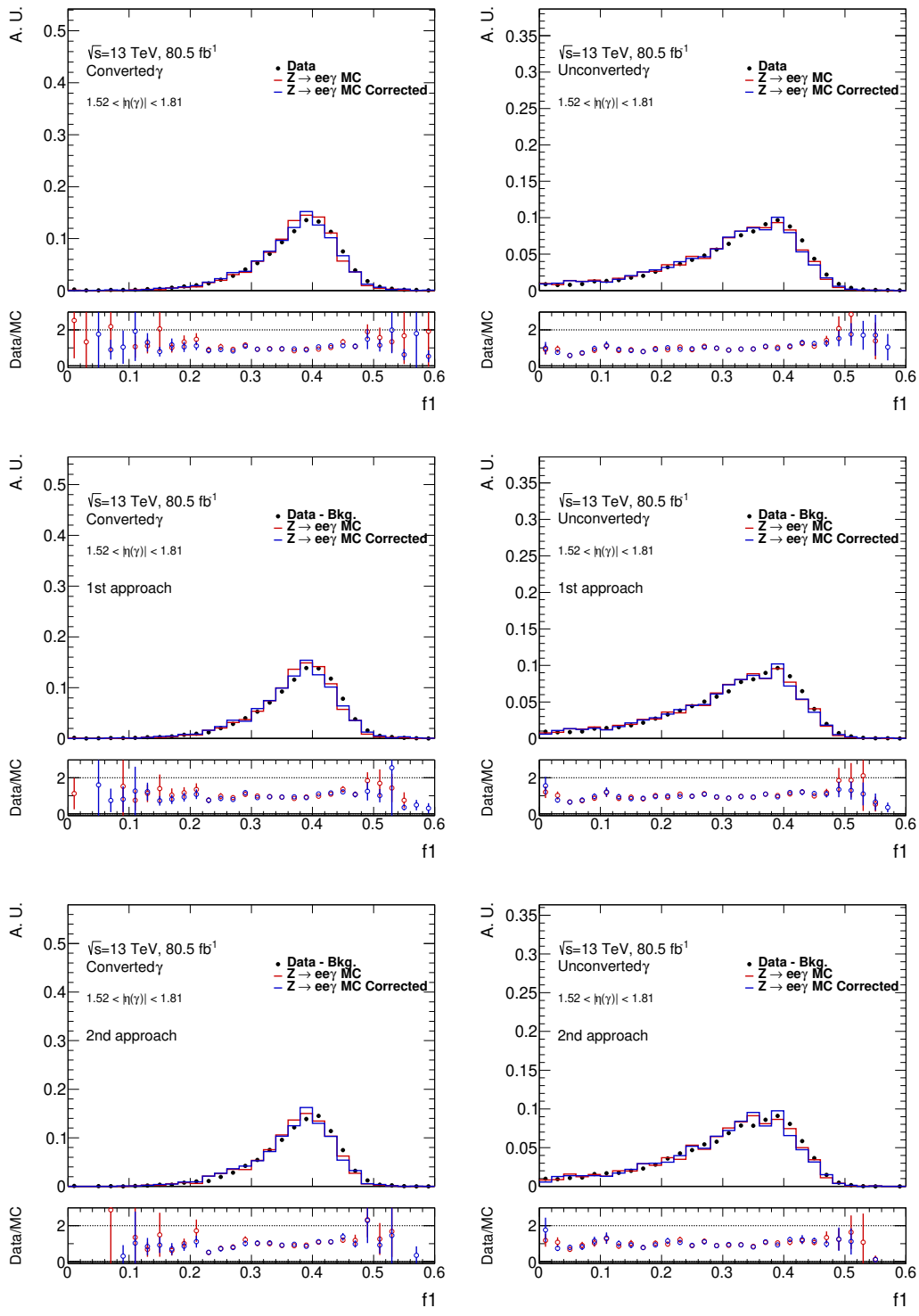

Figure A.9: f1 distributions in data (black) and MC before (red) and after (blue) correction in the 3rd eta region $1.52 < |\eta(\gamma)| < 1.81$. The left (right) column shows for converted (unconverted) photons, three distributions: nominal event selection case (top), 1st approach (middle), and 2nd approach (bottom) applied.

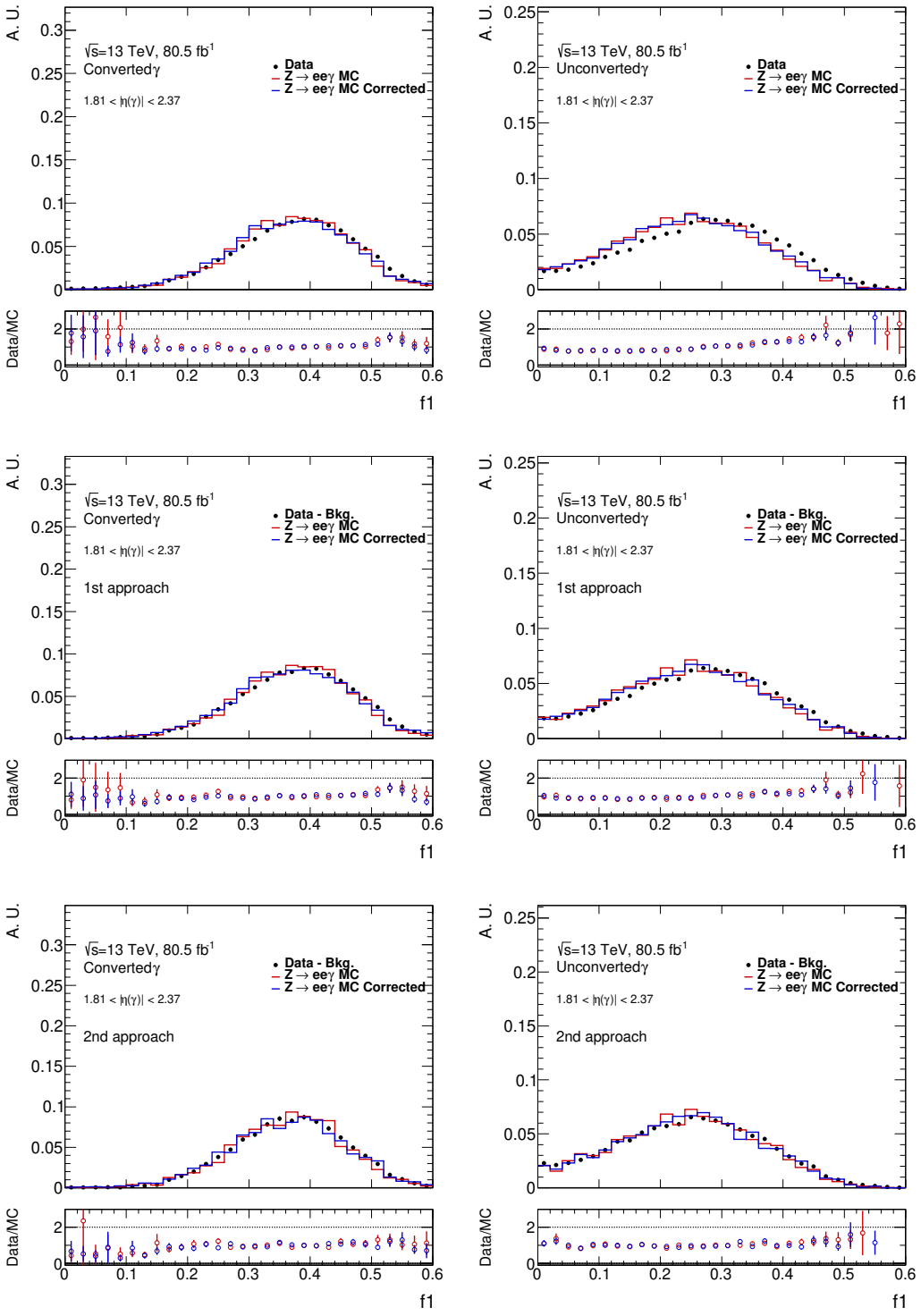

Figure A.10: f1 distributions in data (black) and MC before (red) and after (blue) correction in the 4th eta region $1.81 < |\eta(\gamma)| < 2.37$. The left (right) column shows for converted (unconverted) photons, three distributions: nominal event selection case (top), 1st approach (middle), and 2nd approach (bottom) applied.

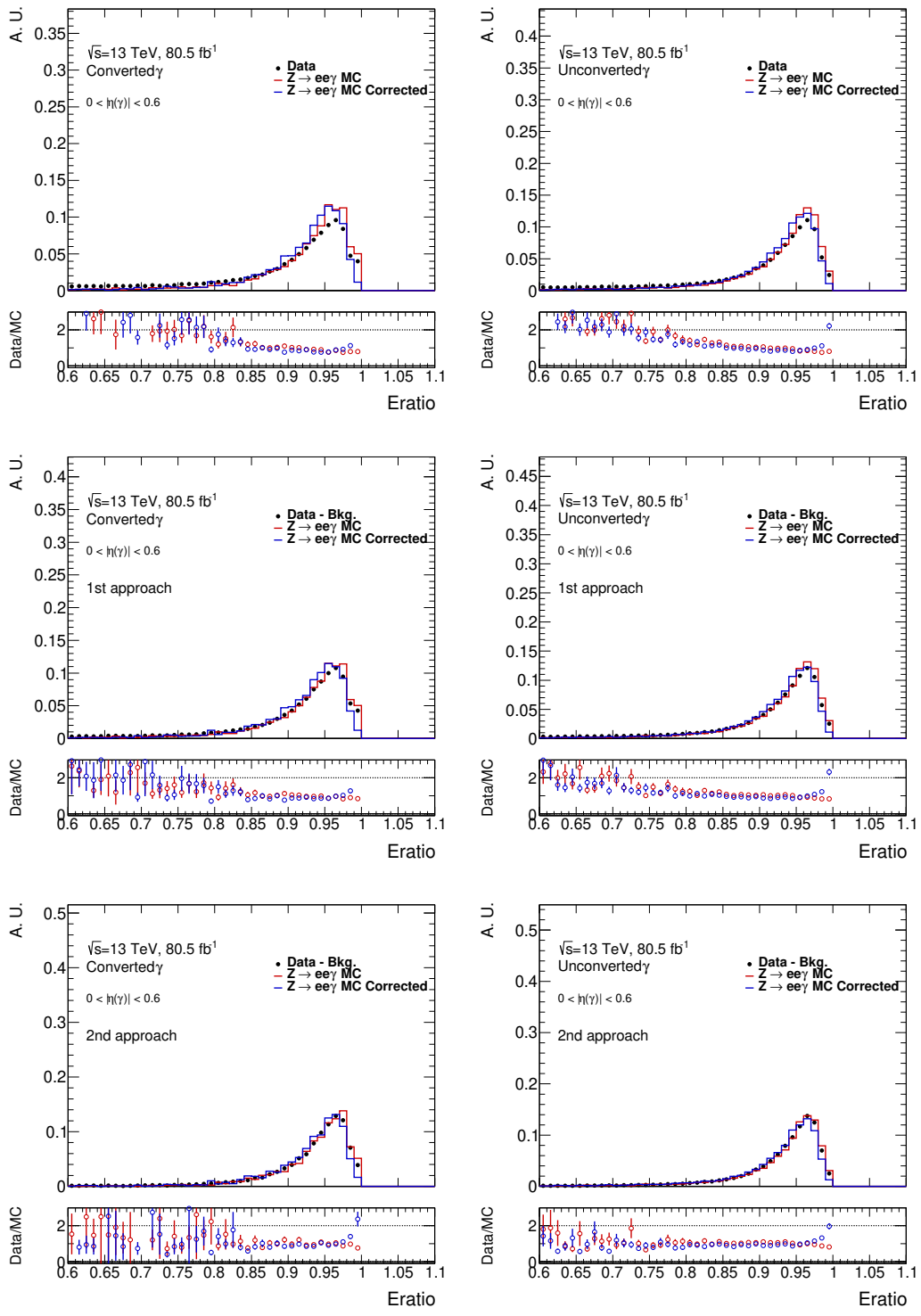

Figure A.11: Eratio distributions in data (black) and MC before (red) and after (blue) correction in the 1st eta region $0 < |\eta(\gamma)| < 0.6$. The left (right) column shows for converted (unconverted) photons, three distributions: nominal event selection case (top), 1st approach (middle), and 2nd approach (bottom) applied.

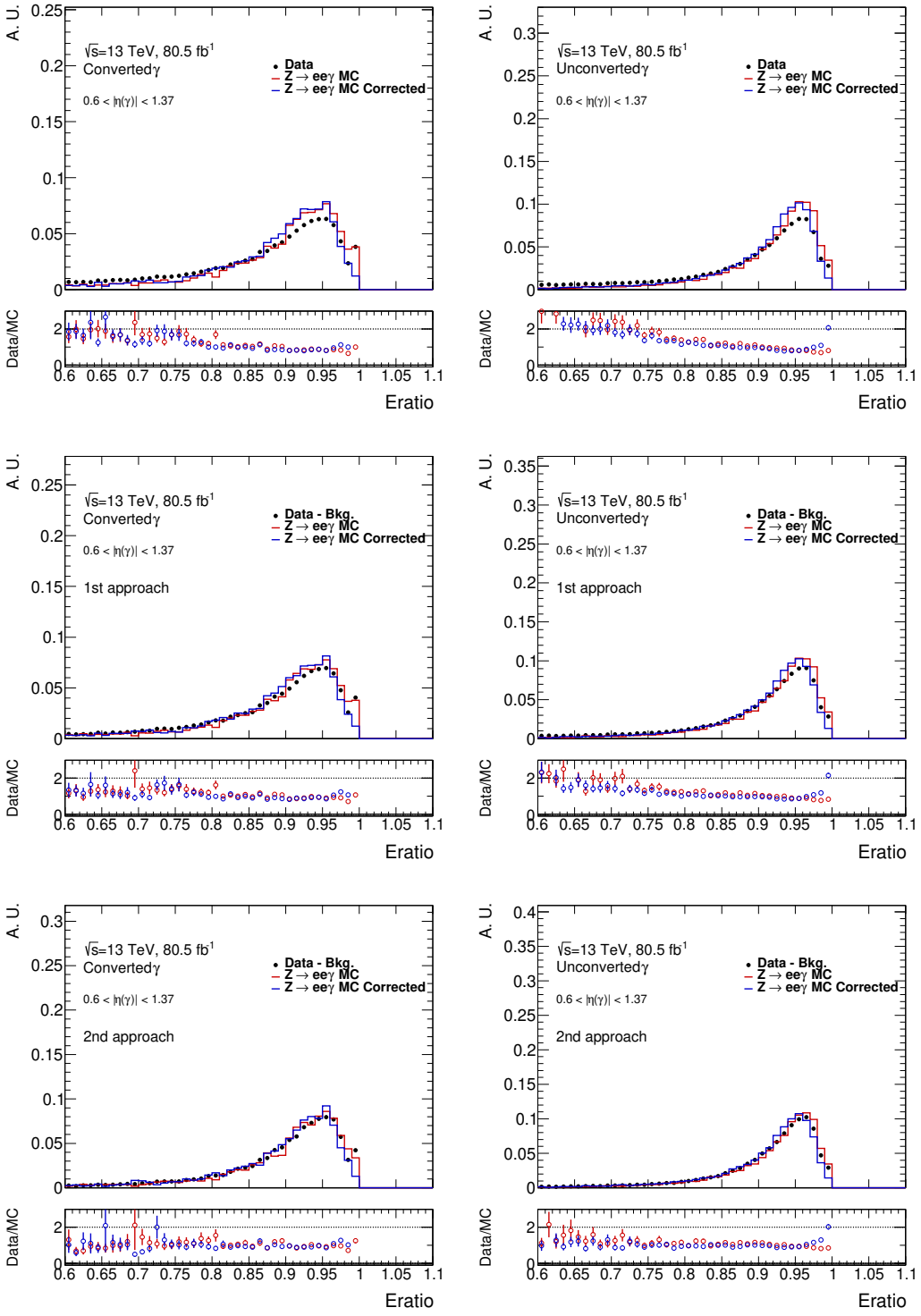

Figure A.12: Eratio distributions in data (black) and MC before (red) and after (blue) correction in the 2nd eta region $0.6 < |\eta(\gamma)| < 1.37$. The left (right) column shows for converted (unconverted) photons, three distributions: nominal event selection case (top), 1st approach (middle), and 2nd approach (bottom) applied.

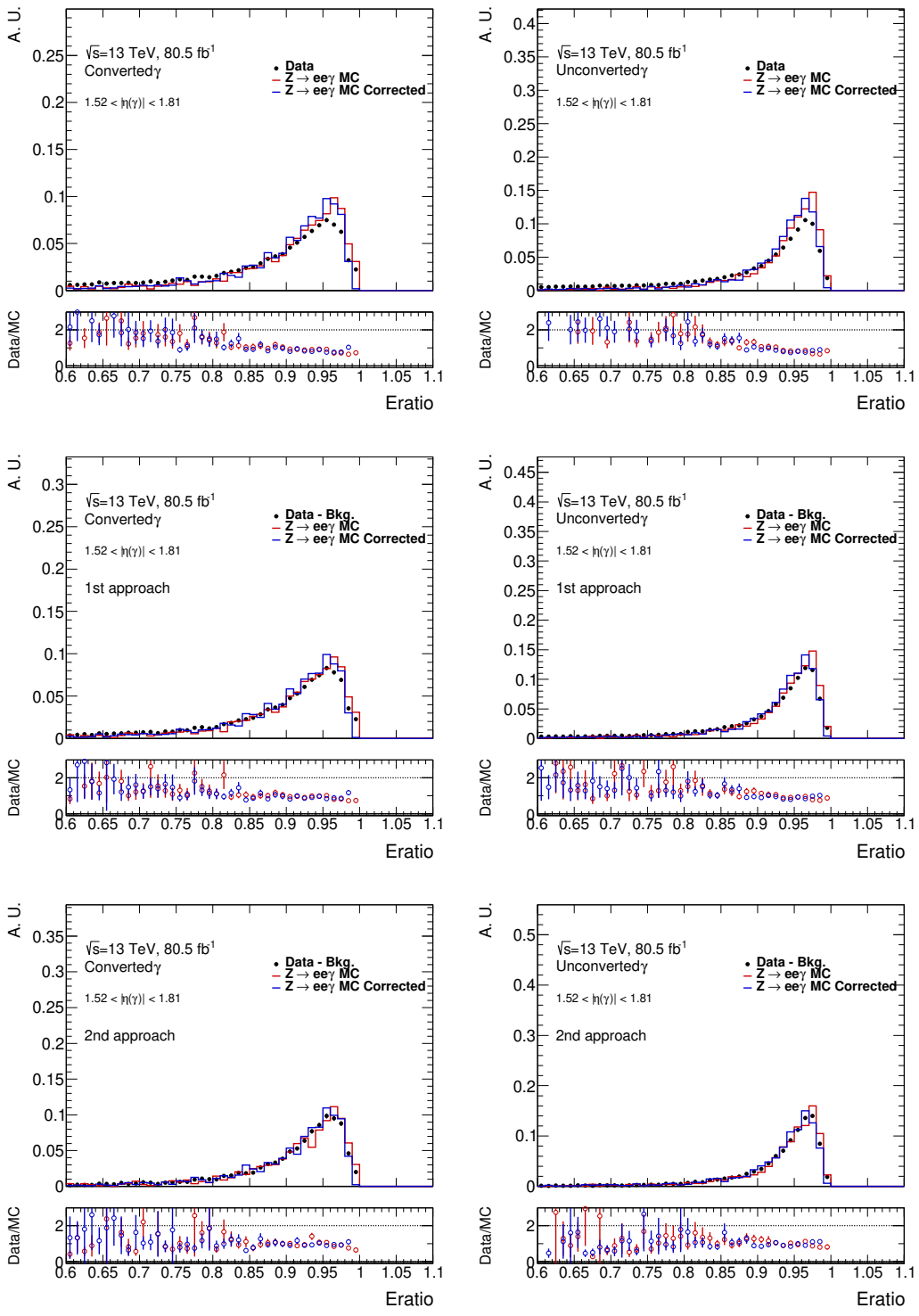

Figure A.13: Eratio distributions in data (black) and MC before (red) and after (blue) correction in the 3rd eta region $1.52 < |\eta(\gamma)| < 1.81$. The left (right) column shows for converted (unconverted) photons, three distributions: nominal event selection case (top), 1st approach (middle), and 2nd approach (bottom) applied.

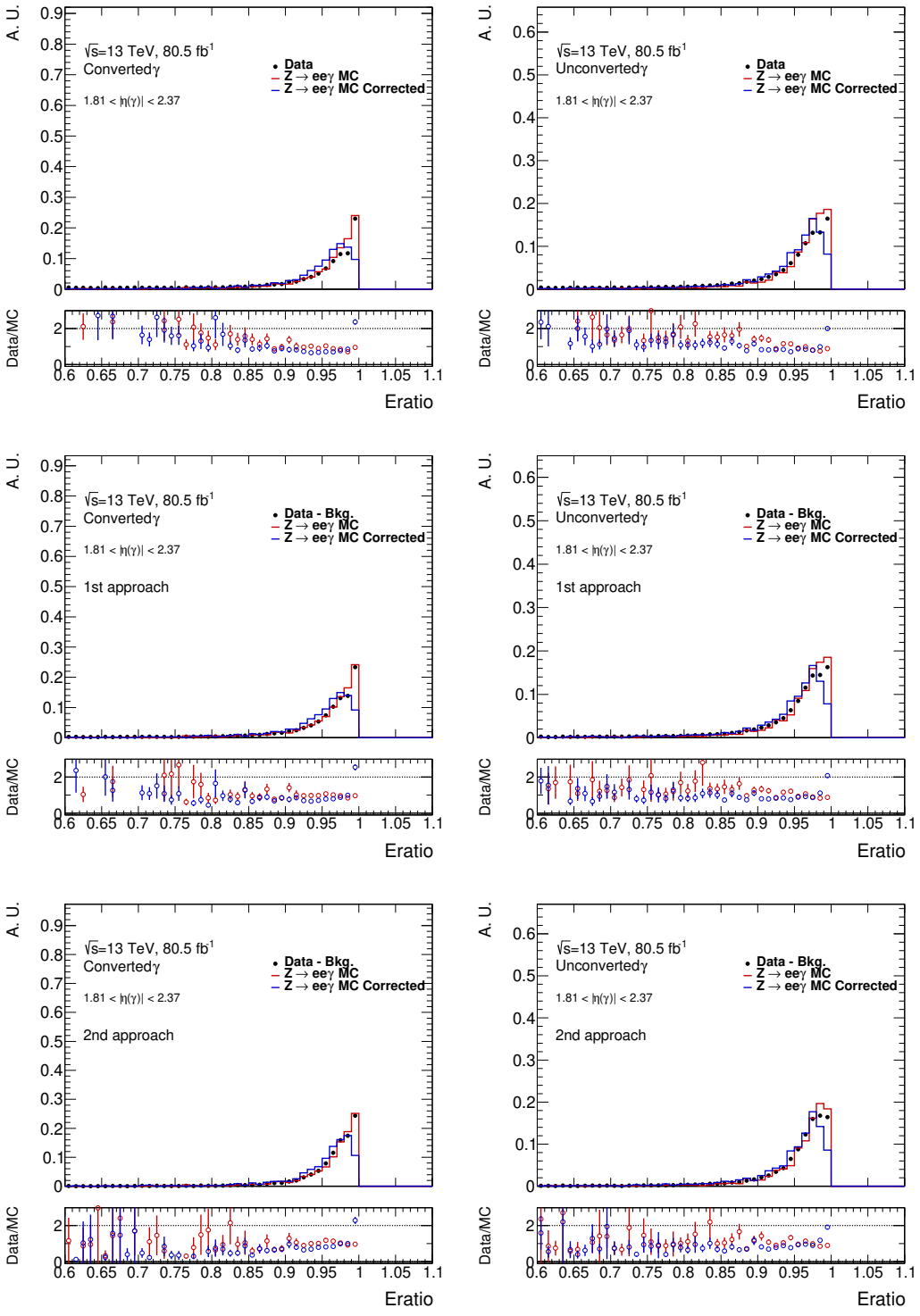

Figure A.14: Eratio distributions in data (black) and MC before (red) and after (blue) correction in the 4th eta region $1.81 < |\eta(\gamma)| < 2.37$. The left (right) column shows for converted (unconverted) photons, three distributions: nominal event selection case (top), 1st approach (middle), and 2nd approach (bottom) applied.

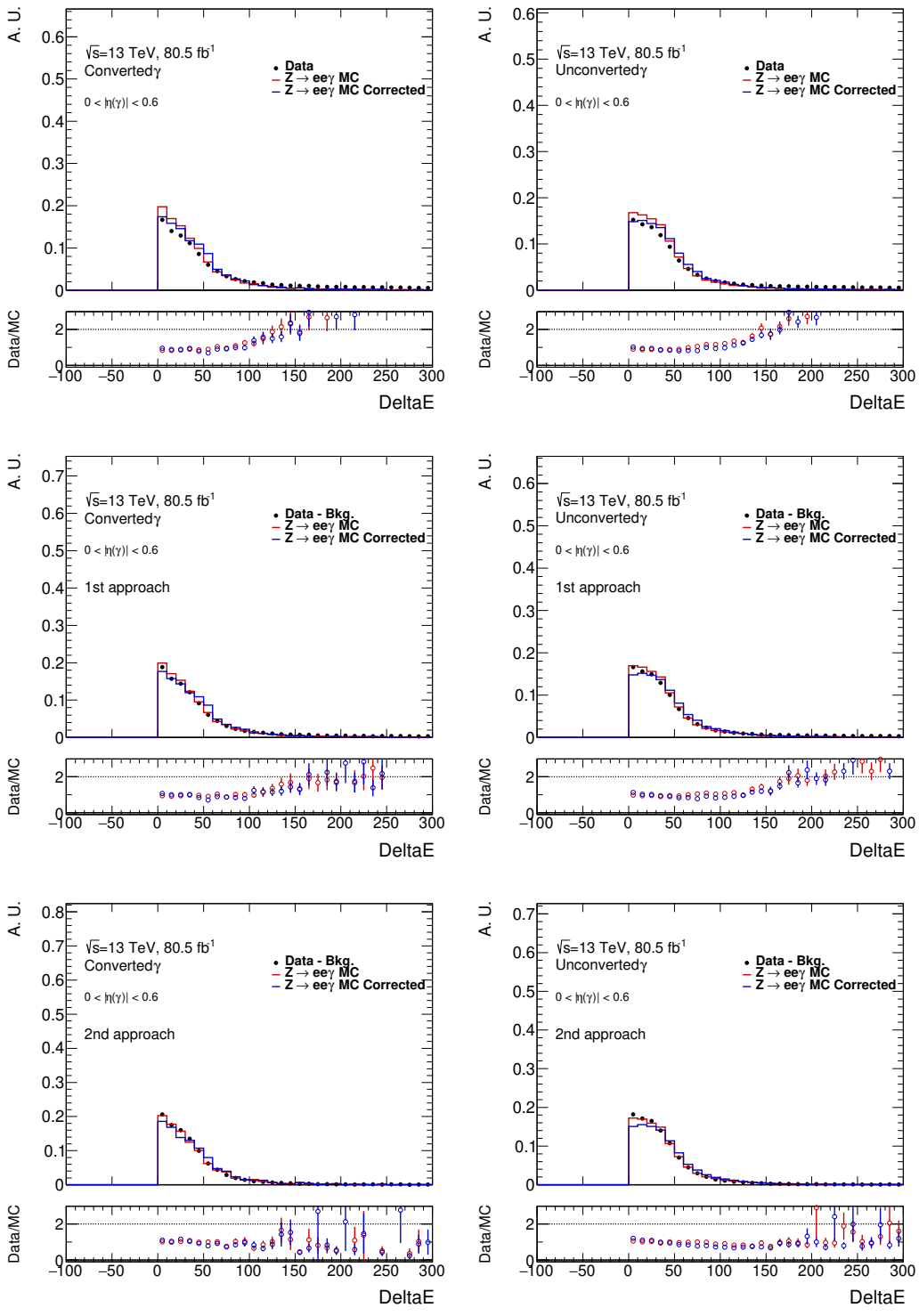

Figure A.15: DeltaE distributions in data (black) and MC before (red) and after (blue) correction in the 1st eta region $0 < |\eta(\gamma)| < 0.6$. The left (right) column shows for converted (unconverted) photons, three distributions: nominal event selection case (top), 1st approach (middle), and 2nd approach (bottom) applied.

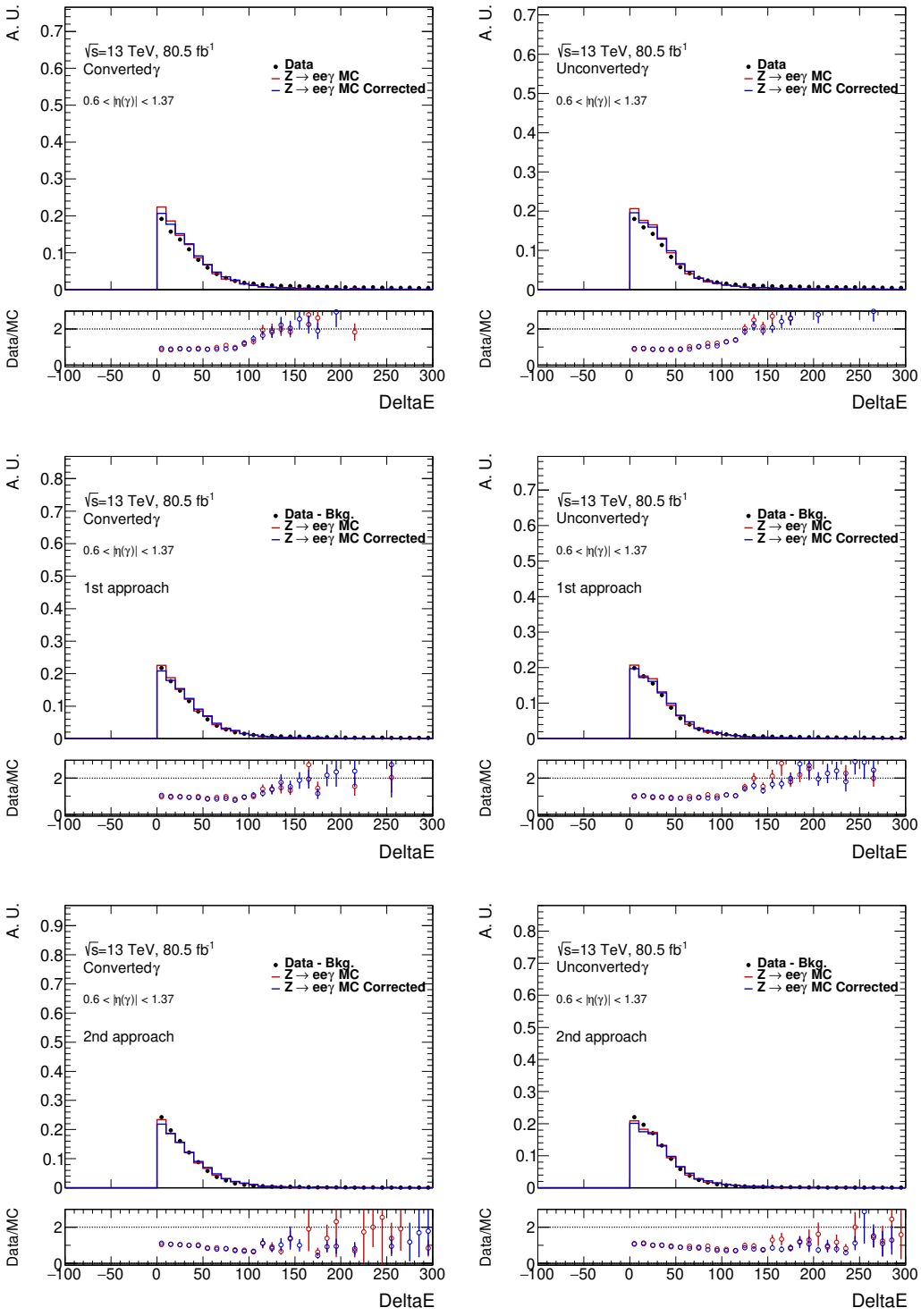

Figure A.16: DeltaE distributions in data (black) and MC before (red) and after (blue) correction in the 2nd eta region $0.6 < |\eta(\gamma)| < 1.37$. The left (right) column shows for converted (unconverted) photons, three distributions: nominal event selection case (top), 1st approach (middle), and 2nd approach (bottom) applied.

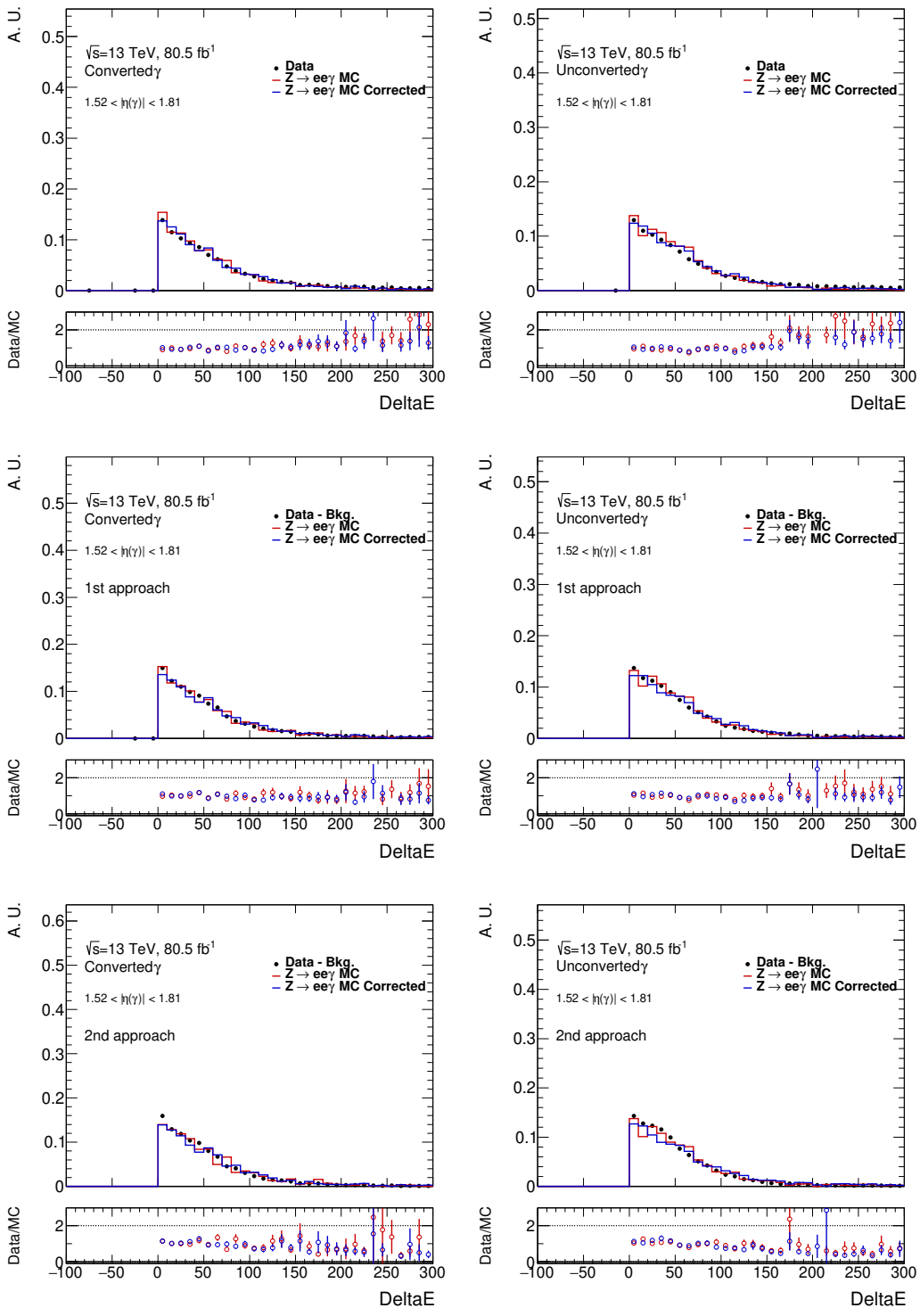

Figure A.17: DeltaE distributions in data (black) and MC before (red) and after (blue) correction in the 3rd eta region $1.52 < |\eta(\gamma)| < 1.81$. The left (right) column shows for converted (unconverted) photons, three distributions: nominal event selection case (top), 1st approach (middle), and 2nd approach (bottom) applied.

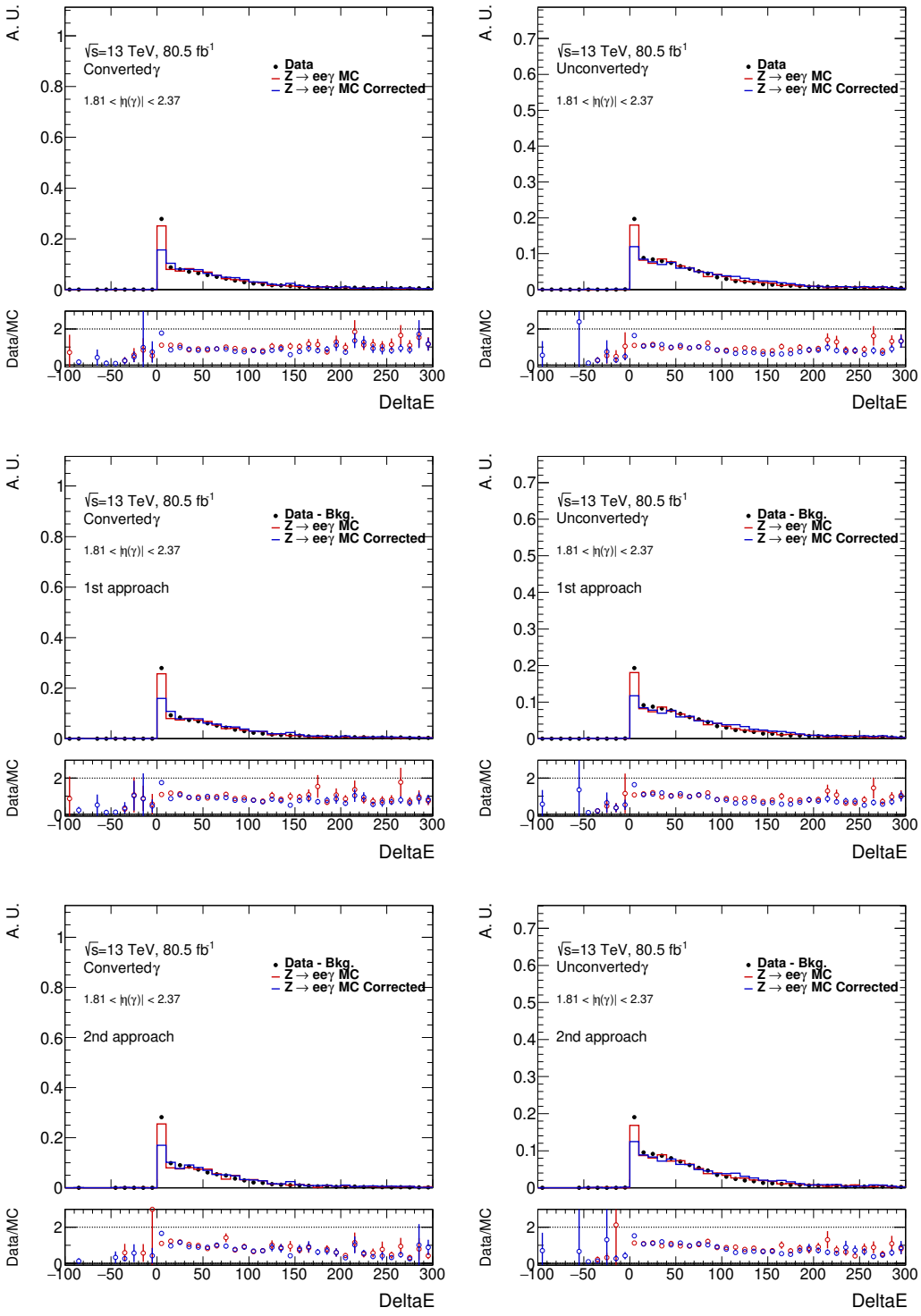

Figure A.18: DeltaE distributions in data (black) and MC before (red) and after (blue) correction in the 4th eta region $1.81 < |\eta(\gamma)| < 2.37$. The left (right) column shows for converted (unconverted) photons, three distributions: nominal event selection case (top), 1st approach (middle), and 2nd approach (bottom) applied.

APPENDIX B

Additional cross-section results

The full covariance matrices of the absolute cross-sections are shown in Tables B.1–B.5 and of the normalised ones are shown in Tables B.6–B.10.

Table B.1: Full covariance matrix of the absolute cross-section as a function of $p_T(\gamma)$, accounting for statistical and systematic uncertainties.

3.42e-02	7.26e-03	3.54e-03	2.44e-03	1.41e-03	9.95e-04	5.24e-04	3.20e-04	1.28e-04	4.19e-05	1.37e-05
7.26e-03	1.14e-02	2.14e-03	1.09e-03	6.80e-04	4.67e-04	2.60e-04	1.69e-04	6.49e-05	2.27e-05	8.39e-06
3.54e-03	2.14e-03	6.57e-03	1.06e-03	3.44e-04	2.61e-04	1.55e-04	9.45e-05	3.62e-05	1.22e-05	4.37e-06
2.44e-03	1.09e-03	1.06e-03	4.19e-03	5.33e-04	2.04e-04	1.28e-04	8.62e-05	3.30e-05	1.21e-05	4.00e-06
1.41e-03	6.80e-04	3.44e-04	5.33e-04	1.91e-03	2.20e-04	7.68e-05	5.32e-05	2.05e-05	7.67e-06	2.67e-06
9.95e-04	4.67e-04	2.61e-04	2.04e-04	2.20e-04	1.12e-03	7.83e-05	3.38e-05	1.38e-05	5.28e-06	1.79e-06
5.24e-04	2.60e-04	1.55e-04	1.28e-04	7.68e-05	7.83e-05	3.99e-04	2.71e-05	8.09e-06	3.08e-06	1.05e-06
3.20e-04	1.69e-04	9.45e-05	8.62e-05	5.32e-05	3.38e-05	2.71e-05	2.08e-04	7.49e-06	2.37e-06	8.79e-07
1.28e-04	6.49e-05	3.62e-05	3.30e-05	2.05e-05	1.38e-05	8.09e-06	7.49e-06	3.25e-05	1.09e-06	3.53e-07
4.19e-05	2.27e-05	1.22e-05	1.21e-05	7.67e-06	5.28e-06	3.08e-06	2.37e-06	1.09e-06	8.87e-06	1.56e-07
1.37e-05	8.39e-06	4.37e-06	4.00e-06	2.67e-06	1.79e-06	1.05e-06	8.79e-07	3.53e-07	1.56e-07	1.51e-06

Table B.2: Full covariance matrix of the absolute cross-section as a function of $|\eta(\gamma)|$, accounting for statistical and systematic uncertainties.

3.95e+00	5.05e-01	3.94e-01	4.18e-01	4.21e-01	3.89e-01	3.39e-01	2.17e-01
5.05e-01	3.83e+00	5.14e-01	4.07e-01	4.21e-01	3.98e-01	3.40e-01	2.15e-01
3.94e-01	5.14e-01	3.38e+00	4.80e-01	4.14e-01	4.06e-01	3.54e-01	2.23e-01
4.18e-01	4.07e-01	4.80e-01	3.69e+00	5.31e-01	4.41e-01	4.02e-01	2.56e-01
4.21e-01	4.21e-01	4.14e-01	5.31e-01	3.24e+00	5.73e-01	4.76e-01	3.12e-01
3.89e-01	3.98e-01	4.06e-01	4.41e-01	5.73e-01	2.70e+00	4.92e-01	3.07e-01
3.39e-01	3.40e-01	3.54e-01	4.02e-01	4.76e-01	4.92e-01	1.81e+00	3.06e-01
2.17e-01	2.15e-01	2.23e-01	2.56e-01	3.12e-01	3.07e-01	3.06e-01	6.07e-01

Table B.3: Full covariance matrix of the absolute cross-section as a function of $\Delta R(\gamma, l)_{\text{min}}$, accounting for statistical and systematic uncertainties.

8.18e+00	8.53e-01	5.64e-01	4.54e-01	3.64e-01	3.49e-01	3.37e-01	3.03e-01	1.62e-01	2.42e-02
8.53e-01	6.08e+00	6.13e-01	3.94e-01	3.12e-01	3.03e-01	3.03e-01	2.71e-01	1.44e-01	2.17e-02
5.64e-01	6.13e-01	4.96e+00	3.94e-01	2.63e-01	2.61e-01	2.69e-01	2.39e-01	1.40e-01	2.42e-02
4.54e-01	3.94e-01	3.94e-01	4.05e+00	3.51e-01	3.21e-01	2.98e-01	2.49e-01	1.81e-01	4.06e-02
3.64e-01	3.12e-01	2.63e-01	3.51e-01	2.15e+00	3.92e-01	3.35e-01	2.66e-01	2.24e-01	5.57e-02
3.49e-01	3.03e-01	2.61e-01	3.21e-01	3.92e-01	1.80e+00	3.46e-01	2.77e-01	2.29e-01	5.70e-02
3.37e-01	3.03e-01	2.69e-01	2.98e-01	3.35e-01	3.46e-01	1.84e+00	2.87e-01	2.26e-01	5.46e-02
3.03e-01	2.71e-01	2.39e-01	2.49e-01	2.66e-01	2.77e-01	2.87e-01	1.06e+00	1.99e-01	4.58e-02
1.62e-01	1.44e-01	1.40e-01	1.81e-01	2.24e-01	2.29e-01	2.26e-01	1.99e-01	6.77e-01	4.13e-02
2.42e-02	2.17e-02	2.42e-02	4.06e-02	5.57e-02	5.70e-02	5.46e-02	4.58e-02	4.13e-02	2.55e-02

Table B.4: Full covariance matrix of the absolute cross-section as a function of $\Delta\phi(l, l)$, accounting for statistical and systematic uncertainties.

5.77e-01	1.34e-01	1.34e-01	1.41e-01	1.41e-01	1.63e-01	1.60e-01	1.80e-01	1.79e-01	2.06e-01
1.34e-01	7.08e-01	1.67e-01	1.74e-01	1.79e-01	2.10e-01	2.08e-01	2.30e-01	2.19e-01	2.66e-01
1.34e-01	1.67e-01	1.03e+00	1.89e-01	1.96e-01	2.27e-01	2.26e-01	2.49e-01	2.29e-01	2.70e-01
1.41e-01	1.74e-01	1.89e-01	1.61e+00	2.09e-01	2.39e-01	2.35e-01	2.63e-01	2.50e-01	2.88e-01
1.41e-01	1.79e-01	1.96e-01	2.09e-01	1.66e+00	2.57e-01	2.55e-01	2.87e-01	2.68e-01	3.13e-01
1.63e-01	2.10e-01	2.27e-01	2.39e-01	2.57e-01	2.66e+00	3.01e-01	3.43e-01	3.17e-01	3.88e-01
1.60e-01	2.08e-01	2.26e-01	2.35e-01	2.55e-01	3.01e-01	2.87e+00	3.33e-01	3.04e-01	3.78e-01
1.80e-01	2.30e-01	2.49e-01	2.63e-01	2.87e-01	3.43e-01	3.33e-01	2.78e+00	3.53e-01	4.23e-01
1.79e-01	2.19e-01	2.29e-01	2.50e-01	2.68e-01	3.17e-01	3.04e-01	3.53e-01	2.91e+00	4.04e-01
2.06e-01	2.66e-01	2.70e-01	2.88e-01	3.13e-01	3.88e-01	3.78e-01	4.23e-01	4.04e-01	4.56e+00

Table B.5: Full covariance matrix of the absolute cross-section as a function of $|\Delta\eta(l, l)|$, accounting for statistical and systematic uncertainties.

2.50e+00	4.66e-01	5.30e-01	4.28e-01	3.54e-01	2.97e-01	2.21e-01	4.21e-02
4.66e-01	2.17e+00	4.68e-01	3.77e-01	3.09e-01	2.64e-01	1.96e-01	3.72e-02
5.30e-01	4.68e-01	2.61e+00	4.35e-01	3.53e-01	2.96e-01	2.25e-01	4.20e-02
4.28e-01	3.77e-01	4.35e-01	2.06e+00	2.89e-01	2.42e-01	1.83e-01	3.50e-02
3.54e-01	3.09e-01	3.53e-01	2.89e-01	1.66e+00	1.98e-01	1.49e-01	2.85e-02
2.97e-01	2.64e-01	2.96e-01	2.42e-01	1.98e-01	1.40e+00	1.26e-01	2.44e-02
2.21e-01	1.96e-01	2.25e-01	1.83e-01	1.49e-01	1.26e-01	7.74e-01	1.86e-02
4.21e-02	3.72e-02	4.20e-02	3.50e-02	2.85e-02	2.44e-02	1.86e-02	2.66e-02

Table B.6: Full covariance matrix of the normalised cross-section as a function of $p_T(\gamma)$, accounting for statistical and systematic uncertainties.

1.36e-05	2.53e-07	-5.27e-07	-4.47e-07	-3.83e-07	-2.64e-07	-2.32e-07	-1.14e-07	-6.16e-08	-2.21e-08	-8.60e-09
2.53e-07	5.11e-06	8.37e-08	-1.83e-07	-1.13e-07	-8.44e-08	-5.64e-08	-2.68e-08	-1.48e-08	-4.60e-09	-1.40e-09
-5.27e-07	8.37e-08	3.38e-06	1.79e-07	-7.28e-08	-3.76e-08	-1.88e-08	-9.50e-09	-5.00e-09	-1.20e-09	-2.00e-10
-4.47e-07	-1.83e-07	1.79e-07	2.32e-06	1.56e-07	9.90e-09	1.27e-08	1.32e-08	4.10e-09	2.20e-09	1.10e-09
-3.83e-07	-1.13e-07	-7.28e-08	1.56e-07	1.10e-06	6.71e-08	9.20e-09	7.80e-09	4.00e-09	1.80e-09	8.00e-10
-2.64e-07	-8.44e-08	-3.76e-08	9.90e-09	6.71e-08	6.57e-07	2.37e-08	5.50e-09	2.70e-09	1.40e-09	6.00e-10
-2.32e-07	-5.64e-08	-1.88e-08	1.27e-08	9.20e-09	2.37e-08	2.38e-07	8.80e-09	2.50e-09	1.20e-09	5.00e-10
-1.14e-07	-2.68e-08	-9.50e-09	1.32e-08	7.80e-09	5.50e-09	8.80e-09	1.25e-07	2.40e-09	7.00e-10	4.00e-10
-6.16e-08	-1.48e-08	-5.00e-09	4.10e-09	4.00e-09	2.70e-09	2.50e-09	2.40e-09	1.98e-08	5.00e-10	2.00e-10
-2.21e-08	-4.60e-09	-1.20e-09	2.20e-09	1.80e-09	1.40e-09	1.20e-09	7.00e-10	5.00e-10	5.50e-09	1.00e-10
-8.60e-09	-1.40e-09	-2.00e-10	1.10e-09	8.00e-10	6.00e-10	5.00e-10	4.00e-10	2.00e-10	1.00e-10	1.00e-09

Table B.7: Full covariance matrix of the normalised cross-section as a function of $|\eta(\gamma)|$, accounting for statistical and systematic uncertainties.

2.19e-03	3.83e-05	-3.69e-05	-6.47e-05	-8.36e-05	-5.51e-05	-2.33e-05	1.14e-05
3.83e-05	2.12e-03	4.06e-05	-6.28e-05	-7.43e-05	-4.83e-05	-1.09e-05	1.76e-05
-3.69e-05	4.06e-05	1.83e-03	-1.39e-05	-7.36e-05	-4.90e-05	-1.51e-05	9.90e-06
-6.47e-05	-6.28e-05	-1.39e-05	1.95e-03	-4.85e-05	-6.63e-05	-3.66e-05	-7.66e-06
-8.36e-05	-7.43e-05	-7.36e-05	-4.85e-05	1.61e-03	-3.30e-05	-5.41e-05	-2.11e-05
-5.51e-05	-4.83e-05	-4.90e-05	-6.63e-05	-3.30e-05	1.32e-03	-2.66e-05	-9.94e-06
-2.33e-05	-1.09e-05	-1.51e-05	-3.66e-05	-5.41e-05	-2.66e-05	8.18e-04	8.01e-06
1.14e-05	1.76e-05	9.90e-06	-7.66e-06	-2.11e-05	-9.94e-06	8.01e-06	2.73e-04

Table B.8: Full covariance matrix of the normalised cross-section as a function of $\Delta R(\gamma, l)_{\text{min}}$, accounting for statistical and systematic uncertainties.

4.88e-03	1.71e-04	2.55e-05	-5.91e-05	-1.50e-04	-1.38e-04	-6.78e-05	3.25e-05	5.92e-05	2.40e-05
1.71e-04	3.50e-03	7.16e-05	-5.96e-05	-1.22e-04	-1.12e-04	-6.00e-05	1.43e-05	2.89e-05	1.33e-05
2.55e-05	7.16e-05	2.89e-03	-6.81e-06	-9.81e-05	-8.54e-05	-4.97e-05	2.51e-06	1.57e-05	9.07e-06
-5.91e-05	-5.96e-05	-6.81e-06	2.34e-03	-2.80e-05	-3.42e-05	-2.90e-05	-8.63e-06	1.43e-05	1.01e-05
-1.50e-04	-1.22e-04	-9.81e-05	-2.80e-05	1.12e-03	7.21e-06	-1.65e-05	-2.21e-05	1.33e-05	1.12e-05
-1.38e-04	-1.12e-04	-8.54e-05	-3.42e-05	7.21e-06	9.09e-04	-8.64e-06	-2.06e-05	9.72e-06	9.03e-06
-6.78e-05	-6.00e-05	-4.97e-05	-2.90e-05	-1.65e-05	-8.64e-06	9.43e-04	-8.35e-06	1.25e-05	8.65e-06
3.25e-05	1.43e-05	2.51e-06	-8.63e-06	-2.21e-05	-2.06e-05	-8.35e-06	5.22e-04	2.16e-05	9.09e-06
5.92e-05	2.89e-05	1.57e-05	1.43e-05	1.33e-05	9.72e-06	1.25e-05	2.16e-05	3.61e-04	1.37e-05
2.40e-05	1.33e-05	9.07e-06	1.01e-05	1.12e-05	9.03e-06	8.65e-06	9.09e-06	1.37e-05	1.42e-05

Table B.9: Full covariance matrix of the normalised cross-section as a function of $\Delta\phi(l,l)$, accounting for statistical and systematic uncertainties.

2.96e-04	1.16e-06	-9.46e-06	-1.71e-05	-2.28e-05	-2.60e-05	-3.16e-05	-2.79e-05	-2.79e-05	-2.80e-05
1.16e-06	3.38e-04	-1.35e-05	-2.13e-05	-2.55e-05	-2.72e-05	-3.19e-05	-3.08e-05	-3.26e-05	-3.09e-05
-9.46e-06	-1.35e-05	5.13e-04	-2.64e-05	-3.25e-05	-3.60e-05	-4.09e-05	-4.05e-05	-4.43e-05	-4.84e-05
-1.71e-05	-2.13e-05	-2.64e-05	8.50e-04	-3.53e-05	-4.14e-05	-4.42e-05	-4.35e-05	-4.29e-05	-4.33e-05
-2.28e-05	-2.55e-05	-3.25e-05	-3.53e-05	8.62e-04	-3.77e-05	-3.95e-05	-4.17e-05	-4.22e-05	-3.49e-05
-2.60e-05	-2.72e-05	-3.60e-05	-4.14e-05	-3.77e-05	1.43e-03	-3.89e-05	-4.41e-05	-4.95e-05	-3.65e-05
-3.16e-05	-3.19e-05	-4.09e-05	-4.42e-05	-3.95e-05	-3.89e-05	1.57e-03	-4.59e-05	-4.83e-05	-3.33e-05
-2.79e-05	-3.08e-05	-4.05e-05	-4.35e-05	-4.17e-05	-4.41e-05	-4.59e-05	1.45e-03	-4.58e-05	-4.05e-05
-2.79e-05	-3.26e-05	-4.43e-05	-4.29e-05	-4.22e-05	-4.95e-05	-4.83e-05	-4.58e-05	1.57e-03	-2.99e-05
-2.80e-05	-3.09e-05	-4.84e-05	-4.33e-05	-3.49e-05	-3.65e-05	-3.33e-05	-4.05e-05	-2.99e-05	2.50e-03

Table B.10: Full covariance matrix of the normalised cross-section as a function of $|\Delta\eta(l,l)|$, accounting for statistical and systematic uncertainties.

1.18e-03	-7.62e-05	-8.68e-05	-7.71e-05	-6.12e-05	-4.76e-05	-3.88e-05	-9.19e-06
-7.62e-05	1.05e-03	-6.63e-05	-5.89e-05	-5.22e-05	-4.18e-05	-3.09e-05	-6.45e-06
-8.68e-05	-6.63e-05	1.24e-03	-6.58e-05	-5.88e-05	-4.75e-05	-3.42e-05	-7.69e-06
-7.71e-05	-5.89e-05	-6.58e-05	1.03e-03	-4.96e-05	-4.02e-05	-2.85e-05	-6.19e-06
-6.12e-05	-5.22e-05	-5.88e-05	-4.96e-05	8.63e-04	-3.34e-05	-2.40e-05	-5.33e-06
-4.76e-05	-4.18e-05	-4.75e-05	-4.02e-05	-3.34e-05	7.56e-04	-1.94e-05	-4.24e-06
-3.88e-05	-3.09e-05	-3.42e-05	-2.85e-05	-2.40e-05	-1.94e-05	4.15e-04	-2.90e-06
-9.19e-06	-6.45e-06	-7.69e-06	-6.19e-06	-5.33e-06	-4.24e-06	-2.90e-06	1.40e-05